Quantum Theory of Complex Ultracold Collisions

Matthew D. Frye

A Thesis presented for the degree of
Doctor of Philosophy

Joint Quantum Centre Durham-Newcastle
Department of Chemistry
University of Durham
England

June 2017

Quantum Theory of Complex Ultracold Collisions

Abstract

This thesis reports on a variety of calculations on cold and ultracold scattering, with a broad theme of how best to consider and understand complex systems in simple ways.

Firstly, we investigate quantum defect theory. We demonstrate that it is not only an excellent model for simple systems, but can also provide simple predictions of the *range* of possible behaviours for complex systems, in particular for a model of collisional losses. These predictions agree well with expensive coupled-channels calculations in cases where the full calculations also predict only the range of possible behaviours.

Secondly, we consider effects relating to thermalisation of cold and ultracold gases. We show that considering the correct transport cross section, $\sigma_\eta^{(1)}$, is important for determination of scattering lengths and their signs by interspecies thermalisation. This cross section is also important to the understanding of high-quality simulations of sympathetic cooling in a microwave trap, which suggest Rb is likely to be a good coolant for CaF. We also correct an error in the interpretation of previous results for sympathetic cooling in a magnetic trap, showing this may work from over 100 mK for Li+CaF and many Kelvin when using atomic hydrogen as a coolant.

Thirdly, we study quantum chaos in ultracold collisions. We find very clear and strong signs of chaos in Li+CaH. We also show that a more strongly coupled system, Li+CaF, is *not* fully chaotic and that there is unexpected structure in the levels of chaos as the CaF rotational constant is varied. We also show that signatures of chaos can emerge in a very simple atom-atom system, Yb($^1S_0$)+Yb($^3P_2$), which interacts on only two Born-Oppenheimer potentials.

Finally, we examine the idea that metastable states in 2-body scattering greatly enhance 3-body recombination at ultracold temperatures. We attempt to put it on a more rigorous theoretical grounding by considering Smith's collision lifetime and related quantities, but those are shown to lack clear interpretations in the ultracold regime. We therefore consider 3-body scattering theory and arrive at some general conclusions about how we expect such 2-body features to appear in 3-body scattering and suggest possible ways forward.

Declaration

I confirm that no part of the material offered has previously been submitted by myself for a degree in this or any other University. Where material has been generated through joint work, the work of others has been indicated.

Acknowledgements

I would first like to thank my supervisor Jeremy Hutson for his advice and guidance throughout my studies, and for constantly pushing me to improve all aspects of my work. I would also like to thank all the other members of the research group during my time: Daniel Brue, James Croft, Maykel González-Martínez, George McBane, Ruth Le Sueur, Jesse Lutz, Dermot Green, Morita Masato, Christophe Vaillant, and Daniel Owens, as well as the numerous undergraduate project students who have passed through the group. Particular thanks to Daniel Brue and Maykel for their invaluable guidance as I was just starting my work in this area, to Ruth for her assistance whenever I have needed to delve into the depths of MOLSCAT, and to George for being such an inspiring presence and enthusiastic educator for the year he was here. I would also like to thank Paul Julienne for many illuminating discussions on a wide variety of topics.

My thanks to my friends away from work, mostly the various incarnations of Trevelyan College MCR. In particular to Chris West, Emma Logan, Guy Barrett, Ollie Bartlett, James Nelson, Patrick Holmes, and Ben Beswick who have, at various times, been housemates, pool teammates, and drinking companions. Thanks also to the various orchestras and musical bands (and members thereof) that I have played in during the past years, as well as the Durham University Society of Change Ringers.

Thanks to my whole family for their continuing support and encouragement (and occasional nagging).

Finally, thanks to EPSRC for funding.

Contents

List of Figures

List of Tables

Chapter 1

Introduction

Cold and ultracold chemistry and physics have progressed dramatically over the past two decades since the first observations of atomic Bose-Einstein condensates (BECs) in 1995 [1–4]. Those seminal experiments marked what seemed to be a natural culmination of the long journey of cooling matter to ever colder temperatures. This progression of cooling produced many important scientific discoveries along the way, from the discovery and isolation of the noble gases [5] to superconductivity [6]. The realisation of BEC – where almost all particles exist in the same macroscopic quantum ground state – and its Fermionic counterpart [7] achieves quantum degeneracy. Although this is far from end of the road for cooling, we can no longer look for major progress or qualitatively new behaviours just from reducing temperatures further. Instead, attention has turned to making, cooling, and understanding more complex systems in order to observe an even richer variety of physics than is shown by the simple atoms of the early BEC experiments.

The novel physics of this cold and ultracold regime can mostly be thought to arise from one of two origins: firstly, the breakdown of Bohr's correspondence principle as temperature falls towards zero, removing the averaging over many quantum states that leads to observed classical behaviour; secondly, the thermal de Broglie wavelength

$$\lambda_{\mathrm{dB}} = \frac{h}{p} = \frac{h}{\sqrt{2mk_{\mathrm{B}}T}} \tag{1.0.1}$$

becomes a dominant length scale. For example, the onset of BEC can be thought

of, in conceptual terms, as either when all the particles begin to occupy the same lowest macroscopic translational level, or when λ_{dB} becomes comparable to the spacings between particles. It can already been seen that the crucial quantity for the interesting effects is rarely just the temperature itself, and other factors such as the mass of the particles can affect what energies and temperatures are of interest. Nonetheless, the physics community has broadly adopted the definition of cold to be below 1 K and ultracold to be below 1 mK.

1.1 Production and uses of cold and ultracold atoms and molecules

Ultracold atoms have been successfully produced for more than two decades. This is almost entirely built on the technique of laser cooling [8–11], which won the Nobel Prize in Physics 1997. The basic scheme of laser cooling (specifically Doppler cooling) is to irradiate a sample with light that is slightly red-detuned from an atomic transition, such that the Doppler shift experienced by a counter-propagating atom will bring it into resonance. The atom absorbs the photon along with its momentum which is opposite to the atom's propagation direction, thereby slowing it. The photon must be reemitted, but the direction is random and so there is still a net slowing effect on the atom. This effect is often combined with magnetic fields in order to assist bringing different velocities of atoms in different spatial regions into or out of resonance with the laser, for example in a Zeeman slower [12] or a magneto-optical trap (MOT) [13].

Doppler cooling has limits of the temperatures it can reach, and likely cannot cool atoms to BEC by itself. The limit is often determined by the natural linewidth of the transition, but there are further 'sub-Doppler' cooling effects that are subsequently used to reach even lower temperatures, such as optical molasses [14–16]. However, there is a fundamental photon-recoil limit beyond which laser-cooling usually cannot proceed. Beyond laser-cooling, evaporative cooling in a pure magnetic trap is used to reduce temperatures further [17, 18]. This was the final stage of cooling used to first achieve BEC [1]. This is often performed by using radio-frequency radiation to

drive transitions to untrapped states at magnetic field reached by only the hottest atoms in the trap. These techniques are now standard in many laboratories around the world.

Not all atoms are well suited to all these techniques. Evaporative cooling requires large numbers and high densities of the atoms, as well as suitable intra-species scattering properties for rethermalisation. In this case, it is possible to sympathetically cool these species by holding them in the same trap as a species which is being cooled. Provided the inter-species scattering properties allow sufficiently quick thermalisation then both species will be cooled. This method was first demonstrated for two different spin states of ^{87}Rb [19], then for different isotopes [20–22], and finally cooling one element with another [23, 24]. This method has greatly expanded the range of atoms that have been brought to ultracold temperatures. In particular, the scattering of identical fermions is strongly suppressed at low energy, so these will never be suitable for evaporative cooling, so sympathetic cooling with another species has been a commonly-used technique used to reach Fermi degeneracy [21–23].

Unfortunately, the techniques that have been so successful for cooling atoms have proved much more challenging to apply to molecules. Laser cooling techniques rely on a great many photon absorbance-emission cycles, so need a very nearly closed transition to work efficiently. However, molecules have a great deal of internal structure so the emission from the excited state will generally populate a mixture of states rather than just the desired state. It is only in the past few years that the difficulties associated with this have been successfully addressed for a very limited class of molecules, as discussed near the end of this section. The search for alternatives has led to a considerable variety of techniques for creating cold and ultracold molecules, with varying degrees of success. These are usually separated into "direct" methods, which take hot and/or fast molecules and make them cold, and "indirect" methods, which take ultracold atoms and convert them into ultracold molecules. So far, indirect methods have been the most successful for creating ultracold molecules in relatively large numbers, and direct methods have only recently achieved cooling to ultracold temperature for a very small number of molecules. However, the direct methods may be able to cool both a wider variety and more complicated molecules.

1.1.1 Production of ultracold molecules: Indirect methods

Indirect methods of producing ultracold molecules start from ultracold atoms and associate them into molecules. The great advantage of these methods is that if the association process is adiabatic then the molecules will produced at the same ultracold temperature as the atoms. The two different methods have been pursued in this area are photoassociation and magnetoassociation.

Photoassociation [25, 26] is essentially equivalent to a spectroscopy experiment: an intense laser field is used to transfer pairs of colliding atoms to a bound state. Initial proposals were to associate pairs of atoms to quasi-bound states on potential curves correlating with excited atomic states, which then spontaneously decay to truly bound states on the lowest potential curves [27–29], and this was first demonstrated experimentally for caesium [30]. An alternative to relying on spontaneous emission is to use stimulated emission from the excited state. This allows all the molecules to be produced in a single state and provides some degree of control over which state is to be populated [31, 32]. However, photoassociation suffers from very poor wavefunction overlap and rely on transfer from transient unbound collisional states, so typically struggle to produce large numbers of molecules.

Magnetoassociation [33] makes use of magnetic Feshbach resonances to associate pairs of atoms to form molecules. The magnetic field in the experiment is varied such that a quasi-bound state above the dissociation threshold moves to below threshold. As this state crosses the threshold, pairs of atoms colliding at the threshold transfer adiabatically from the continuum to the bound state and form very-weakly bound molecules often known as Feshbach molecules [34]. These Feshbach molecules have been formed for many combinations of atoms, mostly alkali-alkali systems [35–42] but recently more exotic atoms such as Dy [43], and there are proposals to magnetoassociate alkali metal atoms with alkaline earth atoms to make molecules with both electric and magnetic dipole moments [44–46].

Once formed, these Feshbach molecules can be transferred to deeper states, including the absolute ground state, by stimulated Raman adiabatic passage (STIRAP) [47, 48]. This involves a transition up to a state corresponding to an excited electronic configuration followed by stimulated emission back down to a lower rovi-

brational state of the original ground electronic state. This process is similar to 2-photon photoassociation, but with three important advantages: the wavefunction overlap is typically better when starting from a bound state rather than a scattering state; the interaction time is not limited by the lifetime of a collision; and the process can be performed coherently. To date, this is the only method to have produced a sample of ultracold molecules in their absolute ground state. The first molecule to be produced in this way was ^{40}K^{87}Rb [49], which was followed by ^{87}Rb^{133}Cs [50, 51], ^{23}Na^{40}K [52], and ^{23}Na^{87}Rb [53].

1.1.2 Production of ultracold molecules: Direct methods

Direct methods of producing ultracold molecules start with molecules at higher temperatures and cool them down to ultracold temperatures. An advantage of this is that in principle a wider variety of molecules can be produced rather than just those made from the limited selection of atoms available at ultracold temperatures. Polyatomic molecules are also likely to be easier to cool directly than by an indirect method. However, direct cooling of molecules to ultracold temperatures has not yet been demonstrated.

Buffer-gas cooling [54–56] makes use of a gas of cold helium atoms to cool hot molecules through simple thermal transport. It is conceptually similar to conventional refrigeration and atomic sympathetic cooling, a gas of cold helium is held in a cell and the target molecules are introduced, typically through laser ablation or a molecular beam [57, 58]. This was first demonstrated for molecules by Doyle [59]. It is generally successful at cooling both internal and translational degrees of freedom for a wide range of molecules [57, 58, 60–66], producing large quantities and high densities of the cooled molecules. The temperatures that can be reached with this method are limited by the temperature at which sufficient density of helium gas can be produced and contained, which typically limits final temperatures to 100s of milli-Kelvin. Additionally, the required additional step of removing the helium once the molecules are cooled is both time-consuming and will degrade the quality of the vacuum.

A more useful version of this method may be the buffer-gas beam [67–72]. The

difference with this method is that the helium and cooled molecules are expelled from the buffer-gas cell to form a beam. This produces a molecular beam that is internally cold, intense, and moving significantly slower than a conventional molecular beam. This set-up is more suitable for producing molecules that can be used in a further stage of an experiment away from the relatively dense sample of helium.

In order to slow a group of molecules in a beam to zero average velocity in the laboratory frame, Stark [73] or Zeeman [74] deceleration[1] [75] is commonly used. This makes use of the Stark or Zeeman effect of the molecules and an electric or magnetic field that oscillates along the path of the molecules. The group of high-field-seeking (low-field-seeking) molecules is slowed as kinetic energy is converted to Stark or Zeeman energy as they travel up the effective potential created by a decreasing (increasing) field; when they approach a minimum (maximum) in the field, it is switched such that the molecules again feel a decreasing (increasing) field. The deceleration caused by each individual rise in Stark or Zeeman energy is small, but if repeated a large number of times this can bring the molecules close enough to stationary to be captured by a suitable trap [76]. A improved version of this technique [77–81] uses continuously varying fields in place of the original sharply switched fields to maintain smoothly moving potential minimum through the length of the decelerater. The velocity of this minimum can then be decreased to slow molecules within it, and could ultimately become a static electric or magnetic trap. Stark and Zeeman deceleration do not cool molecules per se, but can slow the macroscopic motion of a cloud of molecules whose relative motion is cool, such as those produced in a buffer-gas beam. The combination of a buffer gas beam and Zeeman or Stark deceleration is a promising combination to cool a wide variety of molecules from readily available hot sources (e.g., room temperature gas bottle, or laser ablation) down to cold temperatures.

There are other methods that could produce samples of cold atoms. Kinematic, or "billiard ball", cooling [82–85] relies on a single collision, typically with a rare gas atom in a molecular beam, to slow a fast molecule from a molecular beam to rest

[1]Note that this in not the same thing as Zeeman slowing [12] used in atomic cooling, which is a type of laser cooling.

in the laboratory frame. Photostop [86–88] uses the recoil from photodissociation to cancel the laboratory-frame motion of a molecule in a molecular beam and leave one of the dissociated fragments stationary. Kinematic cooling relies on collisions resulting in a particular scattering angle to cancel the velocity of the molecule, and photostop relies on the dissociation fragments separating in the correct direction to cancel the velocity of one of them. Naturally, these conditions are not fulfilled for the majority of the molecules, but both techniques compensate for this by starting from a conventional molecule beam which can contain very large numbers of molecules by the standards of cold and ultracold experiments, and these techniques should be able to produce comparable temperatures and numbers as other cooling techniques.

Unfortunately, the direct cooling methods considered so far cannot reach temperatures below 100 mK with large numbers and high densities, and are not likely to be able to. Therefore, a further "second-stage" cooling technique will be required to reach ultracold temperatures. Direct evaporative cooling has been proposed for this stage [89], but that requires initially large numbers and high densities of molecules, which are rarely achievable. Further, the initial system considered for evaporative cooling was NH [89–91], but further calculations showed that evaporative cooling would likely be impaired by a reactive mechanism [92]. Nonetheless, evaporative cooling has been demonstrated for OH down to a few mK [93].

One of the leading candidates for this second-stage cooling is sympathetic cooling with ultracold atoms [94]. This has been a highly successful technique in the atomic case, but the critical difficulty for molecules relates to the magnetic traps that are most commonly used to trap molecules. These can trap only the low-field-seeking states, which can never be the lowest state so there will always be the possibility of inelastic collisions which will transfer molecules to an untrapped state. There has been much theoretical consideration of which systems might have sufficiently weak inelastic transitions to allow sympathetic cooling [95–107]. A few systems have been suggested as good candidates for sympathetic cooling in a magnetic trap, such as Mg+NH [100, 103], Li+NH [106], and Li+CaH [107]. A particularly important conclusion is that a light coolant will strongly suppress inelastic collisions at low magnetic field due to a large centrifugal barrier in outgoing channels [103, 106, 108];

this suggested the use of atomic hydrogen as a coolant [109, 110] and also that lithium may be a reasonable coolant for a wide variety of molecules.

Sympathetic cooling in traps other than static electric or magnetic traps is not necessarily sensitive to inelastic collisions. Sympathetic cooling in a microwave trap [111] has emerged as a promising alternative to using a magnetic trap [112, 113] as it allows molecules to be trapped in their ground state and therefore removes the possibility of inelastic collisions. This situation is considered in much greater detail in section 3.2 of this thesis.

Finally, laser cooling is a good option as a second-stage cooling technique for some molecules [114]. The crucial factor is for the Frank-Condon factors for the relaxation from the excited electronic state should be nearly diagonal. The numbers of photons that need to be scattered for useful cooling is of the order 10,000, so branching ratios of as little as 0.01% need to be considered. In practice this means that a large number of repumping lasers are needed for effective cooling of molecules, even in the most favourable cases. Some degree of laser cooling has been demonstrated for CaF [115, 116] and YO [117, 118], but the majority of work in this area has been on SrF, including the first demonstration of a molecular MOT [119, 120]. Very recently, temperatures as low as 250 μK have been reported [121, 122] for laser-cooling of SrF, representing the first example of direct cooling to reach ultracold temperatures.

1.1.3 Applications

The uses that ultracold molecules could be put to are many and varied [123]. Firstly, there are fundamental physics effects which will be observed at ultracold temperature. This is exemplified by Bose-Einstein condensation, which may show exciting new behaviours for molecules with electric and magnetic dipole moments [124], and other interesting effects might be observed by exploiting internal structure of the molecules to engineer novel trap geometries [125, 126]. In recent years, there has been growing interest in ultracold molecules (and atoms) that might show effects of quantum chaos [127–130].

There is great interest in the use of ultracold molecules for ultra-high-precision spectroscopy [131]. The low temperatures allow preparation of the single quan-

tum state of interest, and allow long coherence and observation times, dramatically increasing measured signal. Various line-broadening effects are also significantly reduced, in particular velocity-broadening. Certain molecules also have spectroscopic lines that are highly sensitive to certain fundamental physical constants that atoms may be insensitive to. Particular examples of this application are the search for an electron electric dipole moment [132, 133], to show physics beyond the standard model; and placing limits on the time-variation of fundamental physical constants [134], in particular the ratio of the mass of the electron to the mass of the proton, m_e/m_p [135–137].

One of the most exciting prospective uses for ultracold molecules is quantum computing [138–140]. However, that is probably still far removed from current experimental capabilities. What is more imminently feasible is quantum simulation, where ultracold molecules are made to form a model of a certain many-body Hamiltonian that is not computationally solvable with current computing technology, and the solution is read by simply observing the system. A particular focus has been on molecules with an electric dipole in an optical lattice interacting through their long-range (R^{-3}) dipole-dipole interaction, for example work on the molecular Hubbard Hamiltonian [141, 142]. Spin-exchange in an optical lattice have been observed [143], which is a first step towards quantum simulation.

Chemistry at ultracold temperatures behaves very differently from chemistry at hotter temperatures [144]. Single-state control allows unprecedented resolution and direct observation of quantum effects. For example, observations of chemical reactions of ultracold KRb [145] have demonstrated the suppression of collisions of identical fermions in the low-energy limit. There are also chemical reactions, such as Li+CaH→LiH+Ca that can be changed from allowed to forbidden depending on spin states of the reactants [107, 146]. It may therefore be possible to control these reactions with unprecedented precision by controlling initial states and the external magnetic and electric fields [147].

1.2 Scattering Theory

The theory of molecular scattering is quite extensive and good introductions can be found elsewhere [148]. Presented here is an overview of some relevant sections, based on Hutson [149]. Most of the theory will be written in terms of collisions, but many parts are also relevant to near-threshold bound-state calculations; the differences will be discussed towards the end of this section. We will describe most of the theory in the absence of external fields; the theory including these is conceptually very similar but the detailed description is significantly more complicated (see, e.g., Ref. 150). Although some of the calculations in this work do include such fields, understanding the details of such calculations is not needed to understand the results that are important to this work.

The scattering wavefunction (neglecting internal structure) can be written as

$$\Psi(\mathbf{R}) \overset{R\to\infty}{\sim} \Psi_0(\mathbf{R}) + R^{-1} f(\Theta) e^{ikR}, \tag{1.2.2}$$

where $\Psi_0(\mathbf{R})$ is the wavefunction without scattering, assumed to be a plane wave, $\mathbf{R}$ is the separation of the two particles, k is the wavevector, Θ is the scattering angle, and $f(\Theta)$ is the scattering amplitude, which is complex and determines the angular distribution of the scattering. The differential cross section is then

$$\frac{d\sigma}{d\omega} = |f(\Theta)|^2 \tag{1.2.3}$$

and the integral elastic cross section

$$\sigma_{\mathrm{el}} = \iint \frac{d\sigma}{d\omega} d\omega = 2\pi \int \frac{d\sigma}{d\omega} \sin\Theta \, d\Theta. \tag{1.2.4}$$

Some properties of collisions are not determined by the elastic cross section, but by various other effective cross sections, which are often called transport cross sections where they relate to transport properties of dilute gasses. The theory of these cross sections is extensive and discussed elsewhere (e.g. ref. [151]), but here we introduce

one transport cross section,

$$\sigma_\eta^{(1)} = 2\pi \int \frac{d\sigma}{d\omega}(1 - \cos\Theta)\sin\Theta \, d\Theta, \tag{1.2.5}$$

whose relevance to thermalisation will be discussed in chapter 3.

The Schrödinger equation relevant to a non-reactive, 2-body collision in the centre-of-mass (CM) frame is conveniently written

$$\hat{H}(R,\tau)\Psi(R,\tau) = E\Psi(R,\tau) \tag{1.2.6}$$

$$\left[-\frac{\hbar^2}{2\mu}R^{-1}\frac{d^2}{dR^2}R + \frac{\hat{L}^2}{2\mu} + \hat{H}_{\text{int}}(\tau) + V(R,\tau)\right]\Psi(R,\tau) = E\Psi(R,\tau) \tag{1.2.7}$$

where R refers to the inter-molecular separation and τ represents all other coordinates, Ψ is the collision wavefunction, E is the collision energy, μ is the reduced mass for the collision, $\hat{H}_{\text{int}}(\tau)$ is the internal Hamiltonian of the colliding particles at infinite separation, $\hat{L}$ is the operator for the relative angular momentum of the two particles around each other, and $V(r,\tau)$ is the potential, which contains all interactions between the two particles. The coupled-channel approach [152–155] to solving this problem handles the coordinates τ by a basis-set expansion and handles R by propagation on a grid. The total wavefunction is expanded as

$$\Psi(R,\tau) = R^{-1}\sum_i^N \phi_i(\tau)\psi_i(R), \tag{1.2.8}$$

where N is the number of basis functions used in the expansion. The form of the basis set, or "channel functions", $\phi_i(\tau)$, varies depending on upon the system under consideration and how it is represented. They will often be chosen to be eigenfunctions of $\hat{H}_{\text{int}}$, but this is not necessary. Typical examples would include rotational states of a rigid diatom, or electron and nuclear spin functions of an alkali atom. Also included in the channel functions is the angular motion of the two particles about each other, which corresponds to motion in the scattering angle Θ. Eigenstates of $\hat{L}^2$ – spherical harmonics $Y_L^m(\Theta,\phi)$ with partial-wave quantum number $L \geq 0$ and eigenvalue $\hbar L(L+1)$ – are almost always used for this. The

size of the basis set, N, generally has to be increased until numerical convergence is reached.

From here we are in a position construct the coupled equations to be solved. After substituting eq. (1.2.8) into eq. (1.2.7) and projecting onto a basis function ϕ_j, we find

$$\left[\frac{-\hbar^2}{2\mu}\frac{d^2}{dR^2} - E\right]\psi_j(R) = -\sum_i^N W_{ji}(r)\psi_i(R), \tag{1.2.9}$$

where the coupling-matrix elements

$$W_{ji}(r) = \int \phi_j^*(\tau)\left[\hat{H}_{\text{int}}(\tau) + V(r,\tau) + \frac{\hat{L}^2}{2\mu r^2}\right]\phi_i(\tau)d\tau \tag{1.2.10}$$

couple the solutions in different channels to each other. Assuming that the coupling matrix is diagonal asymptotically ($W_{ij}(R) \overset{R\to\infty}{\sim} \delta_{ij}W_{ii}(R)$; if not, it is straightforward to rotate into a basis where it is), we can separate the channels into "open" channels ($E > W_{ii}$), in which the particles have sufficient energy to reach infinite separation, and "closed" channels ($E < W_{ii}$), in which the particles cannot fully separate. We define the channel wavenumber k_i through

$$\frac{\hbar^2 k_i^2}{2\mu} = |E - W_{ii}(\infty)| = |E_{\text{k},i}^{\text{CM}}|, \tag{1.2.11}$$

where $E_{\text{k},i}^{\text{CM}}$ is the kinetic energy of the collision in channel i; the superscript denoting this as being in the CM frame is usually omitted, but will prove important for us in chapter 3.

The boundary conditions are

$$\Psi(R) \overset{R\to 0}{=} 0 \tag{1.2.12}$$

and

$$\Psi(R) \overset{R\to\infty}{\sim} R^{-1}\left[\phi_j(\tau)k_j^{-1/2}e^{-ik_jr+iL_j\pi/2} + \sum_i S_{ji}\phi_i(\tau)k_i^{-1/2}e^{ik_ir-iL_i\pi/2}\right], \tag{1.2.13}$$

where the sum runs over all open channels. The first part of eq. (1.2.13) describes an

incoming wave in channel j and the second part describes outgoing waves that may have been scattered into different channels. The effect of the scattering is described by an S-matrix, $\mathbf{S}$, with elements S_{ji}. The S-matrix is an $N_\mathrm{o} \times N_\mathrm{o}$ unitary complex symmetric matrix, where N_o is the number of open channels. Note that we still refer to this as an S-*matrix* even when there is only 1 open channel and it is a 1×1 matrix, although in that case the scattering is often characterised instead by a phase shift δ which is related to the S-matrix through $S = e^{2i\delta}$.

The short-range boundary condition eq. (1.2.12) does not uniquely define the wavefunction. There are N linearly independent wavefunctions which satisfy it, but we do not know which combination of them we need until they have been propagated to long range and matched to the asymptotic boundary conditions. Therefore, the usual computational procedure is to propagate all N solutions. Each of these solutions has N components, resulting in an $N \times N$ wavefunction matrix $\mathbf{\Psi}(R)$ with elements $\psi_{ij}(r)$, where one index specifies which of the N solutions and the other specifies which channel the component refers to. Although the wavefunctions can generally be complex, we can usually choose numerical solutions such that $\mathbf{\Psi}(R)$ is real for convenience. After propagation, these solutions are matched to a long-range boundary condition

$$\mathbf{\Psi}(r) \overset{r\to\infty}{=} \mathbf{J}(r) + \mathbf{N}(r)\mathbf{K}. \tag{1.2.14}$$

Here, $\mathbf{J}$(r) and $\mathbf{N}$(r) are diagonal matrices whose elements are

$$[\mathbf{J}(r)]_{ij} = \delta_{ij} r k_i^{1/2} j_{L_i}(k_i r) \tag{1.2.15}$$

$$[\mathbf{N}(r)]_{ij} = \delta_{ij} r k_i^{1/2} n_{L_i}(k_i r), \tag{1.2.16}$$

where $j_L(x)$ and $n_L(x)$ are spherical Bessel functions. $\mathbf{K}$ contains all the information about to the completed collision, equivalently to the S-matrix, to which it is related by

$$\mathbf{S} = (1 + i\mathbf{K}_{\mathrm{oo}})^{-1}(1 - i\mathbf{K}_{\mathrm{oo}}) \tag{1.2.17}$$

where K_{oo} is the part of the K-matrix between open channels.

The collision cross sections from asymptotic state α to β (which may be the

same, in the case of an elastic cross section) now become

$$\sigma_{\alpha,\beta} = \frac{\pi}{k_\alpha^2} \sum_{\substack{i\in\alpha \\ j\in\beta}} |\delta_{ij} - S_{ij}|^2. \tag{1.2.18}$$

The notation $i \in \alpha$ refers to all channels i which correspond to level α, which may include several channels, e.g. with different values of L_i. In the case of scattering of structureless particles we can rewrite this in terms of the phase shift for each partial wave, δ_L. In this case, we find

$$\sigma_{\text{el}} = \frac{4\pi}{k^2} \sum_{L=0}^{\infty} (2L+1) \sin^2 \delta_L. \tag{1.2.19}$$

In the case that it is not possible to scatter from channel i to another channel corresponding to the same asymptotic level, the total inelastic cross section can be written as

$$\sigma_{\alpha,\text{inel}} = \frac{\pi}{k_\alpha^2} \sum_{i\in\alpha} 1 - |S_{ii}|^2. \tag{1.2.20}$$

The collision problem can often be factorised into several smaller sets of coupled equations according to symmetry factors, such as different values of total angular momentum. This leads to separate S-matrices each of which contributes to the total cross sections independently.

Propagation methods

A method is needed to numerically propagate solutions generated at short range out to long range to match asymptotic boundary conditions. A primary concern for numerical algorithms when propagating such solutions is the behaviour in classically forbidden regions, where $W_{ii} > E$. In these regions the wavefunction can grow exponentially and can therefore cause numerical problems if care is not taken and its value explodes. Specialised propagation methods have been developed for scattering calculations, the most important of which are those that propagate not

the wavefunction but its log-derivative [156, 157]

$$\mathbf{Y}(R) = \frac{d\mathbf{\Psi}}{dR}\mathbf{\Psi}(R)^{-1}. \tag{1.2.21}$$

It is clear that in the single channel case this will be constant if the wavefunction itself is exponential, and those benefits also apply to the multi-channel case. A more extensive discussion of propagation methods can be found in Ref. [155].

1.2.1 Low-energy scattering

At low energy, scattering is dominated by threshold effects [158]. At low enough energy, scattering for $L \neq 0$ is suppressed by centrifugal barriers, and scattering in the s-wave ($L = 0$) channel is usefully characterised by the scattering length $a_\mathrm{s}(k)$. For scattering with only a single open channel this can be defined as

$$a_\mathrm{s}(k) = \frac{-\tan\delta_0}{k}. \tag{1.2.22}$$

It becomes constant at low enough energy, and in many cases the k-dependence can be safely neglected, but leading correction terms can be understood through effective range theory [159, 160]. The s-wave elastic cross section is

$$\sigma_\mathrm{el} = \frac{4\pi a_\mathrm{s}^2}{1 + a_\mathrm{s}^2 k^2}, \tag{1.2.23}$$

which shows that the elastic cross section takes a constant value of $4\pi a_\mathrm{s}^2$ at low energy, provided a_s is constant and $a_\mathrm{s}k \ll 1$, both of which will always become true at low enough energy. Note that eqs. (1.2.22) and (1.2.23) are not approximations and do not rely on any low-energy arguments, so are therefore accurate at any energy and for any value of a_s, although they may lose physical meaning away from low energy.

The interpretation of the scattering length at zero collision energy is that the wavefunction asymptotically tends towards a straight line, and the scattering length is the radius at which that line (although not necessarily the wavefunction itself) crosses zero. Therefore, the wavefunction is asymptotically the same as it would be

for a system whose potential consists only of a hard wall at $R = a_s$, even if this is negative. This interpretation agrees with the constant elastic cross section $4\pi a_s^2$.

Whenever there is a bound state exactly at threshold, the scattering length is infinite [161]. If the potential is scaled (i.e. $V(R) \to \lambda V(R)$) to make it deeper, then the bound state moves to just below threshold and a_s is large and positive; as the potential is deepened further the state moves further down and the value of a_s decreases. As the potential gets close to supporting another bound state a_s becomes large and negative and then when the new bound state is just at threshold it becomes infinite again. This means that, if there are many bound states, the scattering length can be highly sensitive to the details of the interaction potential. If there is sufficient uncertainty in the potential to cover the range of changing the number of bound states by 1 or more, then that uncertainty translates to a scattering length that could be anywhere between $-\infty$ and ∞. The uncertainties associated with potentials from *ab initio* electronic structure theory do not usually allow calculation of reliable scattering lengths unless the system has very few bound states. High quality interaction potentials for ultracold physics must therefore usually come from comparison with experimental results and careful fitting [162, 163].

If there are several open channels then the scattering length becomes a complex quantity $a(k) = \alpha(k) - i\beta(k)$. It is given for channel i as [164]

$$a_i(k) = \frac{1}{ik_i}\left(\frac{1 - S_{ii}(k)}{1 + S_{ii}(k)}\right). \tag{1.2.24}$$

Like the single-channel scattering length, it becomes constant at low energy, and determines both elastic and total inelastic s-wave cross sections [164]

$$\sigma_{\mathrm{el}} = \frac{4\pi|a_s|^2}{1 + k^2|a_s|^2 + 2k\beta} \tag{1.2.25}$$

and

$$\sigma_{\mathrm{inel}} = \frac{4\pi\beta}{k(1 + k^2|a_s|^2 + 2k\beta)}. \tag{1.2.26}$$

However, it generally does not diverge when there is a state at threshold. In the single-channel case, a diverges when $S_{ii} = -1$ and the denominator in eq. (1.2.24)

is zero, but if there is inelastic scattering then $|S_{ii}| < 1$ and the divergence of the scattering length is suppressed [164].

1.2.2 Resonances

Scattering resonances occur when there is a quasi-bound state which is coupled to the incident channel. They can be caused either by states in a closed channel (Feshbach resonances) or by states in an open channel trapped behind a centrifugal barrier (shape resonances). Either of these will cause sharp features in the scattering properties as a function of energy. If there is only one open channel, then an isolated narrow resonance will cause the phase to vary according to the famous Breit-Wigner form

$$\delta = \delta_{\mathrm{bg}} + \arctan\left(\frac{\Gamma_E}{2(E_{\mathrm{res}} - E)}\right), \tag{1.2.27}$$

where Γ_E characterises the width of the resonance, E_{res} is the position in energy of the resonance, and δ_{bg} is a slowly varying background term. This corresponds to the S-matrix element tracing the unit circle in the complex plane. If there is more than one open channel, then *all* the S-matrix elements trace circles of various radii in the complex plane [165]. The quantity that follows eq. (1.2.27) is the eigenphase sum, which is the sum of the phases associated with the eigenvalues of $\mathbf{S}$.

The situation is different when we consider a fixed collision energy at or near threshold as an external field is varied. The bound state energy typically varies with field in a different way to the threshold, so there is a possibility of a state moving across threshold as a function of an external field. This creates a "zero-energy" Feshbach resonance, and it has been most commonly demonstrated using a varying magnetic field so is sometimes called a magnetic Feshbach resonance [166, 167]. In this case, the important quantity is the scattering length, which varies for the single-open-channel case as [168]

$$a(B) = a_{\mathrm{bg}}\left[1 - \frac{\Delta_B}{B - B_{\mathrm{res}}}\right], \tag{1.2.28}$$

where B_{res} is the field at which the resonance occurs, Δ_B characterises its width, and a_{bg} is the background scattering length away from the resonance. This shows a

pole which coincides with the position at which the bound state crosses threshold, as discussed earlier. Careful control of the magnetic field allows controlled variation of the scattering length to a wide range of values. The use of zero-energy Feshbach resonances in this way has been crucial to a great many aspects of ultracold physics in the past two decades.

If there are multiple open channels, then the behaviour is again more complicated [164]. The pole is suppressed, and the real and imaginary parts of the scattering length show an oscillation, which may either be very large if there is little inelastic decay from the resonant state, or very small if the quasi-bound state is strongly decayed. The scattering length describes a circle in the complex plane

$$a(B) = a_{\mathrm{bg}} + \frac{a_{\mathrm{res}}}{2(B - B_{\mathrm{res}})/\Gamma_B^{\mathrm{inel}} + i}, \tag{1.2.29}$$

where the 'resonance scattering length' a_{res} characterises how large an oscillation a shows and Γ_B^{inel} characterises the inelastic loss from the resonance.

An extensive review on "Feshbach resonances in ultracold gases" can be found in Ref. [169].

1.2.3 Bound states

The coupled-channels method is also applicable to the problem of finding bound states, and is particularly suited to finding weakly-bound states that extend out to large R. The Schrödinger equation, expansion of the wavefunction and resulting coupled equations (eqs. (1.2.7) to (1.2.9)) are the same as the case of scattering. For a bound state, the wavefunction dies to zero not only as $R \to 0$ but also as $R \to \infty$, and at most energies it will not be possible for the wavefunction to satisfy both boundary conditions at the same time. It is therefore necessary to perform a calculation at a particular energy, check to see if it meets the boundary conditions, and if not then refine the energy and repeat the process.

Numerically, a single propagation starting at one end of the range and proceeding to the other end would inevitably run into numerical instability as it is propagating into a classically forbidden region at the end of its propagation. Therefore *two*

propagations are performed, one outwards from a small value of R, $\psi^+(R)$, and one inwards from a large value of R, $\psi^-(R)$, and if the energy is a bound-state energy then it will be possible to match both the wavefunctions and their derivatives at a matching point R_{match} somewhere in a classically allowed region near the middle of the range. As the wavefunctions can be scaled arbitrarily, it will always be possible for their values to be made to match, but the criterion for their derivatives matching is

$$[\psi^+(R_{\mathrm{match}})]'/\psi^+(R_{\mathrm{match}}) - [\psi^-(R_{\mathrm{match}})]'/\psi^-(R_{\mathrm{match}}) = 0 \tag{1.2.30}$$

for the case of a single channel. With the expression in this form, standard numerical techniques for finding zeros of functions can be used to converge on a bound state energy. In the multichannel case, it is again necessary to propagate N independent solution, and the matching condition becomes

$$\det\left[\mathbf{Y}^+(R_{\mathrm{match}}) - \mathbf{Y}^-(R_{\mathrm{match}})\right] = 0, \tag{1.2.31}$$

although numerically it is more convenient to work with eigenvalues of $\mathbf{Y}^+(R_{\mathrm{match}}) - \mathbf{Y}^-(R_{\mathrm{match}})$ rather than the complete determinant [155]. It is also possible to implement a 'node-counting' algorithm that counts the number of eigenvalues below the current energy, thus making it easy to bracket the eigenvalues and ensure that all states in a range are found [153–155, 170].

1.2.4 Computer programs

There are readily available computer programs built to perform coupled-channels calculations as described in this section. We use Hutson's MOLSCAT [171] for scattering calculations, and the closely related BOUND [172] for bound-state calculations. The HIBRIDON package [173] is also available for scattering calculations. We also use FIELD [174] for locating states at a particular energy as a function of an external parameter (such as magnetic field). The procedure is very similar to locating bound states in energy except that it is the field that is varied in place of energy. This is not a formally rigorous process, like finding states in energy is, but works very well in practice.

1.3 Publications arising from this work

- [175] M. D. Frye and J. M. Hutson, *Collision cross sections for the thermalization of cold gases*, Phys. Rev. A 89, 052705 (2014)

- [176] M. D. Frye, P. S. Julienne, and J. M. Hutson, *Cold atomic and molecular collisions: approaching the universal loss regime*, New J. Phys. 17, 045019 (2015)

- [113] J. Lim, M. D. Frye, J. M. Hutson, and M. R. Tarbutt, *Modeling sympathetic cooling of molecules by ultracold atoms*, Phys. Rev. A 92, 053419 (2015)

- [129] D. G. Green, C. L. Vaillant, M. D. Frye, M. Morita, and J. M. Hutson, *Quantum chaos in ultracold collisions between* $Yb(^1S_0)$ *and* $Yb(^3P_2)$, Phys. Rev. A 93, 022703 (2016)

- [130] M. D. Frye, M. Morita, C. L. Vaillant, D. G. Green, and J. M. Hutson, *Approach to chaos in ultracold atomic and molecular physics: Statistics of near-threshold bound states for Li+CaH and Li+CaF*, Phys. Rev. A 93, 052713 (2016)

Chapter 2

Quantum Defect Theory (QDT)

Quantum defect theory (QDT) is a family of powerful theories that exploit the different energy scales between different regions in a scattering or near-threshold bound-state system. QDT was originally developed in the context of atomic Rydberg states [177, 178]; these are electronic states immediately below the ionisation threshold of a neutral atom which can alternatively be considered as near-threshold bound states of the corresponding electron-ion system. In this interpretation, the electron moves primarily in the long-range Coulomb potential outside the ion core. In the simplest case, where there is no deviation from the pure Coulomb interaction, the energy levels are given by

$$E_n = \frac{me^4}{2\hbar^2}\frac{Z^2}{n^2} \tag{2.0.1}$$

where e is the fundamental charge, m is the reduced mass of the electron-ion system, Z is the charge on the ion, and n is the principal quantum number. This is an excellent approximation for atomic hydrogen. However, for more complicated atoms, the energy levels are better approximated by

$$E_n = \frac{me^4}{2\hbar^2}\frac{Z^2}{(n-\mu_n)^2}, \tag{2.0.2}$$

which introduces the "quantum defect" μ_n. This varies slowly with n, which is equivalent to varying slowly with energy. In effect, this separates the problem into two parts: the overall structure of the equation is still the same as eq. (2.0.1), which corresponds to the long-range region where the electron is far from the ion core and

the interaction is well approximated as a pure Coulomb potential; and secondly, the short-range region where the effect of the ion core and the complex interactions associated with it are not explicitly considered, but simply parameterised into a single value μ_n. This value corrects for the effect of the ion core, and varies slowly with energy, leading to a simple solution to a potentially difficult many-electron problem. In fact, some of the ideas of QDT echo earlier work on collisions of neutrons with nuclei by Bethe [161]. In that work, the problem was also separated into a short-range region whose effect was parameterised without consideration of the detailed interactions (the nucleus), and a simplified long-range region (free motion of the neutron); this simple model was used to explain the unexpectedly common appearance of large elastic and neutron-capture cross sections.

Since the initial conception of the theory, further work has greatly expanded and developed QDT, including applying it to electron-ion scattering above threshold [179], multi-channel problems [177, 180, 181], and different kinds of long-range potentials. In particular, it has been realised that the Coulomb potential gives QDT a particularly simple form and that other long-range potentials are usually more complex to deal with [182–184]. In all these cases, the basic idea is the same: the short-range and long-range parts of the problem are approximated in different ways. The short-range part is usually parameterised in some way to avoid dealing with the typically complex interactions in that region; it is also common to approximate the parameterisation either to not vary or vary only slowly with energy. The long-range part is approximated (often quite drastically) to allow solutions to be readily found; the approximations used typically remove many of the difficult details of the system but often also remove distinguishing features that make the system distinct from similar systems. We will therefore often consider the long range to be so generic that is can be thought of as system-independent, but the short range will vary by system. The separation between short- and long-range regions is often mostly conceptual and does not need to be specified exactly, although some numerical methods do require a given location for the change from one region to the other.

In the case of cold and ultracold scattering, there is also a disparity in energy scales that can be exploited in a similar way to the case of Rydberg states. The

collision/binding energies are of the order 1 K or usually much smaller, and the interaction potentials rapidly approach a similar magnitude at long range, but the potentials typically reach the equivalent of 10 to 10,000 K at their deepest points at short range. At long range, the approximations are usually that the interaction potential can be represented by a standard asymptotic form (such as $-C_6 r^{-6}$), and, in multi-channel systems, that there is no coupling between channels. These approximations are usually so drastic that the resulting solutions have no validity except at long range. At short range, the typical approximation is that the solution is independent of energy, or slowly varying, because the range of energy of interest ($\ll 1$ K) is much smaller than the local energy scale ($10 \sim 10000$ K). The application of QDT to cold and ultracold collisions was pioneered by Julienne and Mies [185] and has been taken up by numerous other authors, mainly for collisions of neutral particles [186–195], including scattering of two dipoles [196, 197], and also for ion-atom collisions [198–202]. One particularly successful application of QDT has been in the description of resonances at and near zero energy [203–205].

This chapter is laid out as follows. Section 2.1 sets out the theory of QDT, specifically Gao's expression of QDT including angular-momentum-insensitive QDT (AQDT). In section 2.2 we systematically compare AQDT predictions with calculations on real systems with reliable interaction potentials, demonstrating excellent agreement for simple systems, but showing the limitations of the theory for more complex multi-channel systems. In section 2.3 we develop an effective single-channel model to quantify typical behaviours of complex systems and compares it with realistic calculations on the complex system Li+LiH.

2.1 Theoretical presentation

QDT can be used as either a powerful analytic theory (e.g. [206]) or an efficient numerical technique (e.g. [191]), but in either case the principles are the same. The true solution is described as a linear combination of reference functions with known behaviour at certain points - reference functions are solutions for the problem, under the approximations used in the long-range region. The crucial aspect of QDT

is the transformation between different sets of reference functions with particular behaviours. Typically, two sets of reference functions are used, one that is convenient to describe the solution at short-range, usually with WKB-like normalisation conditions, and the other suitable for matching to asymptotic boundary conditions. Using reference functions allows the transformation from the short-range solution to the asymptotic limit to be described in a small number of parameters. As the reference functions and the transformation are not directly dependent on the particular true solution, these parameters are applicable for a given model of the long-range interactions whatever the short-range details. On a computational level, this allows us to be efficient and not re-calculate solutions in the long-range region for every slight variation in the short-range region. It also facilitates analytic approaches which allow simple relationships to be obtained between short-range parameters and asymptotic observables, and can provide clear insight into the separation of system-dependent and system-independent effects.

We assume that the solution in the short-range region is known and/or parameterised. Recent applications in the literature have obtained this, for example, using explicit coupled-channel calculations [191–193] or a statistical description of a chaotic set of resonances [207, 208], although it is also common just to describe it with one or more parameters which are to be empirically determined. As this short-range solution will be used as a boundary condition, how it is obtained does not make a difference to the basic theory. However, many of the ways in which we use the theory in this work are only applicable if the short-range solution can be approximated to be independent of energy.

Within the general scheme outlined so far, there are many possible implementations. Distinguishing features of these can include some (but not necessarily all) of: how the short-range region is described; what approximations are applied to the long-range region; how the reference functions are defined; and how the transformation between reference functions is parameterised. For cold and ultracold collisions, the most commonly used implementation is that of Mies and Julienne [181, 185, 209, 210], which is similar to the earlier version of Seaton [177] and is excellent for description of resonances [204]. However, we prefer to use Gao's version

in this work as I feel it to be a more naturally elegant mathematical description, and because it helps to emphasise some elements of the system-invariance QDT can show. In particular, it provides a clean separation between parameters characterising the short-range interactions, and parameters relating to the effect of the long-range potential and the transformation of reference functions; by contrast, this distinction can become blurred in the Mies and Julienne description, to the point that in some uses the reference functions and their transformations depend explicitly on the effect of the short-range region, which can obscure much of the commonality between different systems.

2.1.1 Gao's AQDT

The theory presented in this section is predominantly drawn from the work by Gao on single-channel QDT [184, 187, 206, 211–214]. In particular, ref. [184] lays out the important elements of the formalism in a complete and systematic manner, and we base our analysis on that work. Note that particularly careful attention to superscripts and subscripts is needed throughout.

Gao's expression of QDT has been built around his earlier analytic solutions to the Schrödinger equation eq. (1.2.9) with a pure attractive $-C_6 r^{-6}$ potential [211], and we take the same approach here. However, the formalism presented could also be used with other solutions, including numerical solutions calculated using a more realistic long-range potential. The solutions themselves are immensely complicated [211] and will not be discussed in detail here, but they are valid for arbitrary partial wave and energy. We use code that Gao has written to calculate these solutions [215], or quantities pertaining to them as discussed below. The use of these solutions requires the approximation of the potential in the long-range region to consist only of the $-C_6 r^{-6}$ term – the validity of this approximation in calculations on realistic systems is considered in section 2.2.

It will often be convenient to write quantities in terms of the length and energy scales associated with the long-range $-C_6 r^{-6}$ interactions. We use the length scale

$$r_6 = \left(\frac{2\mu C_6}{\hbar^2}\right)^{1/4}, \tag{2.1.3}$$

and energy scale

$$E_6 = \frac{\hbar^2}{2\mu r_6^2}, \tag{2.1.4}$$

which are also used by Gao, although he usually calls them β_6 and s_E respectively. These scales, and the approximation of the interaction potential to just its long-range $-C_6 r^{-6}$ form, allow the Schrödinger equation, eq. (1.2.7), to be rewritten in the dimensionless form

$$\left[-\frac{d^2}{dr_\mathrm{s}^2} - \frac{1}{r_s^6} + \frac{L(L+1)}{r_\mathrm{s}^2} - \epsilon\right] \psi(r_\mathrm{s}) = 0, \tag{2.1.5}$$

where $r_\mathrm{s} = r/r_6$ and $\epsilon = E/E_6$ are the reduced separation and energy. This removes the explicit dependence on system-dependent quantities, C_6 and reduced mass μ, instead replacing them with energy and length scales. This gives rise to many of the ideas involved in "universality", where different systems may show identical behaviour if quantities are measured in units of these scales rather than in absolute scales such as SI units. Other authors sometimes use the length and energy scales $r_\mathrm{vdw} = r_6/2$ and $E_\mathrm{vdw} = \hbar^2/(2\mu r_\mathrm{vdw}^2) = 4E_6$, but those do not rescale the Schrödinger equation in such a convenient way. Another important length scale is the mean scattering length of Gribakin and Flambaum [216],

$$\bar{a} = \frac{2\pi}{[\Gamma(1/4)]^2} r_6 = 0.477\,988\,8\ldots r_6 = 0.955\,977\,6\ldots r_\mathrm{vdw}, \tag{2.1.6}$$

where $\Gamma(x)$ is the Gamma function. which is the most relevant scale for scattering lengths. It is the average value of the scattering length for a system with a potential that behaves as $C_6 r^{-6}$ at long range.[1] We will often give scattering lengths as multiples of $\bar{a}$ throughout this entire thesis. It also has an associated energy scale of $\bar{E} = \hbar^2/(2\mu\bar{a}^2)$. Values of some of these scales are given for example systems in table 2.1.

The reference wave functions are now particular solutions to eq. (2.1.5), which are defined by their boundary conditions. To facilitate using them as a basis for

[1] Technically, it is the Cauchy principal value rather than the average as the scattering length has a non-integrable singularity.

Table 2.1: Energy and length scales for example systems.

System	$C_6/E_\mathrm{h}a_0^6$	μ/u	r_6/Å	$(E_6/k_\mathrm{B})/\mu$K	$\bar{a}$/Å
^{6}Li+^{174}Yb [217]	1594	5.81	40.3	2560	19.3
Mg+NH [99, 218]	158.12	9.23	25.417	4070	12.1
^{87}Rb+Cs [42]	5694	52.55	96.2	49.9	46.0
^{164}Dy+^{164}Dy [128]	2003	81.96	82.77	43.2	39.6
KRb+KRb [219]	16133	63.44	131	22.4	62.5

describing our true solution, they are defined in pairs. Following the definitions and notation of Gao [184], the first reference functions we define are

$$f_L^\mathrm{c}(r_\mathrm{s}) \overset{r_\mathrm{s}\to 0}{\sim} \sqrt{\frac{2}{\pi}} r_\mathrm{s}^{3/2} \cos(r_\mathrm{s}^{-2}/2 - \pi/4) \tag{2.1.7}$$

$$g_L^\mathrm{c}(r_\mathrm{s}) \overset{r_\mathrm{s}\to 0}{\sim} \sqrt{\frac{2}{\pi}} r_\mathrm{s}^{3/2} \sin(r_\mathrm{s}^{-2}/2 - \pi/4). \tag{2.1.8}$$

These are standing-wave solutions that have WKB-like normalisation at short range; these are sometimes referred to as "short-range solutions" because they have known and useful behaviour at short range, but they are defined for all values of r_s. This pair are very similar to the solutions originally calculated by Gao [211] and are central to his description of QDT. In particular, note these these short-range boundary conditions are independent of both energy and angular momentum, although the solutions away from $r_\mathrm{s} = 0$ will obviously vary with both energy and L. Next, we define the equivalent standing-wave solutions normalised at long range,

$$s_L(r_\mathrm{s}) \overset{r_\mathrm{s}\to\infty}{\sim} \sqrt{\frac{2}{\pi k_\mathrm{s}}} \sin(k_\mathrm{s} r_\mathrm{s} - L\pi/2) \tag{2.1.9}$$

$$c_L(r_\mathrm{s}) \overset{r_\mathrm{s}\to\infty}{\sim} \sqrt{\frac{2}{\pi k_\mathrm{s}}} \cos(k_\mathrm{s} r_\mathrm{s} - L\pi/2), \tag{2.1.10}$$

for $\epsilon > 0$, where $k_\mathrm{s} = \sqrt{\epsilon}$; Gao also provides versions for $\epsilon < 0$ in ref. [184] but we will not need them here. These two sets of reference functions are related by

$$\begin{pmatrix} f^\mathrm{c} \\ g^\mathrm{c} \end{pmatrix} = Z^\mathrm{c} \begin{pmatrix} s \\ c \end{pmatrix} = \begin{pmatrix} Z_{fs}^\mathrm{c} & Z_{fc}^\mathrm{c} \\ Z_{gs}^\mathrm{c} & Z_{gc}^\mathrm{c} \end{pmatrix} \begin{pmatrix} s \\ c \end{pmatrix}, \tag{2.1.11}$$

which defines the 2×2 transformation matrix Z^c. This matrix varies with ϵ and

L, but we will usually suppress those labels. The four elements of Z^{c} are not all independent and are limited by $\det(Z^{\mathrm{c}}) = 1$. As part of his solutions for the r^{-6} potential, Gao found explicit, if complicated, analytical expressions for the elements of Z^{c} [211] and we use computer code [215] written by him to evaluate them.

We now consider a particular solution ψ to eq. (2.1.5). We define it as a linear combination of reference solutions,

$$\psi(r_{\mathrm{s}}) = C\left(f^{\mathrm{c}}(r_{\mathrm{s}}) - K^{\mathrm{c}} g^{\mathrm{c}}(r_{\mathrm{s}})\right), \tag{2.1.12}$$

where C is an arbitrary normalisation constant and K^{c} is a short-range K-matrix analogous to the asymptotic K-matrix in eq. (1.2.14). As with the S-matrix, we still call this a K-*matrix* even although we are dealing with a single-channel problem. Equally, we can rewrite eq. (1.2.14) itself in terms of our reference solutions as

$$\psi(r_{\mathrm{s}}) = C'\left(s(r_{\mathrm{s}}) - Kc(r_{\mathrm{s}})\right), \tag{2.1.13}$$

note that the limit in eq. (1.2.14) has become an equality in this case. Combined with eq. (2.1.11), this allows us to write down the relation between the short-range and asymptotic K-matricies as

$$K = \frac{Z^{\mathrm{c}}_{gc} K^{\mathrm{c}} - Z^{\mathrm{c}}_{fc}}{Z^{\mathrm{c}}_{fs} - Z^{\mathrm{c}}_{gs} K^{\mathrm{c}}}, \tag{2.1.14}$$

which is a central equation of QDT.

In addition to the standing-wave reference functions, eqs. (2.1.7) to (2.1.10), we can also define travelling-wave reference functions. These are defined pairs of incoming ($-$) and outgoing ($+$) waves. First at short range, called the inner region by Gao,

$$f^{\mathrm{i}+}(r_{\mathrm{s}}) \overset{r_{\mathrm{s}}\to 0}{\sim} \sqrt{\frac{1}{\pi}} r_{\mathrm{s}}^{3/2} \exp[-i(r_{\mathrm{s}}^{-2}/2)] \tag{2.1.15}$$

$$f^{\mathrm{i}-}(r_{\mathrm{s}}) \overset{r_{\mathrm{s}}\to 0}{\sim} \sqrt{\frac{1}{\pi}} r_{\mathrm{s}}^{3/2} \exp[+i(r_{\mathrm{s}}^{-2}/2)], \tag{2.1.16}$$

and at long range, called the outer region by Gao,

$$f^{\mathrm{o}+}(r_{\mathrm{s}}) \overset{r_{\mathrm{s}}\to\infty}{\sim} \sqrt{\frac{1}{\pi k_{\mathrm{s}}}} e^{i\pi/4} \exp[+ik_{\mathrm{s}}r_{\mathrm{s}}] \tag{2.1.17}$$

$$f^{\mathrm{o}-}(r_{\mathrm{s}}) \overset{r_{\mathrm{s}}\to\infty}{\sim} \sqrt{\frac{1}{\pi k_{\mathrm{s}}}} e^{i\pi/4} \exp[-ik_{\mathrm{s}}r_{\mathrm{s}}]. \tag{2.1.18}$$

These can be written in terms of the standing-wave reference functions as

$$\begin{pmatrix} f^{\mathrm{i}+} \\ f^{\mathrm{i}-} \end{pmatrix} = \frac{e^{i\pi/4}}{\sqrt{2}} \begin{pmatrix} 1 & i \\ 1 & -i \end{pmatrix} \begin{pmatrix} f^{\mathrm{c}} \\ g^{\mathrm{c}} \end{pmatrix} \tag{2.1.19}$$

and

$$\begin{pmatrix} f^{\mathrm{o}+} \\ f^{\mathrm{o}-} \end{pmatrix} = \frac{e^{i\pi/4} i^L}{\sqrt{2}} \begin{pmatrix} i & 1 \\ -(-1)^L i & (-1)^L \end{pmatrix} \begin{pmatrix} s \\ c \end{pmatrix}. \tag{2.1.20}$$

Using the travelling-wave reference functions, we can understand the reflection from and transmission through the long-range potential. A wave travelling outward from short range ($f^{\mathrm{i}+}$) will be partially reflected back towards short range ($r^{(\mathrm{io})} f^{\mathrm{i}-}$) and partially transmitted ($t^{(\mathrm{io})} f^{\mathrm{o}+}$) to long range. These transmissions and reflections can be written as the boundary conditions

$$\psi \overset{r_{\mathrm{s}}\to 0}{\sim} f^{\mathrm{i}+} + r^{(\mathrm{io})} f^{\mathrm{i}-} \tag{2.1.21a}$$

$$\psi \overset{r_{\mathrm{s}}\to\infty}{\sim} t^{(\mathrm{io})} f^{\mathrm{o}+}, \tag{2.1.21b}$$

where we have defined complex reflection and transmission coefficients r and t, and the superscript (io) indicates they are for a wave travelling from the inner region outwards. Note that both sets of travelling wave reference functions are normalised to the same flux such that a reflection or transmission coefficient with magnitude of 1 indicates complete reflection or transmission. As ψ and our basis functions are all solutions to the same linear differential equation, these limits are in fact equalities and so are valid at all r_{s}. Thus we can combine the two limits to write

$$f^{\mathrm{i}+} + r^{(\mathrm{io})} f^{\mathrm{i}-} = t^{(\mathrm{io})} f^{\mathrm{o}+}. \tag{2.1.22}$$

Starting from a wave travelling inwards from long range, we can similarly obtain

$$t^{(\mathrm{oi})} f^{\mathrm{i}-} = f^{\mathrm{o}-} + r^{(\mathrm{oi})} f^{\mathrm{o}+}, \tag{2.1.23}$$

where the superscript (oi) now indicates they refer to a wave travelling from the outer region inwards. Combining these with earlier definitions, these reflection and transmission coefficients can be written explicitly as

$$r^{(\mathrm{io})} = \frac{(Z^{\mathrm{c}}_{fc} + Z^{\mathrm{c}}_{gs}) - i(Z^{\mathrm{c}}_{fs} - Z^{\mathrm{c}}_{gc})}{(Z^{\mathrm{c}}_{fc} - Z^{\mathrm{c}}_{gs}) - i(Z^{\mathrm{c}}_{fs} + Z^{\mathrm{c}}_{gc})} = \sqrt{R^{\mathrm{c}}}\exp[i(\delta^{\mathrm{c}} - \phi^{\mathrm{c}})] \tag{2.1.24}$$

$$r^{(\mathrm{oi})} = (-1)^L \frac{(Z^{\mathrm{c}}_{fc} + Z^{\mathrm{c}}_{gs}) + i(Z^{\mathrm{c}}_{fs} - Z^{\mathrm{c}}_{gc})}{(Z^{\mathrm{c}}_{fc} - Z^{\mathrm{c}}_{gs}) - i(Z^{\mathrm{c}}_{fs} + Z^{\mathrm{c}}_{gc})} = \sqrt{R^{\mathrm{c}}}\exp[i(\delta^{\mathrm{c}} + \phi^{\mathrm{c}})] \tag{2.1.25}$$

$$t^{(\mathrm{io})} = t^{(\mathrm{oi})} = e^{-iL\pi/2} \frac{2}{(Z^{\mathrm{c}}_{fc} - Z^{\mathrm{c}}_{gs}) - i(Z^{\mathrm{c}}_{fs} + Z^{\mathrm{c}}_{gc})} = \sqrt{T^{\mathrm{c}}}\exp[i(\delta^{\mathrm{c}} - (L+1)\pi/2)], \tag{2.1.26}$$

where

$$R^{\mathrm{c}} = 1 - T^{\mathrm{c}} = |r^{(\mathrm{io})}|^2 = |r^{(\mathrm{oi})}|^2 = \frac{(Z^{\mathrm{c}}_{fc} + Z^{\mathrm{c}}_{gs})^2 + (Z^{\mathrm{c}}_{fs} - Z^{\mathrm{c}}_{gc})^2}{(Z^{\mathrm{c}}_{fc} - Z^{\mathrm{c}}_{gs})^2 + (Z^{\mathrm{c}}_{fs} + Z^{\mathrm{c}}_{gc})^2} \tag{2.1.27}$$

and

$$T^{\mathrm{c}} = 1 - R^{\mathrm{c}} = |t^{(\mathrm{io})}|^2 = |t^{(\mathrm{oi})}|^2 = \frac{4}{(Z^{\mathrm{c}}_{fc} - Z^{\mathrm{c}}_{gs})^2 + (Z^{\mathrm{c}}_{fs} + Z^{\mathrm{c}}_{gc})^2} \tag{2.1.28}$$

are reflection and transmission probabilities. The phases defined by

$$\tan\delta^{\mathrm{c}} = \frac{Z^{\mathrm{c}}_{gs} - Z^{\mathrm{c}}_{fc}}{Z^{\mathrm{c}}_{fs} + Z^{\mathrm{c}}_{gc}} \tag{2.1.29}$$

$$\cos\delta^{\mathrm{c}} = \frac{Z^{\mathrm{c}}_{fs} + Z^{\mathrm{c}}_{gc}}{(Z^{\mathrm{c}}_{gs} - Z^{\mathrm{c}}_{fc})^2 + (Z^{\mathrm{c}}_{fs} + Z^{\mathrm{c}}_{gc})^2}, \tag{2.1.30}$$

and

$$\tan\phi^{\mathrm{c}} = \frac{Z^{\mathrm{c}}_{gs} + Z^{\mathrm{c}}_{fc}}{Z^{\mathrm{c}}_{gc} - Z^{\mathrm{c}}_{fs}} \tag{2.1.31}$$

$$\tan\phi^{\mathrm{c}} = \frac{Z^{\mathrm{c}}_{gc} - Z^{\mathrm{c}}_{fs}}{(Z^{\mathrm{c}}_{gs} + Z^{\mathrm{c}}_{fc})^2 + (Z^{\mathrm{c}}_{gc} - Z^{\mathrm{c}}_{fs})^2} \tag{2.1.32}$$

are associated by Gao with transmission and reflection respectively. As these quantities are all written in terms of elements of Z^{c}, they are all readily calculated.

To define a particular solution using travelling wave reference functions, we use an equivalent of an S-matrix. We have

$$\psi(r_{\mathrm{s}}) = C'' \left(f^{\mathrm{i}-}(r_{\mathrm{s}}) + S^{\mathrm{c}} f^{\mathrm{i}+}(r_{\mathrm{s}}) \right), \tag{2.1.33}$$

which defines the short-range S-matrix S^{c} – analogous to the S-matrix of eq. (1.2.13) – which is a complex number with unit magnitude. Again, the long-range reference functions have been chosen to be equivalent to the functions in eq. (1.2.13), which can be rewritten as

$$\psi(r_{\mathrm{s}}) = C''' \left(f^{\mathrm{o}-}(r_{\mathrm{s}}) - (-1)^L S f^{\mathrm{o}+}(r_{\mathrm{s}}) \right), \tag{2.1.34}$$

The relation between the asymptotic and short-range S-matrices can now be written as

$$S = (-1)^{L+1} \left[r^{(\mathrm{oi})} + \frac{t^{(\mathrm{oi})} S^{\mathrm{c}} t^{(\mathrm{io})}}{1 - r^{(\mathrm{io})} S^{\mathrm{c}}} \right], \tag{2.1.35}$$

which can be expanded [184] as

$$S = (-1)^{L+1} \left[r^{(\mathrm{oi})} + t^{(\mathrm{oi})} S^{\mathrm{c}} t^{(\mathrm{io})} (1 + r^{(\mathrm{io})} S^{\mathrm{c}} + (r^{(\mathrm{io})} S^{\mathrm{c}})^2 + \dots) \right]. \tag{2.1.36}$$

Equation (2.1.36) provides a clear physical understanding of the scattering process. It is made up of multiple pathways: reflection off the pure long-range potential; transmission inwards past the long-range potential, followed by a single interaction with the short-range and retransmission out past the long-range potential; then a further series of terms which involve repeated reflections off the long-range potential back towards short range. This last group is responsible for shape resonances when $r^{(\mathrm{io})} S^{\mathrm{c}}$ is close to 1 and successive terms of the sum add constructively. This travelling-wave form of QDT is equivalent to the standing-wave form described earlier, but provides considerable additional insight.

There are several short-range parameters that can be used to describe the system.

We have already described the short range K- and S-matrices, which are related by

$$S^{\mathrm{c}} = \frac{1 + iK^{\mathrm{c}}}{1 - iK^{\mathrm{c}}} \tag{2.1.37}$$

and

$$K^{\mathrm{c}} = \frac{1}{i}\frac{1 - S^{\mathrm{c}}}{1 + S^{\mathrm{c}}}. \tag{2.1.38}$$

Another useful parameter is the short-range phase shift δ^{s} [184], which is related to the previous two parameters by

$$S^{\mathrm{c}} = e^{2i\delta^{\mathrm{s}}} \tag{2.1.39}$$

$$K^{\mathrm{c}} = \tan\delta^{\mathrm{s}}. \tag{2.1.40}$$

Instead of these obviously short-range but somewhat artificial parameters, some authors use the s-wave scattering length at threshold in the same role as a short-range parameter. Although the scattering length is an inherently long-range quantity, it has a one-to-one mapping to the short-range parameters and it is far better known and understood than the short-range parameters. This is conveniently related to the other parameters through [184]

$$\frac{a}{\bar{a}} = 1 + \cot\left(\delta^{\mathrm{s}} - \frac{\pi}{8}\right). \tag{2.1.41}$$

The different formulations and short-range parameters are formally equivalent to each other and should give identical results. In practice, it is usually easiest to perform calculations using K^{c} and the standing-wave formulation, and we will do so in section 2.2, but in section 2.3 it will instead be more convenient to use S^{c} and the travelling wave formulation. However, it is often easier to present and understand results in terms of δ^{s} or $a/\bar{a}$, and we shall normally use those quantities for presenting results.

We make the common QDT approximation that the wavefunction at short range is independent of energy in a region around threshold. This is reasonable because of the separation between the large energy scale at short range and the small energy scale associated with the region around threshold that we are interested in; this can

alternatively be expressed as assuming that the energy range of interest is small compared to the magnitude of the potential at short range. As the wavefunction and the short-range reference functions (eqs. (2.1.7), (2.1.8), (2.1.15) and (2.1.16)) are all independent of energy at short range, then by eqs. (2.1.12) and (2.1.33) so are K^{c} and S^{c}. Additionally, we follow Gao [213] in assuming that the wavefunction at short range is also independent of partial wave L. This relies on a similar assumption that the centrifugal energy is small compared to the potential at short range. As we have deliberately chosen short-range reference functions that are independent of L at short range, then K^{c} and S^{c} are also independent of L. Thus, in this model, all the variation in the scattering properties with L and energy come directly from the long-range potential and are described by the variation of Z^{c} (or other equivalent parameters, such as those used for the travelling-wave description). The combination of these two approximations results in angular-momentum-insensitive QDT (AQDT). Although these approximations may seem drastic, we will show in section 2.2 that they can be astonishingly robust in realistic systems.

2.2 Accurate Representation of Simple Systems with AQDT

Here we demonstrate Gao's AQDT as applied to real systems, and test the limits of its range of validity. Gao's development of the analytic theory has been impressive but has focussed primarily on the abstract aspects rather than concrete results on real, or at least realistic, systems, and few others have used the theory enough to guide expectations about which cases it may be useful for. We therefore want to investigate directly the application of AQDT to a variety of real systems and assess its validity.

2.2.1 Structureless atom+atom systems: Li+Yb and Rb+Yb

The first systems we investigate are Li+Yb and Rb+Yb. These are made up of a ^{2}S alkali-metal atom and a closed-shell ^{1}S alkaline-earth-like ytterbium atom. These

systems do exhibit very narrow Feshbach resonances due to coupling between the alkali-metal hyperfine states due to the dependence of the hyperfine coupling on the internuclear distance R [44–46]. However, these resonances have widths of 100 mG or less. We will focus on the case of collisions far from resonance, which are accurately described by single-channel calculations that neglect both electron and nuclear spin and thus do not depend on magnetic field. We use interaction potentials for LiYb [217] and RbYb [46] from electronic structure calculations, with a fixed long-range C_6 coefficient and the short-range potential scaled as $V \to \lambda V$ to adjust the s-wave scattering lengths as required. This single-channel system is quite close to the ideal AQDT model and good agreement with the AQDT predictions is expected. The length and energy scaling factors r_6 and E_6/k_B are 40.3 Å and 2.56 mK for ^{6}Li^{174}Yb and 82.7 Å and 61.1 μK for ^{87}Rb^{174}Yb. $\bar{a}$ is 19.3 and 39.6 Å for ^{6}Li^{174}Yb and ^{87}Rb^{174}Yb respectively.

The crucial element of AQDT is the relationship between scattering in different partial waves. This is conveniently demonstrated by considering the relationship between the s-wave scattering length and the equivalent quantities for higher partial waves [206] (which are no longer lengths but volumes or hypervolumes). For example the p-wave scattering volume[2] is predicted by AQDT to be

$$\frac{a_\mathrm{p}}{\bar{a}_\mathrm{p}} = -2\left[1 + \frac{1}{a_\mathrm{s}/\bar{a} - 2}\right], \tag{2.2.42}$$

where $\bar{a}_\mathrm{p}$ is the mean p-wave scattering volume [206] given by

$$\bar{a}_\mathrm{p} = \frac{[\Gamma(1/4)]^2}{36\pi} r_6^3. \tag{2.2.43}$$

Figure 2.1(a) shows a_s and a_p for LiYb, from quantum scattering calculations on the realistic potential curves described above, as the potential scaling factor λ is adjusted between 0.8 and 1.2. Figure fig. 2.1(b) shows a_p as a function of a_s over the same range of λ. It may be seen that a_p is indeed a nearly single-valued function of a_s, as predicted by eq. (2.2.42). For a clearer comparison, we also convert these

[2]The p-wave scattering volume a_p is defined by $\tan\delta_\mathrm{p} = -k^3 a_\mathrm{p}$, where δ_p is the p-wave phase shift.

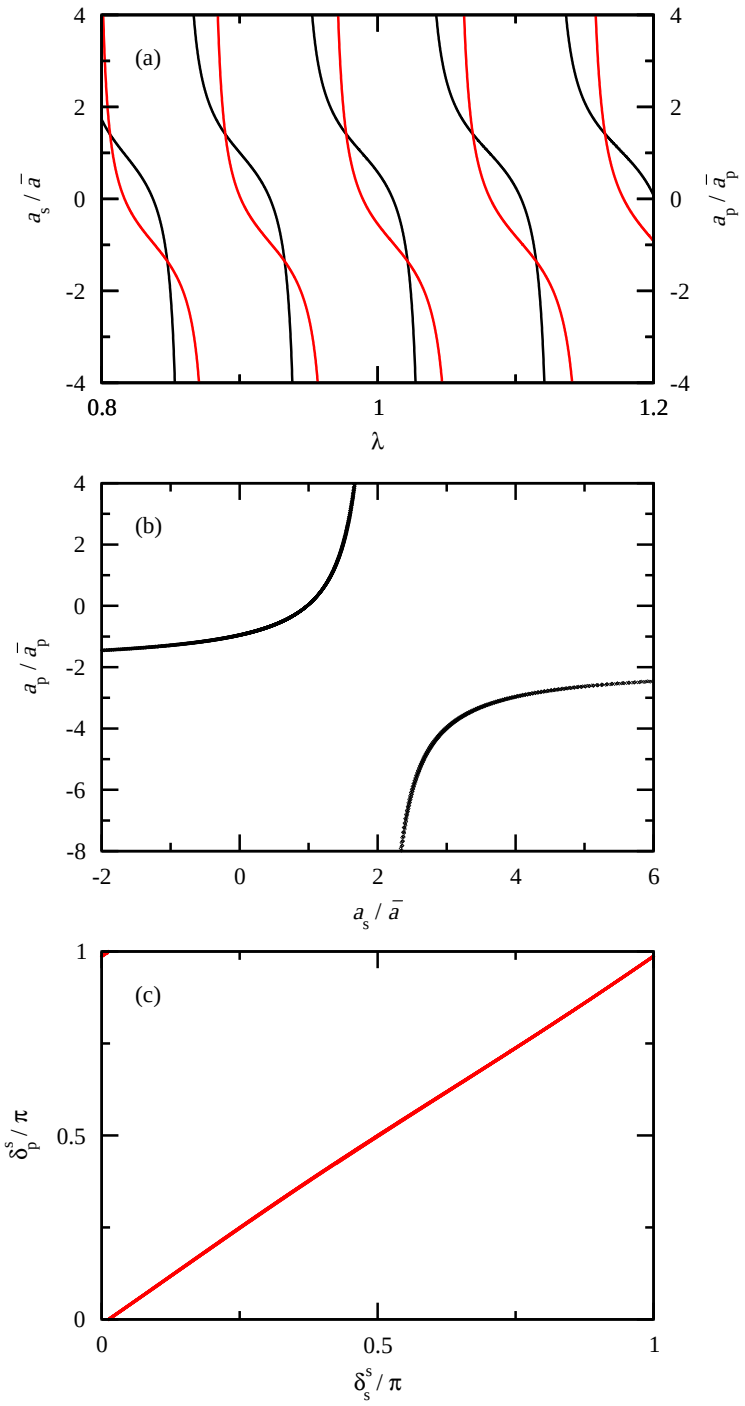

Figure 2.1: (a) s-wave (black, left scale) and p-wave (red, right scale) scattering lengths/volumes, across a wide range of the potential scaling factor, λ; (b) a_p as a function of a_s, showing that the different segments of the line in (a) lie on top of one another; (c) δ^s implied by the s- and p-wave scattering lengths plotted against each other; note that both axes are cyclic, and the line of points continues for a short distance in the top left corner of the plot.

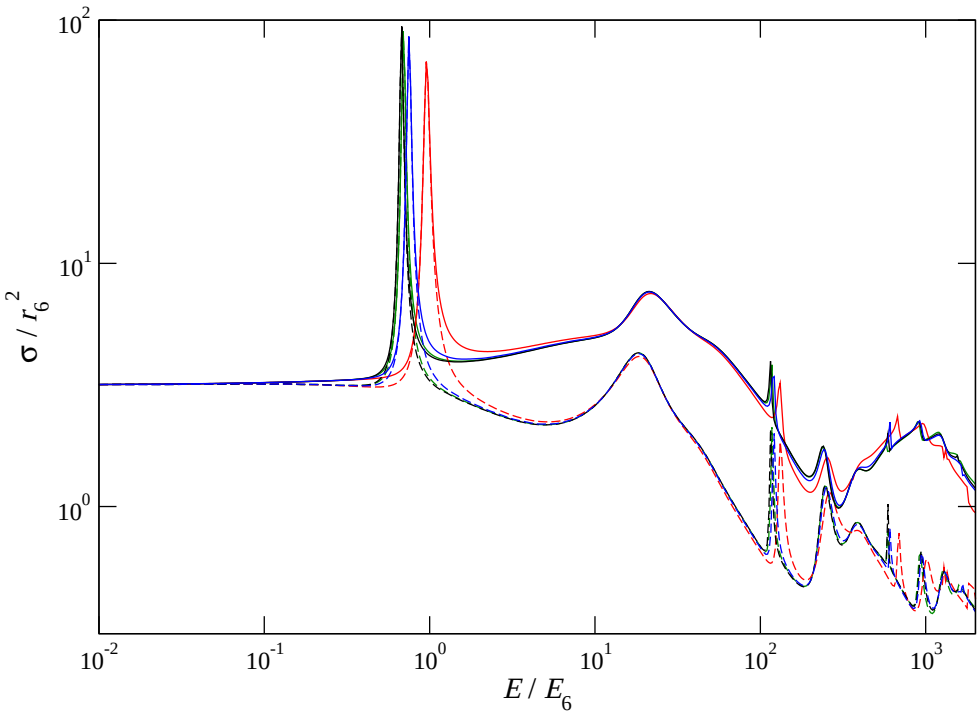

Figure 2.2: Comparison of σ_{el} (solid lines) and $\sigma_\eta^{(1)}$ (dashed lines) in reduced units with a scattering length of $a_{\mathrm{s}} = 1.05\bar{a}$ for LiYb (black) and RbYb (blue), compared with standard AQDT (red) and hard-sphere AQDT (green).

scattering lengths to the short-range phase δ^{s} each implies, as shown in fig. 2.1(c). If the AQDT approximation is correct then these phases will be the same and the points will lie on the main diagonal ($\delta_{\mathrm{s}}^{\mathrm{s}} = \delta_{\mathrm{p}}^{\mathrm{s}}$; in fact, we see that they lie very slightly below. This can be rationalised by noting that increasing the centrifugal contribution to the effective potential reduces the depth and volume of the well and so should be expected to decrease the accumulated phase, so that the p-wave scattering has a lower effective short-range phase compared to the s-wave scattering.

To test the extent of the universal relationship, we have carried out calculations of σ_{el} and $\sigma_\eta^{(1)}$ for RbYb and LiYb for potentials scaled to give identical values of $a_{\mathrm{s}}/\bar{a}$. The results in reduced units are compared for the case of $a_{\mathrm{s}} = 1.05\bar{a}$ in fig. 2.2. According to AQDT, values of a_{s} slightly greater than $\bar{a}$ produce a d-wave shape resonance at low energy, and this appears as a prominent feature for both species in

fig. 2.2. Apart from small differences in resonance positions, the results in reduced units are remarkably similar for LiYb and RbYb up to energies well above $1000E_6$, up to at least 100 mK for RbYb and several Kelvin for LiYb. The calculations on full potential curves are also compared with AQDT [213, 215]. This still replicates the results amazingly well considering the simplicity of the model: the same shape resonances are clearly present and qualitatively correct, although some are shifted from the full calculations by amounts comparable to their width. Nonetheless, the non-resonant part of the cross sections is extremely well reproduced over the energy range. This includes a broad rise in the elastic cross section around $1000E_6$ which is in fact the first of the characteristic 'glory' oscillations [148]; this peak does not appear in $\sigma_\eta^{(1)}$ because glory scattering contributes mainly to small-angle scattering and so does not provide large contributions to this cross section.

The differences between the full calculations and the AQDT results might be caused either by terms in the long-range potential apart from $-C_6r^{-6}$ or by the short-range wavefunction not being independent of energy or angular momentum. We can try to test this latter possibility using a hard-sphere-plus-r^{-6} QDT model to get a more realistic description of the variation of the short-range wavefunction. A hard-sphere of radius r_{HS} is modelled by a boundary condition of $\psi(r_{\mathrm{HS}}) = 0$, which sets K^{c} through eq. (2.1.12). This value of K^{c} now varies with energy and angular momentum, but otherwise the calculation of cross sections proceeds as previously. We choose $r_{\mathrm{HS}} = 0.0986331008173$ to reproduce the zero-energy s-wave scattering length of $1.05\bar{a}$ of the case discussed above; this value of r_{HS} is approximately 4 Å for LiYb, which is slightly further out than the classical turning point for the potential we use for full calculations, which is at about 3 Å, but gives a slightly deeper potential minimum by about 15%. The results are also shown fig. 2.2 in green, where it can be seen that this model provides excellent agreement with the full calculations, comparable with their agreement with each other. This therefore suggests that the small deviations of the full calculations from pure AQDT are due to the assumption that the short-range wavefunction is independent of energy and angular momentum, and the approximation of the long-range potential as $-C_6r^{-6}$ appears to be quite accurate in this case.

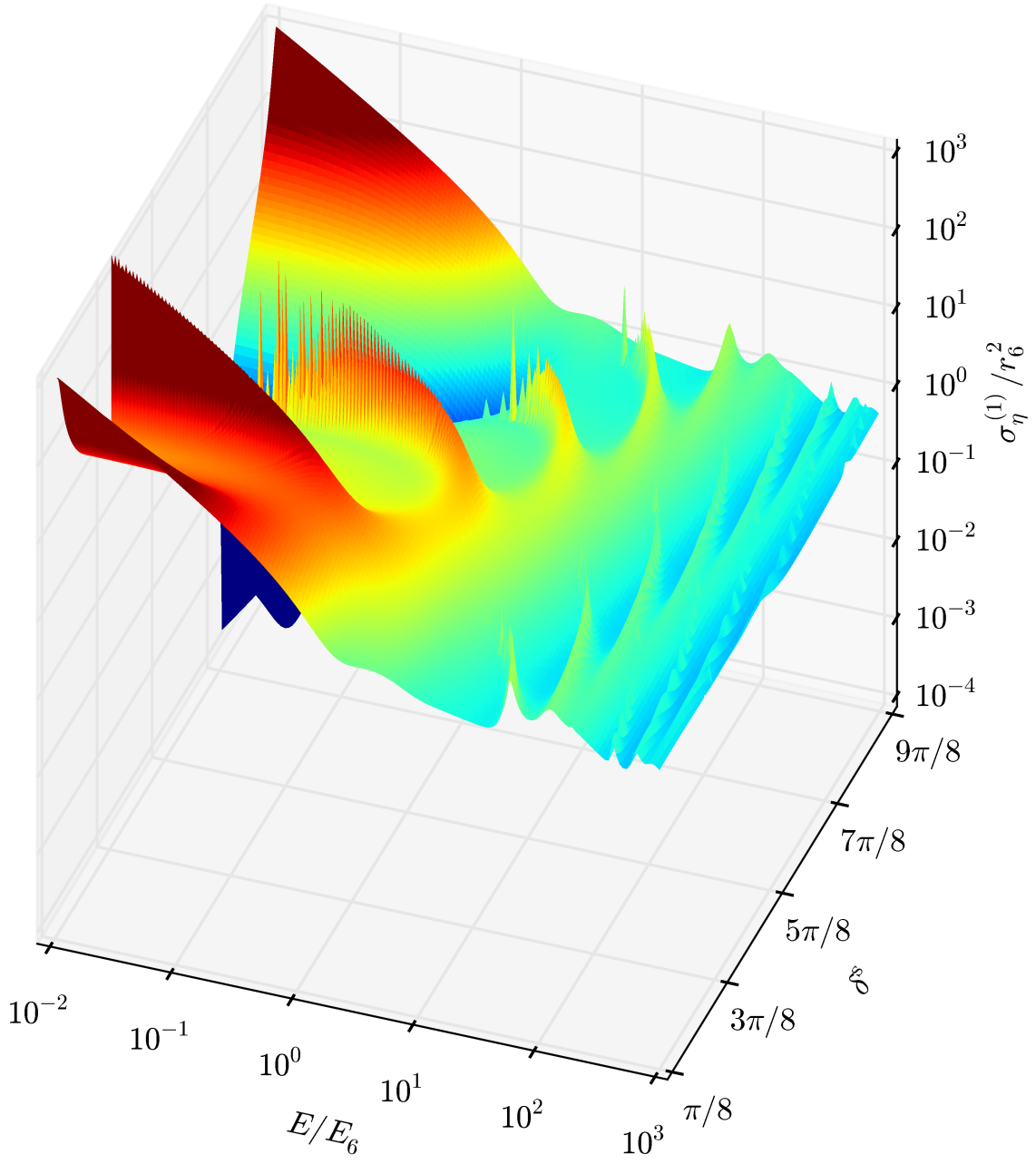

Figure 2.3: The cross section $\sigma_\eta^{(1)}$ for RbYb, as a function of δ^s and the energy in reduced units. Note that the δ^s has been shifted to start at $\pi/8$, and that δ^s is periodic such that $9\pi/8$ is equivalent to $\pi/8$. The spikes visible at the left-hand end of some narrow ridges are artefacts of the finite grid used for plotting.

Figure 2.3 shows $\sigma_\eta^{(1)}$ for RbYb plotted as a surface as a function of $\delta^{\rm s}$ and ϵ. As $a_{\rm s}$ has a pole at $\delta^{\rm s} = \pi/8$, fig. 2.3 shows large peaks at low energy at either end of the $\delta^{\rm s}$ axis. It also shows a deep trough at $\delta^{\rm s} = 7\pi/8$, which curves towards higher $\delta^{\rm s}$ as a function of energy because of a Ramsauer-Townsend minimum [220] that occurs in the s-wave cross section for small negative values of the scattering length.[3] In addition, there are strong features due to shape resonances, which sharpen and eventually become invisible as the energy decreases. The prominent ridge that points towards $\delta^{\rm s} = \frac{3\pi}{8}$, $a_{\rm s} = 2\bar{a}$ at low energy is due to a p-wave resonance, while the narrower ones that point towards $\delta^{\rm s} = \frac{5\pi}{8}$, $a_{\rm s} = \bar{a}$ and $\delta^{\rm s} = \frac{7\pi}{8}$, $a_{\rm s} = 0$ are due to d-wave and f-wave resonances, respectively. A series of ridges due to shape resonances in higher partial waves may also be seen at higher energies, and can be followed up to at least $L = 9$. Their positions closely follow the prediction of AQDT, which is that, at zero energy, resonances with $L \geq 4$ occur at the same location as those with $L - 4$. Figure 2.3 would look very similar for any other single-channel system with potential of the form $-C_6 R^{-6}$ at long range.

2.2.2 Structured atom+atom systems: Rb+Cs

The situation is somewhat more complicated for pairs of alkali-metal atoms and other systems with extensive Feshbach resonances. AQDT still applies usefully to the *background* scattering (away from Feshbach resonances), and in such regions the "universal" behaviour of scattering lengths and cross sections is still expected to apply, at least at relatively low energies. However, understanding the detailed behaviour, including resonant effects, requires coupled-channel calculations using accurate potential curves. We use the example of ^{87}Rb+Cs, for which there are highly accurate potentials available; these and the coupled-channels calculations are described in detail elsewhere [42]. Full coupled-channel calculations on pairs of alkali-metal atoms in a magnetic field become prohibitively expensive for large basis sets, so the cross-section calculations are truncated at $L_{\rm max} = 5$; the AQDT calculations in this section are similarly truncated. The effect of this truncation is

[3] This feature is more clearly visible in comparable plots in section 2.3.

small for almost all the energy range shown. Scattering length calculations need only $L_{\max} = 3$ for convergence.

Figure 2.4 shows s- and p-wave scattering lengths for ^{87}RbCs as magnetic field is varied from 0 to 500 G. Note that in this case the three different M_L components for p-wave scattering are not equivalent and results are presented for each. Figure 2.4 clearly shows a very different picture from that seen in fig. 2.1, as the variation in scattering length is entirely due to Feshbach resonances. These Feshbach resonances cannot be described by the single-channel QDT we use in this chapter; a more complex multi-channel QDT model might be able to model these resonances [189, 221] but that is beyond the scope of this work. This means that the s- and p-wave scattering lengths are not correlated in the way that they were for the single-channel case, which can be seen in fig. 2.4(b) where the results deviate greatly from the line predicted by AQDT. However, the results do still cluster around the background scattering lengths, and these are close to the AQDT line. Note that the p-wave scattering lengths for $|M_L| = 0$ and 1 are split by a small amount; this is expected and directly related to the known multiplet structure of p-wave Feshbach resonances [222].

For a better comparison between RbCs and AQDT, fig. 2.5 shows the scattering lengths as the reduced mass μ is varied[4] from 50 to 60 u with magnetic field fixed at 100 G. Varying μ varies the background scattering as well as resonances, so now we see that the general form of the scattering length variation is similar to that seen in fig. 2.1, but with significant Feshbach resonance structure superimposed. Figure 2.5(b) and (c) show a clear clustering of points around the single-channel AQDT prediction, but with a significant number of points lying well away from this line. Again, we there is a separation between the $|M_L| = 0$ and 1 p-wave scattering lengths and we can now see that this varies with the effective phase; this variation was not explicitly predicted in Ref. [222], but it is implicit in their eqs. (5) and (6) that the splitting will vary. Nonetheless, these results show that the relationships predicted by AQDT do have some use in multi-channel cases like this one, where it

[4]Note that this is not equivalent to varying between different isotopologues as we don't vary the hyperfine interactions from those of ^{87}RbCs.

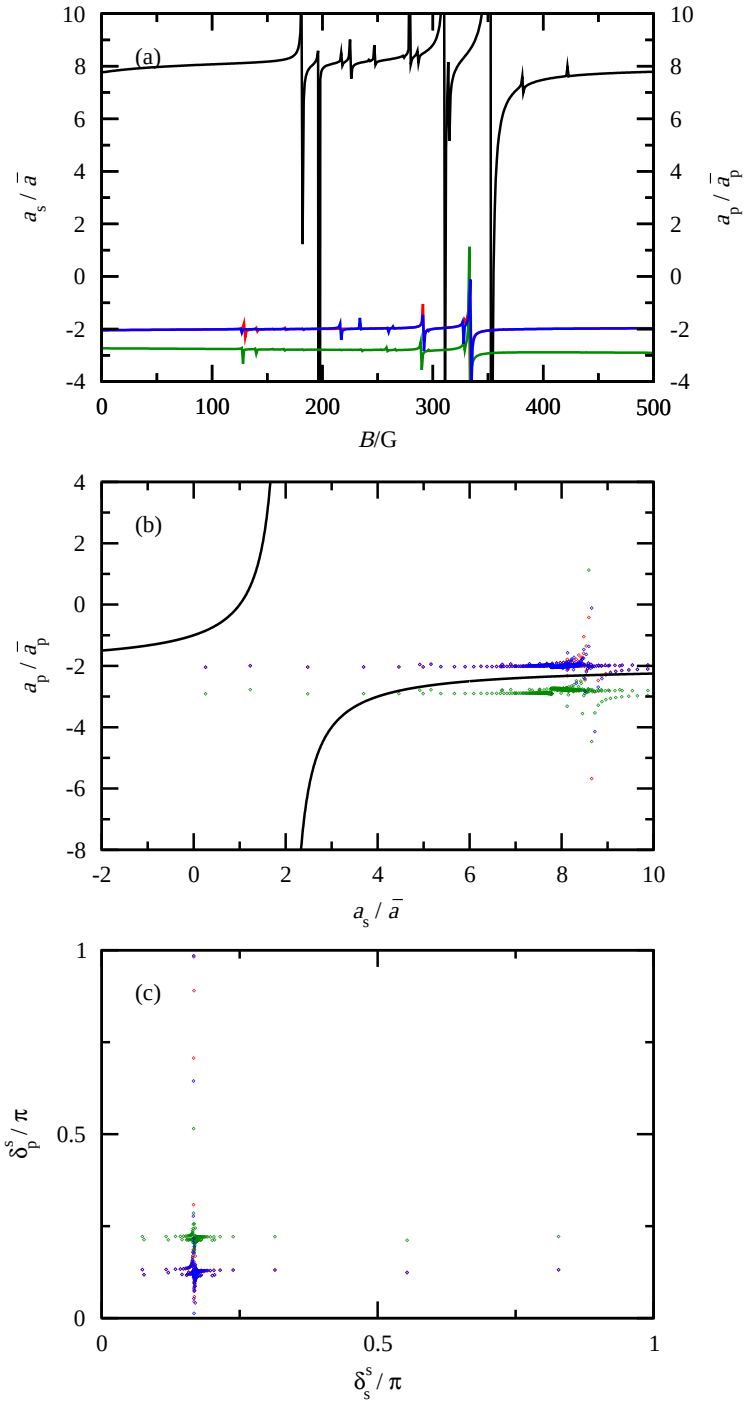

Figure 2.4: Coupled-channel calculations of scattering lengths for ^{87}RbCs as fields is varied from 0 to 500 G. s-wave results are in black, p-wave $M_L = -1$, 0, and 1 in red, green and blue respectively; note that the M_L =-1 and 1 results are very similar so most red points are below blue points and not visible. (a) s-wave (left scale) and p-wave (right scale) scattering lengths/volumes; (b) a_p as a function of a_s, the black line is the AQDT prediction of eq. (2.2.42); (c) δ^s implied by the s- and p-wave scattering lengths plotted against each other.

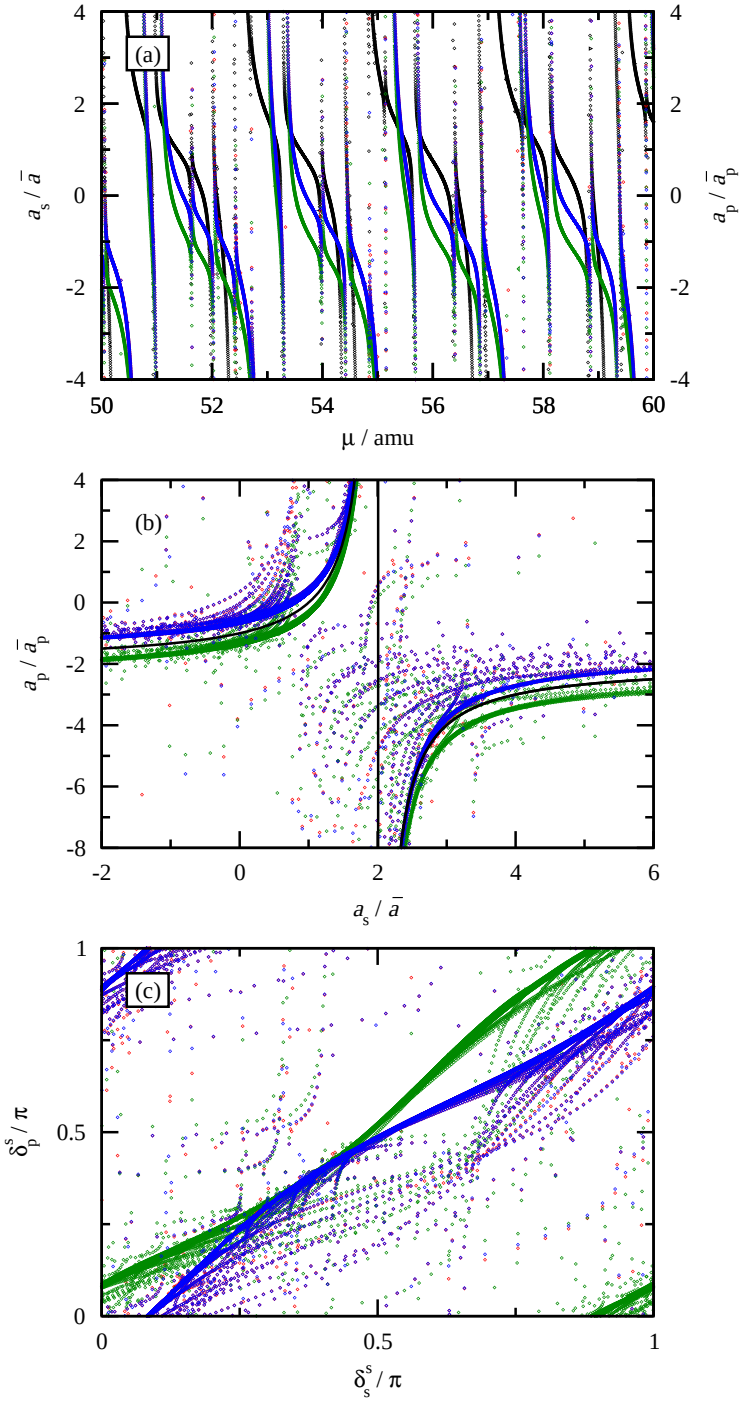

Figure 2.5: Coupled-channel calculations of scattering lengths for ^{87}RbCs as reduced mass is varied from $\mu = 50$ to 60 a.m.u. s-wave results are in black, p-wave $M_L = -1$, 0, and 1 in red, green, and blue respectively; note that the $M_L = -1$ and 1 results are very similar so most red points are below blue points and not visible. (a) s-wave (left scale) and p-wave (right scale) scattering lengths/volumes; (b) a_p as a function of a_s, the black line is the AQDT prediction of eq. (2.2.42); (c) δ^s implied by the s- and p-wave scattering lengths plotted against each other.

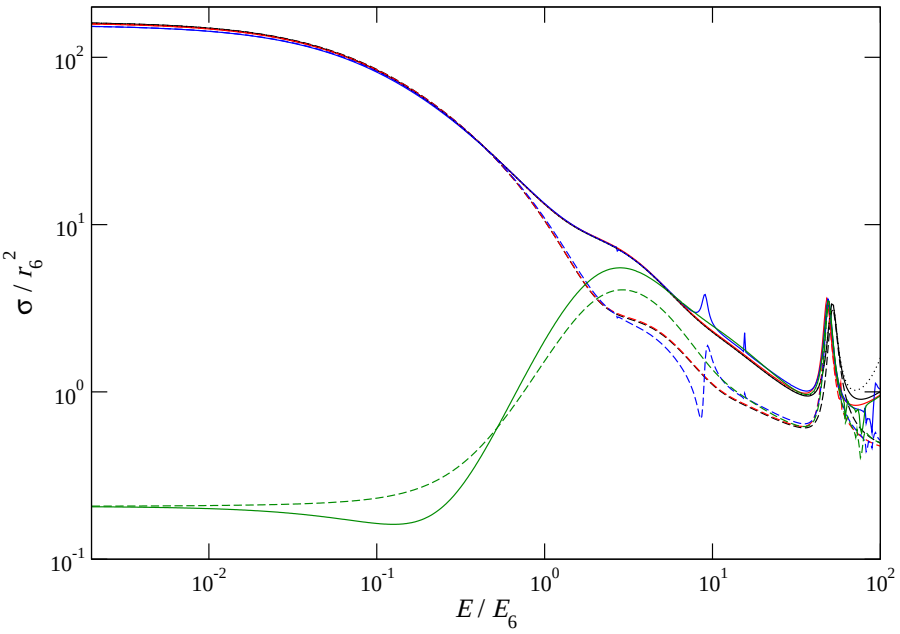

Figure 2.6: Coupled-channel calculations of $\sigma_{\rm el}$ (solid lines) and $\sigma_\eta^{(1)}$ (dashed lines) for RbCs at various magnetic fields: 500 G (non-resonant, red); 313.82 G (resonant but $a_{\rm s} = a_{\rm bg}$, blue); 355 G (resonant, with $a_{\rm s} \neq a_{\rm bg}$, green), compared with single-channel AQDT (black). The coupled-channel calculations are truncated at $L_{\rm max} = 5$. Fully converged AQDT results for $\sigma_{\rm el}$ are shown as a black dotted line and are indistinguishable from the $L_{\rm max} = 5$ results except at the highest energies.

might have been expected that the single-channel formalism would fail completely.

Figure 2.6 compares cross sections for ^{87}RbCs at various magnetic fields B. We consider several cases: (a) at $B = 500$ G, the system is in a non-resonant region and the scattering length is close to its background value $a_{\rm s} = a_{\rm bg} \approx 350$ Å $\approx 7.5\bar{a}$; (b) $B = 313.82$ G, which is in a region with numerous overlapping resonances but where the scattering length is coincidentally close to the background scattering length; and (c) $B = 355$ G, which is near a resonance at a point where the scattering length is small, $a_{\rm s} = 12$ Å. AQDT results for a single channel with $a_{\rm s} = a_{\rm bg}$ are also shown in fig. 2.6. In the non-resonant region, AQDT again gives excellent results for both $\sigma_{\rm el}$ and $\sigma_\eta^{(1)}$. In the resonant region with the same scattering length, the results are again remarkably good, except for a resonant feature that in this case occurs near $10E_6$; here $\sigma_\eta^{(1)}$ shows a characteristic peak and trough because the interference

terms in eq. (3.1.16) pass through both positive and negative values as one of the phases changes rapidly by π. Even when the scattering length is resonantly shifted from its background value, so that the limiting low-energy scattering is different, the cross sections rapidly approach the "universal" form from the background channel once a few partial waves contribute.

2.2.3 A strongly anisotropic system: Li+CaH

As a final example we look at Li+CaH, ignoring all electron and nuclear spins. We will introduce this system more completely in chapter 4, but here it is sufficient to say that it is a highly anisotropic atom+diatom system that is expected to have a strongly multi-channel character. We also note that in section 4.2 and Ref. [130] we show this system to show strong signs of chaos. Figure 2.7(a) shows s- and p-wave scattering lengths for this system as λ is varied, which shows that the scattering is dominated by a large number of Feshbach resonances such that scattering at all values of λ is strongly affected by one or more resonances. The structure that was clearly visible in previous examples can no longer be seen, but there still appears to be some correlation between some of the resonance positions in the two partial waves. Figure 2.7(b) and (c) confirm that there is a remarkable amount of clustering near the single-channel AQDT prediction. This clustering is seen to be below the diagonal in fig. 2.7(c) even more significantly than was seen for LiYb. Although far from exact, many of the points that make up this clustering are close to resonances in one or both partial waves, which suggests that this relationship is holding to some extent even across Feshbach resonances.

We can understand this surprising agreement between partial waves by considering the collision in the body-fixed frame. We can consider the projection of the total angular momentum J (or equivalently the diatom rotation j) onto the intermolecular axis, which is well known in studies of atom-diatom Van der Waals complexes [223] and is given the symbol K. It can take values from $-J$ to $+J$ in integer steps. Blocks of the Hamiltonian with different K are coupled only by Coriolis terms in the body-frame representation of the centrifugal motion; these Coriolis terms are very small compared to the potential anisotropy in the well region, so the Hamiltonian

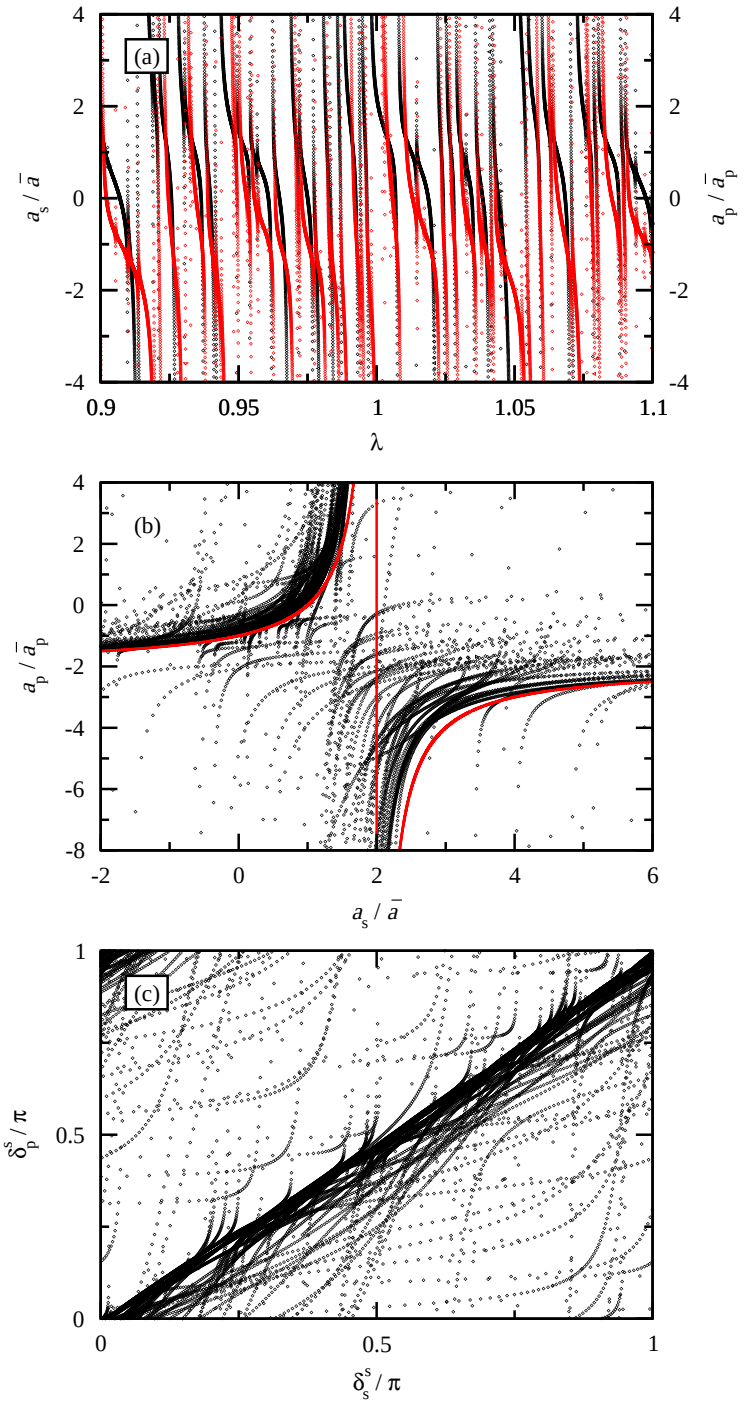

Figure 2.7: Coupled-channel calculations of scattering lengths for LiCaH as λ is varied from 0.9 to 1.1. (a) s-wave (black, left scale) and p-wave (red, right scale) scattering lengths/volumes; (b) a_p as a function of a_s, the red line is the AQDT prediction of eq. (2.2.42); (c) δ^s implied by the s- and p-wave scattering lengths plotted against each other.

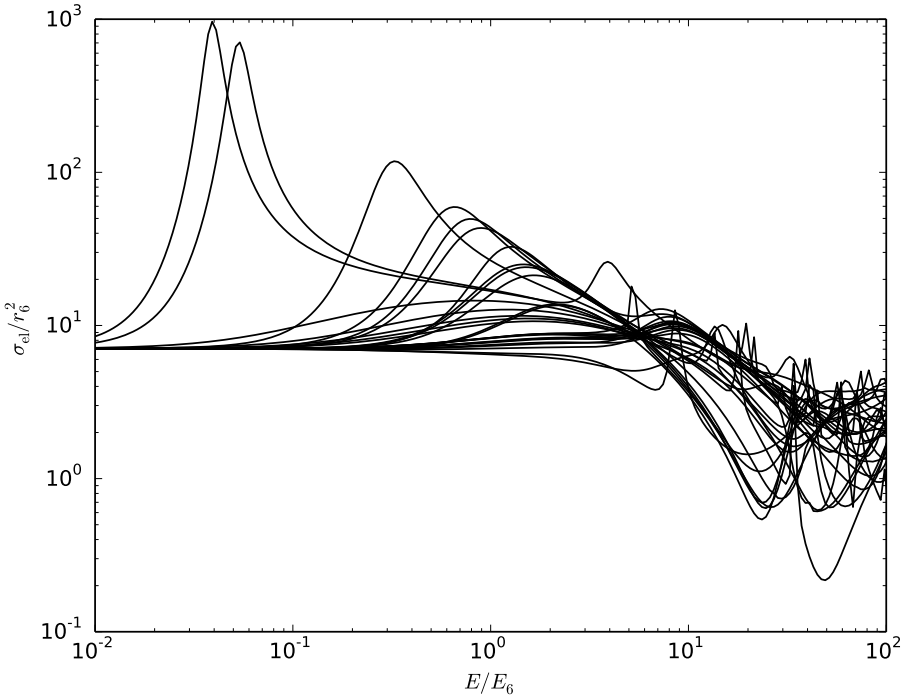

Figure 2.8: Coupled-channel calculations of $\sigma_{\rm el}$ for LiCaH at various values of λ between 0.9 and 1.1 giving the same s-wave scattering length $a_{\rm s} = 29.9$ Å.

can be considered to be nearly block-diagonal with blocks labeled by $|K|$ and parity. Thus, the s-wave scattering in $J = 0$ and the p-wave scattering in $J = 1$ both have contributions that correspond to $K = 0$, and the $J = 1$ scattering also has a $|K| = 1$ component. The $K = 0$ components of the two partial waves will differ only by a centrifugal term, which we have assumed to be negligible at short-range under AQDT. Thus the expected short-range phase from just the $K = 0$ part of the Hamiltonian is the same for both s-wave and p-wave scattering, even if it completely dominated by Feshbach resonances. In this picture, the only difference between the two partial waves comes from the presence of the $|K| = 1$ block of the Hamiltonian, which will cause resonances in $J = 1$ but not $J = 0$. Inspection of fig. 2.7(a) on a larger scale shows the p-wave scattering length does indeed show additional, mostly narrow, resonances compared to the s-wave scattering length. In this case, the single channel model does not provide the full picture, but it does still provide a remarkably good approximate model for the typical relationship between scattering in different partial waves, even in a system that also shows signs of chaos.

Figure 2.8 shows cross sections calculated for a number of values of λ which give the same scattering length. These calculations use $J_{\max} = 10$ which is expected to be sufficient to converge the calculations over the range shown. The single-channel AQDT model predicts that these will all give the same variation of the cross section with energy. As they have the same scattering length they all have the same cross section in the low-energy limit but they rapidly diverge from each other as E increases and show a wide variety of differing behaviours. These results fail to agree with the single-channel prediction much more significantly than the results in fig. 2.7 for two reasons. Firstly, the cross sections depend on many partial waves rather than just the two considered in fig. 2.7, and these higher partial waves have contributions from more blocks of $|K|$ so are increasingly likely to vary from the AQDT prediction. Secondly, the arguments presented for good agreement in fig. 2.7 only suggested that the short-range phase is constant between partial waves at a particular energy ($E = 0$), but they do not make a similar argument for the other QDT assumption that it does not vary with energy, therefore even the contribution from a single partial wave will be expected to not agree with the AQDT prediction and vary rapidly with energy. Thus there is clearly no useful prediction that could be provided by AQDT in this case.

2.3 Modelling Typical Behaviour of Complex Systems

To describe complex systems – including those such as KRb+KRb that may be intractable using coupled-channel methods – different approaches are needed. Considerable success has been achieved with effective single-channel QDT methods that take account of short-range loss, whether inelastic or reactive, with a single parameter. In particular, the model of Idziaszek and Julienne [190] successfully explained the temperature dependence of reactive KRb+KRb collisions at temperatures below 1 μK. They also showed that in the limit of complete loss at short range, the loss rate is independent of the scattering length, which was termed the "universal" limit. This model was later extended [196] to handle the additional r^{-3} dipole-dipole po-

tential that exists when the KRb molecules are oriented with an external electric field; Kotochigova [219] and Gao [224, 225] have also worked on similar models. More recently, Jachymski *et al.* [194, 195] have extended this theory up to the high-temperature limit, and used it to interpret merged-beam experiments on Penning ionisation in collisions of metastable He with Ar [226]. In this section, we undertake a systematic and complete exploration of the behaviour of elastic and loss cross sections from an effective single-channel model. We then compare these results with full coupled-channel calculations on a prototype strongly coupled system, based on rotationally inelastic collisions of LiH with Li atoms.

To model loss, the single-channel QDT model now needs two short-range parameters. One of these describes the interaction without loss, while the other describes the probability that loss will occur when the particles reach short range. For the former parameter, Idziaszek and Julienne [190] used the reduced "background" scattering length $s = a/\bar{a}$.[5] We prefer to use the short-range phase δ^{s} defined in eq. (2.1.41) to map the behaviour onto a finite range. We use the same loss parameter y as Idziaszek and Julienne [190], which has the property that $y = 0$ corresponds to no loss and $y = 1$ corresponds to complete loss at short range. However, we change to the travelling wave representation for convenience. This gives a short-range S-matrix

$$S^{\mathrm{c}} = \left(\frac{1-y}{1+y}\right) e^{2i\delta^{\mathrm{s}}}. \tag{2.3.44}$$

This formulation already makes clear that the collisional properties of the system are independent of δ^{s} (and hence of a) in the limit of $y \to 1$ ($|S^{\mathrm{c}}| \to 0$), and that this can be known from the construction of the problem without the need to actually solve it. Now that S^{c} is not unitary, the corresponding K^{c} is not generally real; thus in this case we find it easier to solve the QDT equations in the travelling wave formalism.

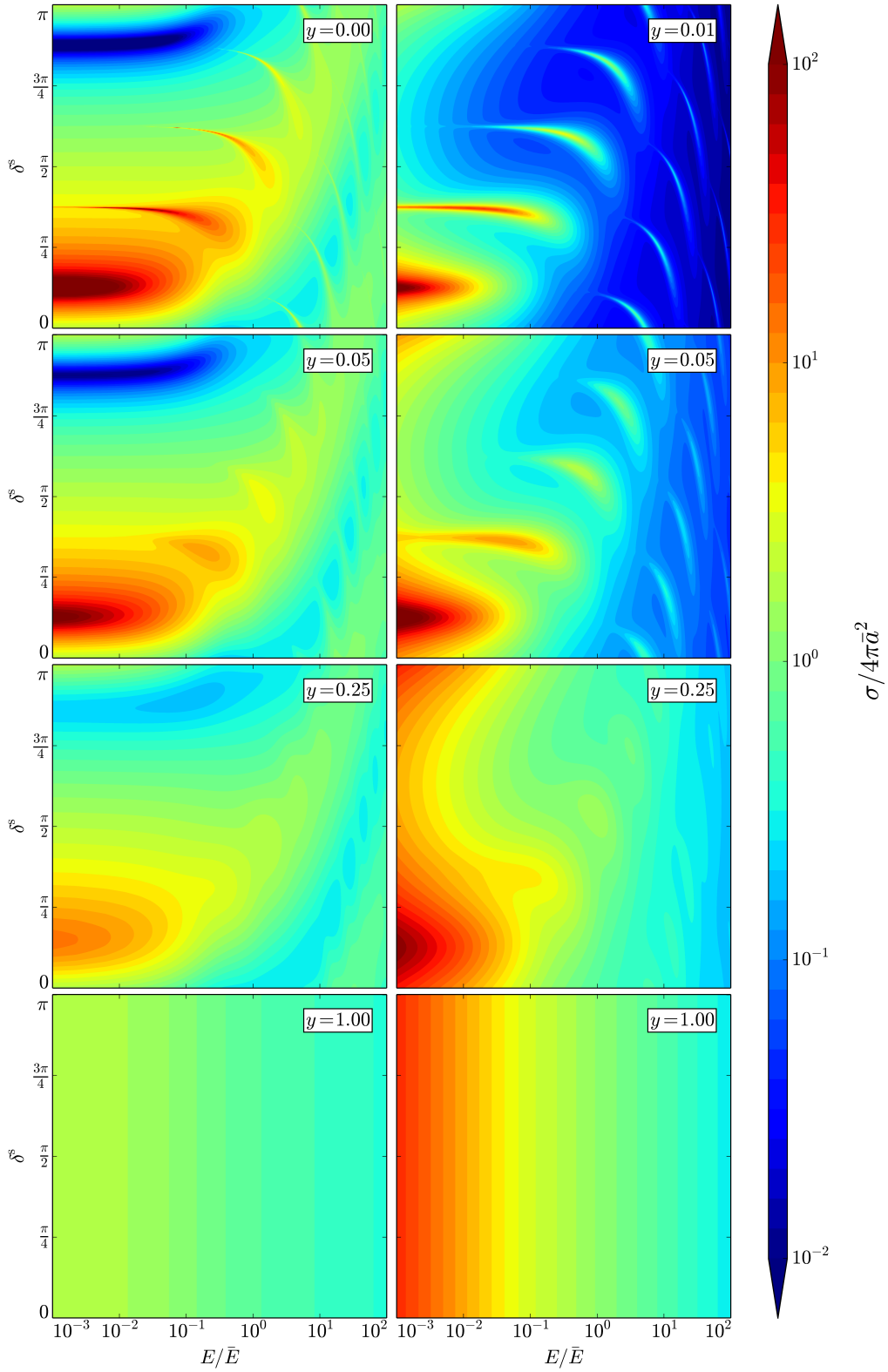

Figure 2.9: Contour plots of the elastic (left) and loss (right) cross sections for distinguishable particles as a function of reduced energy $E/\bar{E}$ and short-range phase shift δ^s for selected values of the loss parameter y.

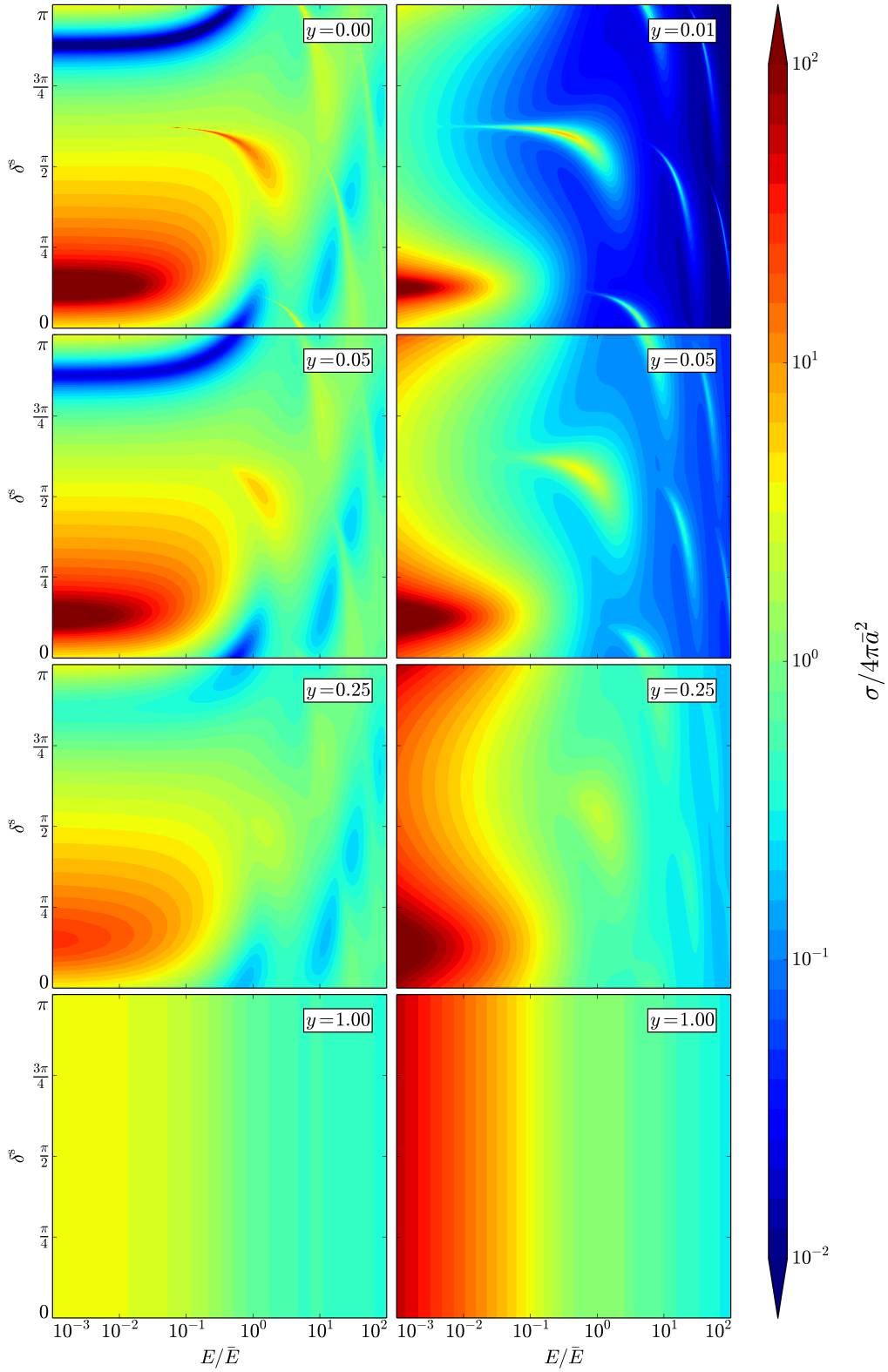

Figure 2.10: Contour plots of the elastic (left) and loss (right) cross sections for identical bosons as a function of reduced energy $E/\bar{E}$ and short-range phase shift δ^s for selected values of the loss parameter y.

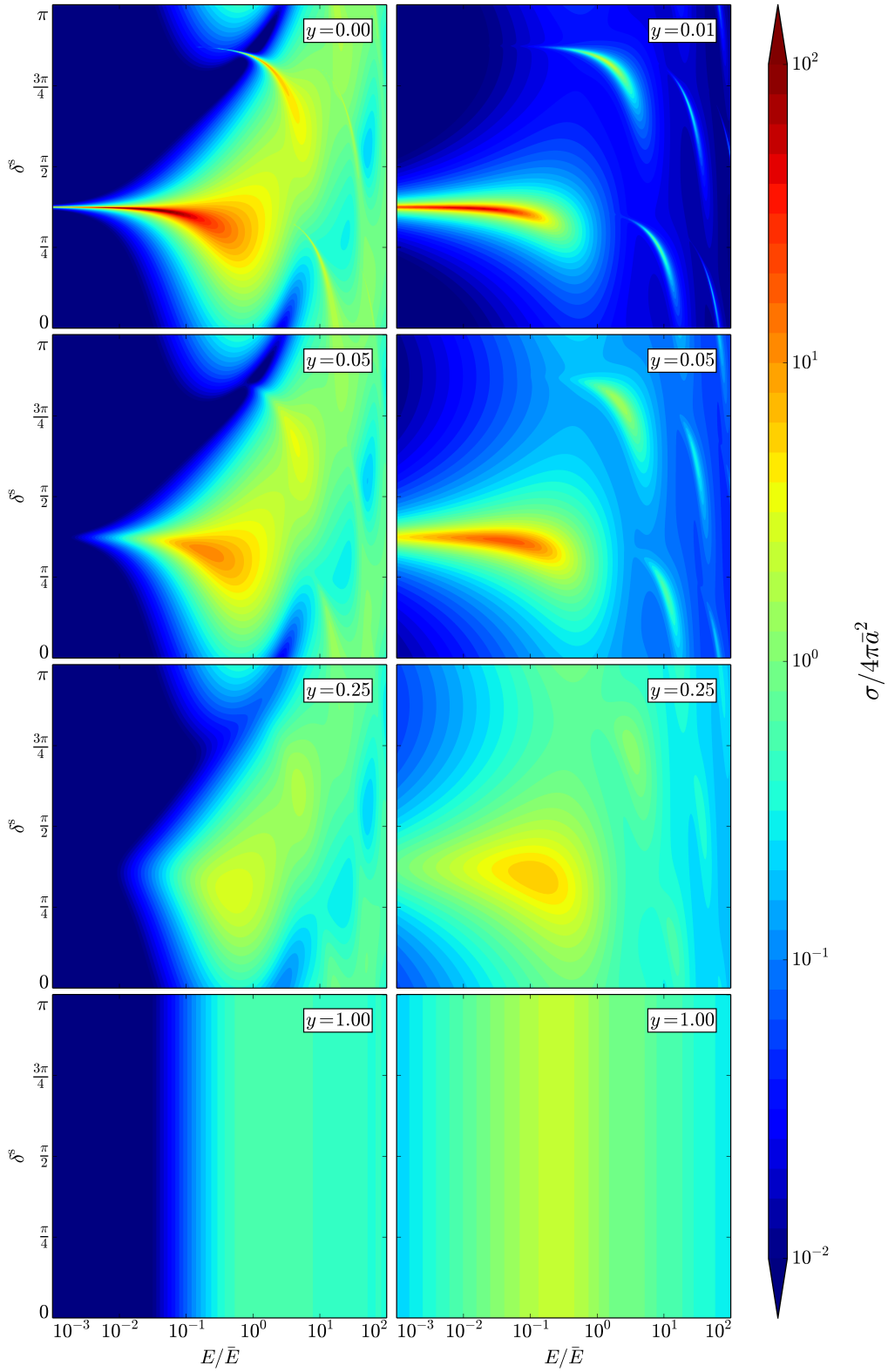

Figure 2.11: Contour plots of the elastic (left) and loss (right) cross sections for identical fermions as a function of reduced energy $E/\bar{E}$ and short-range phase shift δ^{s} for selected values of the loss parameter y.

2.3.1 Results of the single-channel model

Figures 2.9 to 2.11 show the elastic and loss cross sections for selected values of the loss parameter y, as a function of the short-range phase shift δ^s and the reduced energy $E/\bar{E}$, for distinguishable particles, identical bosons, and identical fermions, respectively. Versions of these figures with every value of y from 0 (fully elastic) to 1 (the universal loss regime) in steps of 0.01 are provided in the Supplemental Material of Ref. 176, both as pdf files and animated into short videos.

We consider first the case of distinguishable particles. At $y = 0$ (fig. 2.9(a)), low-energy scattering is dominated by s-wave features. There is a large peak near $\delta^s = \pi/8$, which corresponds to infinite scattering length, and a deep trough around $\delta^s = 7\pi/8$, which corresponds to zero scattering length. There is a set of sharp shape resonances that curve towards their zero-energy positions: p-wave at $\delta^s = 3\pi/8$, d-wave at $\delta^s = 5\pi/8$, and further partial waves at increments of $\pi/4$. Thus a shape resonance in partial wave $L + 4$ has the same zero-energy position as that in partial wave L [212], e.g. an h-wave ($L = 5$) shape resonance curves towards the same zero-energy position as the p-wave ($L = 1$) resonance. The plots are cyclic in δ^s with period π, so that the contours along the top edge of each plot are the same as those along the bottom edge. It may be noted that the trough corresponding to zero scattering length curves upwards as a function of energy; this arises because of a Ramsauer-Townsend minimum [220] that occurs in the s-wave cross section for small negative values of the scattering length. Note that this case is almost identical to the results shown previously for Rb+Yb in fig. 2.3.

There is by definition no loss cross section for $y = 0$; for $y = 0.01$ (fig. 2.9(b)) there is very little loss except close to the shape resonances: little flux is lost in each interaction with the short-range region, so it is only at a shape resonance that there are many interactions with the short-range region and loss becomes important. Shape resonances cause visible features at least as high as $L = 11$ in the plots for $y = 0$ and 0.01. Note that there is a large peak in the s-wave loss near $\delta^s = \pi/8$, even though s-wave collisions cannot have shape resonances *per se*: at low enough

[5] In this instance a actually refers to the scattering length of the reference potential, see Ref. 190 for more details.

energies the long-range potential reflects outgoing flux even with no barrier, so that the multiple interactions with the short-range region that are characteristic of shape resonances can still occur.

As the loss parameter y increases from 0, the features in the cross sections broaden out and eventually disappear, reaching the "universal loss" regime described by Idziaszek and Julienne [190]. Most of the features described above are still visible at $y = 0.05$, though the shape resonances are lower and do not persist to such low energy. However, the features have largely washed out by $y = 0.25$. The amplitude of variations in σ_{loss} as a function of δ^{s} decreases steadily as y increases. It should be noted that, even though $y = 1$ corresponds to complete loss at short range, it does *not* give the maximum possible overall loss rate. Values of $y < 1$ can sometimes give even faster loss rates because of the possibility of resonant enhancement.

The results for identical bosons (fig. 2.10) show similar features to those for distinguishable particles, except that there are no odd-L shape resonances. However, the results for identical fermions (fig. 2.11) are visually very different, because of the lack of an s-wave background at low energy. The shape resonances (this time for odd L only) are therefore even more prominent.

Many experiments use thermal samples. Figure 2.12 shows the rate constants for loss processes as a function of temperature, for selected values of y, for distinguishable particles (left) and identical fermions (right). The major features of the plots remain, but it may be seen that some of the higher-energy structure is washed out by averaging over kinetic energy. In particular, shape resonances due to partial waves with $L > 3$ are barely visible.

2.3.2 Comparison with coupled-channel calculations

Most of the real collision systems of interest in ultracold physics are multichannel in nature and have both shape and Feshbach resonances. As a prototype strongly-coupled system, we carry out coupled-channel calculations on Li+LiH, but we also calculate scattering at rotationally excited thresholds to explore the effects of inelastic loss. The length and energy scales for Li+LiH are $\bar{a} = 16.2$ Å and $\bar{E}/k_{\mathrm{B}} = 24.5$ mK, giving a p-wave barrier height of 6.1 mK.

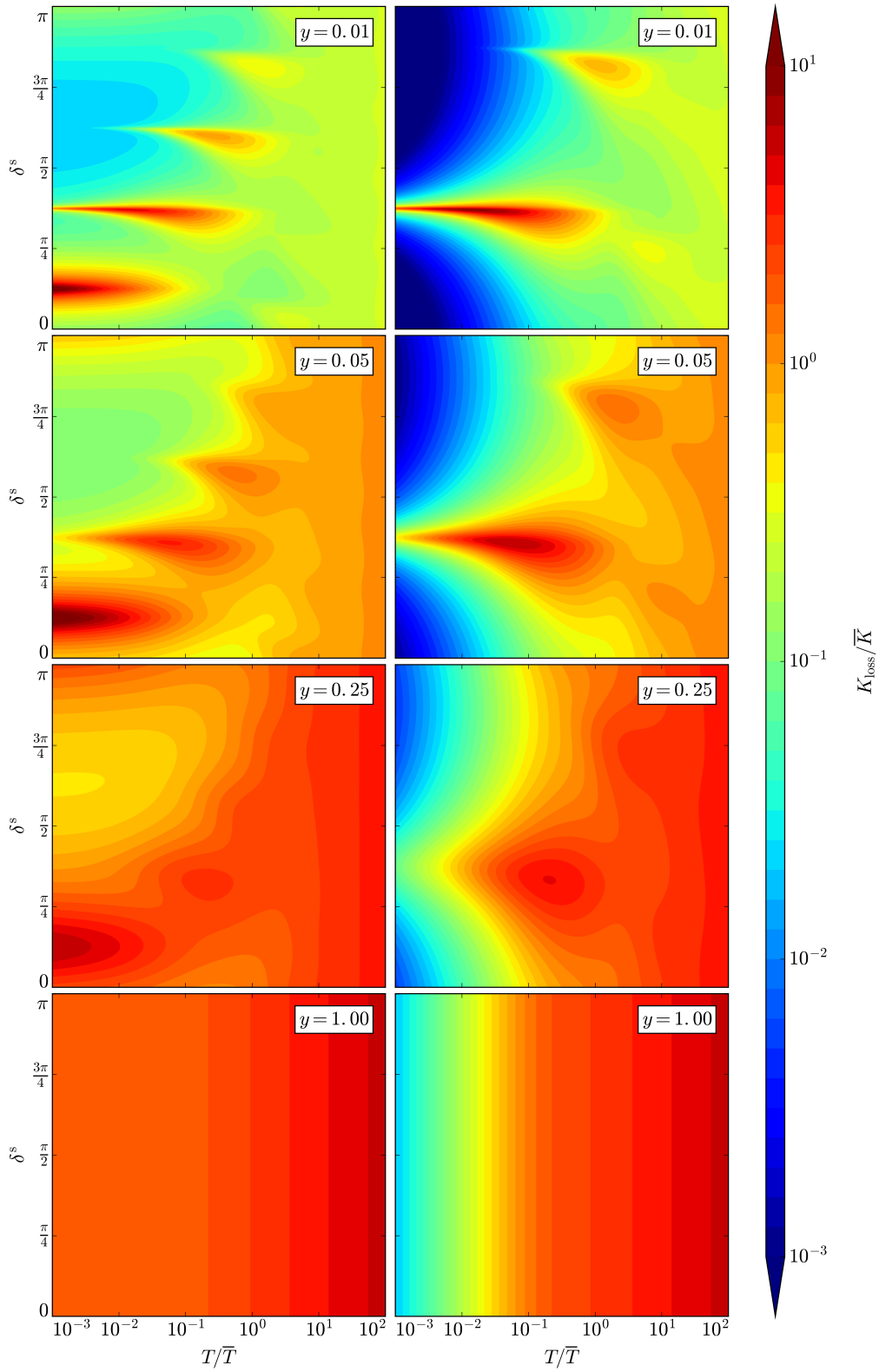

Figure 2.12: Contour plots of the thermally averaged loss rate for distinguishable particles (left) and identical fermions (right) as a function of reduced temperature $k_{\mathrm{B}}T/\bar{E}$ and short-range phase shift δ^{s} for selected values of the loss parameter y. The loss rate is scaled by $\bar{K} = \bar{a}h/\mu$.

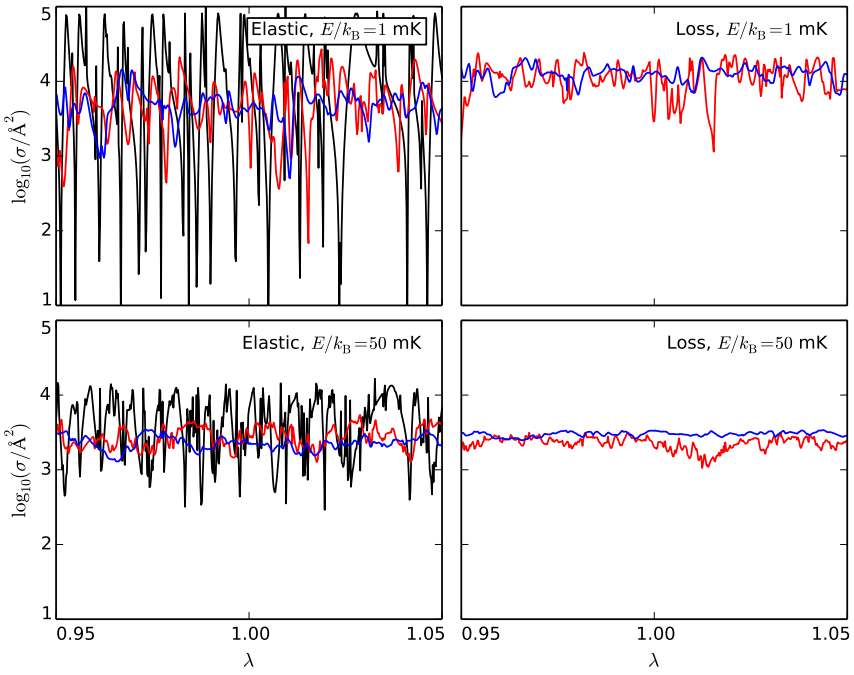

Figure 2.13: Elastic (left) and total inelastic (right) cross sections for Li+LiH collisions for initial rotational levels $j = 0$ (black), 3 (red), and 6 (blue) at kinetic energies $E/k_B = 1$ mK (top) and 50 mK (bottom) as a function of the potential scaling factor λ. Note the steadily decreasing amplitude of oscillations as initial j increases.

Figure 2.13 shows the calculated elastic and total inelastic cross sections for Li+LiH collisions for initial rotational levels $j = 0$, 3 and 6 at kinetic energies $E/k_B = 1$ mK and 50 mK as the scaling factor λ is varied across the range $0.95 < \lambda < 1.05$. Rotationally inelastic collisions are dominated by couplings at distances much smaller than $\bar{a}$. $E/k_B = 1$ mK is in the s-wave regime, so the cross sections for initial $j = 0$ show very large peaks and deep troughs. These correspond to poles and zeroes in the s-wave scattering length as successive atom-diatom bound states pass through threshold and cause Feshbach resonances. At $E/k_B = 50$ mK, peaks and troughs are still visible, but are less pronounced because of contributions from higher partial waves and the overall k^{-2} factor in the expressions for cross sections [106].

For successively higher initial j values, the number of inelastic channels increases and inelastic scattering becomes progressively stronger. The poles in scattering length that occur for initial $j = 0$ are replaced by finite oscillations that diminish in amplitude as the inelasticity increases [164]. The amplitude of the oscillations in the cross sections thus decreases as initial j increases, even in the s-wave regime.

The interaction potential of ref. [227] has an estimated uncertainty of only 0.05%, which is unusually precise for potentials from electronic structure calculations. In cases where the uncertainty is 1 to 5%, which is more typical, it is sufficient to span many oscillations in the cross sections in a plot such as fig. 2.13. Under these circumstances it is not meaningful to regard the results of scattering calculations on a single potential as predictions for the physical system, and it is essential to understand the *range* of results that may be obtained across the uncertainties in the potential [100, 228]. It is clear from fig. 2.13 that the range of possible results is very large for purely elastic collisions in the s-wave regime, but diminishes both when loss is present (for initial $j > 0$) and when there are significant contributions from several partial waves [106].

As shown earlier, even without loss ($j = 0$), the scattering for $L > 0$ in a complex system like Li+LiH is not fully determined by the value of δ^s obtained for $L = 0$. In addition, for $j > 0$ the value of y obtained by inverting eq. (2.1.35) is a fast function of λ, even in the s-wave regime, and is also L-dependent. Nevertheless, it is useful to

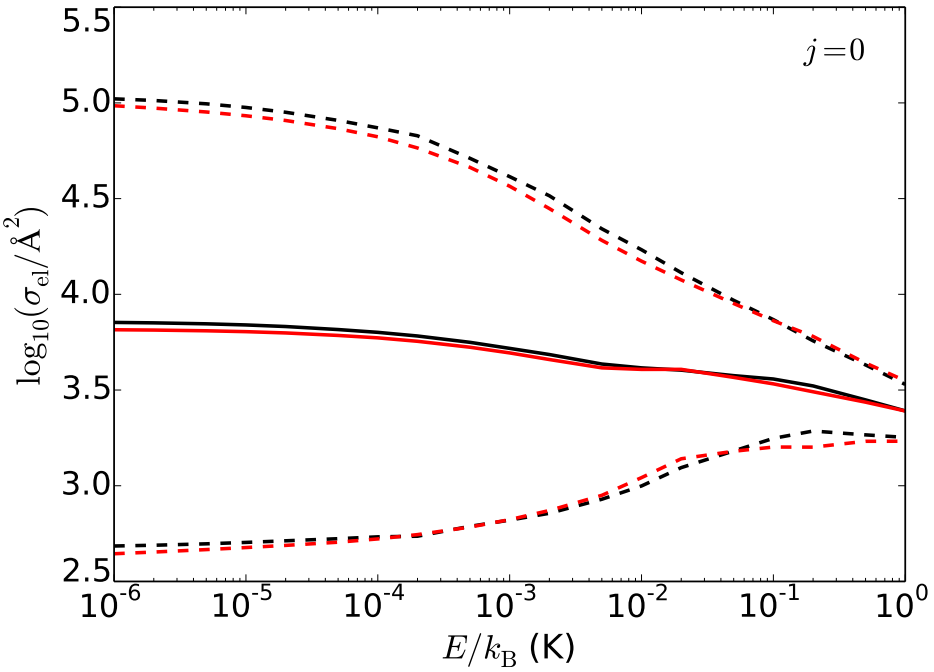

Figure 2.14: Mean values and mean ± 1 standard deviation of $\log_{10}(\sigma_{\mathrm{el}}/\mathrm{Å}^2)$ from the single-channel model with $y = 0$ (red), compared with the corresponding quantities from coupled-channel calculations for Li+LiH collisions with initial $j = 0$ (black).

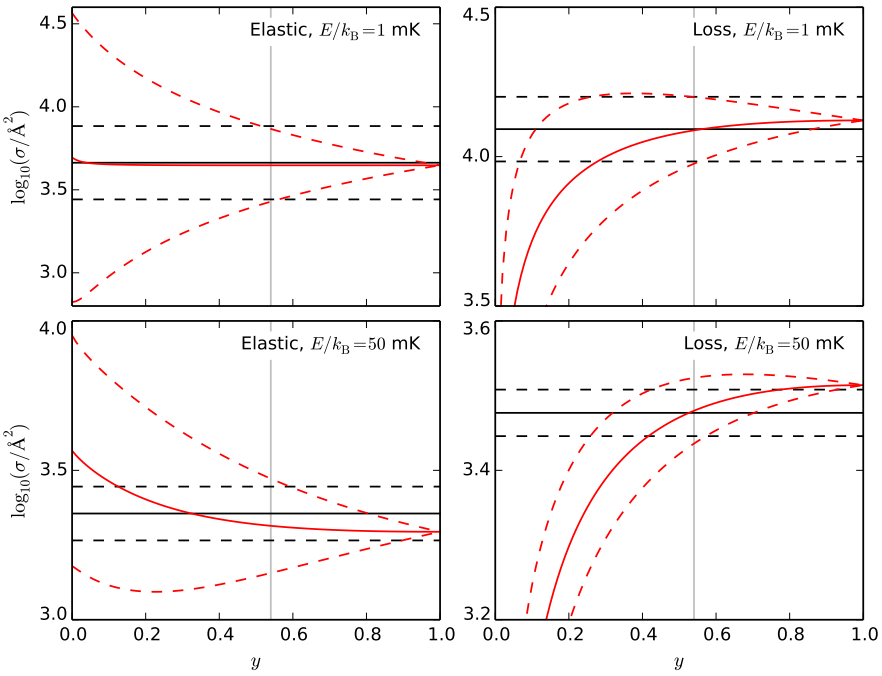

Figure 2.15: Mean values and and mean ± 1 standard deviation of $\log_{10}(\sigma_{\rm el}/\text{Å}^2)$ (left) and $\log_{10}(\sigma_{\rm loss}/\text{Å}^2)$ (right) from the single-channel model (red) for collision energies $E/k_{\rm B}$ = 1 mK (top) and 50 mK (bottom) as a function of y, compared with the corresponding quantities from coupled-channel calculations for for Li+LiH collisions with initial $j = 6$ (black horizontal lines). The vertical grey lines indicate $y = 0.57$, which gives the best agreement between the single-channel model and coupled-channel calculations for $j = 6$ at low energy.

compare the *distribution* of elastic and inelastic cross sections obtained from coupled-channel calculations (as λ is varied over the range shown in the Figures) with that obtained from the single-channel model (as $\delta^{\rm s}$ is varied from 0 to π for a given value of y). Figure fig. 2.14 shows this comparison for the mean and mean ± 1 standard deviation of $\log \sigma_{\rm el}$ as a function of collision energy for the case of initial $j = 0$, where there are no inelastic channels, so $y = 0$. It may be seen that the single-channel model (with no adjustable parameters whatsoever) quite accurately reproduces the energy-dependence of both the mean and standard deviation, despite the fact that most of the structure in fig. 2.13 comes from Feshbach resonances rather than shape resonances.

For higher initial j, where inelastic scattering is possible, we need to choose a value of y before comparing the coupled-channel and single-channel results. The

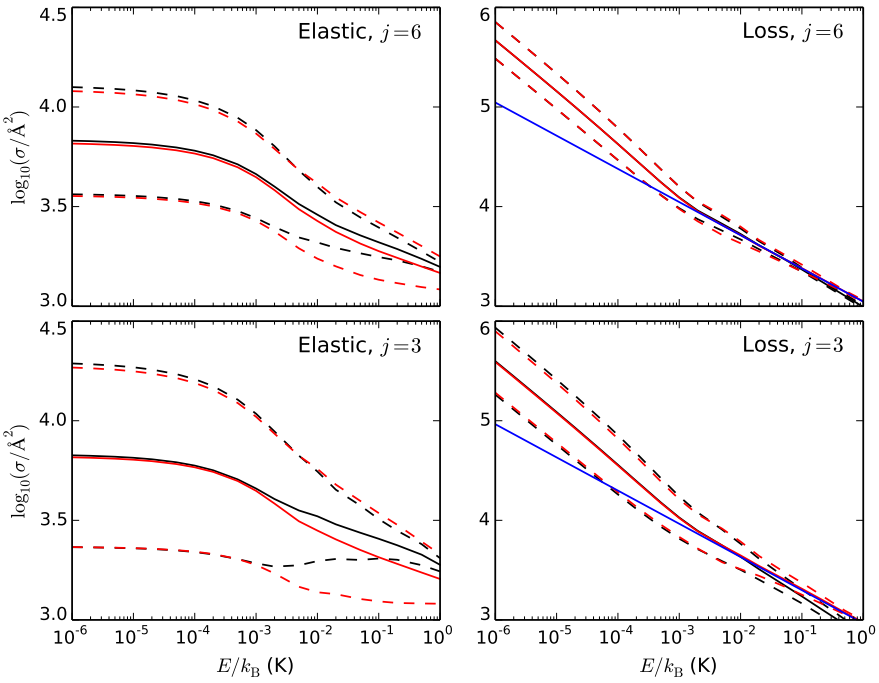

Figure 2.16: Mean values and and mean ± 1 standard deviation of $\log_{10}(\sigma_\text{el}/\text{Å}^2)$ (left) and $\log_{10}(\sigma_\text{loss}/\text{Å}^2)$ (right) from the single-channel model (red) and coupled-channel calculations (black) for Li+LiH collisions with initial $j = 6$ (top) and $j = 3$ (bottom) as a function of collision energy. The single-channel calculations use $y = 0.57$ for $j = 6$ and $y = 0.23$ for $j = 3$. The blue lines show the classical Langevin cross section multiplied by the reaction probability $P^\text{re} = 4y/(1 + y)^2$.

upper panels of fig. 2.15 show the mean and mean ± 1 standard deviation for $\log \sigma_{\mathrm{el}}$ and $\log \sigma_{\mathrm{loss}}$ for initial $j = 6$ at $E/k_{\mathrm{B}} = 1$ mK from coupled-channel calculations (horizontal lines), compared with those calculated from the single-channel model as a function of y (converging lines). It may be seen that $y \approx 0.57$ approximately reproduces the low-energy distributions. The lower panels of fig. 2.15 show the corresponding plots at 50 mK; the single-channel model with $y = 0.57$ still reproduces the distribution of σ_{loss} fairly well, and is also qualitatively correct for σ_{el}, though it somewhat overestimates the standard deviation in this case. The full energy-dependence for $y = 0.57$ is shown in the upper panels of fig. 2.16; there are quantitative differences, but the single-channel model is nevertheless remarkably accurate for the distribution of both elastic and inelastic cross sections over the range of energies shown. For comparison fig. 2.16 also shows the classical Langevin cross section multiplied by the reaction probability $P^{\mathrm{re}} = 4y/(1+y)^2$ [194].

The agreement between the coupled-channel calculations and the single-channel model does deteriorate somewhat for lower values of initial j. This is to be expected, because these cases have fewer open loss channels and it is therefore more likely that flux that is initially lost from the incoming channel will subsequently return to it, violating one of the assumptions of the single-channel model. The lower panels of fig. 2.16 show the case of initial $j = 3$, where the low-energy distribution is reasonably well described by $y = 0.23$. In this case, however, the higher-energy cross sections calculated from the single-channel model deviate somewhat from the coupled-channel results, particularly for the elastic cross sections. Nevertheless, qualitative agreement remains.

We have verified that the agreement between the coupled-channel calculations and the single-channel model improves steadily from initial $j = 1$ to 6, as the number of open loss channels increases. Initial $j = 1$ is a special case. In the presence of inelastic scattering, individual Feshbach resonances exhibit both a peak and a dip in the real and imaginary parts of the complex scattering length, and hence in the loss cross section [164]. When there is a single dominant loss channel, the dip in the s-wave cross section can be very deep [229] (and reaches $\sigma_{\mathrm{loss}} = 0$ when there is only one loss channel). This behaviour skews the distribution of $\log_{10} \sigma_{\mathrm{loss}}$ at the

low end, particularly for initial $j = 1$. For higher initial j, the effect is reduced by additional loss channels, and at higher energies it is reduced by contributions from higher partial waves.

2.4 Conclusions and Future Work

In this chapter we have investigated AQDT in a series of increasingly complex systems. The theory was expected to provide a good model of the simple single-channel alkali+Yb systems at low energy, but it turned out to be more robust than expected and provide an excellent single-parameter model of the scattering over a remarkably large range of energy. It even captured the first effects of glory scattering, which is usually considered to be well outside the realm of cold collisions, suggesting that elements of this theory may have useful applications beyond this immediate field. This also confirms that there is only one independent parameter relating to the details of the short-range potential which is important in cold (and not so cold) scattering in systems of this type; this justifies the emphasis placed on determination of the scattering length. In the moderately complicated alkali+alkali system, the very simple AQDT predictions provided robust predictions of characteristics of background scattering, even if it inevitably failed to describe the Feshbach resonances of the system. Finally, in the case of a strongly coupled system – where the single-channel AQDT model was expected to fail completely – we found that it *still* provided a remarkably good approximate model for the relationship between partial waves at low energy. For such complex systems AQDT is more suitable as a guide to typical behaviour rather than making specific quantitative predictions, but it is nonetheless remarkable that such a simple single-channel model has any validity.

Now that the limits of the simple single-channel AQDT model have been investigated, a possible future direction would be to investigate more complicated QDT models and how well they represent the more complicated systems. For example, a frame-transformation multichannel QDT model with two independent short-range parameters has proved to be a successful model for some alkali+alkali systems [189, 221, 230, 231]. It would be interesting if a similar model could be successfully

applied to more complex systems. It would be of particular interest if a system which shows signs of chaos – such as Yb(^{1}S$_0$)+Yb(^{3}P$_2$) [129] (as we will discuss in chapter 4) – could be accurately described using only a small number of parameters. The application of such a model to scattering involving one or more molecules could also be interesting because it may help determine the number of independent parameters needed to describe the short-range interactions.

We then pursued further the idea of representing typical behaviour rather than specific detailed results, this time to model collisional loss. We implemented the travelling-wave QDT of Gao to model loss with a non-unitary short-range S-matrix. The results of this QDT model are enlightening in themselves and illustrate some interesting points about losses in scattering as well as clarifying the approach to the universal loss regime of Idziaszek and Julienne [190]. The comparison of these results with coupled channel calculations of rotationally inelastic collisions was highly successful, with the model reliably and quantitatively reproducing the range of typical results with only one or zero fitted parameters. In the case that full calculations will only give us a range of typical results anyway – as is common in ultracold scattering due to uncertainties in the potential – this method has great potential.

These last results suggest a remarkable possibility for inferring the behaviour of cold collisions at higher temperatures from calculations in the s-wave regime. For a system with enough open channels to be well described by a single-channel model, it would be possible to perform coupled-channel calculations for incoming $L = 0$ only and use the results (as a function of a potential scaling factor λ) to determine a short-range loss parameter y. The single-channel approach could then be used to predict the range of possible loss rates at higher energy, without the need to carry out explicit coupled-channel calculations for higher initial L.

One possible future direction is including the important physical effect of centrifugal suppression of inelastic collisions into our model, to assess typical behaviours for that case. Multichannel QDT has previously been shown to be capable of describing centrifugal suppression accurately in a simple system [218]. The most important case of centrifugal suppression is for collisions in a small magnetic field, which typically require relatively large and complicated basis sets. This has made explicit

calculations for systems of this type challenging and computationally expensive, especially at energies above the s-wave regime and for complex systems. This is exactly the case for which our model is expected to be most useful.

Chapter 3

Thermalisation

The thermalisation of clouds of atoms and molecules is important in many areas in cold and ultracold physics. Most obviously, it is crucial for many direct cooling methods, in particular sympathetic, buffer-gas, and evaporative cooling. It is also often used as an easily observable signature of collisions, which can be used to obtain an estimate of the magnitude of the scattering length or a cross section [232, 233]. A particular example of this is the use of the variation in thermalisation rates to observe magnetic Feshbach resonances (e.g., [234]). The ability to estimate the magnitude of the scattering length can also be important as a simple method for refining potentials; this is usually fairly approximate, but early in the investigations into a system even such approximate estimates can be useful in directing and understanding further work on the system in question.

It is often supposed that the rate of thermalisation is determined by the elastic cross section σ_{el} [56, 112, 235]. Recall[1] that this is given as a simple integral over the differential cross section (DCS) $d\sigma/d\omega$,

$$\sigma_{\mathrm{el}} = \int \frac{d\sigma}{d\omega} d\omega = 2\pi \int \frac{d\sigma}{d\omega} \sin\Theta \, d\Theta, \tag{3.0.1}$$

where Θ is the deflection angle in the centre-of-mass frame. However, collisions that cause only small deflections of the collision partners contribute fully to the elastic cross section but make very little contribution to kinetic energy transfer and thus

[1] This was described previously in section 1.2, but repeated here for the purposes of discussion.

to thermalisation. The appropriate cross section that takes this into account is the transport cross section $\sigma_\eta^{(1)}$ that was introduced in eq. (1.2.5),

$$\sigma_\eta^{(1)} = 2\pi \int \frac{d\sigma}{d\omega}(1 - \cos\Theta)\sin\Theta \, d\Theta, \tag{3.0.2}$$

which has been used extensively in the context of transport properties at higher temperatures [236, 237]. It determines the binary diffusion coefficient for a mixture, and contributes to the shear viscosity coefficient.

The relevance of $\sigma_\eta^{(1)}$ to thermalisation of ultracold gases has been pointed out by Anderlini and Guéry-Odelin [238] (who call it $\widetilde{\sigma}$), but no study of how it behaves has been made for the conditions relevant to thermalisation of ultracold atoms and molecules. In section 3.1 we explore how this cross-section arises and its behaviour for real and realistic systems. Then, in section 3.2, we proceed to explore the effect that this cross section, and a generally anisotropic DCS, has on prospects for sympathetic cooling in a microwave trap. For this we use systems and other details directly related to ongoing experimental efforts to use sympathetic cooling. Finally, in section 3.3, we apply what we have learned through the chapter to improve our understanding of the prospects of sympathetic cooling in a magnetic trap. This includes correcting an error in interpretation of centre-of-mass and lab-frame energies in previous work on the subject, which can have significant effects for systems with considerable mass imbalance.

3.1 Differential Cross Sections and Integral Cross Section for Thermalisation

In this section, we first re-derive eq. (3.0.2) in more detail than was given by Anderlini and Guéry-Odelin [238]. We then give examples in section 3.1.2 of differential cross sections and how they affect the integral cross-sections σ_{el} and $\sigma_\eta^{(1)}$ for realistic potentials. Finally, we consider how this work affects the determination of scattering lengths from thermalisation measurements in real experiments on alkali+Yb systems.

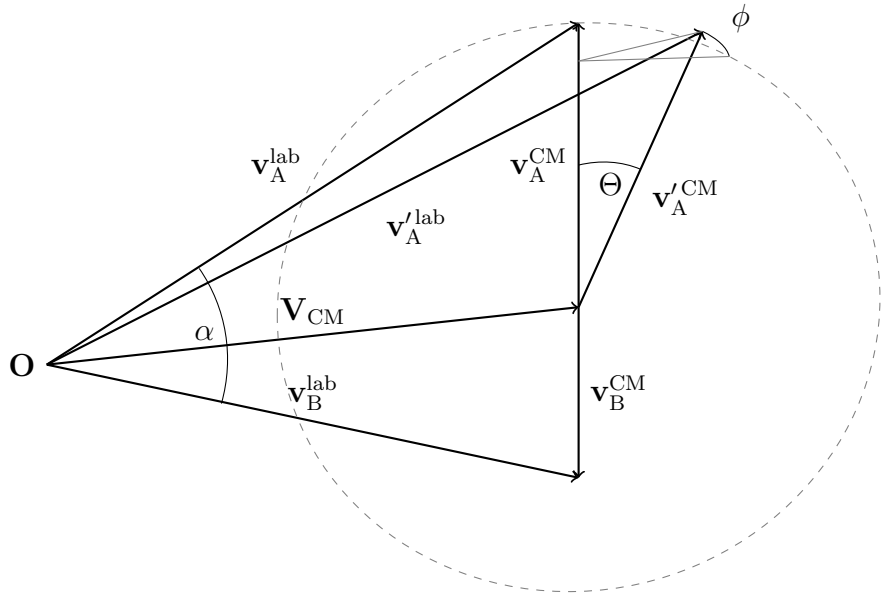

Figure 3.1: Newton diagram for an elastic collision of two particles, A and B. The notation is described in the text. For clarity final velocities are shown only for A.

3.1.1 Effect of Scattering Angle on Energy Transfer

We consider a classical model of collisional energy transfer. The approximations involved in this are that there are only two-body collisions and that the macroscopic motion of particles around the trap can be considered to be classical, although the microscopic collision dynamics which determine the DCS can still be quantum in nature. Such a model has been shown to be valid for collisional relaxation of collective motion down to temperatures about twice the temperature of quantum degeneracy [239, 240], and it is reasonable to assume that a similar range of validity will be applicable for thermalisation; however, as degeneracy is approached a fully quantum description will be needed (e.g. [241]). This approximation may also break down if three-body collisions are enhanced, for example due to the effects of Effimov physics or the effects considered in chapter 5.

A Newton diagram for an elastic collision of two particles, A and B, is shown in fig. 3.1. The initial velocities in the laboratory frame are labeled $\mathbf{v}_X^\mathrm{lab}$,[2] where X is

[2]Through this chapter we will use superscript labels to indicate whether a velocity or energy is in the laboratory frame or the centre-of-mass frame, and be explicit throughout. The reader should be aware that other authors are sometimes not so explicit.

either A or B. This gives the velocity of the centre of mass (CM) as[3]

$$\mathbf{V}_{\mathrm{CM}} = \frac{\mathbf{v}_{\mathrm{A}} m_{\mathrm{A}} + \mathbf{v}_{\mathrm{B}} m_{\mathrm{B}}}{m_{\mathrm{A}} + m_{\mathrm{B}}}, \tag{3.1.3}$$

where m_X is the mass of particle X. The velocities of each particle in the centre of mass frame are then given as

$$\mathbf{v}_X^{\mathrm{CM}} = \mathbf{v}_X^{\mathrm{lab}} - \mathbf{V}_{\mathrm{CM}}, \tag{3.1.4}$$

and the relative velocity is

$$\mathbf{v}_{\mathrm{rel}} = \mathbf{v}_{\mathrm{A}}^{\mathrm{lab}} - \mathbf{v}_{\mathrm{B}}^{\mathrm{lab}} \tag{3.1.5}$$

$$= \mathbf{v}_{\mathrm{A}}^{\mathrm{CM}} - \mathbf{v}_{\mathrm{B}}^{\mathrm{CM}}, \tag{3.1.6}$$

which is the same in both frames, so does not need a label for which frame it is in. The total kinetic energy of the system can be written either as a sum of terms from each particle, or as a sum of centre-of-mass and relative terms

$$E_{\mathrm{k}} = E_{\mathrm{k,A}}^{\mathrm{lab}} + E_{\mathrm{k,B}}^{\mathrm{lab}} \quad = \frac{1}{2} m_{\mathrm{A}} |\mathbf{v}_{\mathrm{A}}^{\mathrm{lab}}|^2 + \frac{1}{2} m_{\mathrm{B}} |\mathbf{v}_{\mathrm{B}}^{\mathrm{lab}}|^2 \tag{3.1.7}$$

$$= E_{\mathrm{k,CM}} + E_{\mathrm{k,rel}} \quad = \frac{1}{2}(m_{\mathrm{A}} + m_{\mathrm{B}}) |\mathbf{V}_{\mathrm{CM}}|^2 + \frac{1}{2} \mu |\mathbf{v}_{\mathrm{rel}}|^2, \tag{3.1.8}$$

where μ is the reduced mass as in previous chapters. The energy of the relative motion $E_{\mathrm{k,rel}} = (1/2)\mu|\mathbf{v}_{\mathrm{rel}}|^2$ is the quantity used in scattering calculations, i.e. the E in eqs. (1.2.7) and (1.2.9); we will often call this quantity the energy in the centre-of-mass frame $E_{\mathrm{k}}^{\mathrm{CM}}$.

At this point, we emphasise the importance of correctly considering the difference between laboratory frame energies and centre-of-mass frame energies, especially for the purposes of thermalisation. In particular, if one particle (B) is approximated as being stationary ($\mathbf{v}_{\mathrm{B}}^{\mathrm{lab}} = 0$) – which is often reasonable in a cooling experiment

[3]Note that the subscript labels this as the velocity of the centre of mass (in the laboratory frame), not a velocity in the centre-of-mass frame. We could technically write this as $\mathbf{V}_{\mathrm{CM}}^{\mathrm{lab}}$, but that would be overly pedantic.

where the coolant cloud (B) is much colder than the target to be cooled (A) – then we can write

$$E_{\mathrm{k}} = E_{\mathrm{k,A}}^{\mathrm{lab}} = E_{\mathrm{k,CM}} + E_{\mathrm{k}}^{\mathrm{CM}} \tag{3.1.9}$$

$$E_{\mathrm{k}}^{\mathrm{CM}} = E_{\mathrm{k,A}}^{\mathrm{lab}} - E_{\mathrm{k,CM}} \tag{3.1.10}$$

$$= E_{\mathrm{k,A}}^{\mathrm{lab}} \frac{m_{\mathrm{B}}}{m_{\mathrm{A}} + m_{\mathrm{B}}} \tag{3.1.11}$$

$$= E_{\mathrm{k,A}}^{\mathrm{lab}} \frac{\mu}{m_{\mathrm{A}}}. \tag{3.1.12}$$

This means that when cooling with a species that is significantly lighter than the target to be cooled, the collision energies that need to be considered in scattering calculations can be much lower than the temperature of the target cloud. In the case of particularly light coolants such as H [109, 110], or Li [106], this factor can easily be an order of magnitude. This effect lessens as the temperature of the target cloud approaches that of the coolant and the latter can no longer be well approximated to be stationary.

We now consider the effect a collision has on the colliding particles. Here we need to consider only elastic collisions, because inelastic (or reactive) collisions will lead to trap loss and are thus considered separately. As is well known, conservation of energy and momentum means that in the centre-of-mass frame the collision rotates the velocity vectors but does not alter their magnitude. This is shown in fig. 3.1, where velocity vectors after the collision are denoted with a prime, e.g. $\mathbf{v}_{\mathrm{A}}'^{\mathrm{CM}}$ is the velocity of particle A in the CM frame after the collision. In our case, the rotation (or rather, probability of a given rotation) will be determined from the differential cross section eq. (1.2.3) calculated in microscopic quantum scattering calculations, although it could equally be obtained from an equivalent classical calculation. The rotation is conveniently parameterised by two angles in the CM frame, Θ and ϕ, as shown in fig. 3.1. Note that while Θ is the familiar scattering angle, ϕ is not usually explicitly considered in scattering calculations as the cylindrical symmetry in the CM frame means that scattering usually does not depend on this angle. There is an exception to this in the case that there is some external field which breaks this symmetry.

Although there is no change in the magnitude of the velocity and so no apparent energy transfer in the centre-of-mass frame, there is an energy transfer once transformed back to the laboratory frame; generally $E_{\mathrm{k,A}}^{\mathrm{lab}} \neq E_{\mathrm{k,A}}'^{\mathrm{lab}}$. Another way to think about this is that the partitioning of kinetic energy between CM and relative motions given by eq. (3.1.8) cannot be changed by an elastic collision, but the partitioning of kinetic energy between A and B given by eq. (3.1.7) can be changed. This change in energy is given by

$$\Delta E_{\mathrm{k,A}} = E_{\mathrm{k,A}}'^{\mathrm{lab}} - E_{\mathrm{k,A}}^{\mathrm{lab}} = \frac{1}{2} m_{\mathrm{A}} |\mathbf{v}_{\mathrm{A}}'^{\mathrm{lab}}|^2 - \frac{1}{2} m_{\mathrm{A}} |\mathbf{v}_{\mathrm{A}}^{\mathrm{lab}}|^2 \tag{3.1.13}$$

$$= \frac{\mu}{m_{\mathrm{A}} + m_{\mathrm{B}}} (1 - \cos\Theta) \left[-m_{\mathrm{A}} |\mathbf{v}_{\mathrm{A}}^{\mathrm{lab}}|^2 + m_{\mathrm{B}} |\mathbf{v}_{\mathrm{B}}^{\mathrm{lab}}|^2 + (m_{\mathrm{A}} - m_{\mathrm{B}}) |\mathbf{v}_{\mathrm{A}}^{\mathrm{lab}}| \, |\mathbf{v}_{\mathrm{B}}^{\mathrm{lab}}| \cos\alpha \right]$$

$$+ \mu |\mathbf{v}_{\mathrm{A}}^{\mathrm{lab}}| \, |\mathbf{v}_{\mathrm{B}}^{\mathrm{lab}}| \, \sin\alpha \, \sin\Theta \, \cos\phi \tag{3.1.14}$$

where α is the angle between $\mathbf{v}_{\mathrm{A}}^{\mathrm{lab}}$ and $\mathbf{v}_{\mathrm{B}}^{\mathrm{lab}}$. Averaging this quantity assuming that the direction of the initial velocity vectors are uniformly random on a sphere and that the scattering is uniform in ϕ we obtain

$$\langle \Delta E_{\mathrm{k,A}} \rangle = \frac{2\mu}{m_{\mathrm{A}} + m_{\mathrm{B}}} (1 - \cos\Theta)(E_{\mathrm{k,B}}^{\mathrm{lab}} - E_{\mathrm{k,A}}^{\mathrm{lab}}). \tag{3.1.15}$$

This shows the efficiency of energy transfer in collisions, and so thermalisation, to be proportional to $1 - \cos\Theta$. This results in the use of the transport cross section $\sigma_\eta^{(1)}$ given by eq. (3.0.2).

We can immediately consider the behaviour of $\sigma_\eta^{(1)}$ in some simple cases. When the scattering is isotropic - such as in the s-wave regime - the factor of $1 - \cos\Theta$ is averaged out and $\sigma_\eta^{(1)} = \sigma_{\mathrm{el}}$. Indeed, when any single partial wave dominates, such as may occur near a resonance, the DCS will be symmetric about $\Theta = \pi/2$ and $\sigma_\eta^{(1)} = \sigma_{\mathrm{el}}$. At higher collision energies there are typically large contributions to the elastic cross section from small-angle scattering which will have little or no impact on thermalisation. We thus expect qualitatively different behaviour of the two cross sections at the high-energy limit; in particular, the elastic cross section for systems with potentials with a long-range attractive tail shows distinctive glory oscillations [148] which we expect to be absent from $\sigma_\eta^{(1)}$. It is also worth noting

that in the high-energy limit for hard-sphere scattering, the quantum elastic cross section is approximately twice the classical cross section, but is also approximately half comprised of small-angle 'shadow' scattering [148] which contributes little to thermalisation. Therefore, in this case, $\sigma_\eta^{(1)}$ will agree between classical and quantum scattering. We expect that $\sigma_\eta^{(1)}$ will in general agree between quantum and classical calculations in a suitable limit of classical behaviour, even though σ_{el} does not generally agree in a such a limit. In particular, we will later show that the high-energy classical and quantum $\sigma_\eta^{(1)}$ agree for a model Lennard-Jones potential.

Anderlini and Guéry-Odelin [238] also provide an alternative expression for $\sigma_\eta^{(1)}$ in terms of partial-wave phase shifts δ_L,

$$\sigma_\eta^{(1)} = \frac{2\pi}{k^2} \sum_{0 \le L \le L' < \infty} \alpha_{L,L'} \sin\delta_L \sin\delta_{L'} \cos(\delta_L - \delta_{L'}) \tag{3.1.16}$$

where $\alpha_{L,L} = 4L + 2$, $\alpha_{L,L+1} = -(4L + 4)$, and $\alpha = 0$ otherwise. This expression is the one we use to calculate $\sigma_\eta^{(1)}$ in the single-channel case and is also useful for interpretation in the few partial wave regime. However, it is not suitable for calculating the cross section in more complex cases, for example when there is coupling between channels of different partial waves, or when there is inelastic scattering. Equation (3.1.16) shows $\sigma_\eta^{(1)}$ to be composed of the same terms as the elastic cross section, eq. (1.2.19), plus additional interference terms between consecutive partial waves. For random phase shifts, these interference terms are more often negative than positive, which emphasises that the very nature of the partial wave expansion biases scattering towards the forward direction. In the case of multiple open channels, $\sigma_\eta^{(1)}$ is no longer given by eq. (3.1.16) but it can still be simply calculated from S-matrix elements [150] and is conceptually similar.

3.1.2 Differential Cross Sections

Here we give examples of differential cross sections and show how they contribute to $\sigma_\eta^{(1)}$. We use calculations on a Lennard-Jones (L.-J.) potential

$$V(r) = \frac{C_{12}}{r^{12}} - \frac{C_6}{r^6}. \tag{3.1.17}$$

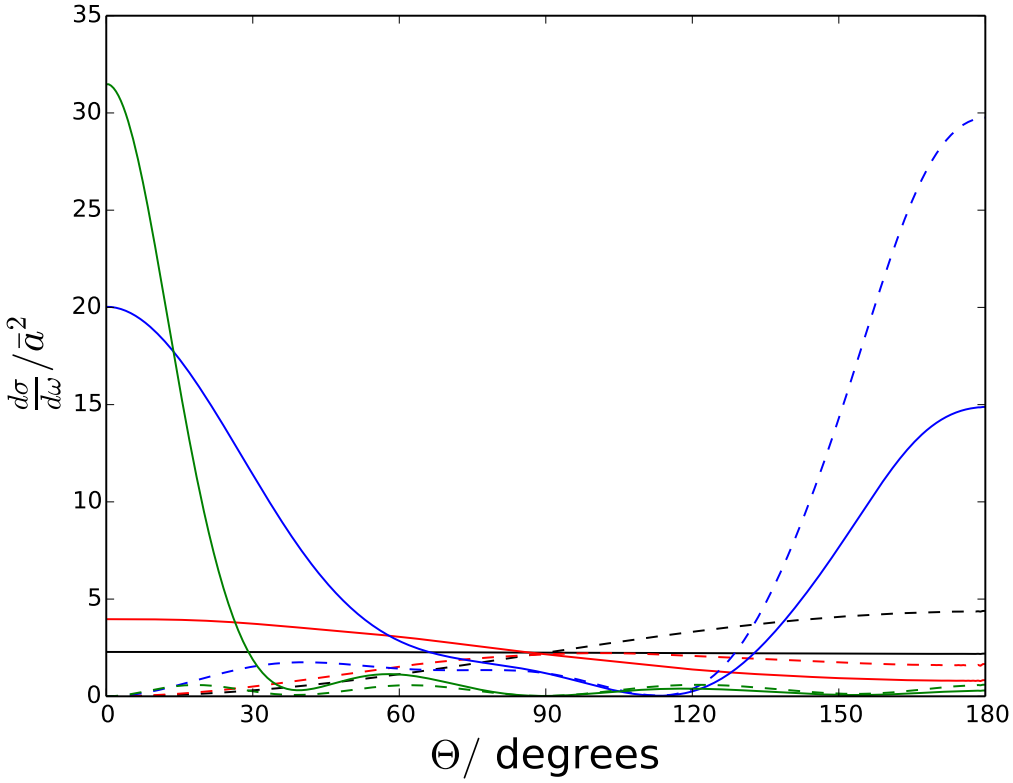

Figure 3.2: Differential cross sections for the model L.-J. potential with $a/\bar{a} = 1.5$ at $E/E_6 = 0.010$ (black), 0.50 (red), 5.2 (blue), and 50 (green). Dashed lines show the DCS weighted by $1 - \cos\Theta$.

Section 2.2 tells us that the results for this model system are a good model for any single-channel system with a long-range form of C_6R^{-6}. They can also be thought of as capturing typical behaviours of more complex systems, by analogy with section 2.3. We emphasise this by presenting results in reduced units and avoiding discussion of the particular parameters of the model.[4] We focus on a typical moderate scattering length of $1.5\bar{a}$, but will use other scattering lengths as appropriate.

Figure 3.2 shows selected DCSs for energies from $0.01E_6$ to $50E_6$. Note that the integral cross sections are not simply integrals under these curves as eqs. (1.2.4) and (3.0.2) include a weight of $\sin\Theta$.[5] It can be seen that at the lowest energy

[4]For reference, we use those used to describe Rb+CaF in section 3.2.

[5]We could have included this weighting or plotted the DCSs as a function of $\cos\Theta$ (as we will do in a later section), but at this stage we choose to leave these DCSs as they are to provide simple qualitative understanding.

$E = 0.01E_6$, there is only s-wave scattering so the DCS is isotropic. As energy increases, the isotropy is broken by contributions from higher partial wave and at $E = 0.5E_6$ the DCS shows a small amount of anisotropy. This energy is about twice the p-wave centrifugal-barrier height, but still below the d-wave barrier, which is consistent with the simple angular dependence observed; complex patterns would need contributions from many more partial waves. In this case, the anisotropy favours forward scattering but at this energy does not yet form a clear forward peak, but other cases (different values of $a/\bar{a}$) may instead favour backward scattering. By $E = 5.2E_6$, there is a clear but broad forward peak, and also a peak in backward scattering. The former is common (but not universal) amongst different cases at this energy, but the latter is a relatively uncommon feature. Note how the $1 - \cos\Theta$ weighting almost completely suppresses the forward peak, but in this case compensates somewhat by enhancing the backward peak. Finally, at $E = 50E_6$, the DCS has a higher but narrower forward peak and oscillations near zero at larger angles. This qualitative behaviour is common between different cases, although the quantitative details will vary. Now, the $1 - \cos\Theta$ suppresses the forward peak even more dramatically as it is concentrated at lower Θ, but there is now no compensating backward scattering. It is clear that in this final case $\sigma_\eta^{(1)}$ will be considerable smaller than σ_{el}.

Figure 3.3 shows contributions to σ_{el} and $\sigma_\eta^{(1)}$ from eq. (1.2.19) and eq. (3.1.16). At low energy, both cross sections are composed of only the constant s-wave contribution (red solid line); $\sigma_\eta^{(1)}$ deviates from this at significantly lower energy than σ_{el} because the interference term between $L = 0$ and 1 (red dashed line) begins to contribute at lower energy than the pure $L = 1$ term (green solid line). Note that this interference term is negative; as previously mentioned it is typical for these terms to be negative, but in other cases they can be positive, for example the $L = 1$ and 2 interference term (green dashed line) begins positive. There is a large peak in both integral cross sections around $E = 10E_6$ which comes from the d-wave contribution (blue). This is not a shape resonance as it is above the centrifugal barrier, but can be thought of as a continuation of one and is associated with the phase in the d-wave channel rapidly increasing from zero; this rapid phase variation causes, as expected,

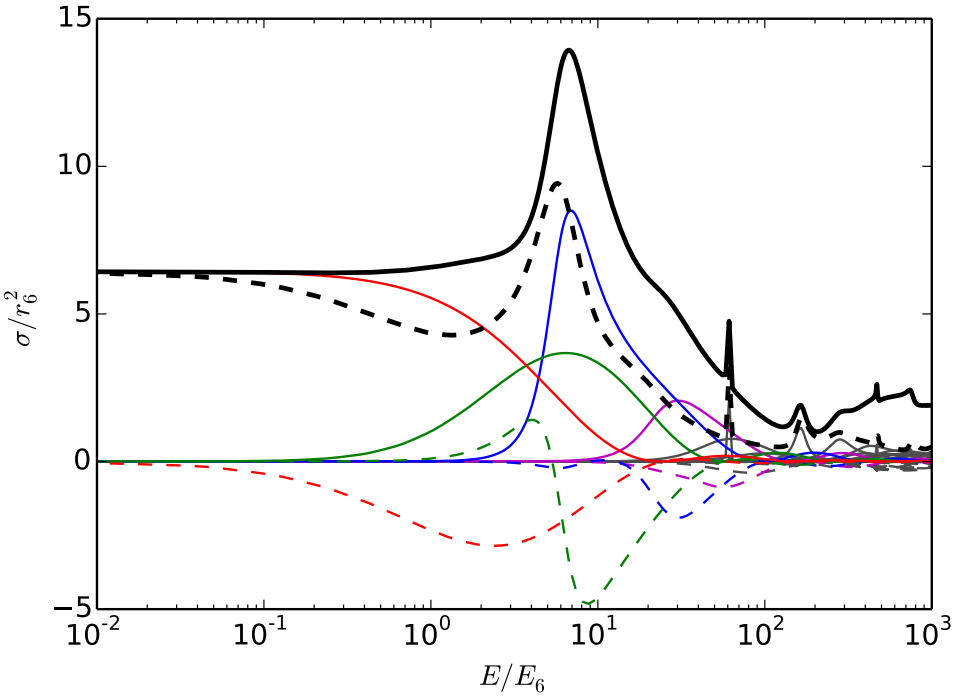

Figure 3.3: Integral cross sections σ_{el} (heavy solid line) and $\sigma_\eta^{(1)}$ (heavy dashed line) for the model L.-J. potential with $a/\bar{a} = 1.5$. The lighter lines show individual contributions to these cross sections: solid lines show the $L = L'$ terms in that contribute to both σ_{el} and $\sigma_\eta^{(1)}$, and the dashed lines show the $L' = L+1$ interference terms that only contribute to $\sigma_\eta^{(1)}$. Coloured lines show the contributions for $L = 0$ (red), 1 (green), 2 (blue), and 3 (magenta), the contributions from higher partial waves are all in grey. Note that the vertical axis is linear rather than logarithmic as would be normal for plots of cross sections.

a large peak in the pure d-wave contribution, but it also changes the sign of the $L = 1$ and 2 interference term, as the term $\cos(\delta_1 - \delta_2)$ in eq. (3.1.16) changes sign as δ_2 rapidly changes and takes the difference $\delta_1 - \delta_2$ through plus or minus π. This also happens less obviously for the $L = 2$ and 3 interference term. Although several of the features just described are particular to this case, they serve to demonstrate the picture of the various positive and negative contributions to the cross sections – as in eq. (3.1.16) – in the few-partial-wave regime. At higher energies and partial waves, the picture is more cluttered and this way of thinking about $\sigma_\eta^{(1)}$ becomes less useful.

3.1.3 Thermalisation Cross Sections for determining scattering lengths

A common application of measurements of thermalisation rates is to determine the s-wave scattering length a_s of an ultracold system [232, 233]. This is a relatively easy measurement to perform on a new experimental system and can give a direct measurement of a scattering length without the potentially difficult process of fitting an interaction potential. However, the problems with this method are that there are usually large uncertainties associated both with the measurement of the thermalisation itself and the densities needed for interpreting those measurements. The other problem is that, in the ultracold limit, positive and negative scattering lengths give equivalent results and so thermalisation measurements in the s-wave regime might only be able to determine the magnitude of the scattering length, and measurements at higher energies would be needed to determine the sign [232]. It is often also possible to determine the sign directly from accurate spectroscopic measurements of near-threshold bound states. This is often provides a more accurate and reliable measurement of the scattering length, but thermalisation measurements are usually quicker and easier. Therefore, in this section will focus on determination of the sign of a_s through thermalisation measurements and the importance of using the thermalisation cross section $\sigma_\eta^{(1)}$ for this.

In this section we will use the example of alkali metal atoms colliding with ytterbium, and in particular Li+Yb. As discussed in section 2.2.1, such systems can be

well approximated as single-channel systems and characterised by just the scattering length. Determining the scattering length is critical for predicting the positions of the very narrow Feshbach resonances that these systems actually exhibit [44–46]. There have been thermalisation measurements for a series of isotopologues of Rb+Yb [242, 243] where the variation between the numerous different isotopologues conveniently resolves the sign ambiguities of the individual measurements. Those results also agree with 2-colour photoassociation spectroscopy of near-threshold bound states [244, 245], and the various isotopologues of RbYb are now well understood [246].

There have also been thermalisation measurements for ^{6}Li+^{174}Yb [247, 248], which suggest an s-wave scattering length $|a_\mathrm{s}| \approx 8$ Å but do not indicate its sign. Note that performing measurements on different isotopologues of LiYb can not resolve the sign of the scattering length. This is because changing the Li isotope to ^{7}Li alters the reduced mass by too much to allow useful comparison with ^{6}Li, and changing the Yb isotope barely affects the reduced mass due to the mass disparity [248]. Indeed thermalisation measurements on ^{6}Li+^{173}Yb [248] are indistinguishable from those on ^{6}Li+^{174}Yb, within experimental uncertainties. Neither this unfavourable case nor the highly favourable case of Rb+Yb should be considered typical.

Thermalisation measurements from ultracold scattering are usually assumed to be determined by only s-wave scattering, but the sign of a_s could be determined from thermalisation measurements where higher partial waves contribute. Figure 3.4(a) shows σ_el and $\sigma_\eta^{(1)}$ for ^{6}Li+^{174}Yb and $a_\mathrm{s} = \pm 8$ Å: it may be seen that the cross sections for positive and negative scattering lengths deviate from one another substantially above 40 μK, and σ_el and $\sigma_\eta^{(1)}$ start to differ significantly in the same region. Thus measurements at temperatures high enough to determine the sign of the scattering length should take into account the difference between σ_el and $\sigma_\eta^{(1)}$.

The thermalisation measurements for ^{6}Li^{174}Yb were performed at low temperatures (< 500 μK [248] and ~ 100 μK [247]) well below the p-wave barrier. Therefore it was assumed that only s-wave collisions contributed to scattering. However, we have just shown that in this case we expect deviations from pure s-wave behaviour from energies well below this temperature. Ivanov et al. [247] did include an effective-

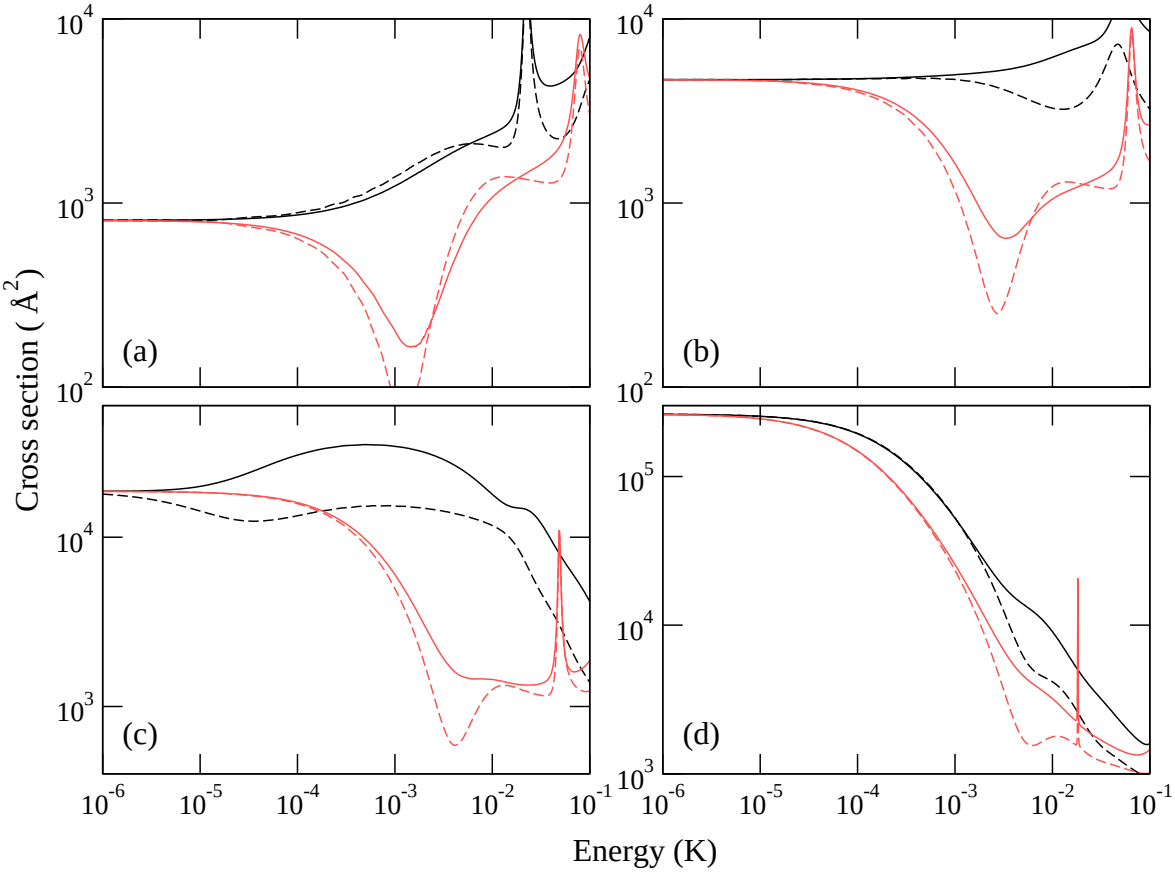

Figure 3.4: LiYb cross sections. σ_{el} (solid lines) and $\sigma_\eta^{(1)}$ (dashed lines) for positive (black) and negative (red) signs of the scattering length for different values of the magnitude of the scattering length: (a) $|a_{\mathrm{s}}| = 8$ Å (b) $|a_{\mathrm{s}}| = \bar{a} = 19.3$ Å (c) $|a_{\mathrm{s}}| = 2\bar{a} = 38.6$ Å (d) $|a_{\mathrm{s}}| = 7.5\bar{a} = 145$ Å

range correction to capture some of the energy dependence of the scattering, but that cannot describe the thermalisation cross section $\sigma_\eta^{(1)}$. Therefore, the thermalisation measurements already performed were at a sufficiently high energy that they might in principle be able to determine the sign of the scattering length. Additionally, the two cross sections reported were measured at different temperatures: Ivanov et al. report $a = 13 \pm 3\ a_0$, which is 6.9 ± 1.6 Å for cooling from 110 to 40 μK; Hara et al. report $a = 10 \pm 2$ Å for cooling from 500 to 200 μK. This apparent increase in the magnitude of the scattering length will correspond to an increase in the cross section, which is what is expected if the scattering length is positive (see fig. 3.4(a)). However, the relatively small size of this effect and the large uncer-

tainties of the measurements mean that we cannot definitively assign this scattering length as positive without a more thorough investigation.

The remaining panels of fig. 3.4 show analogous results for other values of $|a_s|$, in order to illustrate the range of possible behaviour for other systems. It may be seen that in most cases σ_{el} and $\sigma_\eta^{(1)}$ are reasonably similar at energies up to about 100 μK (about $0.04E_6$); this may be compared with the p-wave barrier height of 2.8 mK. However, the difference between σ_{el} and $\sigma_\eta^{(1)}$ begins at much lower energies (near 1 μK) for values of a_s near $+2\bar{a}$. This is because there is a p-wave shape resonance close to zero collision energy when $a_s = +2\bar{a}$, in accordance with AQDT. Although in this case there is a very weakly bound state rather than a shape resonance per se, the low-energy p-wave scattering is still resonance enhanced, and so introduces interference terms into eq. (3.1.16) even at very low energy. These results show that in an experiment to determine the *sign* of a scattering length from thermalisation measurements, it is important to consider the correct thermalisation cross section $\sigma_\eta^{(1)}$.

Thermalisation measurements have been performed on ^{87}Rb^{171}Yb at energies higher than the s-wave regime [249]. As the sign of the scattering lengths were already understood for Rb+Yb, this experiment was not specifically analysed for this purpose. However, there were signs of a Ramsauer-Townsend minimum observed, which might have proved a useful test of this theory if this case was not already understood.

There are ongoing experiments to co-trap Cs and Yb and attempt magnetoassociation [46, 250, 251]. The magnitudes and signs of scattering lengths are *not* known in advance for these systems, and they will need to be determined experimentally. Initial thermalisation measurements have just recently begun on this system and preliminary results will soon be available. Because of the large reduced mass of this system, the p-wave barrier will be quite low and so the thermalisation may show strong effects of scattering in higher partial waves. This provides a clear prospect of an imminent experimental application for the work in this section.

[Note added after submission: Thermalisation measurements for Cs+^{170}Yb and Cs+^{174}Yb have now been made by the group of S. L. Cornish, and thermalisation

cross sections have been extracted from them. We have fitted these to theoretical calculations, and hence determined scattering lengths for all stable isotopologues of CsYb. We also showed that using $\sigma_\eta^{(1)}$ rather than σ_{el} gives a small but clear improvement to the fitting, and may show a significantly larger effect for other isotopes. A paper describing both the experimental and theoretical work has been submitted and a preprint is available [252].]

3.1.4 Conclusions

In this section we have considered effects relating to thermalisation of cold and ultracold gases, mostly in the context of sympathetic cooling. The primary results to the use of the transport cross section $\sigma_\eta^{(1)}$ for thermalisation in place of the elastic cross section σ_{el}. This is not novel in itself, but there has been little attention and discussion of this cross section until now. We have considered its application to determination of scattering lengths from interspecies thermalisation measurements, and determined that considering the correct cross section becomes important at about the same energies that it is possible to distinguish between positive and negative scattering lengths. We are hopeful that ongoing experiments on Cs+Yb will allow us to apply these ideas to real experiments in the near future.

3.2 Simulating Sympathetic Cooling of CaF by Li or Rb in a Microwave Trap

In order to understand thermalisation in more detail, we directly simulate the process of sympathetic cooling in a microwave trap. In previous work [112], sympathetic cooling of a cloud of LiH molecules by ultracold Li atoms was simulated using a simple model. The collisions were taken to be isotropic and determined by the elastic cross section. This is appropriate for s-wave-dominated collisions at very low energy. However, as discussed in the previous section it will most likely not be a good approximation for collisions outside the s-wave regime. Here, we introduce a new collision model that takes account of the full energy dependence of the collision

cross section and the corresponding differential cross sections. We show that this model produces significantly slower sympathetic cooling in the early stages than the original hard-sphere model. We also consider approximations to the full model and show that a model that uses hard-sphere scattering based on the energy-dependent transport cross section $\sigma_\eta^{(1)}$ [175] produces accurate results for the cooling of the molecules but not for heating and loss of the coolant atoms.

The previous modelling work [112] explored sympathetic cooling in three different types of trap: a static electric trap, an alternating current (ac) trap, and a microwave trap. A static electric trap can confine molecules only in rotationally excited states, and it was found that for Li+LiH the ratio of elastic to rotationally inelastic collisions was too small for such molecules to be cooled before they were ejected from the trap. An ac trap can confine molecules in the rotational ground state, so there are no inelastic collisions, but elastic collisions can transfer molecules from stable to unstable trajectories and it was found that this eventually causes all the molecules to be lost. A microwave trap [111, 253] can confine molecules in the absolute ground state, around the antinodes of a standing-wave microwave field, and sympathetic cooling in such a trap was found to be feasible on a timescale of 10 s [112]. The microwave trap brings the benefits of a high trap depth and large trapping volume for polar molecules, especially compared to an optical dipole trap. In the present work, we simulate sympathetic cooling in a microwave trap in detail. We consider the following specific, experimentally realistic, scenario. Cold CaF molecules are produced either in a magneto-optical trap [119, 120] or by Stark deceleration [254, 255]. In the first case the temperature might be about 2 mK, and in the second about 30 mK. The molecules are loaded into a magnetic trap, and then transported into a microwave trap. Here, the molecule cloud is compressed in order to improve the overlap with the atomic coolant, and this raises the initial temperature of the molecules to 20 mK and 70 mK respectively. A distribution of atoms, either ^{7}Li or ^{87}Rb, with an initial temperature of 100 μK, is trapped magnetically and is overlapped with the cloud of molecules. We simulate the way in which elastic collisions reduce the molecular temperature towards the atomic temperature. Blackbody heating out of the rovibrational ground state can be reduced below $10^{-4}\,\mathrm{s}^{-1}$

by cooling the microwave trap to 77 K [256].

We start by describing our scattering calculations and the cross sections we obtain. Then we describe the simulation method we use, and study how the choice of collision model affects the simulation results. Next, we examine the cooling dynamics and evaluate which coolant, Rb or Li, is likely to be the best in practical situations. Because the cross section is very sensitive to the exact form of the atom-molecule interaction potential, especially at low energies, we study sympathetic cooling for a range of typical values of the s-wave scattering length. In addition to cooling the molecules, collisions either heat the atoms, raising the final temperature, or eject atoms from the trap, reducing the atomic density. These effects are particularly important if the atom number does not greatly exceed the molecule number. We study these effects and explain the results in terms of appropriate partial integrals over differential cross sections. Finally, we investigate how evaporative cooling of the atoms can be used to speed up the sympathetic cooling rate and lower the final temperature obtained.

The work in this section relies heavily on simulations - described here and in Ref. [113] - which were performed by J. Lim and M. R. Tarbutt. The calculations of the potentials and the various cross sections were performed by myself with J. M. Hutson. The analysis and discussion of all the results in this section was a joint effort between all four authors of Ref. [113].

3.2.1 Scattering calculations

Exact scattering calculations on systems as complex as Li+CaF and Rb+CaF are not currently feasible. The combination of a deep chemical well, very large anisotropy of the interaction potential, and small CaF rotational constant mean that a very large rotational basis set would be needed for convergence. In addition, even if converged results could be achieved, uncertainties in the potential surface mean that no single calculation could be taken to represent the true system and many calculations on many surfaces would be needed to explore the range of possible behaviours [257]. Instead we model the interactions with a simple single-channel model potential which we choose to be the Lennard-Jones potential eq. (3.1.17). As

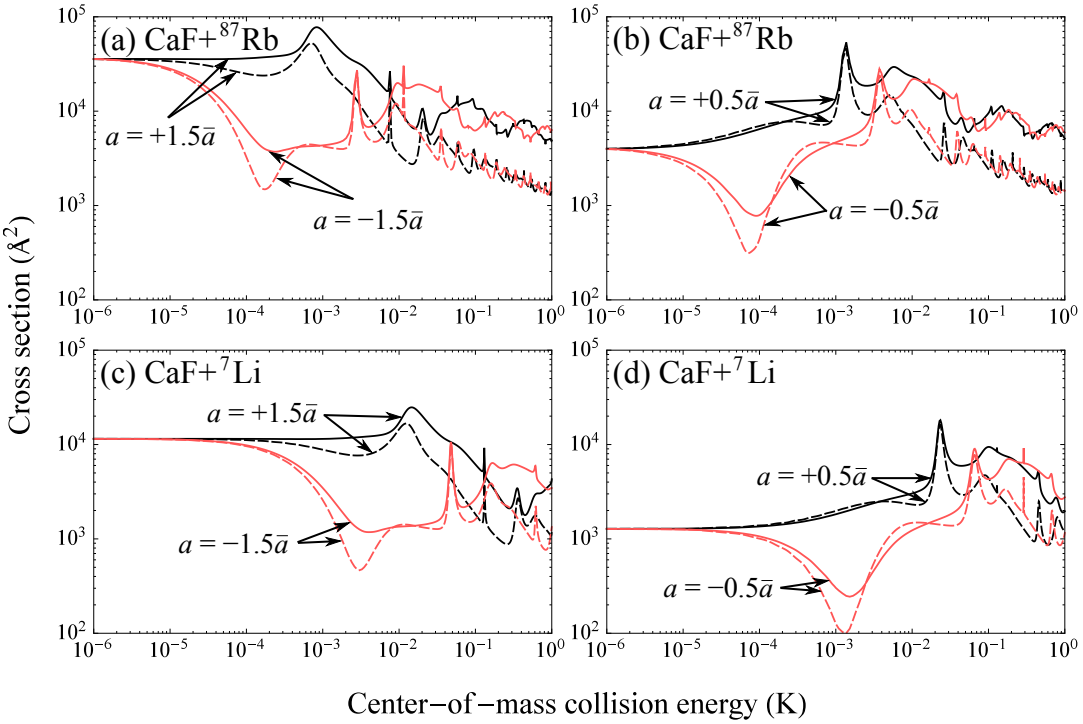

Figure 3.5: Total elastic cross section, σ_{el} (solid lines), and transport cross section, $\sigma_{\eta}^{(1)}$ (dashed lines), for positive (black) and negative (red) signs of the scattering length. (a) CaF+^{87}Rb, $|a| = 1.5\bar{a}$; (b) CaF+^{87}Rb, $|a| = 0.5\bar{a}$; (c) CaF+^{7}Li, $|a| = 1.5\bar{a}$; (d) CaF+^{7}Li, $|a| = 0.5\bar{a}$.

we have shown in section 2.2, while a simple single-channel model cannot be expected to reproduce a full coupled-channel calculation, it can quantitatively reproduce the *range* of behaviours shown by full calculations.

We obtain Lennard-Jones parameters for Li+CaF from *ab initio* calculations [130]. We obtain $C_{6,\mathrm{Li+CaF}} = 1767\,E_\mathrm{h}a_0^6$ from direct fitting to the isotropic part of the long-range potential. We set $C_{12,\mathrm{Li+CaF}} = 2.37 \times 10^7\,E_\mathrm{h}a_0^{12}$ to reproduce the depth of the complete potential, which is 7224 cm^{-1}. We use the depth of the complete potential in preference to the depth of the isotropic part of the potential because the very large anisotropy at short range means the isotropic part of the potential is not representative of the interaction. To obtain a C_6 parameter for Rb+CaF we first separate $C_{6,\mathrm{Li+CaF}}$ into induction and dispersion contributions. Induction contributions for both systems are readily calculated from known values of the CaF dipole moment [258] and the static polarisabilities of the atoms [259]. The dispersion contribution for Rb+CaF can then be calculated from the dispersion contribution for Li+CaF using Tang's combining rule [260] with known homonuclear diatomic dispersion coefficients [259], atomic polarisabilities [259] and a calculated CaF polarizability of $\alpha_\mathrm{CaF} = 137\ a_0^3$. The sum of these contributions gives $C_{6,\mathrm{Rb+CaF}} = 3084\,E_\mathrm{h}a_0^6$. We estimate, by analogy to calculations on methyl fluoride [261], that the well depth for Rb+CaF will be about 2.5 times shallower than for Li+CaF. This sets $C_{12,\mathrm{Rb+CaF}} = 1.8 \times 10^8\,E_\mathrm{h}a_0^{12}$.

For our purposes, the key property of a potential is the s-wave scattering length, a, that it produces. In the present work, we vary the C_{12} coefficient over a small range (with C_6 fixed) to vary the scattering length. We focus on four typical scattering lengths, $a = -1.5\bar{a}$, $-0.5\bar{a}$, $+0.5\bar{a}$, $+1.5\bar{a}$. $\bar{a} = 20.2$ Å for Li+CaF and 35.7 Å for Rb+CaF.

The calculated elastic and transport cross sections for Li+CaF and Rb+CaF are shown in fig. 3.5 for our chosen selection of scattering lengths. At low energy, in the s-wave regime, the cross sections have constant limiting values of $4\pi|a|^2$. This is the same for both σ_el and $\sigma_\eta^{(1)}$, because pure s-wave scattering is isotropic. The cross sections for positive and negative scattering lengths go to the same low-energy limit. However, as energy increases, the cross sections all diverge from one another. Those

for negative scattering lengths, especially $a = -0.5\bar{a}$, show dramatic Ramsauer-Townsend minima as the scattering phase shift, and hence the s-wave cross section, passes through a zero [148]. For $\sigma_\eta^{(1)}$ this minimum is further deepened by destructive interference between s-wave and p-wave scattering [175]. For $a = +1.5\bar{a}$ a peak in both cross sections is seen (near 10^{-3} K for Rb+CaF). This is a d-wave feature corresponding to the energy of the centrifugal barrier maximum. At higher energies, there are various shape resonances present for all cases. Nevertheless, once many partial waves contribute, the cross sections become less dependent on scattering length and approach classical limits.

We note that, as explained in section 2.2, the cross sections for the two systems for the same value of $a/\bar{a}$ are nearly identical, apart from constant factors in energy and cross section. The scaling in energy is determined by $\bar{E} = 9.51$ mK for Li+CaF and 0.543 mK for Rb+CaF. This scaling means that, while the Rb+CaF cross sections are almost independent of scattering length at 10 mK and above, the Li+CaF cross sections are highly sensitive to scattering length at any energy below 100 mK.

For stationary atoms the molecular kinetic energy in the laboratory frame, $E_{\mathrm{CaF}}^{\mathrm{lab}}$, is related to the collision energy in the center-of-mass frame, E^{CM}, by $E_{\mathrm{CaF}}^{\mathrm{lab}} = (m_{\mathrm{CaF}}/\mu)E^{\mathrm{CM}}$, where $\mu = m_{\mathrm{CaF}}m_{\mathrm{at}}/(m_{\mathrm{CaF}}+m_{\mathrm{at}})$ is the reduced mass of the collision system, m_{CaF} is the molecular mass and m_{at} is the atom mass. The ratio $E_{\mathrm{CaF}}^{\mathrm{lab}}/E^{\mathrm{CM}}$ is 9.40 for Li+CaF and 1.68 for Rb+CaF. This introduces a further energy scaling between the two systems in addition to the difference in $\bar{E}$.

Because the molecules are in the ground state, and the rotational excitation energy is far greater than the available collision energy, we assume that there are no inelastic collisions. It is known that there can be molecule-molecule inelastic collisions in the presence of the microwave field, even when the microwave frequency is well below the first rotational resonance [262, 263]. This is a concern for evaporative cooling of molecules, but less so for sympathetic cooling, where the density of molecules can be low. It is worth studying whether there can be atom-molecule inelastic collisions induced by the microwave field, but that is beyond the scope of this section.

3.2.2 Simulation method

The simulations described here were designed, implemented, and run by M. R. Tarbutt and J. Lim, but their description is presented here as it is essential for understanding the work in this section. They assume that ground-state CaF molecules are confined around the central antinode of a standing-wave microwave field, formed at the centre of an open microwave cavity [253]. The interaction potential of the molecules with the microwave field is

$$U(\mathbf{r}) = -\Delta U \exp\left[-\frac{x^2}{w_x^2} - \frac{y^2}{w_y^2}\right] \cos^2\left(\frac{2\pi z}{\lambda}\right), \tag{3.2.18}$$

where ΔU is the trap depth and we take $\Delta U/k_{\mathrm{B}} = 400\,\mathrm{mK}$, $w_x = 16.3\,\mathrm{mm}$, $w_y = 15.3\,\mathrm{mm}$, and $\lambda = 21.3\,\mathrm{mm}$ [253]. The initial phase-space distribution of the molecules is assumed to be

$$\begin{aligned} f(\mathbf{r},\mathbf{p}) &= \frac{n_{0,\mathrm{CaF}}}{(2\pi m_{\mathrm{CaF}} k_{\mathrm{B}} T)^{3/2}} \\ &\times \exp\left[-\frac{U(\mathbf{r}) - U(0) + p^2/(2m_{\mathrm{CaF}})}{k_{\mathrm{B}} T}\right], \end{aligned} \tag{3.2.19}$$

where T is the initial temperature of the molecules and $n_{0,\mathrm{CaF}}$ is the initial density at the centre of the trap, which is fixed such that the total number of molecules is $N_{\mathrm{CaF}} = 10^5$. For most simulations, the temperature is taken to be $T = 70\,\mathrm{mK}$ in order to study sympathetic cooling from a high temperature. A distribution of ultracold atoms is overlapped with the molecules. The atoms are in a harmonic magnetic trap whose depth is 1 mK. The distribution of atoms in phase space is assumed to depend only on their energy. Therefore, at all times, the atoms have a Gaussian spatial distribution and a thermal velocity distribution with temperature T_{at}. They have an initial temperature of $100\,\mu\mathrm{K}$, an initial central density of $10^{11}\,\mathrm{cm}^{-3}$, and an initial number of 10^9. The corresponding initial $1/e$ radius is 1.2 mm. The approximation that the molecules are confined only by the microwave field, and the atoms only by the magnetic field, is a reasonable one, though the model could be extended to use the complete potential of both species in the combined fields.

For each molecule, the simulation proceeds as follows. The equation of motion

in the microwave trap is solved for a time step Δt which is much smaller than the mean time between collisions. Then, using the current position, $\mathbf{r}$ and velocity, $\mathbf{v}$, of the molecule, whether or not there should be a collision is determined as follows. The velocity of an atom is chosen at random from a thermal distribution with temperature $T_{\rm at}$. From the atomic and molecular velocities they calculate the collision energy in the center-of-mass frame, $E^{\rm CM}$. The collision probability is $P = n_{\rm at}(\mathbf{r})\sigma(E^{\rm CM})v_{\rm r}\Delta t$, where $v_{\rm r}$ is the relative speed of the atom and molecule, $n_{\rm at}$ is the atomic density, and $\sigma(E^{\rm CM})$ is either $\sigma_{\rm el}$ or $\sigma_\eta^{(1)}$ (see section 3.2.3). A random number is generated in the interval from 0 to 1, and if this is less than P a collision occurs. If there is no collision, the velocity of the molecule is unchanged. If there is a collision, the velocities are transformed into the center-of-mass frame, a deflection angle is determined as described below, and the new velocities transformed back into the laboratory frame. If the new total energy (kinetic energy plus trapping potential) is sufficient for the atom to escape from the trap, the atom, and its energy prior to the collision, are removed. The change in energy is shared among all the remaining atoms. Otherwise, the atom remains in the trap and the change in kinetic energy is shared between all the atoms. This algorithm is followed for each molecule in the distribution. The density and temperature of the atom cloud are updated to account for the atom loss and atom heating at this time step, and then the simulation proceeds to the next time step.

With the choice of trap depth and initial atom temperature, there is a small evaporative cooling effect due to atom-atom collisions. For Rb, over the 50 s timescale of the simulations, 8% of the atoms are lost and the temperature falls to 80 μK. Prior to section 3.2.8, this evaporative cooling effect is neglected in our simulations because we wish to isolate effects that are due to atom-molecule collisions. Then, in section 3.2.8, atom-atom collisions are included to explore the effects of evaporative cooling.

As we will see, the molecular velocity distributions obtained during the cooling process are far from thermal. There are some molecules that never have a collision during the whole simulation and so remain at high energy throughout. Almost all these molecules have a kinetic energy greater than 10 mK, and they disproportion-

ately skew the mean kinetic energy of the sample as a whole. Our interest is in the molecules that cool, and so we separate the kinetic energy distribution into two parts, above and below 10 mK. To express how well the cooling works, we give the fraction of molecules in the low-energy part, and their mean kinetic energy, both as functions of time.

3.2.3 Collision models

The models discussed here were implemented - and the simulations run - by Tarbutt and Lim, but they were conceived, and the results interpreted, jointly.

In previous modelling [112], atoms and molecules collided like hard spheres. In this model, the momenta in the centre-of-mass frame before and after a collision, $\mathbf{p}_c$ and $\mathbf{p}'_c$, are related by

$$\mathbf{p}'_c = \mathbf{p}_c - 2(\mathbf{p}_c \cdot \hat{\mathbf{e}})\hat{\mathbf{e}}, \tag{3.2.20}$$

where $\hat{\mathbf{e}}$ is a unit vector along the line joining the centres of the spheres, given by

$$\hat{\mathbf{e}} = \hat{\mathbf{p}}_c\sqrt{1 - |\mathbf{b}|^2} + \mathbf{b}, \tag{3.2.21}$$

where $\hat{\mathbf{p}}_c$ is a unit vector in the direction of $\mathbf{p}_c$ and $\mathbf{b}$ is a vector that lies in a plane perpendicular to $\mathbf{p}_c$ and whose magnitude is the impact parameter divided by the sum of the radii of the two spheres. For each collision, $\mathbf{b}$ is chosen at random from a uniform distribution, subject to the constraints $\mathbf{b} \cdot \mathbf{p}_c = 0$ and $|\mathbf{b}| \leq 1$.

The lines labeled (i) in fig. 3.6 show how the cooling proceeds for CaF + Rb when we use the hard-sphere model and choose the cross section to be independent of energy and equal to $4\pi\bar{a}^2 = 1.59 \times 10^{-16}\,\mathrm{m}^2$. The cross section is shown in fig. 3.6(a), while the cold fraction and the mean kinetic energy of that fraction are shown in parts (b) and (c), both as functions of time. As explained in section 3.2.2, the cold fraction is defined as the fraction with kinetic energy below 10 mK. The cold fraction increases rapidly, and that fraction thermalises quickly with the atoms. After just 4 s, 85% of the molecules are in the cold fraction and their mean energy is within 50% of the 100 μK temperature of the coolant atoms.

The energy-independent hard-sphere (EIHS) model described above is reasonable

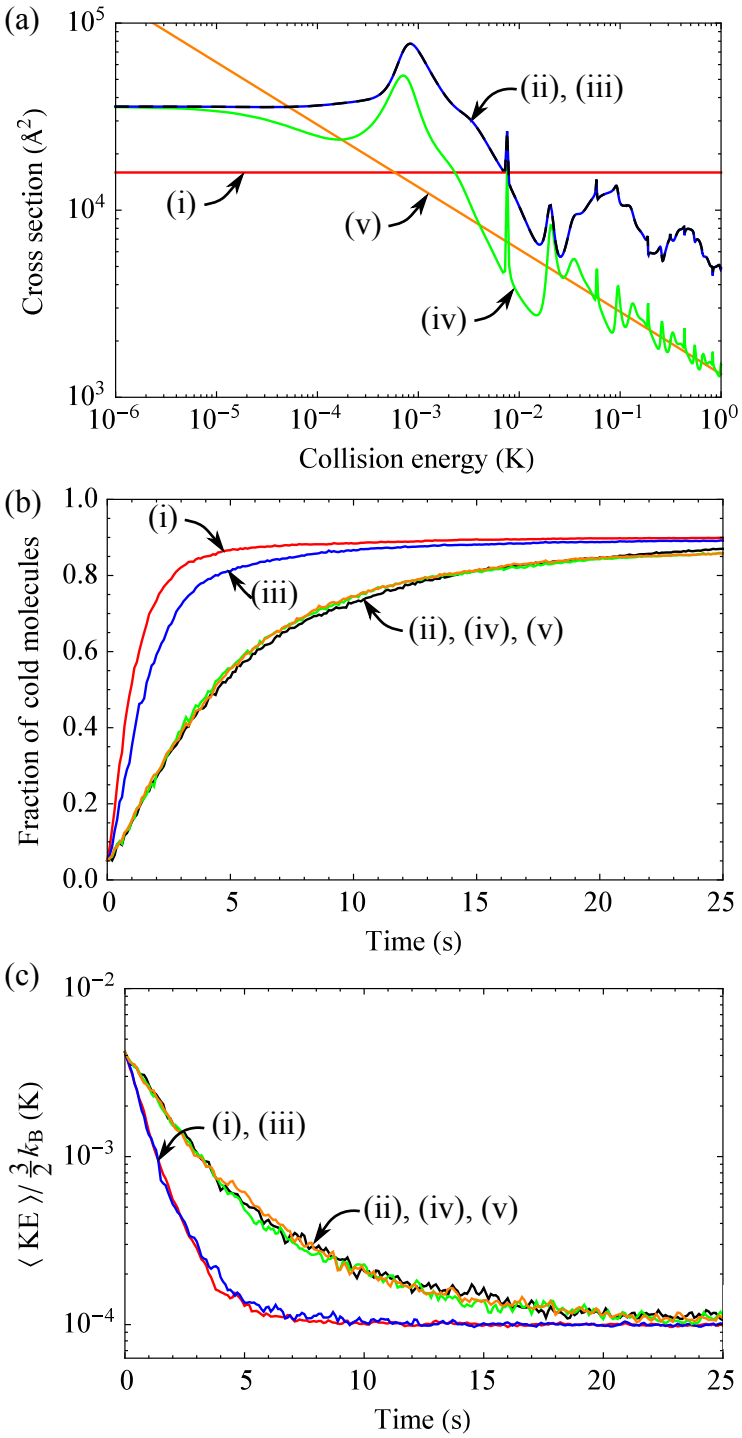

Figure 3.6: Results of various collision models: (i) hard-sphere model with energy-independent cross section $4\pi\bar{a}^2$; (ii) full energy-dependent differential cross section model; (iii) hard-sphere model with $\sigma_{\mathrm{el}}(E^{\mathrm{CM}})$; (iv) hard-sphere model with $\sigma_\eta^{(1)}(E^{\mathrm{CM}})$; (v) hard-sphere model with classical approximation to $\sigma_\eta^{(1)}(E^{\mathrm{CM}})$. The graphs show: (a) Cross section versus collision energy; (b) fraction of molecules with kinetic energy below 10 mK versus time; (c) mean kinetic energy of that fraction versus time. The coolant is Rb and $a = +1.5\bar{a}$.

at very low energy, but it has three deficiencies. First, it neglects the fact that the low-energy cross sections are actually $4\pi a^2$, where a is the true scattering length as opposed to the mean scattering length. The true scattering length can take any value between $-\infty$ and $+\infty$, but is generally unknown for a specific system until detailed measurements are available to determine it. Secondly, the EIHS model neglects the fact that real cross sections are strongly energy-dependent, usually showing resonance structure on a background that drops off sharply with increasing energy, as shown in fig. 3.6(a). Thirdly, collisions with small deflection angles (forwards scattering) do not contribute efficiently to cooling, and the EIHS model neglects the fact that differential cross sections (DCS) at higher energies tend to be dominated by such forwards scattering, because many collisions encounter only the attractive long-range tail of the interaction potential.

To remedy all these deficiencies, we introduce here a new model that we call the full DCS model. For this we calculate realistic integral and differential cross sections, as described above, for a variety of choices of the scattering length a. We use the elastic cross section $\sigma_{\rm el}(E^{\rm CM})$ from these calculations to determine the collision probability. This cross section is curve (ii) in fig. 3.6(a), and it is smaller than in the EIHS model at collision energies above 8 mK, but larger below 8 mK. We then select a deflection angle Θ from a random distribution that reproduces the full differential cross section, $d\sigma/d\omega$, at energy $E^{\rm CM}$. To select a deflection angle at random from this distribution, we form the cumulative distribution function,

$$S(\Theta) = \frac{2\pi}{\sigma_{\rm el}} \int_0^{\Theta} \frac{d\sigma}{d\omega} \sin(\Theta') d\Theta', \tag{3.2.22}$$

select a random number r between 0 and 1, and find the value of Θ where $S(\Theta) = r$.

The full DCS model is our most complete one and we have used it for all the simulations in the following sections. Its results for the choice $a = +1.5\bar{a}$ are shown by the lines labeled (ii) in fig. 3.6. It may be seen that the cooling proceeds more slowly than in the EIHS model. It takes 14 s for the cold fraction to reach 80% and for the energy of that fraction to be within 50% of the temperature of the atoms. The slower cooling is mainly due to the dominance of forward scattering at higher

energies.

There are three approximations to the full-DCS model that are worth considering because they avoid the tabulation of differential cross sections and cumulative distributions. The first of these is to use a hard-sphere collision model but to take the full energy-dependent elastic cross section from fig. 3.6(a). This produces the cooling behaviour labeled (iii) in fig. 3.6(b) and (c). It may be seen that this model produces cooling slightly slower than the EIHS model, but considerably faster than the full DCS model. The second and more satisfactory approximation is to use a hard-sphere collision model but to take the full energy-dependent transport cross section $\sigma_\eta^{(1)}$, shown as line (iv) in fig. 3.6(a). We label this approach EDT-HS. It produces the cooling behaviour labeled (iv) in fig. 3.6(b) and (c). It may be seen that it models the cooling of the molecules very accurately, because it takes proper account of the reduced efficiency of small-angle collisions for sympathetic cooling. However, as will be seen below, the EDT-HS approach does *not* adequately model heating and loss of the coolant atoms.

It is worth exploring whether a classical calculation of $\sigma_\eta^{(1)}$ would suffice. Unlike the elastic cross section, $\sigma_{\eta,\mathrm{class}}^{(1)}$ is finite because the factor of $1-\cos\Theta$ suppresses the divergence due to forwards scattering. We have calculated $\sigma_{\eta,\mathrm{class}}^{(1)}$ for the Lennard-Jones potentials described above,

$$\sigma_{\eta,\mathrm{class}}^{(1)} = 2\pi \int_0^\infty b[1-\cos\Theta(b)]db, \tag{3.2.23}$$

where b is the impact parameter and $\Theta(b)$ is the classical deflection function [148]. We find that it is very well approximated by the power law $\sigma_\eta^{(1)}(E^{\mathrm{CM}}) = A(E^{\mathrm{CM}}/C_6)^{-1/3}$, with the dimensionless constant $A = 4.79$. This cross section is labeled (v) in fig. 3.6(a). It agrees well with the quantum-mechanical $\sigma_\eta^{(1)}(E^{\mathrm{CM}})$ for Rb+CaF at high energies, as we would expect when many partial waves contribute. Remarkably, the temperature and cold fraction shown for this model in fig. 3.6 agree very well with those for model (ii), even as the temperature approaches $100\,\mu$K. This is an atypical result because, for $a = +1.5\bar{a}$, $\sigma_{\eta,\mathrm{class}}^{(1)}$ is within a factor of about three of the quantum-mechanical $\sigma_\eta^{(1)}$ at all energies above $3\,\mu$K. For other values of a, the

two cross sections can differ by more than a factor of three at energies below about $2\bar{E}$, which is around 1 mK for Rb+CaF. Note that the classical approximation will be less successful for a lighter coolant such as Li where $\bar{E}$ is far higher.

3.2.4 Approximate cooling rates

From the transport cross sections, $\sigma_\eta^{(1)}$, in fig. 3.5 we can make a useful estimate of the cooling rate of molecules as a function of their kinetic energy. For this estimate, we assume stationary atoms with a uniform density $n_{\rm at} = 10^{11}\,{\rm cm}^{-3}$. The cooling rate is

$$\frac{dE_{\rm CaF}^{\rm lab}}{dt} = n_{\rm at}\sigma(E^{\rm CM})v\overline{\Delta E}, \tag{3.2.24}$$

where $v = (2E_{\rm CaF}^{\rm lab}/m_{\rm CaF})^{1/2}$ is the speed of the molecule and $\overline{\Delta E}$ is the average energy transfer for a hard-sphere collision. ΔE is given explicitly as

$$\Delta E = -\left(\frac{2\mu}{m_{\rm CaF}+m_{\rm at}}\right)(1-\cos\Theta)E_{\rm CaF}^{\rm lab}. \tag{3.2.25}$$

Figure 3.7 shows the cooling rate coefficients obtained this way, which although only approximate are helpful for understanding the numerical results presented later. For collisions with Rb at energies above 10 mK, the cooling rate does not depend strongly on the s-wave scattering length. This is the energy regime where the a-independent classical approximation to $\sigma_\eta^{(1)}(E^{\rm CM})$ described in section 3.2.3 is accurate. Due to the small reduced mass in the lithium case, the classical limit is reached only for temperatures above 200 mK, and so the cooling rate depends sensitively on a over the whole energy range of interest. When a is negative there is a minimum in the cooling rates corresponding to the Ramsauer-Townsend minimum in $\sigma_\eta^{(1)}(E^{\rm CM})$. For Rb, at $a = -1.5\bar{a}$, this minimum is near 100 μK, which is close to the temperature of the atoms in our simulations and so will not have a significant impact on the thermalisation. For Li, the minimum occurs for kinetic energies between 1 and 10 mK, and so it has a strong effect on the thermalisation. Finally, we note that in the ultracold limit the cooling rate is almost an order of magnitude higher for Rb than for Li, reflecting the larger value of $\bar{a}$ for Rb + CaF relative to Li + CaF.

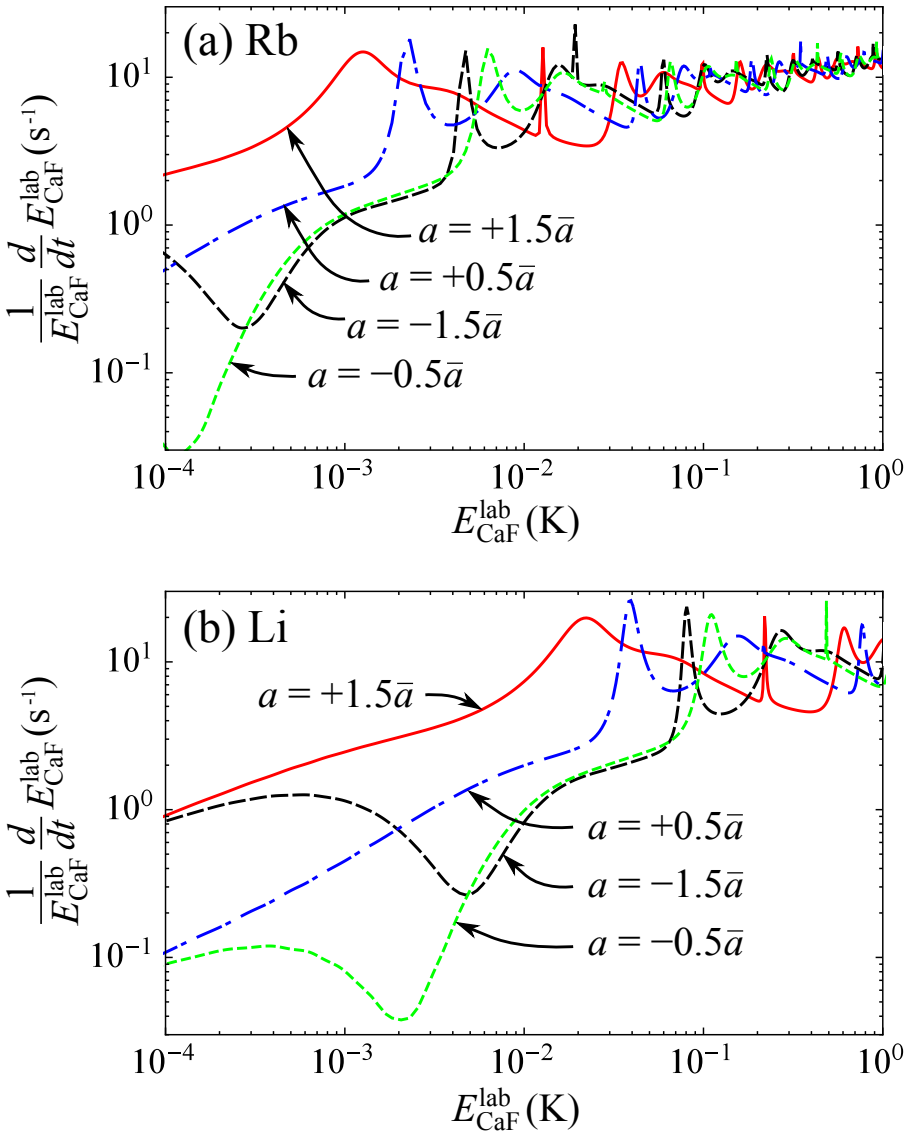

Figure 3.7: Cooling rate coefficient of molecules as a function of their kinetic energy, estimated from eq. (3.2.24), when the coolant is (a) Rb and (b) Li, and for various values of the s-wave scattering length: $a = +1.5\bar{a}$ (red solid line), $a = +0.5\bar{a}$ (blue dash-dot line), $a = -0.5\bar{a}$ (green dotted line), and $a = -1.5\bar{a}$ (black dashed line).

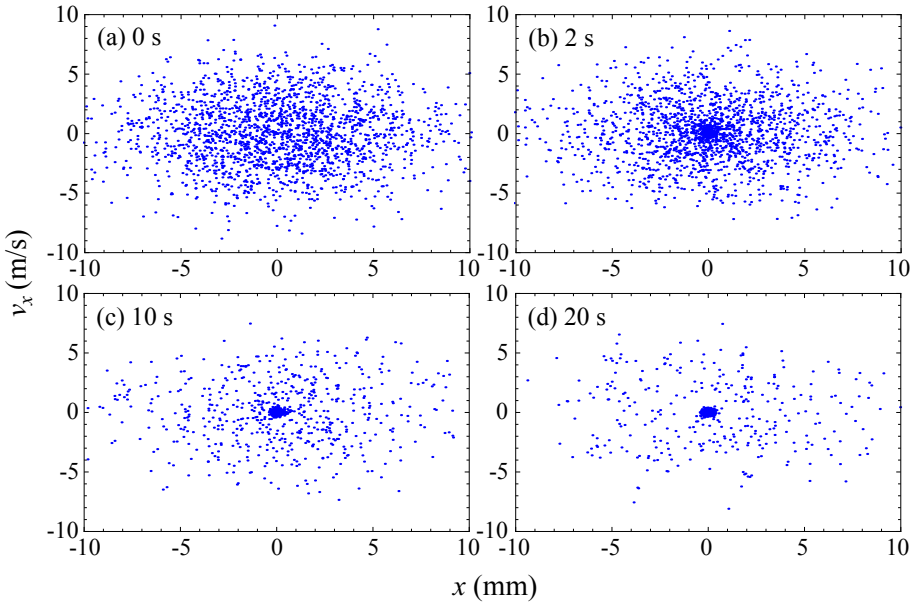

Figure 3.8: Time evolution of the phase-space distribution of molecules in the x direction. The cooling times are (a) 0 s, (b) 2 s, (c) 10 s, and (d) 20 s. The coolant is Rb and $a = +1.5\bar{a}$.

3.2.5 Cooling dynamics

Figure 3.8 shows the evolution of the (x, v_x) phase-space distribution of CaF when Rb atoms are used as the coolant, for the case where the s-wave scattering length is $a = +1.5\bar{a}$. At $t = 0$ (fig. 3.8(a)), the molecules fill the phase-space acceptance of the trap. At later times, more and more molecules congregate at the trap centre as they are cooled by collisions with the atoms. After 20 s (fig. 3.8(d)), the distribution has separated into two parts. The majority are cooled to the centre, but there are some that remain uncooled. These are molecules that have large angular momentum around the trap centre and so are unable to reach the centre where the atomic density is high. At $x = 3$ mm for example, the atomic density, and hence the collision rate, is a factor of 1000 smaller than at the centre, and so molecules at this distance are unlikely to collide with atoms on the 20 s timescale shown in the figure. These molecules can be cooled by expanding the size of the atom cloud, but only at the expense of the overall cooling rate [112].

Figure 3.9(a) shows histograms of the kinetic energy distribution of the molecules at three different times, 2, 10 and 20 s, when the coolant is Rb and $a = +1.5\bar{a}$. These are the same times as chosen for the phase space distributions in fig. 3.8, and

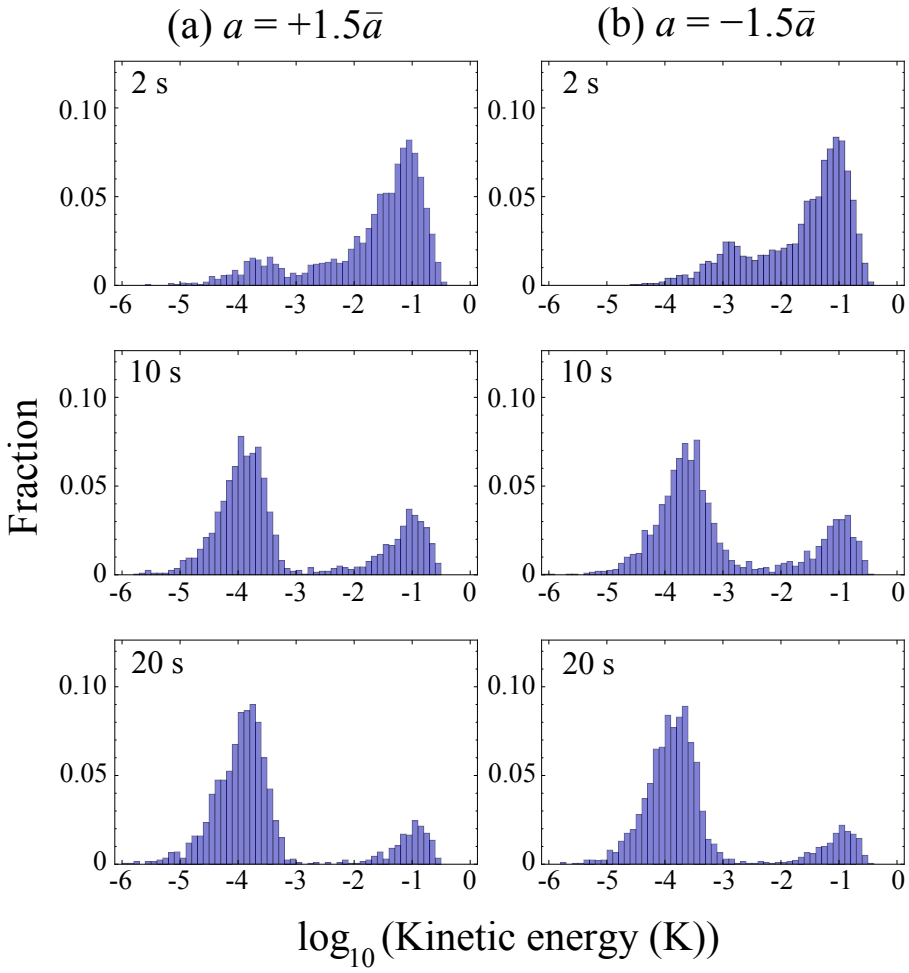

Figure 3.9: Kinetic energy distributions after 2 s, 10 s, and 20 s. The coolant is Rb. Left panels have $a = +1.5\bar{a}$ while right panels have $a = -1.5\bar{a}$.

the results come from the same simulation. The initial distribution is a Maxwell-Boltzmann distribution with a temperature of 70 mK, truncated at the trap depth of 400 mK. The distribution rapidly separates into two parts, those that cool and those that do not. The latter are the molecules that never reach the trap centre because of their large angular momentum, as discussed above. A significant fraction of molecules are cooled below 1 mK after just 2 s. After 10 s the majority are in this group, and after 20 s this cold fraction is almost fully thermalised with the atoms. We return to part (b) of fig. 3.9 in the next section.

3.2.6 Sensitivity to the scattering length and the choice of coolant

At low energies, cross sections are very sensitive to the exact form of the scattering potential, as shown in fig. 3.5, and cannot be calculated accurately without independent knowledge of the scattering length. In our model Lennard-Jones potential, the full energy-dependence of the cross section is determined once the s-wave scattering length, a, is fixed. Here, we study how the simulation results change as we vary the value of a. The choice of coolant is also a crucial consideration, and so we compare the results for Li and Rb as coolants.

Evolution of the kinetic energy distributions

Figure 3.9 compares how the kinetic energy distributions evolve for two cases: $a = +1.5\bar{a}$ and $a = -1.5\bar{a}$, with Rb as the coolant. At 2 s the two distributions are similar. The main difference is that the distribution extends to lower energies for $a = +1.5\bar{a}$. The similarity is due to the similar cooling rates at the high energies, as shown in fig. 3.7(a), while the difference at low energy is due to the far higher cooling rate for $a = +1.5\bar{a}$ at energies below 1 mK (compare the solid red and black dashed lines in fig. 3.7(a)). Exactly the same trend is seen after 10 s of cooling. Once again, the high-energy parts of the distributions are very similar, but the distribution extends to lower energies for the $a = +1.5\bar{a}$ case. After 20 s the majority of the molecules have fully thermalised with the atoms and the two distributions are very

similar to one another.

Figure 3.10 shows the corresponding histograms for the case of Li. Here, the cooling proceeds more slowly and so we have added a fourth pair of histograms showing the distributions after 40 s. There is a great contrast between the positive and negative scattering lengths in this case. For $a = +1.5\bar{a}$ the distribution evolves in a very similar manner to the Rb case, but when $a = -1.5\bar{a}$ it takes a long time for the molecules to reach energies below 10 mK. This is the effect of the Ramsauer-Townsend minimum which reduces the cooling rate estimated in fig. 3.7(b) to $0.25\,\mathrm{s}^{-1}$ for kinetic energies near 20 mK. Because the minimum is broad in energy, and there is a large mass mismatch between CaF and Li, a collision cannot take a molecule directly across the minimum. The molecules have to be cooled *through* the minimum by multiple collisions, and that takes a long time. Once molecules have passed through this minimum, cooling to ultracold temperatures occurs on a similar timescale to the $a = +1.5\bar{a}$ case.

Cold fraction and mean kinetic energy

Figure 3.11(a) shows the fraction of molecules with kinetic energy less than 10 mK, as a function of time, for various values of a when the coolant is Rb. This fraction is entirely insensitive to a. This is because the cooling rate is independent of a for energies above 10 mK, as we saw in fig. 3.7. After 5 s about 50% of the molecules are in this cold fraction, and after 20 s this exceeds 80%. Figure 3.11(b) shows the cold fraction versus time when the coolant is Li. We find a strong dependence on a in this case. When $a = +1.5\bar{a}$, the increase in the cold fraction with time is similar to the Rb case. For this value of a there is a maximum in the cooling rate at a kinetic energy of about 70 mK (see fig. 3.7(b)), which happens to match the initial temperature of the molecules, and so the cooling to below 10 mK proceeds rapidly. The cold fraction reaches 50% after 4 s in this case. The increase in the cold fraction is slower for $a = +0.5\bar{a}$, reaching 50% after 16 s. The accumulation of cold molecules is exceedingly slow when a is negative. When $a = -1.5\bar{a}$, the Ramsauer-Townsend minimum is at $E_{\mathrm{CaF}}^{\mathrm{lab}} = 20\,\mathrm{mK}$, and it takes a long time for the molecules to cool through this minimum. The cold fraction reaches 50% after 40 s in this case. When

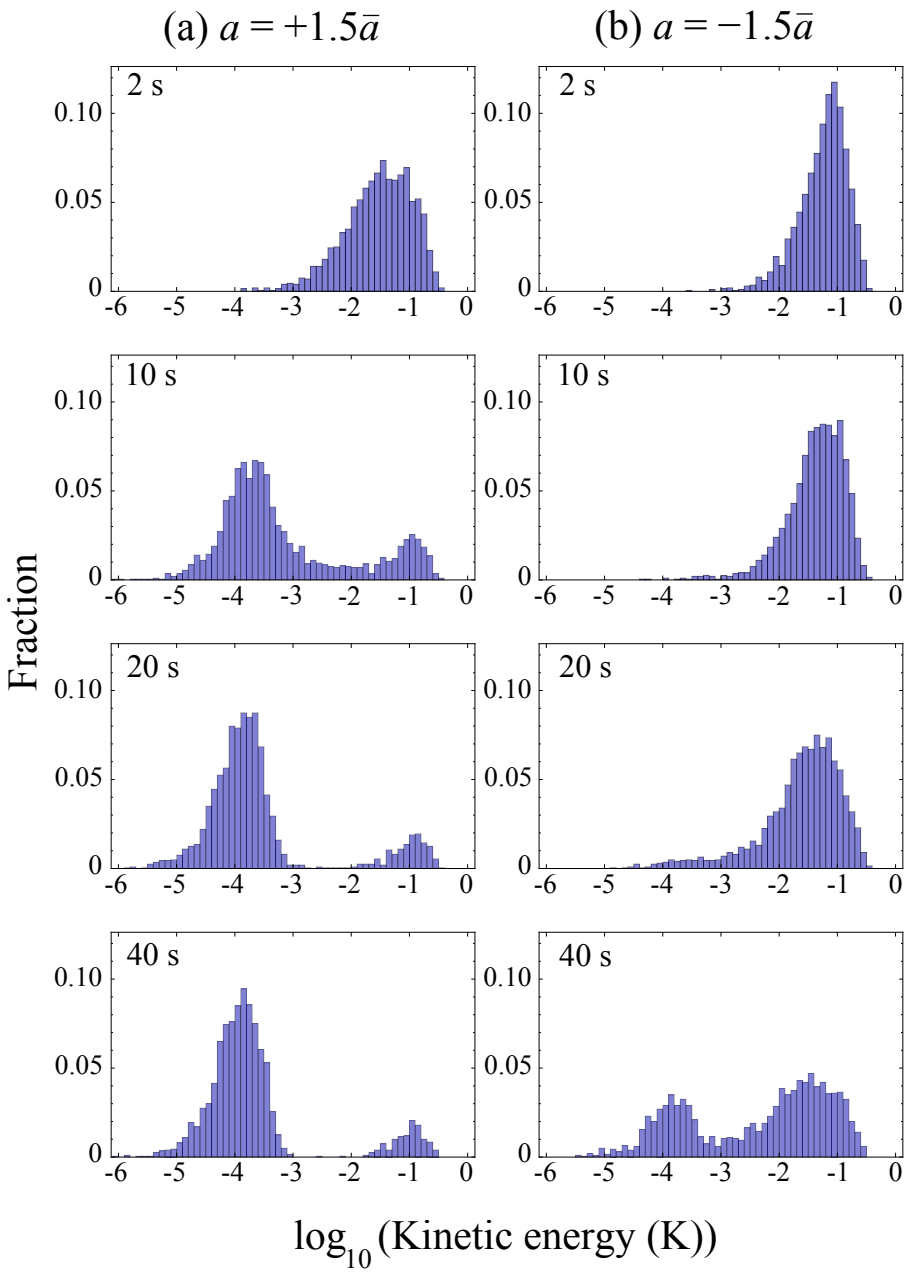

Figure 3.10: Kinetic energy distributions after 2 s, 10 s, 20 s and 40 s. The coolant is Li. Left panels have $a = +1.5\bar{a}$ while right panels have $a = -1.5\bar{a}$.

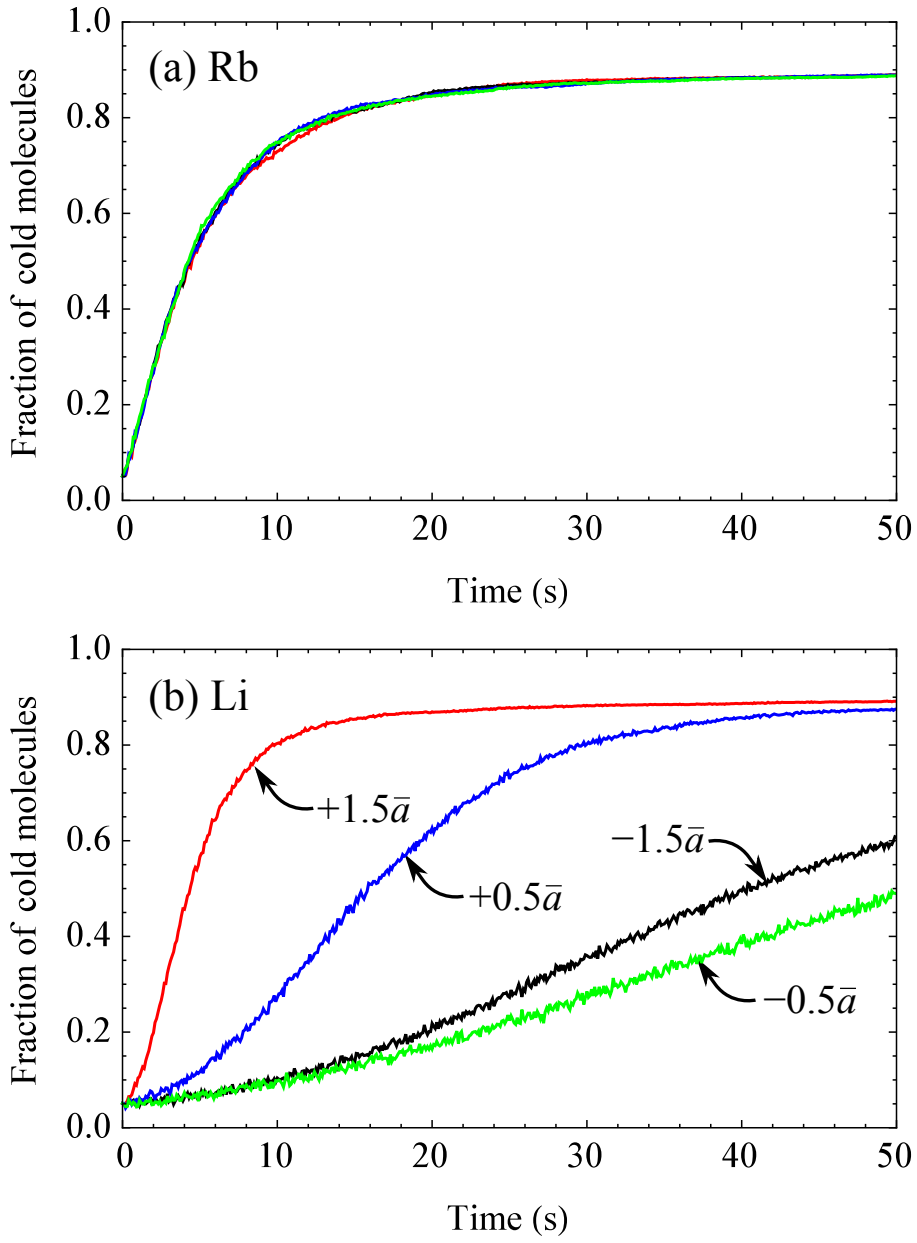

Figure 3.11: Fraction of molecules with kinetic energy below 10 mK as a function of time for (a) Rb, and (b) Li, for four different values of the scattering lengths: $a = +1.5\bar{a}$ (red), $a = +0.5\bar{a}$ (blue), $a = -0.5\bar{a}$ (green), and $a = -1.5\bar{a}$ (black).

$a = -0.5\bar{a}$, the Ramsauer-Townsend minimum is shifted to $E_{\mathrm{CaF}}^{\mathrm{lab}} = 10\,\mathrm{mK}$, but the cross section at the minimum is a factor of five smaller, and so the cooling is even slower, taking 50 s to reach 50%.

Figure 3.12(a) shows the mean kinetic energy of the cold fraction as a function of time for various values of a when Rb is used as the coolant. As for the cold fraction itself, this measure is almost independent of a. This may seem surprising, since the cooling rates estimated in fig. 3.7(a) show a strong dependence on a below a few mK. However, the mean kinetic energy is strongly influenced by molecules with kinetic energies close to the 10 mK cutoff that defines the cold fraction, and at this energy the cooling rates show little dependence on a. We find a small difference in the cooling rates between positive and negative scattering lengths. For the positive a values the molecular temperature is within a factor of two of the atomic temperature after 10 s, while for the negative a values this takes 14 s. Figure 3.12(b) shows how the mean kinetic energy of the cold fraction evolves when Li is used as a coolant. In this case, the cooling depends sensitively on a. When $a = +1.5\bar{a}$ the evolution is similar to the Rb case. The cooling is much slower when $a = +0.5\bar{a}$ because the low-energy cross-section is nine times smaller. The cooling is even slower when a is negative. This is because, in the energy region between 1 and 10 mK, the Ramsauer-Townsend minimum greatly suppresses the cooling rate relative to the positive a case, and because molecules with energies in this range have a strong influence on the mean.

The fraction of molecules that are cooled below 10 mK depends on the initial temperature, T_{i}. Figure 3.13 compares this fraction for $T_{\mathrm{i}} = 20\,\mathrm{mK}$ and 70 mK, for the case where Rb is the coolant and $a = +1.5\bar{a}$. These two initial temperatures correspond to temperatures of 2 mK and 30 mK prior to compression of the cloud in the microwave trap. When $T_{\mathrm{i}} = 20\,\mathrm{mK}$, more than 99% of the molecules are cold within 10 s.

3.2.7 Atom heating and loss

The energy transferred from molecules to atoms will either eject atoms from the trap, or will heat them up. As described in section 3.2.2, we suppose that atoms are

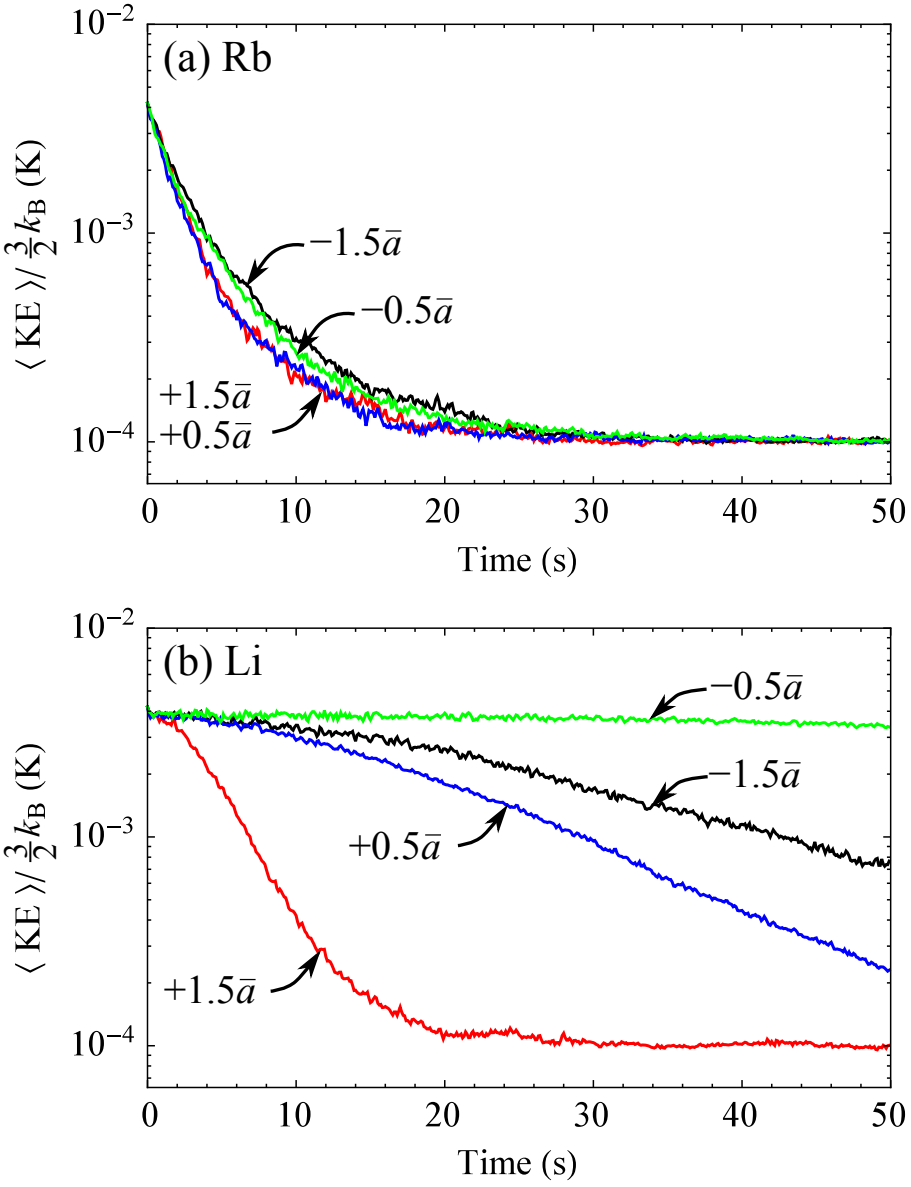

Figure 3.12: Mean kinetic energy of the cold fraction as a function of time when the coolant is (a) Rb and (b) Li, and for various values of the s-wave scattering length: $a = +1.5\bar{a}$ (red), $a = +0.5\bar{a}$ (blue), $a = -0.5\bar{a}$ (green), and $a = -1.5\bar{a}$ (black).

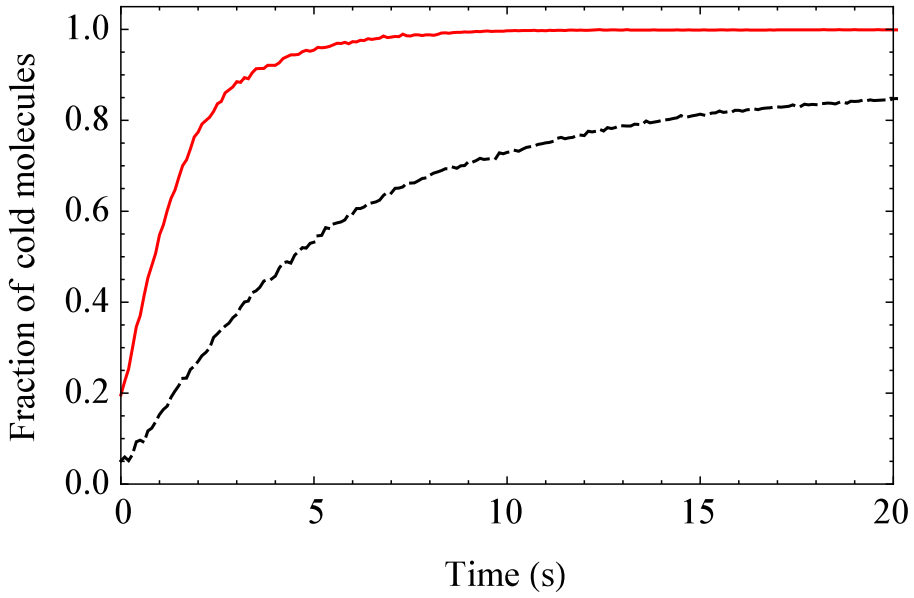

Figure 3.13: Fraction of cold molecules as a function of time for the initial temperatures of $T_\mathrm{i} = 20\,\mathrm{mK}$ (red solid line), and $T_\mathrm{i} = 70\,\mathrm{mK}$ (black dashed line). The coolant is Rb and $a = +1.5\bar{a}$.

lost from the trap if their total energy exceeds 1 mK. This could be the actual depth of the trap, or an "rf knife" might be used to cut off the trap at this depth. Here, we investigate the heating and loss of atoms and the consequences for sympathetic cooling. We note that while the EDT-HS collision model correctly captures the molecule cooling dynamics by using $\sigma_\eta^{(1)}$ is used as the cross section, it does not model correctly the atom heating and loss. Here, we highlight the difference between these two approaches by comparing the results obtained from the EDT-HS model and the full DCS model.

Figure 3.14 shows how the heating and loss rates of the atoms change with time in the full DCS model and the EDT-HS model for the case of 10^5 molecules and 10^9 atoms. The two models show similar trends, so we first discuss these trends and then consider the differences between the models. At early times the majority of the molecules have energies far above the atom trap depth and so most collisions cause atom loss, rather than heating. The loss rate is high while the heating rate is low. Nevertheless, there is still some heating due to small-angle collisions with the molecules which transfer only a little energy to the atoms. The loss rate increases during the first second because the collision cross section and the atom-molecule

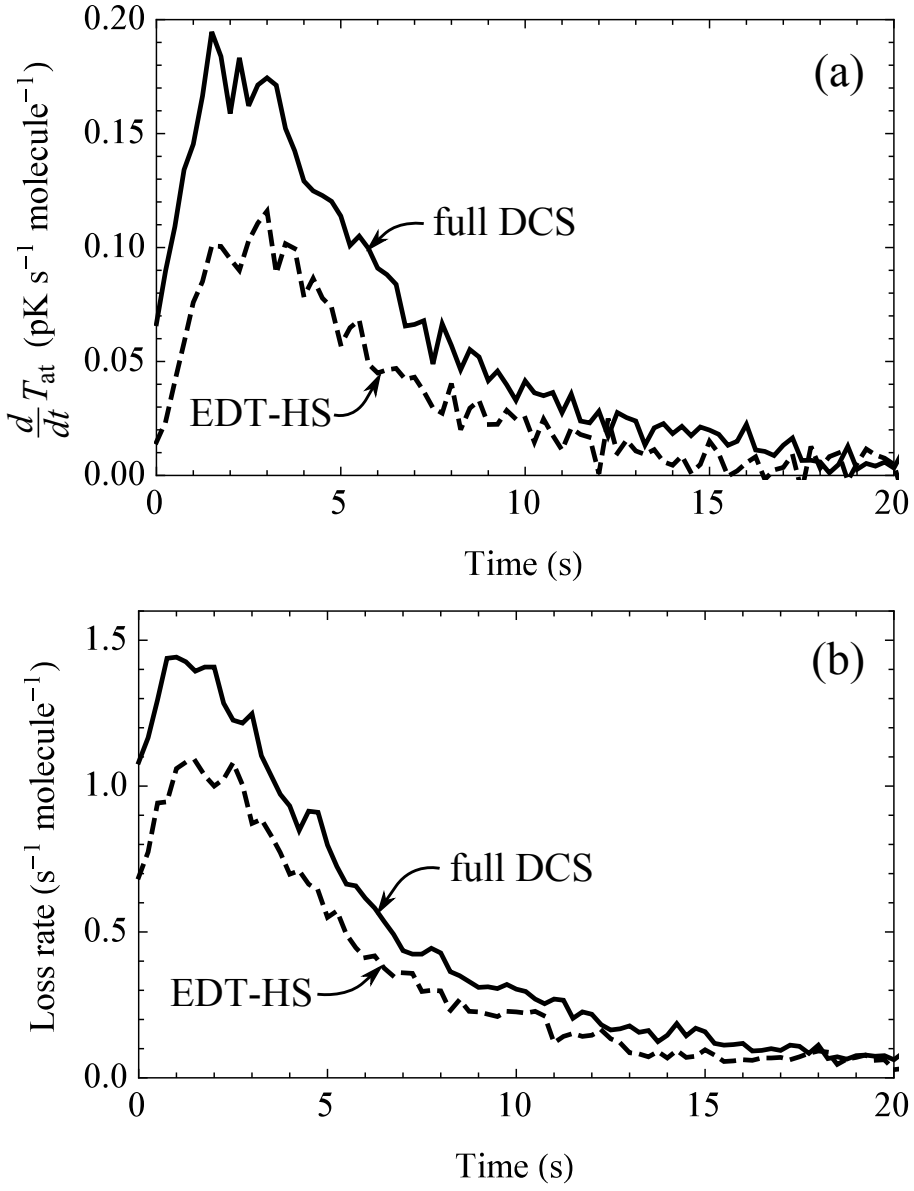

Figure 3.14: (a) Atom heating rate per molecule and (b) atom loss rate per molecule for the EDT-HS model (dashed line) and the full DCS model (solid line). The coolant is Rb, $a = +1.5\bar{a}$, and the molecules have an initial temperature of 70 mK. There are 10^5 molecules and 10^9 atoms.

overlap both increase as the molecules are cooled. As time goes on the loss rate falls because the molecules are cooler and there are fewer collisions with enough energy to kick atoms out of the trap. For the same reason the heating rate initially increases, but then decreases again as the molecules have less energy to transfer to the atoms. For most of the 20 s period, the full DCS model gives more atom heating and more atom loss than the EDT-HS model. Only at long times, once the atoms and molecules are almost fully thermalised, do the two models give the same results.

Integrating the results of the full DCS model shown in fig. 3.14, we find that the total temperature increase of the trapped atoms is 1.3 pK per molecule, while the total loss is 10 atoms per molecule. The energy deposited into the atom cloud is only 1.8% of the initial energy of the molecular cloud. In this sense, the sympathetic cooling process is remarkably efficient.

We now turn to how the atom heating and loss rates can be *understood*, and explain why the two models give different results. Whether an atom is heated or lost depends on the kinetic energy kick it receives in the collision, as given by eq. (3.2.25) if the atoms are assumed to be stationary. An atom at the centre of the trap is lost from the trap if the energy transferred in the collision exceeds the trap depth, $\Delta E > E_{\mathrm{trap}}$. This occurs if the deflection angle exceeds a critical angle Θ_{crit} given by

$$\cos\Theta_{\mathrm{crit}} = 1 - \left(\frac{m_{\mathrm{CaF}} + m_{\mathrm{at}}}{2\mu}\right)\left(\frac{E_{\mathrm{trap}}}{E_{\mathrm{CaF}}^{\mathrm{lab}}}\right). \tag{3.2.26}$$

At laboratory-frame energies below critical energy $E_{\mathrm{crit}} = ((m_{\mathrm{CaF}} + m_{\mathrm{at}})/4\mu)E_{\mathrm{trap}}$, no loss is possible, assuming stationary atoms at the centre of the trap. This energy is 2.63 mK for Li+CaF and 1.04 mK for Rb+CaF. All collisions below this energy and collisions above this energy where $\Theta < \Theta_{\mathrm{crit}}$ will not eject atoms from the trap, but still transfer energy and so heat the atom cloud, by an amount proportional to $1 - \cos\Theta$. This suggests the possibility of defining cross sections for atom heating and loss as partial integrals of the differential cross section,

$$\sigma_{\mathrm{loss}} = 2\pi \int_{-1}^{\cos\Theta_{\mathrm{crit}}} \frac{d\sigma}{d\omega} d\cos\Theta, \tag{3.2.27}$$

$$\sigma_{\text{heat}} = 2\pi \int_{\cos\Theta_{\text{crit}}}^{1} \frac{d\sigma}{d\omega}(1-\cos\Theta)d\cos\Theta. \tag{3.2.28}$$

It is convenient to write these as integrals over $d\cos\Theta$ instead of $\sin\Theta\, d\Theta$ because the $\cos\Theta$ form allows us to show plots in which the integrals are simply areas that can be estimated by eye. Note that if $E_{\text{CaF}}^{\text{lab}} < E_{\text{crit}}$ then $\sigma_{\text{heat}} = \sigma_{\eta}^{(1)}$, because all collisions cause heating rather than loss. For the full DCS model these integrals must be evaluated numerically, but in the hard-sphere model the DCS are isotropic, $d\sigma_{\text{HS}}/d\omega = \sigma_{\text{HS}}/(4\pi)$, and the integrals can be evaluated analytically to give

$$\sigma_{\text{loss,HS}} = \frac{1}{2}(1+\cos\Theta_{\text{crit}})\sigma_{\text{HS}} \tag{3.2.29}$$

and

$$\sigma_{\text{heat,HS}} = \frac{1}{4}(1-\cos\Theta_{\text{crit}})^2\sigma_{\text{HS}}. \tag{3.2.30}$$

Figure 3.15 shows differential cross sections at two energies that correspond to $E_{\text{CaF}}^{\text{lab}} = 2$ mK and 20 mK for Rb+CaF. Both full differential cross sections and those from the EDT-HS model are shown (solid and dashed black lines respectively), and the corresponding quantities weighted by $1-\cos\Theta$ are shown in red. The values of Θ_{crit} at the two energies are shown as vertical lines. Integrals over the complete range of $\cos\Theta$ under the black lines correspond to σ_{el}, and under red lines correspond to $\sigma_{\eta}^{(1)}$; the latter is the same for the full DCS and EDT-HS models by construction. σ_{loss} is the area under the black lines to the left of Θ_{crit}, and σ_{heat} is the area under the red lines to the right of Θ_{crit}. It can be seen that at 20 mK the full DCS has a very large forwards peak; this dominates σ_{heat}, even though its contribution is suppressed by the $1-\cos\Theta$ weighting. The resulting σ_{heat} is many times larger than in the EDT-HS model, which has no forward peak. The full DCS also has a secondary peak near $\cos\Theta = 0.75$, which is outside Θ_{crit} and so contributes to atom loss; the resulting σ_{loss} is also larger than in the EDT-HS model. At the lower energy of 2 mK, Θ_{crit} is near $\Theta = \pi/2$. There is still a large forwards peak but it no longer dominates due to the changed range of integration, leading to similar cross sections for the two models.

Figure 3.16 shows how the heating and loss cross sections vary over the range

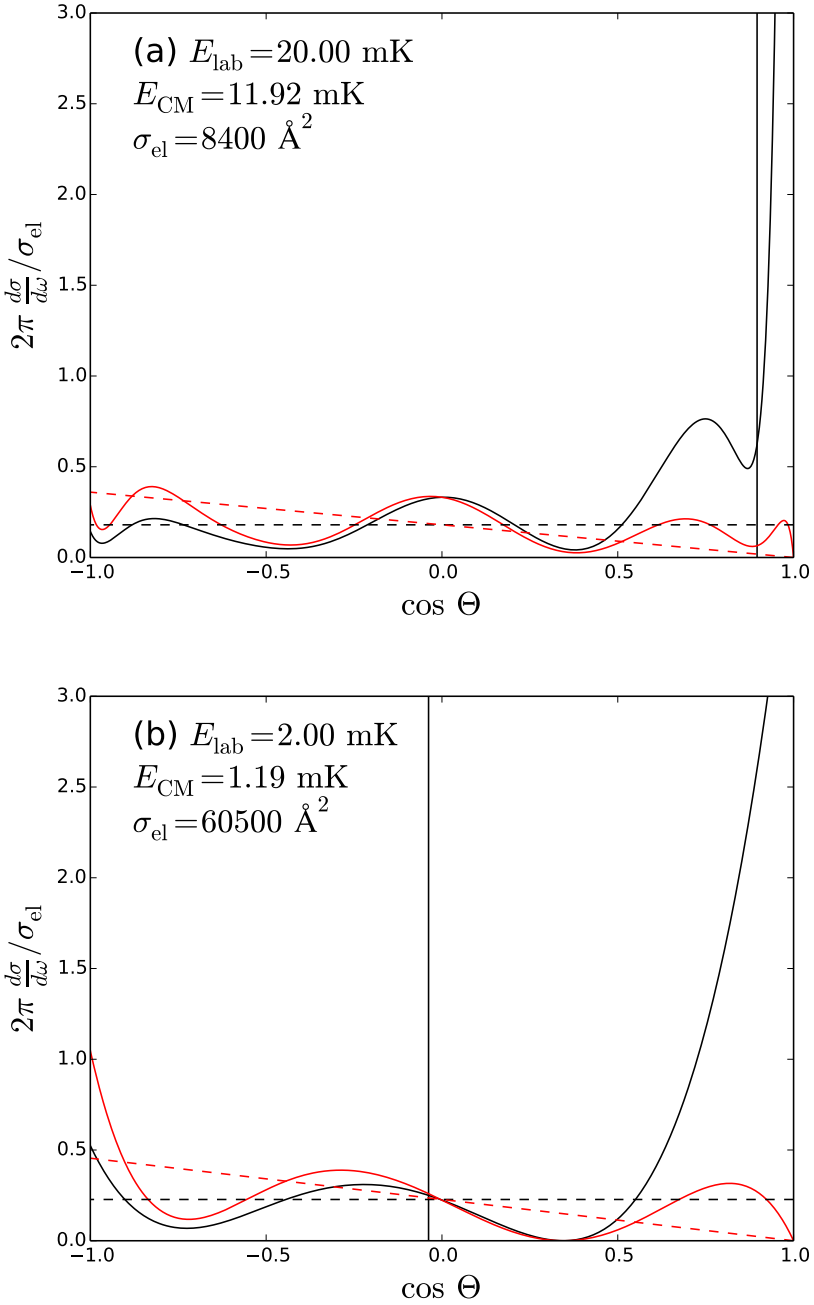

Figure 3.15: Differential cross sections and their contributions to heating and loss. The solid black line shows the full quantum-mechanical $d\sigma/d\omega$, while the solid red line shows $(1-\cos\Theta)d\sigma/d\omega$; the dashed lines show the corresponding quantities for the EDT-HS model. The vertical line shows the value of Θ_{crit}. (a) $E_{\mathrm{CaF}}^{\mathrm{lab}} = 2\,\mathrm{mK}$. (b) $E_{\mathrm{CaF}}^{\mathrm{lab}} = 20\,\mathrm{mK}$. The coolant is Rb and $a = +1.5\bar{a}$.

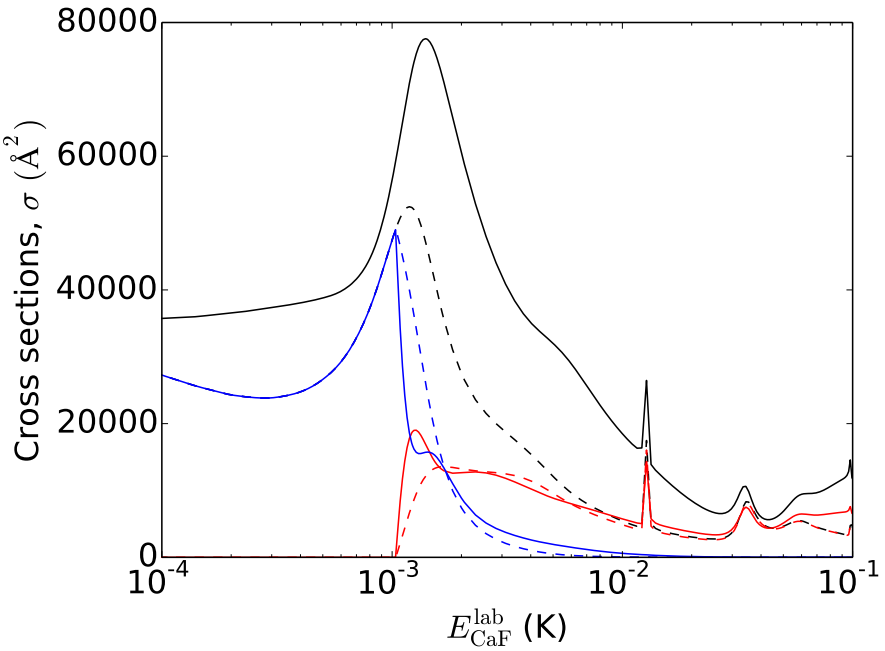

Figure 3.16: Loss (red) and heating (blue) cross sections as a function of CaF laboratory energy for the EDT-HS model (dashed lines) and the full DCS model (solid lines). σ_{el} (solid black line) and $\sigma_\eta^{(1)}$ (dashed black line) are shown for comparison. The coolant is Rb and $a = +1.5\bar{a}$.

of energies relevant to the cooling process. As explained above, at low energy, $E_{\mathrm{CaF}}^{\mathrm{lab}} < E_{\mathrm{crit}}$, we have $\sigma_{\mathrm{heat}} = \sigma_\eta^{(1)}$ and $\sigma_{\mathrm{loss}} = 0$. Above E_{crit} the heating cross section falls off rapidly; for the EDT-HS model it falls to negligibly small values by a few mK. The cross section for the full DCS is several times larger than that for the EDT-HS model in this tail, but it also falls towards zero. The loss cross sections for the two models agree surprisingly well ($\pm \sim 30\%$) in an intermediate energy range from about 2 mK to 60 mK; the extent of this similarity is greatest for this particular scattering length ($a = +1.5\bar{a}$), but it also exists up to about 20 mK for the other scattering lengths investigated. Above this intermediate range, σ_{loss} for the full DCS model does become larger than for the EDT-HS model, as we expect. The large peak around 1.5 mK in the elastic cross section is a d-wave feature that causes a large amount of backwards scattering around that energy; this significantly enhances the loss cross section because at this energy Θ_{crit} is still near backwards scattering.

The overall effect is that the full DCS model gives significantly larger rates of

both atom heating and atom loss than the EDT-HS model, especially at higher energies, exactly as we see in fig. 3.14. This is at first sight surprising because each atom-molecule collision causes either atom heating or atom loss. However, at higher energies the total collision rate is considerably greater in the full DCS model than in the EDT-HS model, because the former is determined by σ_{el} and the latter by $\sigma_{\eta}^{(1)}$.

The effects of atom heating and loss will, of course, be most significant when the atom number does not greatly exceed the molecule number. Table 3.1 shows the results of simulations for a variety of molecule numbers, with the atom number fixed at 10^9, and once again compares the full DCS and EDT-HS models. In the first three rows, the trap depth for the atoms is 1 mK. When the atom number is 100 times the molecule number, atom heating and loss are not significant effects. For each molecule, the first few collisions carry away most of the energy, and almost all of these collisions cause atom loss, rather than heating. Thus, for this case, 11% of the atoms are lost, and the atom cloud heats up by just 13 μK. The molecules thermalise completely with the atoms, and the majority are in the cold fraction. When the atom number is only 10 times the molecule number, the effects are far more dramatic. At the end of the simulation only 2.2% of the atoms remain, and the temperature of those remaining has increased to 259 μK. Since there are so few atoms remaining, only 70% of the molecules now reach kinetic energies below 10 mK, and the temperature of this fraction is increased to 596 μK. The EDT-HS collision model underestimates the atom loss and atom heating, and it predicts more cold molecules, with a lower final temperature, than the full DCS model.

It is interesting to explore whether the atomic trap depth of 1 mK used in the simulations above is optimum. The last three rows of table 3.1 show the results of simulations with the atomic trap depth increased to 5 mK. As expected, this results in less atom loss and more atom heating. The fraction of cold molecules increases a little, but the temperature of the cold fraction increases significantly. This is especially evident when the atom number is only 10 times the molecule number. It is clear that large atomic trap depths are not necessarily beneficial for sympathetic cooling, and indeed there might be advantages in adjusting the trap depth as cooling

Table 3.1: The effect on the cooling process of different molecule numbers (N_{mol}), with atom number fixed at 10^9, for two values of the trap depth E_{trap}: 1 mK and 5 mK. The columns give the fraction of remaining atoms f_{at}, the atomic temperature T_{at}, the fraction of cold molecules f_{mol}, and the molecular temperature T_{mol} after 50 s. The main values are for the full DCS model, and the values in brackets are for the EDT-HS model.

E_{trap}	N_{mol}	f_{at} (%)	T_{at} (μK)	f_{mol} (%)	T_{mol} (μK)
1 mK	10^7	89 (92)	113 (107)	89 (89)	113 (108)
	5×10^7	38 (59)	159 (136)	88 (88)	168 (144)
	10^8	2.2 (18)	259 (180)	70 (83)	596 (246)
5 mK	10^7	95 (96)	151 (133)	90 (89)	153 (134)
	5×10^7	75 (79)	396 (291)	90 (91)	435 (299)
	10^8	50 (57)	704 (518)	85 (87)	927 (624)

proceeds.

3.2.8 The effect of evaporative cooling

Tarbutt and Lim also considered the effect of evaporatively cooling the atoms, to allow cooling of the molecules to even lower temperatures. The methods and results are described in detail in the final section of Ref. [113] and only the results are summarised here. They suppose that the evaporation is done in the magnetic trap by applying an rf field which induces transitions between trapped and anti-trapped Zeeman states at a value of magnetic field only reachable by the most energetic atoms (an "rf knife"). The evaporative cooling of the atoms follows the theory described in [264]. The rf knife is set such that an atom is lost if its energy exceeds $\eta k_{\mathrm{B}} T$, such that the parameter η determines how rapidly the evaporative cooling proceeds.

Figure 3.17(a,b) shows the fraction of molecules with kinetic energy below 1 mK, and the mean kinetic energy of that fraction, using $a = +1.5\bar{a}$ and three different values of η: 5.52, 6.67, and 8.14. It can be seen that for all three values of η sympathetic cooling works well in this case and the molecules reach 1 μK in 30 – 50 s. Note that the times taken to reach this temperature are purely atomic effects and are not influenced by the sympathetic cooling. In particular, in the case of $\eta = 5.52$ the cooling slows significantly after about 20 s, which is because too many atoms have been lost due to the aggressive evaporative cooling. Therefore, the fastest

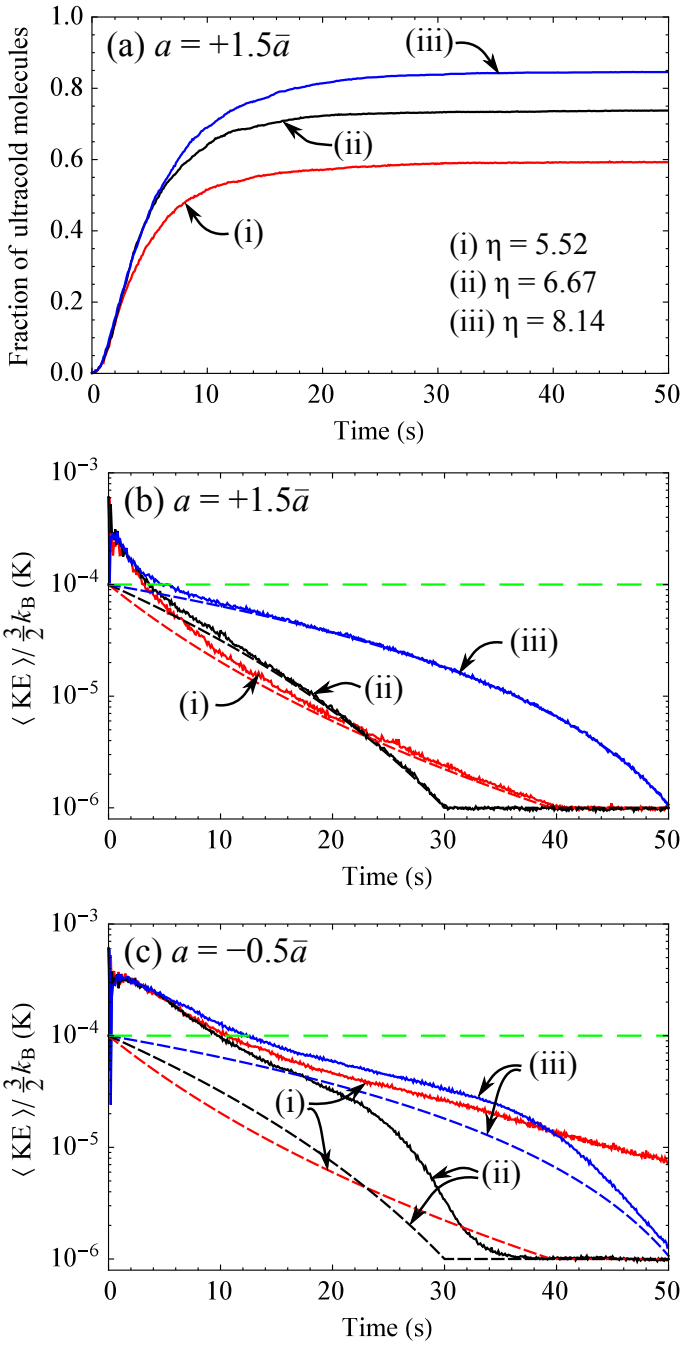

Figure 3.17: Sympathetic cooling of molecules with evaporative cooling applied to the atoms. Graphs show the time evolution of (a) the fraction of molecules with kinetic energy below 1 mK, when $a = +1.5\bar{a}$; (b) the mean kinetic energy of the ultracold fraction when $a = +1.5\bar{a}$; (c) the mean kinetic energy of the ultracold fraction when $a = -0.5\bar{a}$. (i, black) $\eta = 5.52$, (ii, red) $\eta = 6.67$, (iii, blue) $\eta = 8.14$. In (b) and (c), the dashed lines show how the atomic temperature evolves. The long-dash green line shows the atom temperature without evaporative cooling.

cooling is found for the intermediate value of η

Finally, we consider the case where $a = -0.5\bar{a}$. This is a highly unfavourable case compared to $a = +1.5\bar{a}$, both because the elastic cross section in the ultracold limit is nine times smaller and because there is a deep Ramsauer-Townsend minimum in the cross section for collision energies slightly below 100 μK, as can be seen in fig. 3.5. The fraction of molecules with kinetic energy below 1 mK is almost unchanged from that shown in fig. 3.17(a) because at energies higher than 1 mK the cross sections for the two values of a are not too different. Figure 3.17(c) shows how the mean kinetic energy of the ultracold fraction evolves when $a = -0.5\bar{a}$. Because of the lower collision rate, the mean kinetic energy of the molecules lags behind that of the atoms, instead of the two being locked together as they are in the case of $a = +1.5\bar{a}$. The molecules are slow to reach 20 μK for all values of η, because they have to cool through the Ramsauer-Townsend minimum to do so. In particular, for $\eta = 5.52$, the atoms cool too quickly and the molecules have not thermalised with the atoms even after 50 s. However, cooling is successful for the other two values of η and again the cooling of the molecules is fastest for the intermediate value. We see that, even for this unfavourable value of a, evaporative cooling of the atoms can bring the molecule temperature down to 1 μK on a reasonable timescale, provided a suitable value of η is chosen. It is clear that knowledge of the actual atom-molecule scattering length will be needed to choose the optimum conditions for evaporative cooling.

3.2.9 Conclusions

In this section, we have addressed the methodology for modelling sympathetic cooling of molecules by ultracold atoms, and we have studied in detail the results of simulations for a prototype case where ground-state CaF molecules in a microwave trap are overlapped with ultracold Li or Rb atoms in a magnetic trap. This work leads to a number of conclusions which we now summarise.

Previous work on sympathetic cooling used a hard-sphere model of collisions. This is appropriate at very low energies (in the s-wave regime), but breaks down badly for heavy molecules in the millikelvin regime. Even with a properly energy-dependent elastic cross section, σ_{el}, we have shown that a hard-sphere model sig-

nificantly over-estimates the cooling rate for collision energies above the s-wave scattering regime. A hard-sphere collision model that uses the energy-dependent momentum transport cross section, $\sigma_\eta^{(1)}$, gives the correct molecule cooling rate, but underestimates both the heating of the atoms and the loss of atoms from the trap. We have therefore used the full differential cross section to model atom-molecule collisions, so that the cooling of the molecules and the associated heating and loss of atoms are all modelled accurately.

We have studied sympathetic cooling of CaF with both Rb and Li over a range of typical values of the atom-molecule scattering length a. We find that Rb offers significant advantages over Li as a coolant for ground-state molecules. The mean scattering length $\bar{a}$ is almost twice as large for Rb, and so it is likely that the true scattering length will also be larger for Rb. The mean energy transfer is proportional to $\mu/(m_{\mathrm{CaF}} + m_{\mathrm{at}})$ which is 0.48 for Rb, but only 0.19 for Li. If a happens to be negative there can be a deep Ramsauer-Townsend minimum in the cross section. For Li, the minimum typically occurs when $E_{\mathrm{CaF}}^{\mathrm{lab}}$ is between 1 and 10 mK, and the molecules cool very slowly because their energies must pass through this minimum. For Rb, the minimum is shifted down an order of magnitude in energy, and so the molecules do not encounter the minimum until they have reached the ultracold regime. For Li, the cooling rate is very sensitive to the actual value of a, while for Rb the initial cooling rate is fairly insensitive to a because the Rb+CaF cross section conforms closely to a classical result, independent of a, down to temperatures near 1 mK. This brings less uncertainty about the likely results of sympathetic cooling experiments if Rb is used. These advantages of Rb as a coolant are likely to extend to other molecules of a similar or greater mass. Finally, it is experimentally easier to prepare large, dense samples of ultracold Rb than of ultracold Li.

It should be noted that the preference for Rb over Li applies only to ground-state molecules that cannot be lost from the trap through inelastic collisions. For molecules in static magnetic or electric traps, a light collision partner such as Li, Mg or H provides a higher centrifugal barrier than a heavy one such as Rb, and this may be important for suppressing low-energy inelastic collisions [100, 106, 110].

For molecules with an initial temperature of the molecules of 70 mK, cooled by Rb

with a temperature of 100 μK and a peak density $10^{11}\,\mathrm{cm}^{-3}$, we find that, after 10 s, 75% of the molecules have cooled into a distribution with a temperature of 200 μK. If the initial temperature of the molecules is reduced to 20 mK, this fraction increases to 99% due to improved overlap between molecule and atom clouds. By arranging for the atom trap depth to be far below the initial molecule temperature, we can ensure that the majority of the energy in the molecule cloud is removed by atoms that are lost from the trap, instead of heating the atom cloud. For efficient cooling the atom number should exceed the molecule number by at least a factor of 100. By applying evaporative cooling to the atoms, the molecules can be sympathetically cooled more rapidly, or they can be cooled to far lower temperatures. For values of the scattering length in the likely range, and with a suitable choice of evaporation ramp, 70% of the molecules can be cooled to 1 μK within about 30 s. These are all encouraging results: using experimentally achievable atom numbers, densities and temperatures, sympathetic cooling to ultracold temperatures can work on a timescale that is short compared to achievable trap lifetimes. A good starting point for such experiments would be a mixed-species magneto-optical trap of molecules and atoms.

3.3 Updated Prospects for Sympathetic Cooling of Magnetically Trapped Molecules

We now briefly consider how the ideas explored in this chapter affect our understanding of the prospects for sympathetic cooling in a magnetic trap. For trapping in a static magnetic trap, the molecules must be in a low-field-seeking state, which can never be their lowest state. Therefore, inelastic collisions will always be possible for sympathetic cooling in a magnetic trap; these will cause trap loss either through large kinetic energy release or through transfer to an untrapped state. This has led to a rule of thumb that for successful sympathetic cooling in a magnetic trap, the ratio of elastic to inelastic cross sections, $\gamma_{\mathrm{el}} = \sigma_{\mathrm{el}}/\sigma_{\mathrm{inel}}$, must be 100 or greater. A definitive justification for this number seems elusive; Ref. [56] is often cited, but

that paper is far from definitive as concerns the general case,[6] although the ratio of 100 probably is a reasonable target in practical terms. Much of the theoretical effort in this area has been focussed on finding systems where this criterion is met [96–102, 106, 107, 110].

As an example we consider Mg+NH, which was the first molecular system to be shown to have the required ratio of elastic to inelastic cross section [100]. We consider collisions of NH in its $m_s = +1$ state, where s is the spin quantum number of the unpaired electron of the NH molecule and m_s is the projection of s onto the space-fixed magnetic-field axis. Mg is a ^{1}S atom and is therefore structureless. We neglect hyperfine interactions on both collision partners. The calculations are described in detail elsewhere [100, 218].

We can immediately say that the relevant ratio to asses sympathetic cooling is $\gamma_{\text{th}} = \sigma_\eta^{(1)}/\sigma_{\text{inel}}$, rather than γ_{el}. Figure 3.18 shows contour plots of both γ_{el} and γ_{th} for Mg+NH. It can be seen that the use of $\sigma_\eta^{(1)}$ makes relatively little difference to the overall behaviour and interpretation of these results. This is fairly unsurprising, given the two cross sections differ by only a small factor in the region of energy we are interested in. The most notable difference is that the region where the ratio is only just larger than 100 is significantly wider when using $\sigma_\eta^{(1)}$, but as this is still likely to lead to successful sympathetic cooling it does not affect the conclusions. Indeed, the effect of using $\sigma_\eta^{(1)}$ is much smaller than the effects of including hyperfine interactions [103]. However, the results *are* quantitatively different and, where possible, $\sigma_\eta^{(1)}$ (and γ_{th}) should be used in preference to σ_{el} (and γ_{el}) for assessing the likelihood of success of sympathetic cooling.

There is an additional effect that was not accounted for in previous theoretical work on this topic. The relevant scattering calculations were performed using centre-of-mass energies, as usual, but were not subsequently interpreted in terms of laboratory frame energies that are of primary interest to experimentalists. As discussed in sections 3.1.1 and 3.2.1, if the coolant atoms are approximated as being

[6] It is written in the context of buffer-gas cooling not sympathetic cooling; refers to a number of collisions needed for cooling rather than a ratio of elastic to inelastic cross sections; is for a single specific case for which the number of collisions is actually ~ 250.

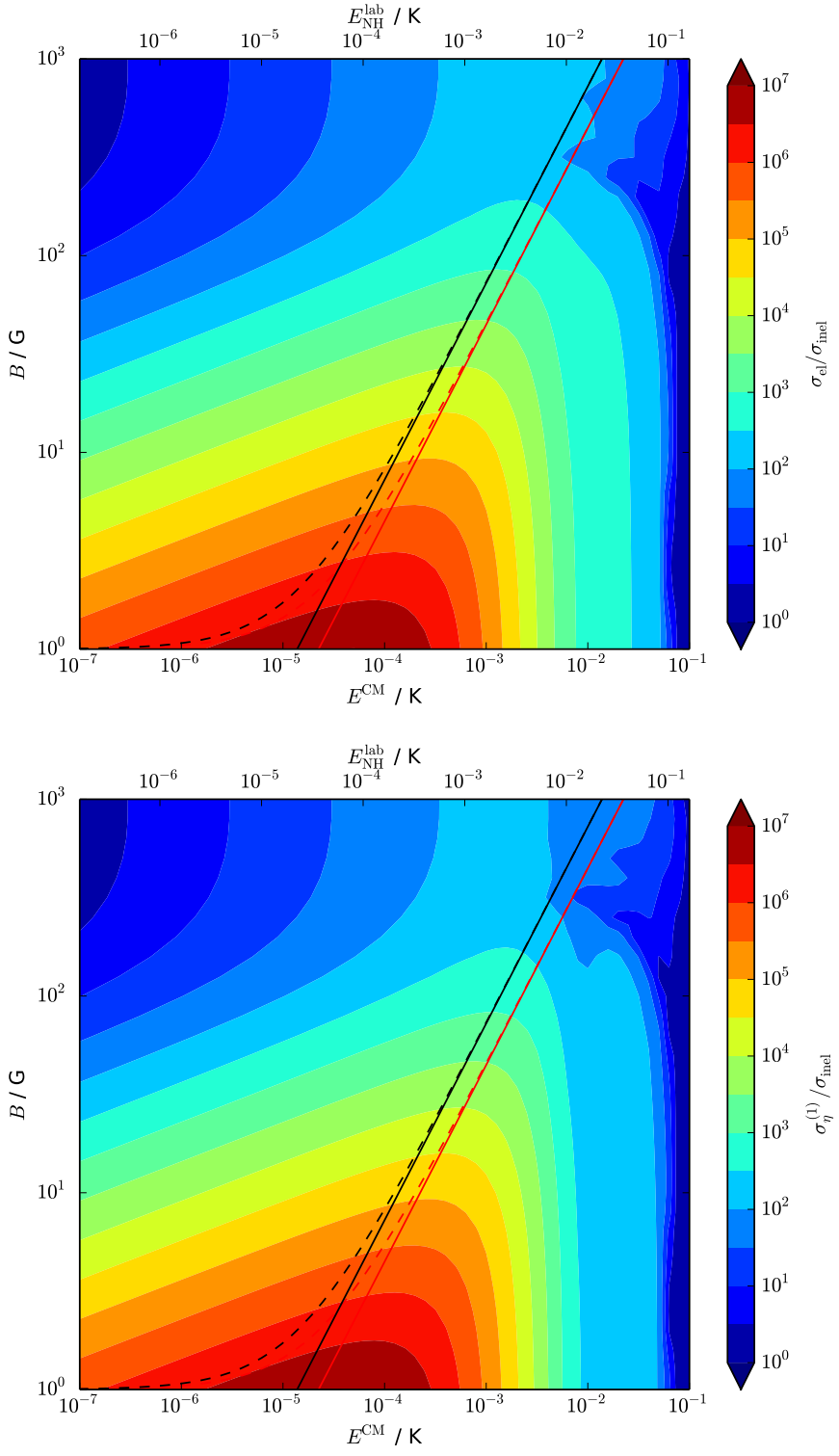

Figure 3.18: Contour plots of ratios of cross sections: $\sigma_{\mathrm{el}}/\sigma_{\mathrm{inel}}$ (top) and $\sigma^{(1)}_{\eta}/\sigma_{\mathrm{inel}}$ (bottom) for Mg+NH. The black lines show the upper bound of the field sampled by 99.9% of the molecules in a cloud with a temperature of $E^{\mathrm{lab}}_{\mathrm{NH}}/k_{\mathrm{B}}$, in an unbiased trap (solid) and a trap with a bias field of $B = 1$ G (dashed). For comparison, the red lines show the equivalent quantity for a temperature of $E^{\mathrm{CM}}/k_{\mathrm{B}}$, which was incorrectly used in some previous publications.

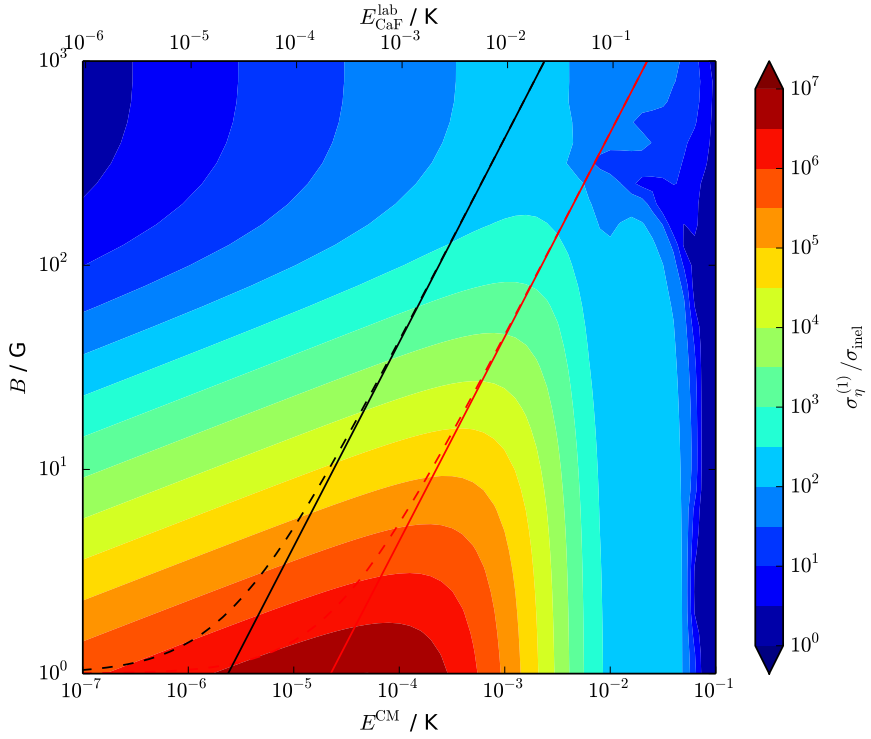

Figure 3.19: Contour plots of ratios of cross sections: $\sigma_\eta^{(1)}/\sigma_{\mathrm{inel}}$ for the cross sections of Mg+NH but with ratio between CM and laboratory frame energies of Li+CaF. The lines are as in the previous figure.

stationary in the trap, the laboratory frame energy of the molecules is higher than the CM energy by a factor of m_{mol}/μ. This can significantly affect the interpretation of the calculations, in particular it can scale the temperature below which sympathetic cooling is likely to be successful. In Mg+NH, the factor is 1.626, and although this appears to be a relatively modest factor it could make a large difference to the number of molecules able to be cooled to the starting temperature. This is also shown in fig. 3.18 by the secondary x-axis showing $E_{\mathrm{NH}}^{\mathrm{lab}}$, which allows correct interpretation of the contour plot under the approximation that the coolant Mg atoms are stationary. Additionally, previous work included estimates for the maximum field experienced by 99.9% of the molecules at a particular temperature, which had been incorrectly calculated using the CM energies; this is now calculated correctly, using the laboratory frame energies.

The effect of this mass-scaling can be much larger and highly significant for heavier molecules or lighter coolant atoms. For example, for ^{7}Li+CaF there are reasonable prospects that $\gamma_{\mathrm{th}} > 100$ at collision energies below about 20 mK. This is because of centrifugal suppression in the outgoing channel [103, 106, 108]. However, the mass scaling factor is 9.404, so sympathetic cooling might be possible from laboratory energies 150-200 mK for the molecules. Figure 3.19 shows the cross sections of Mg+NH but with the ratio between CM and laboratory energies of Li+CaF to illustrate the magnitude of this effect. This is a very significant difference because existing direct cooling methods, such as Stark or Zeeman deceleration or buffer-gas cooling, can sometimes cool significant numbers of molecules down to 100-200 mK but generally struggle to reach lower temperatures. Therefore, cooling starting at 150 mK is likely to be experimentally feasible whereas cooling starting at 20 mK is likely not to be feasible, so this effect might be crucial in a practical realisation of sympathetic cooling in a magnetic trap.

Similarly large mass scaling factors will also occur in systems using atomic hydrogen as a coolant [109, 110] (15.9 for H+NH, 17.9 for H+OH). This may allow cooling from initial molecule temperatures of several Kelvin, which will significantly reduce the pre-cooling necessary and may result in much larger molecule numbers if sufficiently large numbers and high densities of hydrogen atoms can be produced.

Chapter 4

Chaos in Ultracold Scattering Systems

In recent years, interest in ultracold physics has turned to increasingly complex systems. Examples include collisions of high-spin atoms [43, 265–269] and ground-state molecules [49–51, 104, 145]. The theory needed for a full description of these systems is often prohibitively difficult; for example, two erbium atoms interact on 91 potential curves [127], and even small molecular systems such as Li+CaF become extremely challenging when all spins are included [270]. In such a case it is unrealistic to fit precise potentials to experimental results in the manner that has been so successful for simple atomic systems such as Rb+Cs [42] and might even be envisaged for a system like Mg+NH. Instead it is possible that the dynamics are stochastic with levels described by random matrix theory (RMT) [271, 272].

A qualitative understanding of the dynamics of these highly complex systems is important for both theorists and experimentalists. For a simple system, theory can in principle give a complete description, but for a fully chaotic system specific predictions are likely to be impossible. For example, it is unlikely to be possible to map out the near-threshold bound states navigated by Feshbach molecules except empirically [43]. If a collision is chaotic in nature, the collision complex will ergodically explore the entire phase-space and the two collision partners may be trapped together for a long time. In ultracold collisions, this may be long enough for a third body to collide with the complex, which is likely to lead to the loss of all the particles

involved from the trap [207].

The idea of describing energy levels of a complex system as eigenvalues of a random matrix was first proposed by Wigner [273–275] in an effort to describe resonances in the scattering of neutrons from complex nuclei. These ideas were expanded through the 1950's and 60's by various authors [276–281], most notably Dyson whose seminal series of papers [282–285] established much of the underlying theoretical structure of RMT. During this period, the Gaussian Orthogonal Ensemble (GOE) was first described; this quickly became the most commonly used RMT ensemble. Although these ideas were originally developed in the context of energy levels of complex nuclei, they were quickly applied to other physical systems such as electronic states of transition metal atoms [278] and Rydberg states of Hydrogen in a magnetic field [286]. The discussion of such systems originally referred to "complex" or "random" systems, but the Bohigas-Giannoni-Schmit (BGS) conjecture [287] made the link to "chaotic" systems - in this context, systems for which the classical dynamics are chaotic. This conjecture states that the quantum mechanical energy levels of a system that is classically chaotic follow the same statistical fluctuations as the GOE (for a time-reversal independent system). The BGS conjecture remains unproven, but there are strong indications of its validity in the semiclassical limit [288, 289] and there is much evidence supporting it from both theory and experiment.

The idea of applying theories of chaos and RMT to cold and ultracold collisions was first suggested by Bohn et al. [290] for O_2. However, this idea only gained significant traction in the ultracold physics community after later studies [207, 208] emphasised the potential enhancement of 3-body collision rates due to long-lived 2-body collisions. This effect was proposed as a mechanism by which molecules which are expected to be immune to 2-body inelastic and reactive collisions might still show fast trap loss. Of particular interest are alkali dimers: these have been produced in their absolute ground state for several atomic combinations; and for some of the combinations all 2-body reactive collisions should be energetically forbidden at ultracold temperatures [291]. There have been preliminary signs of this kind of rapid trap loss for molecules that were expected to be collisionally stable [50, 52, 53],

although attributing the loss to chaos and long-lived 2-body collisions is still highly speculative. This argument will be explored in greater depth in chapter 5, but it is predicated upon the idea that the systems in question are chaotic, and it is this aspect that will be the focus of this chapter.

Signatures of quantum chaos have now been experimentally observed in ultracold collisions of high-spin atoms. These studies analysed the distribution of magnetic Feshbach resonances in Er+Er [127, 128] and Dy+Dy [128] and found that they showed some key features expected of chaotic systems but that they were not consistent with a fully chaotic system. Theoretical bound-state calculations were also performed on the two systems [127, 128] which were broadly in agreement with the conclusions from the experimental results. However, calculations on Li+Er found statistics consistent with a random but non-chaotic level distribution [292]. A re-analysis of the erbium results [293] showed that the deviations from chaotic predictions might arise because some narrow resonances are not observed in the experiment. These ideas have also been used as a basis for a QDT toy model by Jachymski and Julienne [294].

This chapter will begin with a discussion of some of the theory of RMT, and how it applies to ultracold systems in section 4.1, as well as details of how we perform statistical analysis of our results. In section 4.2 we consider the specific atom+diatom systems Li+CaH and Li+CaF. Here, we investigate both the signatures of chaos observed, and the development of order under certain conditions which partially destroys the chaos in both expected and unexpected ways. In section 4.3 we turn our attention to the atom+atom system Yb+Yb*, which has similarities to the Er and Dy systems investigated experimentally but with a much simpler structure.

The work in this chapter is drawn from work published in Refs. 129 and 130 and significant parts of the work were collaborative between all 5 authors of those publications. The code used to perform the statistical analysis described in section 4.1 and used in sections 4.2 and 4.3 was created jointly by C. L. Vaillant and myself. The bound state calculations in section 4.2 were performed jointly by M. Morita and myself. The calculations in section 4.3 were performed by C. L. Vaillant and D. G. Green. The analysis and interpretation of results was generally collaborative

between all the authors, but lead by myself for the atom+diatom work in section 4.2.

4.1 Introduction to RMT as Applied to Ultracold Scattering and Near-Threshold Bound States

Here we will give a very brief overview of RMT and in particular the GOE. This will hopefully both illustrate the key points needed to understand our use of RMT, and provide a starting point for a student first approaching this challenging field, as I was at the start of this project. There is a great deal of secondary literature available on this subject, although much of it is near incomprehensible to those not already familiar with the basics in this field. Sources we have found particularly useful include "Random Matricies" by Mehta [271] and the early sections of "Random matrix theories in quantum physics: common concepts" by Guhr et al. [272], in particular we found this review was the most useful source of references into the primary literature; "Quantum signatures of chaos" by Haake [295] is a more technical text, and covers less of the material we are interested in than the other references, but it is clearly and precisely written and has been useful for clarifying technical points; "The transition to chaos: conservative classical systems and quantum manifestations" by Reichl [296] covers an extensive range of the topics relevant to our work, but as a result does not always have the same focus or clarity of some of the other sources.

Random matrix theory does not seek to describe the specific details of a system, but instead tries to model statistical properties of the system. RMT can, in principle, be applied to a vast range of types of system, but we will focus on it as applied to chaotic time-reversal-invariant systems. This is both the most commonly studied case and the one relevant to the physical systems we are interested in understanding. Some of these systems of interest will include a magnetic field, which breaks conventional time-reversal symmetry, but they still have the correct symmetry under time-reversal plus a geometric symmetry such as a reflection, so behave in the same way as time-reversal-symmetric systems. If all remaining geometric symmetries were removed from such a system with additional external fields (such

as radio-frequency radiation) it may show behaviour corresponding to a different symmetry class [297]. Such considerations, and further possible symmetry classes, are beyond our current investigations. Note that many texts give general results applicable to several symmetry classes in terms of a parameter usually labelled as β, for our case this should take the value $\beta = 1$.

The Gaussian Orthogonal Ensemble (GOE) is the standard RMT model for chaos in systems with time-reversal-invariant Hamiltonians. It is a set of real symmetric $N \times N$ matrices $\mathbf{H}$, with probability distribution

$$P(\mathbf{H}) = C \exp\left(-\frac{\mathrm{tr}(\mathbf{H}^2)}{2}\right), \tag{4.1.1}$$

where C is a normalisation constant. This can be rewritten as probability distributions for diagonal and off-diagonal elements

$$P_{ii}(H_{ii}) = C' \exp\left(-\frac{H_{ii}^2}{2}\right), \tag{4.1.2}$$

$$P_{ij}(H_{ij}) = C'' \exp\left(-H_{ij}^2\right), \tag{4.1.3}$$

respectively. The underlying assumptions that lead to this distribution are that all elements are uncorrelated and that the probability density does not change under orthogonal transformation, $P(\mathbf{O}^{\mathrm{T}}\mathbf{H}\mathbf{O}) = P(\mathbf{H})$ for all $N \times N$ orthogonal matrices $\mathbf{O}$. Note that alternative choices of scaling are sometimes used, but these do not materially change the results. It can be seen that the GOE has off-diagonal elements that are on the order of the spread of the diagonal elements and so for large N are much larger than the average separation of diagonal elements. In this way, the GOE can be seen as a limit of strong coupling.

It is instructive to immediately present two theoretical results about the eigenvalues of a GOE matrix, x_i for $i = 1, \ldots, N$. These are given for the usual limit $N \to \infty$, although in practice they are typically robust for even moderate values of $N \approx 10$ to 100. The overall distribution of the density of eigenvalues is

$$\rho(x) = \frac{1}{\pi}\sqrt{2N - x^2} \tag{4.1.4}$$

for $-\sqrt{2N} < x < \sqrt{2N}$ and $\rho(x) = 0$ otherwise [277]. This is known as Wigner's semicircle law. Note that both the width of the semicircle and the density at zero energy scale as $\sqrt{N}$, so are infinite in the limit $N \to \infty$. Either, but not both, of these divergences can be avoided by choosing a different scaling in eqs. (4.1.1) to (4.1.3), although we will not need to do so here. The full distribution for the set of eigenvalues x_i for $i = 1, \ldots, N$, can be written as

$$P(x_1, \ldots, x_N) = C''' \prod_{n=1}^{N} \exp\left(-\frac{x_n^2}{2}\right) \prod_{m<n} (x_n - x_m). \tag{4.1.5}$$

The terms $x_n - x_m$ show that the levels repel each other: there is a linearly vanishing probability of finding two levels close to each other. This is a key result for the GOE. This level repulsion is more clearly quantified in the nearest-neighbour spacings (NNS) s_i, which are given in units of the local mean spacing $D = 1/\rho$. These are distributed according the Wigner surmise

$$P(s) = \frac{\pi s}{2} \exp\left(-\frac{\pi s^2}{4}\right), \tag{4.1.6}$$

which is also known as the Wigner-Dyson distribution. Equation (4.1.6) is an approximation, but it is a good one and sufficient for most purposes; for more details see the discussion by Haake [295]. It should be noted that simply picking spacings randomly from eq. (4.1.6) and using them to generate a series of level positions does *not* correctly model a series of eigenvalues from the GOE as it neglects correlations beyond the nearest neighbour, which are very important in many circumstances.

The BGS conjecture links a chaotic system with the GOE, but it is important to appreciate that there are two different limiting cases for systems that are *not* chaotic. Some systems have highly structured energy-level patterns; the most extreme example of this is a harmonic oscillator, but a similar degree of regularity is exhibited by the levels of any single-channel system and by a rigid rotor. Other non-chaotic systems can have completely random (Poissonian) level patterns, without level repulsion. Such systems are often referred to in the chaos literature as *regular* systems, by analogy with the corresponding classical dynamics. To a spectroscopist,

however, the term regular implies structure and can lead to confusion. We therefore prefer to use the term *random* to describe systems with Poissonian level statistics.

For a system to be chaotic requires very large coupling matrix elements, as shown by eqs. (4.1.1) to (4.1.3). In the context of near-threshold bound states or low-energy collisions, this can occur when the anisotropic terms in the interaction are comparable in magnitude to the depth of the isotropic potential, which determines the spread of diagonal elements. As we will see, the highly anisotropic potentials of Li+CaH, Li+CaF and Yb+Yb* would seem to fulfil this: the majority of the potential well is contained in the anisotropic terms of many thousands of cm^{-1}. In contrast, the Er+Er and Dy+Dy potentials used in Ref. 128 have anisotropies around 10% of their well depths.[1] In this way it is perhaps not surprising that there are deviations from GOE predictions for Er+Er and Dy+Dy, whereas we might at first sight expect better agreement for Li+CaH, Li+CaF, and Yb+Yb*.

4.1.1 Statistical analysis of level sequences

To determine if a set of levels, either calculated or experimental, is well described by the GOE - and thus the system they came from is chaotic - we must analyse statistics calculated from the levels. A great many statistics are available to perform this analysis (see for example chapter 16 of Mehta's book [271]) but work on ultracold collisions so far has focused on two of the simplest quantities: the NNS distribution and the level number variance; we also analyse these two quantities.

Such statistical analysis would usually be performed on a series of levels in energy with the Hamiltonian defining the system fixed. However, the underlying RMT concerns distributions taken over an ensemble of different Hamiltonians. The assumption that the distributions over energy (for a single Hamiltonian) are the same as those over Hamiltonians is known as spectral ergodicity [299]; this is a known property of RMT [299] but not necessarily of real systems. In recent ultracold collision studies [127, 128, 294], statistical analysis was performed on a series of zero-energy

[1] The anisotropy considered in Ref. 128 is based entirely on dispersion effects [298]. The spread of dispersion coefficients for different potential curves of Er-Er is 10% of their mean value, and that for Dy-Dy is 9% of their mean value.

resonance positions as magnetic field was varied. Such experiments sample many different Hamiltonians - albeit in a much more limited and structured way than RMT - and so may provide a more authentic comparison with RMT than an energy spectrum would, even if it was available. In place of the spectral ergodicity hypothesis, we now need only to assume that different Hamiltonians are sampled in a representative way. We will also consider zero-energy resonances as a potential scaling factor λ is varied. This also varies the Hamiltonian but without the theoretical complexities or computational expense that make calculations including magnetic fields prohibitively difficult for some systems. In this respect λ may be considered a poor man's magnetic field.

For the statistical analysis of the levels we follow the methods of Mehta [271] and Guhr et al. [272]. We denote the series of n experimental or calculated level positions as X_i for $i = 1, \ldots, n$, where X would conventionally represent energy but here can also represent magnetic field or λ. Note that we observe only a fraction of the total number of levels in the system, so $n \ll N$. First we 'unfold' the level positions to remove any systematic variation in the density and to set the levels on a dimensionless scale with unit mean spacing. To do this we construct the cumulative spectral function, also known as the staircase function,

$$S(X) = \sum_{i=1}^{n} \Theta(X - X_i), \tag{4.1.7}$$

where $\Theta(x)$ is the Heaviside step function. We then fit a smooth function, $\xi(X)$, to $S(X)$. In the systems we analyse here, fitting with a quadratic function is sufficient as the original staircase is already very nearly linear. The unfolded positions are then given as $\xi_i = \xi(X_i)$.[2] The nearest-neighbour spacings (NNS) are given by $s_i = \xi_{i+1} - \xi_i$ for $i = 1, \ldots, n-1$.

As previously stated, the NNSs for a chaotic system are expected to follow the Wigner-Dyson distribution, eq. (4.1.6). In contrast, if the system is random the

[2]In general, $S(X)$ can be decomposed as $S(X) = \xi(X) + S_{\text{fl}}(X)$, where $\xi(X)$ is a smooth part given by the cumulative mean level density, and $S_{\text{fl}}(X)$ describes fluctuations about this average. The unfolding procedure rescales the staircase function $S(X) \to S(\xi) = \xi + S_{\text{fl}}(\xi)$, i.e., to unit average density, isolating the fluctuating part that is of interest.

NNSs will follow a Poissonian distribution

$$P_{\mathrm{P}}(s) = \exp(-s)\,. \tag{4.1.8}$$

If the system is structured, there is no generic NNS distribution we expect it to follow. For a harmonic oscillator the NNS is simply a delta function, $P_{\mathrm{HO}}(s) = \delta(s-1)$, but more complicated forms of structure will lead to other distributions. For example, a multi-dimensional harmonic oscillators typically has an NNS distribution that is more strongly peaked than the Wigner-Dyson distribution [300]. However, we will not investigate this further but instead simply focus on the chaotic and Poissonian cases. Qualitative impressions of the statistics can be given by histograms of the spacings, but it is also desirable to have quantitative measures.

Real systems do not exactly follow either $P_{\mathrm{WD}}(s)$ or $P_{\mathrm{P}}(s)$. There are various formulas for interpolating between the two [301–303]. The most commonly used of these is the Brody distribution [301],

$$P_{\mathrm{B}}^{(\eta)}(s) = c_\eta(\eta+1)s^\eta \exp\left(-c_\eta s^{\eta+1}\right), \tag{4.1.9}$$

where

$$c_\eta = \left[\Gamma\left(\frac{\eta+2}{\eta+1}\right)\right]^{\eta+1}, \tag{4.1.10}$$

and η is known as the Brody parameter. Despite its lack of theoretical foundation[3] this NNS distribution has remained popular and widely used because of its simplicity and versatility; it is the one that has been used in recent publications in ultracold physics and is the one that we use in this chapter.

We obtain a value of η for a set of spacings by maximum likelihood estimation [304]. We maximise the likelihood function,

$$L(\eta) = \prod_i P_{\mathrm{B}}^{(\eta)}(s_i), \tag{4.1.11}$$

[3]In particular, the fractional power behaviour as $s \to 0$ runs contrary to typical arguments which suggest the behaviour should always be linear in this limit and it is the derivative that should vary.

to find η. As a matter of computational practicality, we actually calculate and maximise the logarithm of the likelihood

$$l(\eta) = \ln L(\eta) = \sum_i \ln P_{\mathrm{B}}^{(\eta)}(s_i). \tag{4.1.12}$$

The uncertainty of η is

$$\sigma = \left(-\frac{d^2}{d\eta^2} \ln L(\eta) \right)^{-\frac{1}{2}}. \tag{4.1.13}$$

The fitted value for the Brody parameter quantifies the visual information seen in NNS histograms: Poisson statistics yield $\eta = 0$ and chaotic statistics yield $\eta = 1$.

The NNS distribution by nature captures information only about short-range correlations but chaos is predicted to have effects over long ranges as well [271, 272]. Therefore we also consider the level number variance

$$\Sigma^2(\Delta\xi) = \langle \hat{S}^2(\Delta\xi, \xi) \rangle - \langle \hat{S}(\Delta\xi, \xi) \rangle^2, \tag{4.1.14}$$

where $\hat{S}(\Delta\xi, \xi)$ counts the number of levels in the interval $[\xi, \xi + \Delta\xi]$ and the average is taken over the starting values ξ. This characterises the spread in the numbers of levels in intervals of length $\Delta\xi$ and probes long-range correlations. For the GOE, it rises logarithmically as

$$\Sigma^2(\Delta\xi) = 2\pi^{-2} \left[\ln(2\pi\Delta\xi) + \gamma + 1 - \frac{\pi^2}{8} \right] + \mathcal{O}(\Delta\xi^{-1}), \tag{4.1.15}$$

where $\gamma = 0.5772\ldots$ is Euler's constant; for Poissonian statistics it rises linearly as $\Sigma^2(\Delta\xi) = \Delta\xi$; and for a regular system it will oscillate around a constant value. While there have been some attempts to interpolate between Poissonian and GOE behaviours of the number variance, there is no direct analogue to the Brody distribution so we restrict ourselves to qualitative statements about the transition between the two limiting behaviours.

4.2 Li+CaH and Li+CaF

Atom+diatom systems provide excellent prototype systems to investigate chaotic behaviour. If vibrational excitation and electron spins are neglected, the systems have two internal degrees of freedom; this is the minimum for classical chaos and probably also for a quantum system to follow the predictions of RMT [287]. The required formalisms [155, 223, 305] and programs to perform the necessary calculations [171, 172] are well developed, readily available, and relatively straightforward. There are many atom+diatom systems that are of interest at low temperatures, including Rb+KRb [145], N+NH [105] and Li+CaH [306]. In particular, there is good progress towards obtaining CaH or CaF at cold and ultracold temperatures by buffer-gas cooling [59, 62], Stark deceleration [307], laser cooling [115, 116], or sympathetic cooling [113], and considerable interest in investigating their collisional properties with Li or other alkali metals [107, 146, 308]. Therefore, the first systems we investigate for signatures of chaos are Li+CaH and Li+CaF.

4.2.1 Potential energy surface and bound-state calculations

The interaction between Li(^{2}S) and CaH/CaF($^2\Sigma$) gives rise to singlet and triplet electronic states of ^{1}A′ and ^{3}A′ symmetries. For sympathetic cooling in an external magnetic field, Li and CaH/CaF would be prepared in magnetically trappable spin-stretched states, in which all the quantum numbers for the projections of angular momentum onto the magnetic field direction have their maximum values. Such collisions occur primarily on the potential energy surface for the ^{3}A′ state, so we use this surface for our calculations. For Li+CaH, we use the *ab initio* ^{3}A′ interaction potential calculated by Tscherbul et al. [107], and for Li+CaF we use the surface calculated in [130].[4] For both systems, the diatom bond length is held at its equilibrium value throughout.

The resulting ^{3}A′ potential energy surfaces are shown in fig. 4.1. It may be seen that they are strongly anisotropic, with a deep well (7063 cm^{-1} for CaH and 7258 cm^{-1} for CaF) at slightly bent Li-X-Ca geometries. The overall behaviour of the

[4]The potential in Ref. 130 was calculated by M. Morita.

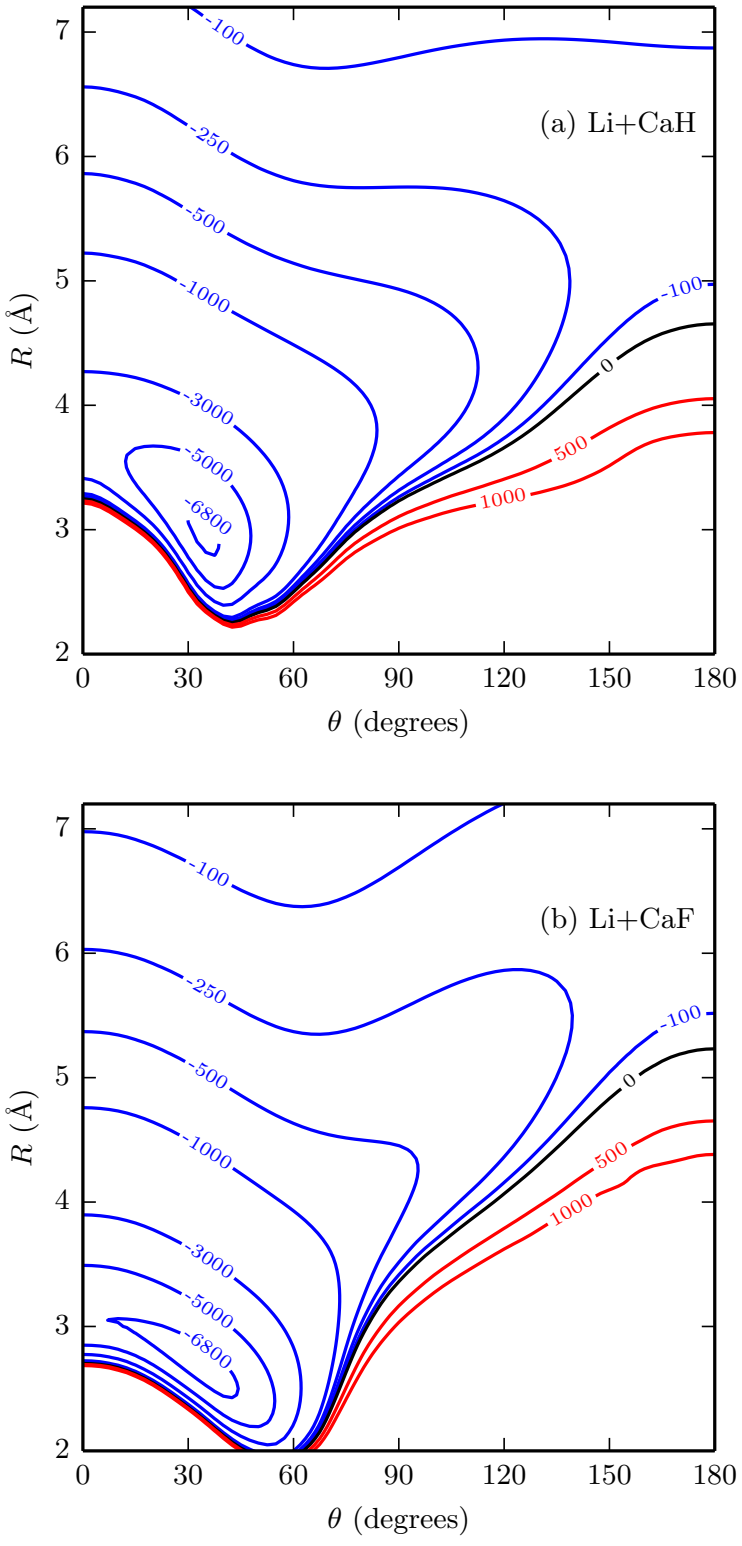

Figure 4.1: The *ab initio* ^{3}A′ interaction potential for (a) Li+CaH and (b) Li+CaF. Contours are labeled in cm^{-1}. R is the distance from the Li atom to the centre of mass of the diatom and θ is the angle between the diatom bond and the inter-particle vector, $\theta = 0°$ corresponds to the Li-H(F)-Ca geometry. The diatom bond length is fixed at its equilibrium value.

two surfaces is similar, though the Li+CaF interaction is slightly stronger and more anisotropic.

As previously explained we will focus on zero-energy bound states and resonances as a function of potential scaling parameter λ due to the difficulties associated with performing calculations on Li+CaH and Li+CaF in magnetic fields. The calculations themselves are the same as those performed in section 2.2.3, except that we now focus on bound state calculations rather than scattering calculations. We have modified the program FIELD [174] to locate bound states as a function of λ rather than an applied electromagnetic field. We also use BOUND [172] for calculations of bound states away from threshold. Since the diatom rotational constants, b, are very small ($b_{\mathrm{CaH}} = 4.2766$ cm^{-1} [107] and $b_{\mathrm{CaF}} = 0.339$ cm^{-1} [309]), we need very large basis sets of diatom rotational functions for convergence. Unless otherwise stated, we use basis functions with rotational quantum numbers up to $j_{\mathrm{max}} = 55$ and 120 for CaH and CaF, respectively.

The real systems include diatom vibrations and electron and nuclear spins. The harmonic frequencies for CaH and CaF are 1298 and 589 cm^{-1}, respectively. Since the well depth is significantly larger than this, there will be states from channels involving diatom vibrational excitation in the region around threshold, although they may be sparse in energy. These are neglected in our calculations. There will also be considerable extra density of levels due to the spin multiplicities, although it is not clear whether the spins will be fully involved in any chaotic dynamics or if they will be spectators. The present results are therefore for model systems, based on the real systems but not taking account of their full complexity.

4.2.2 Results: Li+CaH

We begin by analysing Li+CaH for total angular momentum $J = 0$ and $0.7 \leq \lambda \leq 1.6$. Figure 4.2 shows the calculated level positions for $J = 0$, the staircase function, a histogram of the NNS distribution, and the level number variance. This serves as an example of the statistical preparation and fitting described in section 4.1.1; all further sequences in this section and section 4.3 were analysed in the same way. The NNS distribution clearly shows the key features of a Wigner-Dyson distribution:

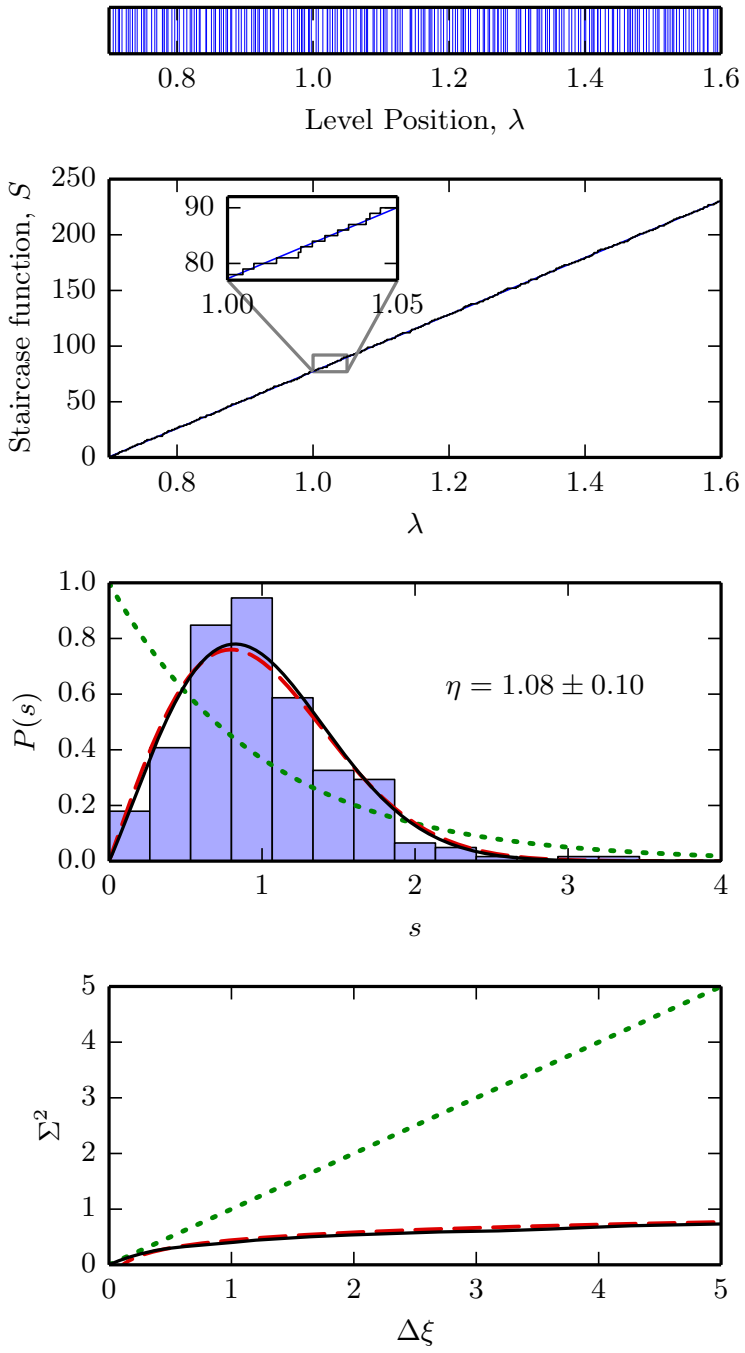

Figure 4.2: Statistical analysis of calculated levels of Li+CaH ($J = 0$, $0.7 \leq \lambda \leq 1.6$). From top: Level positions in λ; Staircase function, with fitted smooth function $\xi(X)$ in blue; Histogram of NNS distribution, green dotted and red dashed lines are Poisson and Wigner-Dyson distributions respectively, black line is Brody distribution using the fitted η; and level number variance, green dotted and red dashed lines are Poisson and GOE predictions respectively.

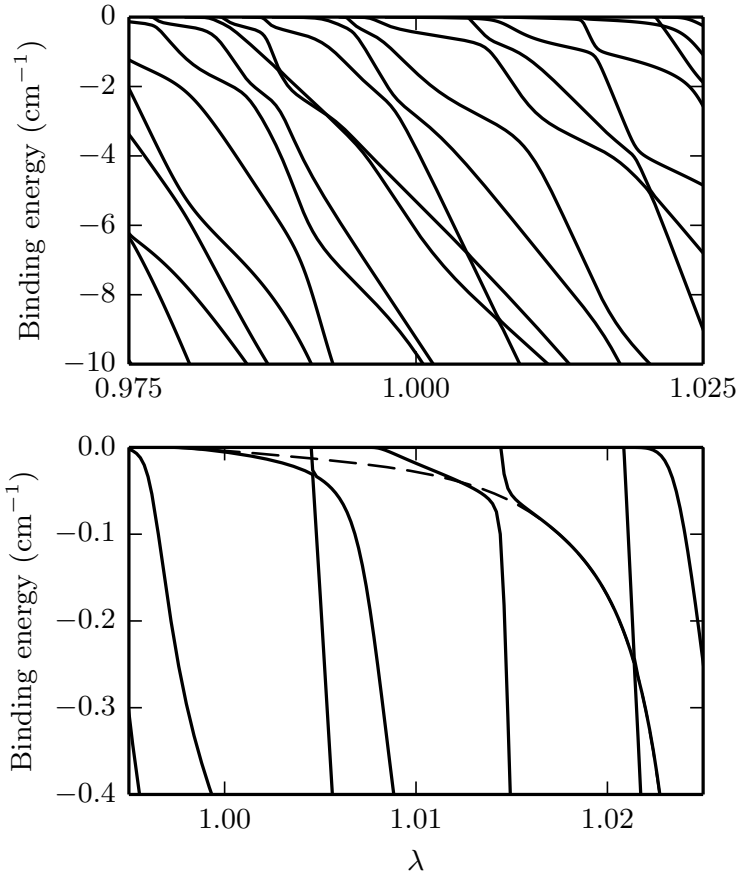

Figure 4.3: Near-threshold bound states as a function of λ for Li+CaH ($J = 0$). The bottom panel shows an expanded view with a state approaching threshold, crossed by several steeper states. The dashed line has been added to follow this state through the avoided crossings and help guide the eye.

linear repulsion at small spacing and a tail that dies off rapidly. The fitted Brody parameter, $\eta = 1.08 \pm 0.10$, is consistent with GOE predictions, and the level number variance also follows the GOE prediction almost exactly. This Brody parameter may be compared with values in the region 0.5 to 0.7 found for Er+Er and Dy+Dy [128]. Li+CaH thus shows the clearest evidence yet found of chaotic behaviour in a realistic ultracold collisions.

Figure 4.3 shows near-threshold bound states for $J = 0$ for a small range of λ. The top panel shows bound states to a depth of 10 cm^{-1}, where the levels interact and undergo avoided crossings with a wide variety of strengths. The lower panel is an expanded view showing a state with a long tail curving towards threshold. This state is crossed by several steeper states with avoided crossings of varying

widths, including a crossing around $\lambda = 1.007$ that appears quite broad on this scale. Bound states with these features have been observed experimentally in Dy+Dy [269], although in our case the state is much more deeply bound (by a factor of about 100 in the natural units defined by the asymptotic van der Waals interaction [169]). It is not a 'halo' state because its wave function is mostly inside the outer classical turning point [33], but its presence in Li+CaH demonstrates that states with clear threshold behaviour can persist across several avoided crossings even in a system with statistics close to the GOE limit.

Next we consider higher values of J, which correspond to higher partial waves at the lowest rotational threshold. Figure 4.4 shows histograms of NNS for J=1, 3, and 8. These notably do *not* show the linear level repulsion at small spacings expected for complete chaos. Instead there appears to be a finite probability of zero spacing. The corresponding Brody parameters are in the region of 0.4. Although at first sight this suggests a substantially reduced degree of chaos compared to $J = 0$, such a distribution can also occur for two overlapping but non-interacting chaotic spectra [278, 302]. This suggests that there is some form of symmetry or good quantum number present in the system. However, we have already taken account of all rigorous symmetries, so the quantity concerned must be only *approximately* conserved. On a finer scale, the NNS distribution does indeed show some limited level repulsion.

The nearly conserved quantum number can be understood in the body-fixed reference frame, rather than the space-fixed frame that we use in the coupled-channel calculations. It is the projection of the total angular momentum J (or equivalently the diatom rotation j) onto the intermolecular axis, which is well known in studies of atom-diatom van der Waals complexes [223] and is given the symbol K. It can take values from $-J$ to $+J$ in integer steps. Blocks of the Hamiltonian with different K are coupled only by Coriolis terms in the body-frame representation of the centrifugal motion; these Coriolis terms are very small compared to the potential anisotropy in the well region, so the Hamiltonian can be considered to be nearly block-diagonal with blocks labeled by $|K|$ and parity.

It is possible to carry out coupled-channel calculations in the body-fixed frame,

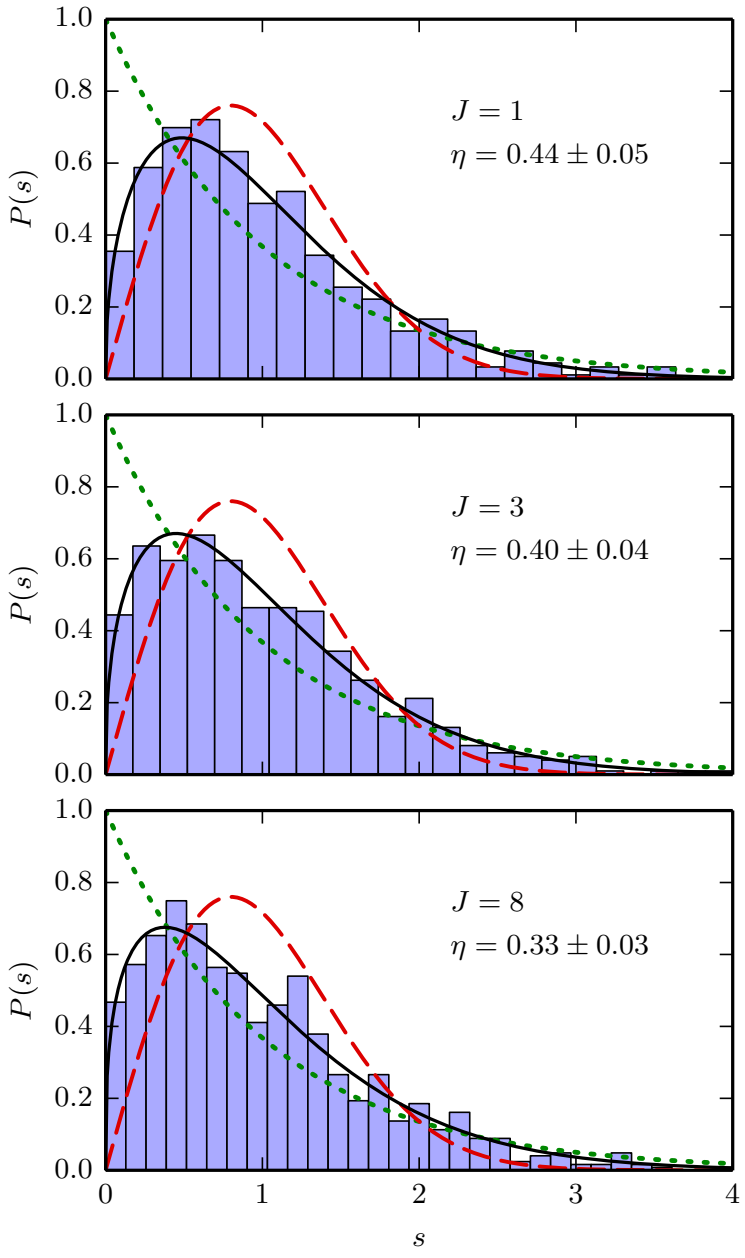

Figure 4.4: Nearest-neighbour spacing distributions for Li+CaH: $J = 1$ ($0.5 \leq \lambda \leq 1.5$), $J = 3$ ($0.8 \leq \lambda \leq 1.4$), and $J = 8$ ($0.8 \leq \lambda \leq 1.3$). Lines are as in fig. 4.2.

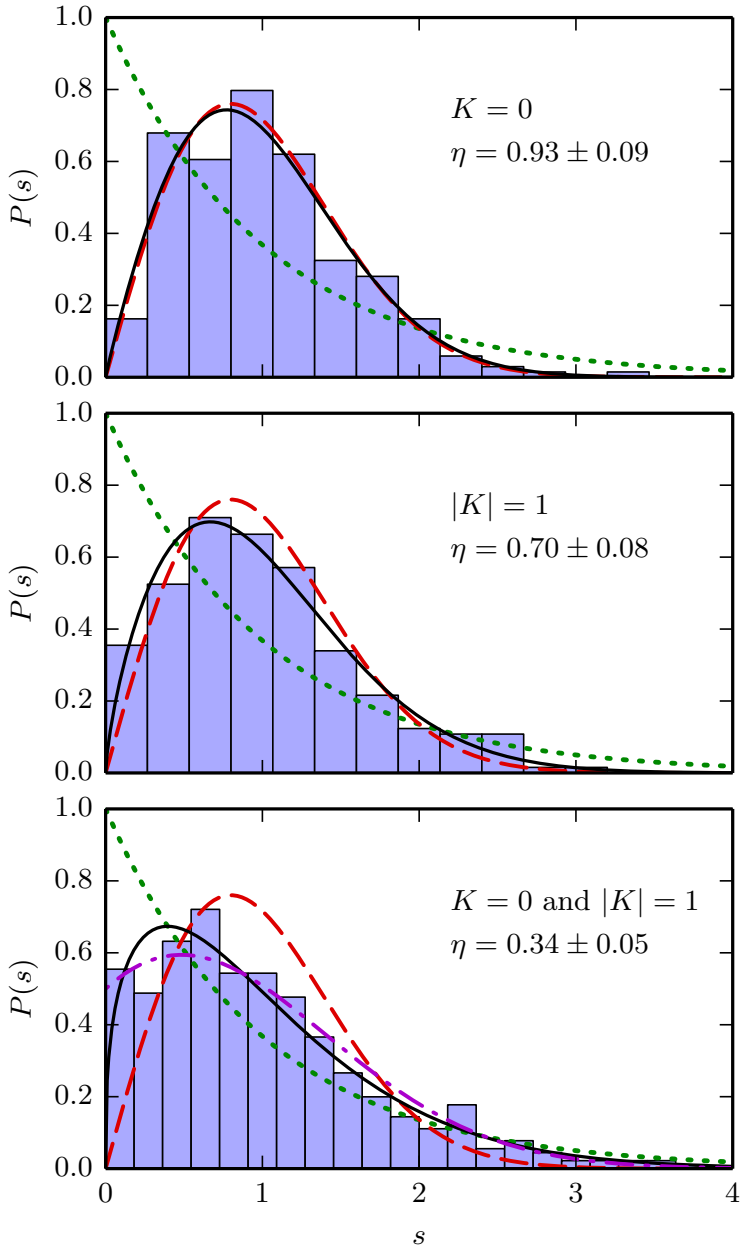

Figure 4.5: NNS distributions for Li+CaH ($J = 1$, $0.5 \leq \lambda \leq 1.5$) using the helicity-decoupling approximation. $K = 0$; $|K| = 1$; $K = 0$ and $|K| = 1$. Lines are as in fig. 4.2, magenta dash-dot line in the bottom panel is the predicted NNS distribution for two overlapping GOEs.

neglecting the Coriolis terms off-diagonal in K. This makes the problem block-diagonal and is known as helicity decoupling; it is often an effective technique for calculations of atom-diatom bound states [223]. Figure 4.5(a) and (b) show NNS distributions for the separate $K = 0$ and $|K| = 1$ blocks. There is no further hidden symmetry and so the NNS distributions are once again close to the Wigner-Dyson limit. Figure 4.5(c) shows the statistics for the superposition of the two individual level sequences. This last case is close to that of two GOE level sequences which overlap but are not coupled. The resulting NNS distribution can be obtained from equation (3.69) of [272], and is also shown in fig. 4.5(c). It differs from the Wigner-Dyson distribution most obviously in that it does not vanish at zero spacing. It is in good agreement with the results from helicity decoupling calculations and explains the qualitative behaviour of the $J \neq 0$ distributions in fig. 4.4.

The remaining differences between fig. 4.4(a) and fig. 4.5(c) are due to the Coriolis terms. The quantitative effect of these terms on the statistics is beyond the scope of our work here, but it is nevertheless informative to look at the pattern of bound states near threshold. Figure 4.6 shows bound states for $J = 1$ within 10 cm^{-1} of threshold for a small range of λ, both from a full calculation and within the helicity decoupling approximation. The $K = 0$ levels for $J = 1$ are only slightly shifted from the levels for $J = 0$ (top panel of fig. 4.3). The $|K| = 1$ levels are quite different but show the same qualitative features of many avoided crossings of a wide variety of strengths. However, in the helicity decoupling approximation, levels with one value of $|K|$ do not interact with those of different $|K|$; this gives rise to a large number of true crossings, producing an NNS distribution with finite probability at zero spacing. In the full calculation, which takes account of the Coriolis coupling between the blocks, the overall pattern of levels is similar but there are now narrow avoided crossings between levels of different $|K|$. These are typically much narrower than those between levels of the same $|K|$. This confirms our picture of a nearly conserved quantum number, with only weak coupling between states of different $|K|$. This is closely related to the relationship between the scattering in $L = 0$ and 1 that was seen for this system in section 2.2.3.

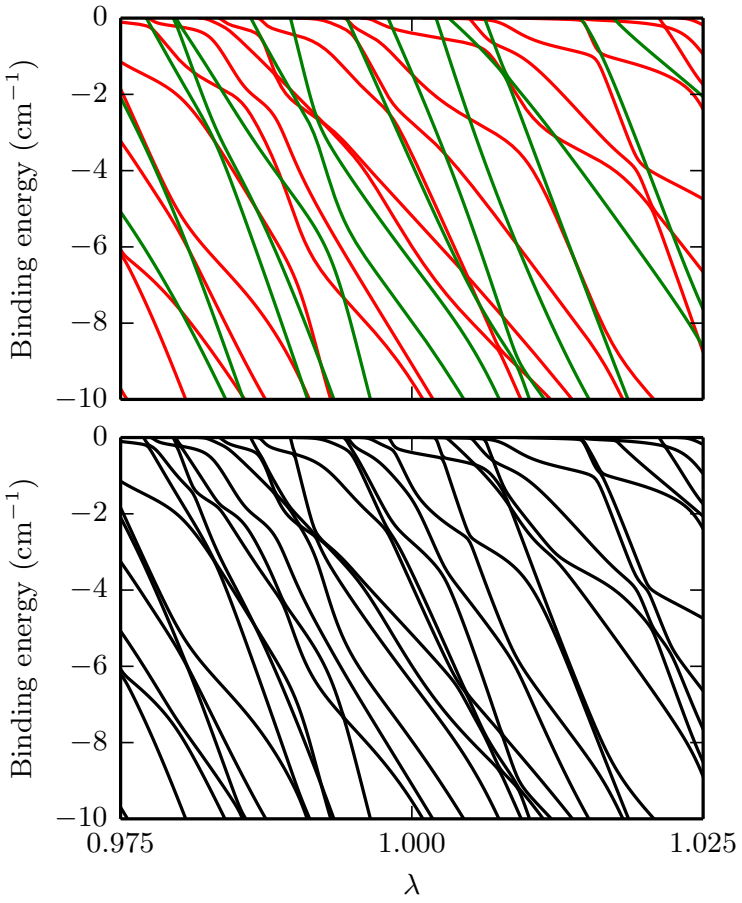

Figure 4.6: Near-threshold bound states as a function of λ for Li+CaH ($J = 1$): using the helicity-decoupling approximation (top; red: $K = 0$, green: $|K| = 1$); and full calculation (bottom).

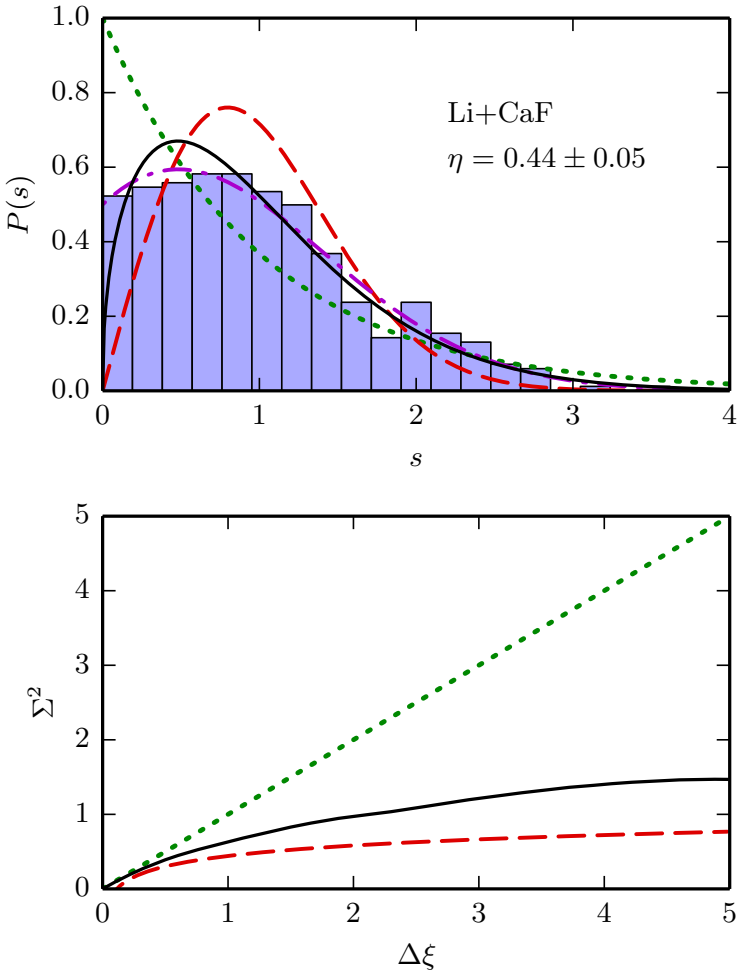

Figure 4.7: Calculated statistics for Li+CaF ($J = 0$, $0.8 \leq \lambda \leq 1.4$): NNS distribution, and level number variance. Lines are as in previous figures.

4.2.3 Results: Li+CaF

The second system we consider is Li+CaF. The rotational constant for CaF is about 13 times smaller than that for CaH, while the potential surface is quite similar. The ratio of the anisotropy to b is thus significantly greater for CaF than for CaH. This stronger effective coupling might be expected to give equal or greater amounts of chaos for Li+CaF compared to Li+CaH.

We have performed coupled-channel calculations for Li+CaF ($J = 0$) using the same methods as for Li+CaH, but with a larger basis set because of the smaller value of b. Figure 4.7 shows the resulting level statistics. Remarkably, the NNS distribution does not appear to show level repulsion, even for $J = 0$, but neither

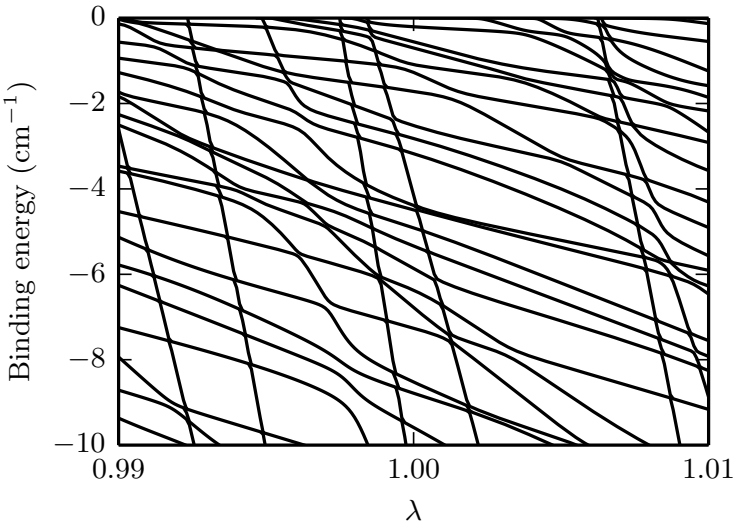

Figure 4.8: Near-threshold bound states as a function of λ for Li+CaF ($J = 0$).

does it resemble a Poisson distribution; the fitted Brody parameter is only 0.44. Once again the distribution bears a close resemblance to the case of two overlapping but non-interacting GOE spectra as discussed for the helicity-decoupled $J = 1$ case for Li+CaH. This again hints at the possibility of some unexpected partially good quantum number, but in this $J = 0$ case it cannot be the projection $|K|$. The level number variance for Li+CaF (J=0) is also some way from the GOE prediction, although it does level off at high spacings, in contrast to that in other near-chaotic examples [128, 294].

Figure 4.8 shows the binding energies of near-threshold levels for Li+CaF ($J = 0$) as a function of λ. It may be seen that some bound states have very steep energy gradients with respect to λ and that these states interact weakly with those with shallower gradients.[5] In this respect the pattern shows a clear systematic difference from that observed for Li+CaH (fig. 4.3), where all $J = 0$ states appeared significantly coupled and the levels could not easily be separated into classes.

There has been a great deal of work on the energy levels of atom-diatom systems, largely aimed at understanding the dynamics of van der Waals complexes [223]. For low anisotropies, the diatomic molecule executes hindered rotation in the com-

[5]Although visually there may seem to be relatively few steep states for Li+CaF, counting them with respect to λ at fixed energy reveals that approximately 1/3 of the levels are of this type.

plex, and the resulting internal rotation is only weakly coupled to the intermolecular stretching motion. However, when the effective anisotropy is comparable to or larger than the diatom rotational constant, there is significant mixing of diatom rotational states. As the anisotropy increases further, the internal rotation is transformed into a bending vibration of the triatomic molecule. Correlation diagrams showing how this transition occurs have been given in ref. [223] for complexes with both linear and non-linear equilibrium geometries. The low-lying levels of a non-linear species such as Li-CaH or Li-CaF eventually execute low-amplitude bending vibrations about their non-linear equilibrium. The degree of mixing between bending and stretching degrees of freedom typically depends on their relative frequencies: if the bending is either much faster or much slower than the stretching then the modes can be separated in a Born-Oppenheimer sense [310–312], but if the frequencies are comparable then they are strongly mixed.

The situation is more complicated for highly excited states, such as the near-dissociation states that give rise to Feshbach resonances in the present work. Some highly excited states have unstructured nodal patterns that fill the energetically accessible space, but there are others with simple nodal patterns that sample restricted regions of space [313–316]. However, the paths along which such states are localized may be complicated ones that do not correspond to obvious quantum numbers. Because of this, it may be difficult to identify the specific nearly conserved quantity that divides the states in fig. 4.8 into separate classes. Nevertheless, the level statistics appear to indicate that such a quantity exists.

4.2.4 Results: Variable rotational constant

To understand better the puzzling difference between Li+CaH and Li+CaF, we attempt to interpolate between our two systems and extrapolate beyond them. Since the two potential energy surfaces are so similar, we use the surface and reduced mass for Li+CaH throughout this section, and vary the rotational constant. We increase the number of rotational basis functions from 55 to 350 as b decreases from 100 to 0.01 cm^{-1} to obtain converged level positions.

Figure 4.9 shows the fitted Brody parameter as a function of rotational constant.

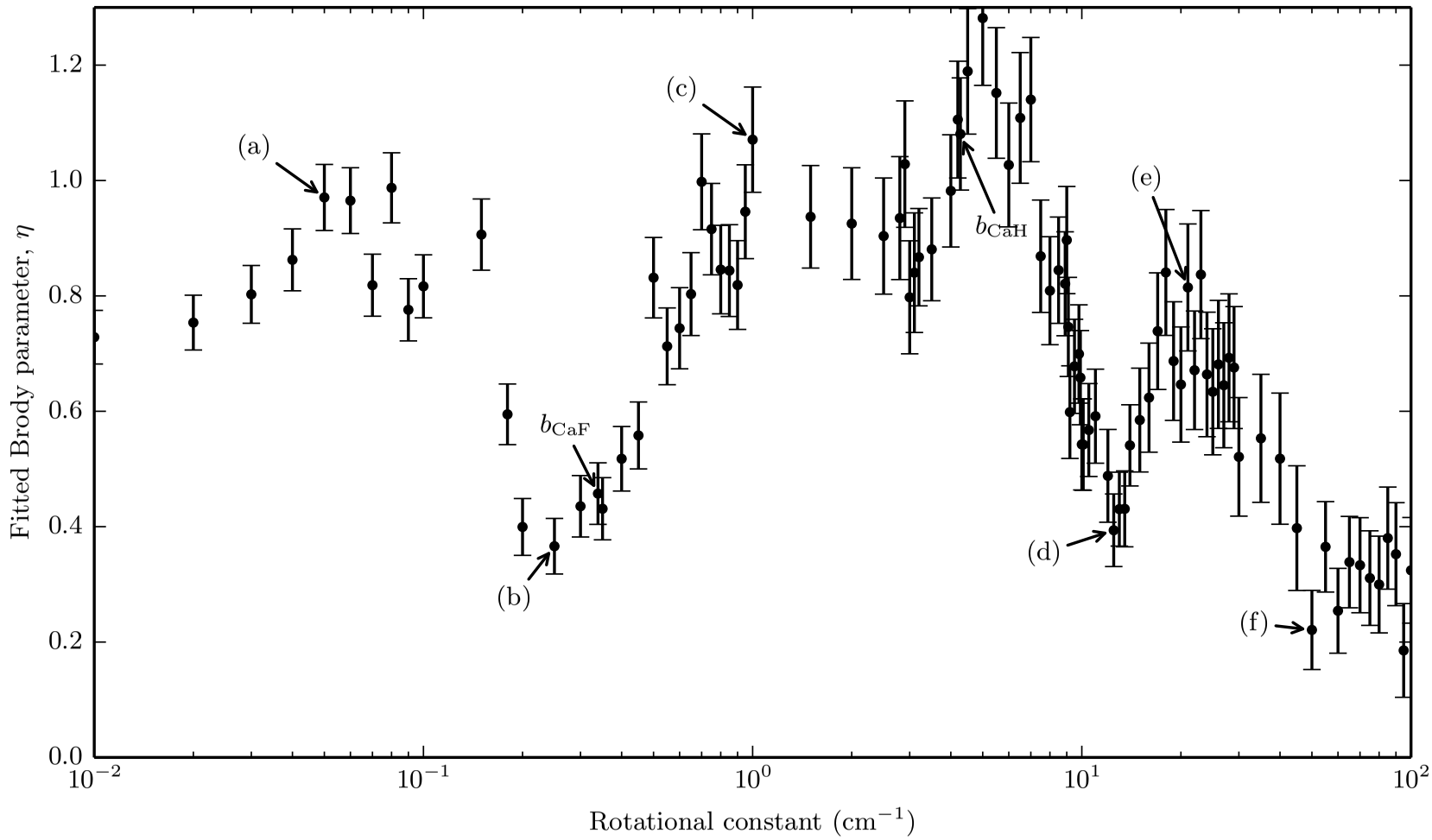

Figure 4.9: Rotational constant dependence of fitted Brody parameter for Li+CaH ($J = 0$). Labeled points are: (a) 0.05, (b) 0.25, (c) 1.0, (d) 12.5, (e) 21, (f) 50 cm^{-1}. b_{CaF} and b_{CaH} are also indicated.

This shows an astonishing structure. It can be seen that b_{CaH} lies in a relatively wide region from 0.7 to 7 cm^{-1} where η is near unity, so that the systems can be said to be chaotic. Towards lower rotational constant the fitted Brody parameter falls sharply to about 0.4 in the region between 0.2 and 0.4 cm^{-1} – in which b_{CaF} lies – but it then rises rapidly back to values near unity for $0.05\ \mathrm{cm}^{-1} < b < 0.08\ \mathrm{cm}^{-1}$ before beginning to fall slowly again. At higher values of b, there is another steep and narrow trough centred around 12 cm^{-1}, followed by a steady decrease towards zero as the angular and radial motions become increasingly uncoupled.

Figure 4.10 shows statistics for sample values of the rotational constant b. Those for the lowest value, $b = 0.05\ \mathrm{cm}^{-1}$ [fig. 4.10(a)] show almost perfect agreement with the GOE predictions for both NNS distribution and level number variance; the fitted Brody parameter is $\eta = 0.97 \pm 0.06$. The second value, $b = 0.25\ \mathrm{cm}^{-1}$, is close to $b_{\mathrm{CaF}} = 0.339\ \mathrm{cm}^{-1}$, but the NNS distribution [fig. 4.10(b)] differs from that seen for Li+CaF in fig. 4.7(a), with noticeably more level repulsion despite a lower η. $b = 1.0$ cm^{-1} [fig. 4.10(c)] is within the same region of high η as b_{CaH} and also shows clear signs of chaos. $b = 12.5\ \mathrm{cm}^{-1}$ [fig. 4.10(d)] is located in a narrow trough of low η and the statistics appear to be similar to case (b). $b = 21\ \mathrm{cm}^{-1}$ [fig. 4.10(e)] is located above the trough in η; the Brody parameter is only 0.8 but the statistics show all the qualitative features expected of a chaotic system. The statistics for $b = 50\ \mathrm{cm}^{-1}$ [fig. 4.10(f)] show an NNS distribution that is close to Poissonian ($\eta = 0.16$) because the rotational constant is large enough for the rotational and stretching motions to be significantly decoupled and the conditions for chaos no longer exist. However, the number variance does not rise linearly as in the Poisson case; instead it reaches a peak and turns downwards. The inset shows that, on a larger scale, this is the first in a complex series of oscillations, which we attribute to the onset of regularity and do not interpret further in this paper.

The presence of oscillations in the Brody parameter in fig. 4.9 is puzzling. The argument given in section 4.2.3 above would predict a single maximum in the Brody parameter when the effective bending and stretching frequencies are comparable for near-threshold states, dropping off when the frequencies are very different. Figure 4.9 does appear to show such a maximum, but the argument does not explain the

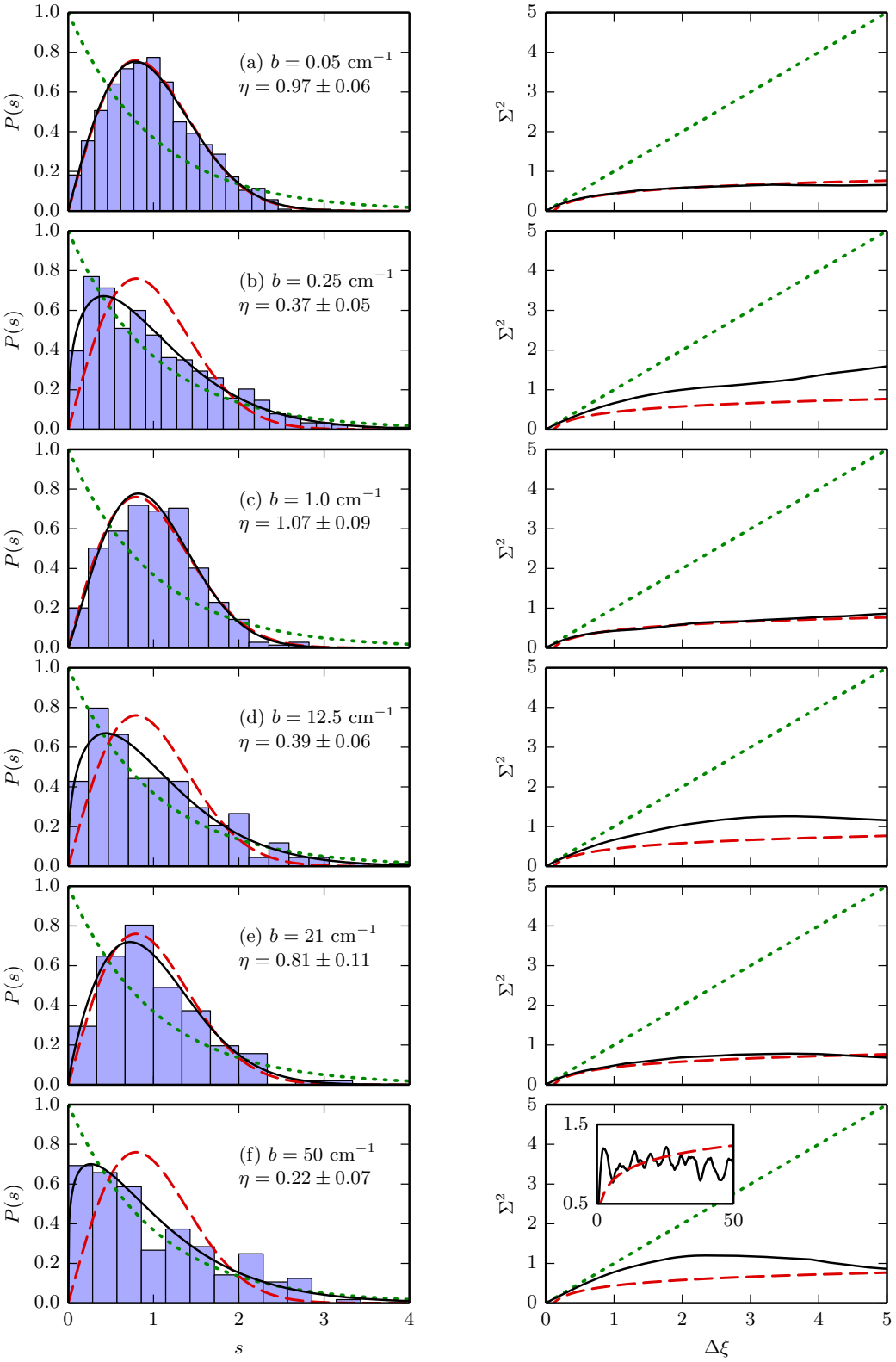

Figure 4.10: Examples of the NNS distribution (left) for values of rotational constant highlighted in fig. 4.9, and the corresponding level number variance (right). Lines are as in previous figures.

deep minima that seem to be present either side of it. It is possible that the flanking maxima correspond to effective bending frequencies that match the stretching frequencies for different stretching states, or that are rational multiples of effective stretching frequencies.

4.3 $Yb(^1S_0)+Yb^*(^3P_2)$

There are numerous obstacles to performing realistic calculations on Er+Er and Dy+Dy. Obtaining sensible *ab initio* potentials for the large number of short-range states is currently not feasible; the high-spin nature of the atoms makes the required angular momentum algebra challenging, although should not present any fundamental problems; and the large number of potentials together with the large number of partial waves required [127] makes the number of channels for a calculation very large and may make coupled-channel calculations numerically intractable. Therefore, we choose a different atom+atom system, which shares some features with the erbium and dysprosium systems, but is very much simpler to perform calculations on.

The calculations and analysis in this section were principally done by C. L. Vaillant and D. G. Green.

4.3.1 Calculation of near-threshold bound states

$Yb(^1S_0)+Yb(^3P_2)$ is a particularly simple case of atom-atom interactions with strong anisotropy. In a spin-orbit-free representation, there are only four electronic states arising from the interaction, of which two ($^3\Sigma_g$ and $^3\Pi_g$) contribute to the symmetry block which includes s-wave scattering. When spin-orbit coupling is included, there are three Born-Oppenheimer curves that correlate with the $^1S_0+^3P_2$ threshold. This contrasts with 49 and 81 curves for the $^3H_6$ and $^5I_8$ states of the submerged f-shell atoms Er and Dy.

The Schrödinger equation is solved using the atom-atom Hamiltonian described in Ref. 318, except that in the present case $Yb(^3P_j)$ interacts with a structureless partner. The interaction potential $\hat{V}$ can be written as the Legendre expansion

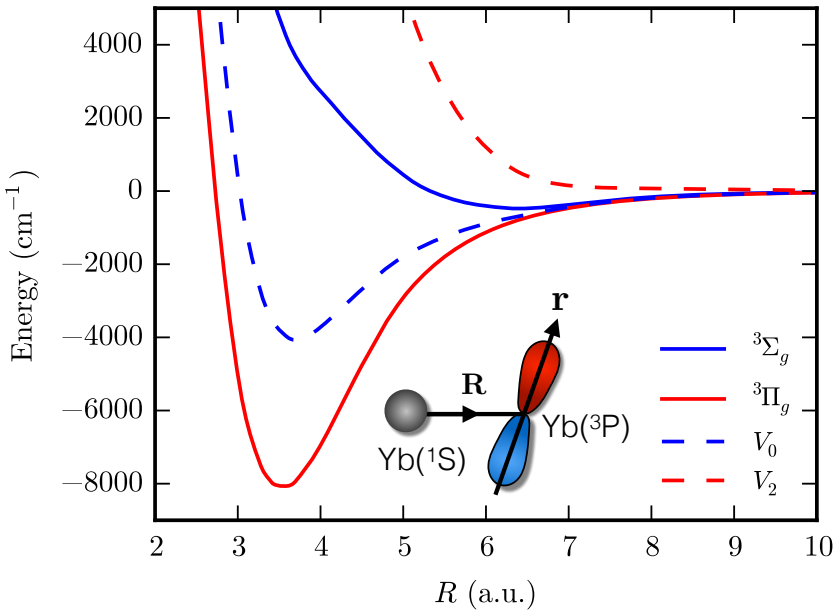

Figure 4.11: Interatomic potentials for Yb(^{1}S)+Yb(^{3}P). Σ and Π Born-Oppenheimer potentials calculated from [317] (red lines). Isotropic $V_0(R)$ and anisotropic $V_2(R)$ Legendre expansion coefficients, as described in the text (blue lines).

$\hat{V}(\mathbf{R}, \hat{\mathbf{r}}) = \sum_{k=0,2} V_k(R) P_k\left(\hat{\mathbf{R}} \cdot \hat{\mathbf{r}}\right)$ [319, 320], where $\mathbf{R}$ is the internuclear separation vector and $\hat{\mathbf{r}}$ is a unit vector describing the orientation of the occupied Yb 6p orbital. The expansion coefficients are $V_0 = (V_\Sigma + 2V_\Pi)/3$ and $V_2 = 5(V_\Sigma - V_\Pi)/3$ [321, 322], where V_Σ and V_Π are the $^3\Sigma_g$ and $^3\Pi_g$ Born-Oppenheimer potentials. Figure 4.11 shows the $^3\Sigma_g$ and $^3\Pi_g$ potentials of Ref. [317], together with V_0 and V_2. Physically, the anisotropy is due to the 6p valence electron of [Xe]4f^{14}6s6pYb(^{3}P). As a result, the anisotropy in this system is much larger than in the Er+Er and Dy+Dy systems, which involve f-shell electrons submerged beneath a closed 6s shell [127, 128]. The potentials are extrapolated at long range with the dispersion form $-C_6/R^6$ [323], using calculated dispersion coefficients of 2999 and 2649 $E_\mathrm{h} a_0^6$ [324] for the $^3\Sigma_g$ and $^3\Pi_g$ states respectively. The spin-orbit interaction is taken to be independent of $\mathbf{R}$, with a coupling constant that gives the correct splitting between the ^{3}P$_2$ and ^{3}P$_1$ states [325].

At zero field the total angular momentum is a good quantum number. In the absence of a field, the space-fixed total angular momentum basis set $|(ls)jLJM_J\rangle$ [320] is used. Here the atomic orbital and spin angular momenta l and s couple to give a resultant j, which then couples to the end-over-end angular momentum

L to give the total angular momentum J. At finite magnetic field, the partially uncoupled basis set $|(ls)jm_jLM_L\rangle$ is used, where m_j and M_L are the projections of j and L onto the field axis, respectively [318]. Values of L up to $L_{\max} = 22$ are included, for which the pattern of the Feshbach resonance spectrum is converged. Increasing the value of $L_{\max}$ introduces additional bound states, but they are very weakly coupled to the entrance channel.

In this section, we consider resonances in s-wave collisions of Yb(^{3}P$_2$) in its $m_j = -2$ state. This is the lowest component of the $j = 2$ manifold. Inelastic decays to the $j = 0$ and $j = 1$ manifolds in 2-body collisions with Yb(^{1}S) are slow, with a decay rate coefficient that has been measured to have an upper bound of 10^{-13} cm^3 s^{-1} at fields below 1 G [326]. Green et al. [327] have performed coupled-channel calculations of the inelastic rate over the range 0 to 2000 G, and found the background rate coefficient to be significantly smaller than this bound, on the order of 10^{-17} cm^3 s^{-1}. The slow background 2-body decay makes experiments on to find resonances viable, through either 3-body or 2-body losses, both of which can be enhanced by the resonances.

As in the previous section, we use FIELD as modified to converge on levels (and thus resonance positions) as a function of potential scaling factor λ as well as magnetic field. In order to locate resonances at the $j = 2$, $m_j = -2$ threshold, basis functions for $j = 0$ and 1 were omitted, corresponding to neglect of the slow inelastic decays considered above. We expect this approximation to have no significant effect on level statistics.

4.3.2 Results and discussion

Figure 4.12(a)–(f) shows the NNS distribution and number variance for a sequence of 1000 resonance positions, calculated with respect to λ on the range [0.9,1.13], in external magnetic fields of 0 G, 100 G and 700 G. In the absence of a field, the NNS distribution and the number variance are close to those expected for Poisson statistics, with a Brody parameter $\eta = 0.06 \pm 0.03$. However, application of a magnetic field induces a clear transition towards chaotic statistics. Figure 4.12(g) shows the Brody parameter η as a function of field B: it rises steadily from close

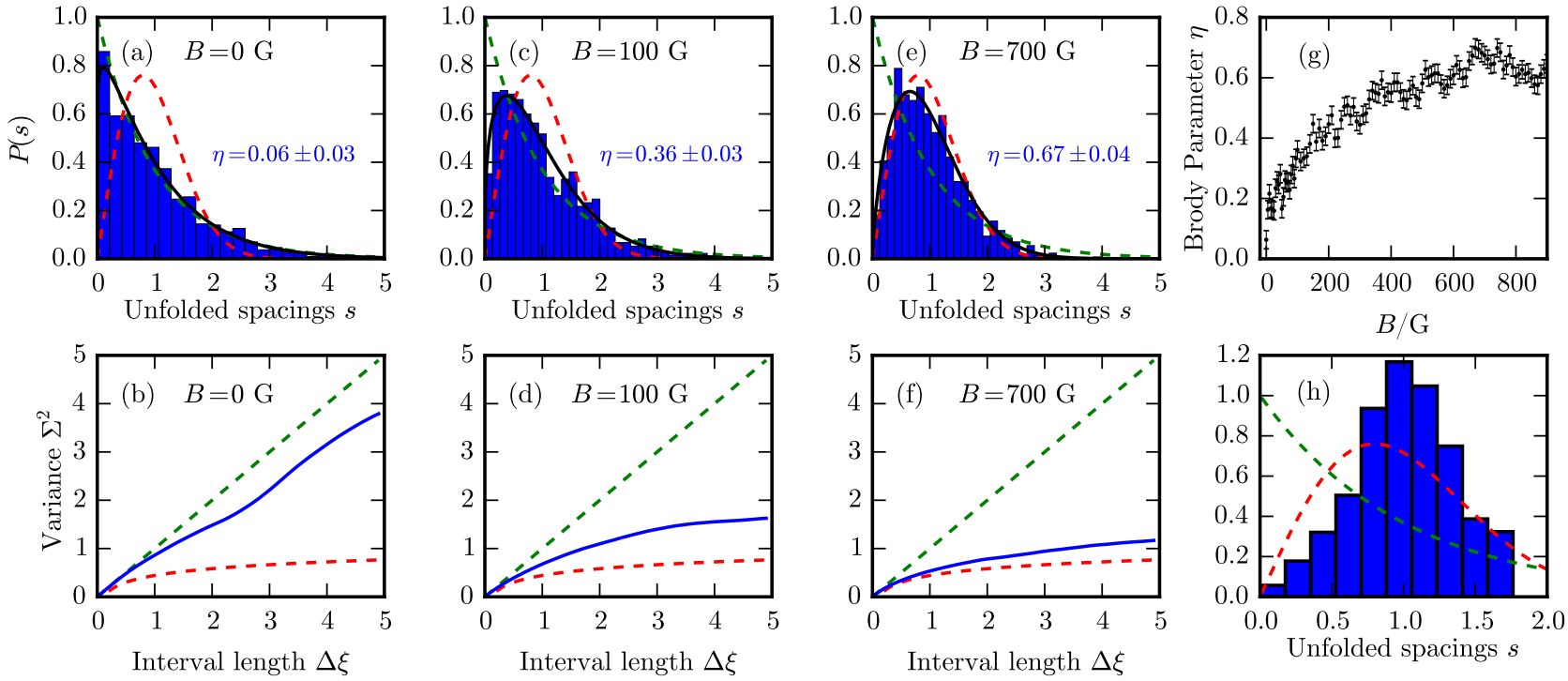

Figure 4.12: Statistical analysis of Feshbach resonance positions with respect to potential scaling factor λ. (a), (c) and (e) show the NNS distributions $P(s)$: coupled-channel results (blue histograms); fitted Brody distributions (black lines, with the corresponding Brody parameters stated); Poisson and Wigner-Dyson distributions (green and red dashed lines, respectively). (b), (d) and (f) show the corresponding number variances $\Sigma^2(\Delta\xi)$: coupled-channel results (blue solid lines); Poisson and GOE results (green and red dashed lines respectively). (g) Calculated Brody parameter as a function of magnetic field. (h) NNS distribution for individual blocks of total angular momentum J in the absence of the magnetic field, averaged over $J = 2, \ldots, 20$.

to zero at $B = 0$ to a value around 0.6 at fields above 500 G. The high-field value is comparable to that observed experimentally for Er and Dy [128]. The number variance also changes steadily from near-Poissonian to chaotic behaviour as the field increases, following the GOE prediction at high field more strongly than for Er and Dy.

Let us consider further the result at zero field, where the total angular momentum J is a good quantum number. In fig. 4.12(h) we show the NNS distribution for individual Hamiltonian blocks of a given total angular momentum J, averaged over values of $J = 2, \ldots, 20$ to obtain improved statistics.[6] Although this superficially resembles a Wigner-Dyson distribution, except that there is a cutoff at large spacing, the levels associated with individual blocks of the total Hamiltonian are in fact highly structured. They correspond to the superposition of nearly independent sequences for $|\Omega| = 0$, 1 and 2, where Ω is the projection of J onto the interatomic axis.[7] It is evident that the Poisson statistics exhibited by the full spectrum at zero field result from superposition of these structured spectra.

In both section 4.2 and thus far in this section we have considered the distribution of resonances with respect to an interatomic potential scaling factor. We now consider the distribution of Feshbach resonances with respect to magnetic field, for homonuclear collisions involving the four most abundant bosonic isotopes of Yb. The typical density of resonances is ~ 0.05 G^{-1}. This is comparable to that found in Cs [163] and Li+Er [292], but much less than that observed in the Er and Dy systems, where it can be as large as ~ 4 G^{-1} (for bosonic isotopes) [127, 128].

Figure 4.13 shows the NNS distributions and number variances for ^{170}Yb, ^{172}Yb, ^{174}Yb and ^{176}Yb in the field range 400 to 2000 G. The statistics show strong signatures of chaos in each case, with Brody parameters ranging from 0.5 to about 1 and number variances much closer to the GOE predictions than to Poisson statistics. We emphasise that the statistics depend on the potential scaling factor as well as

[6] The average is performed by first calculating the unfolded spacings for each J, before combining the sets and normalizing the resulting histogram.

[7] The cutoff at approximately $s = 1.8$ in fig. 4.12(h) is consistent with the vibrational spacing for the $|\Omega| = 2$ potential at dissociation, calculated with respect to λ. This is the deepest of the three potentials, and is equivalent to the $^3\Pi_g$ potential.

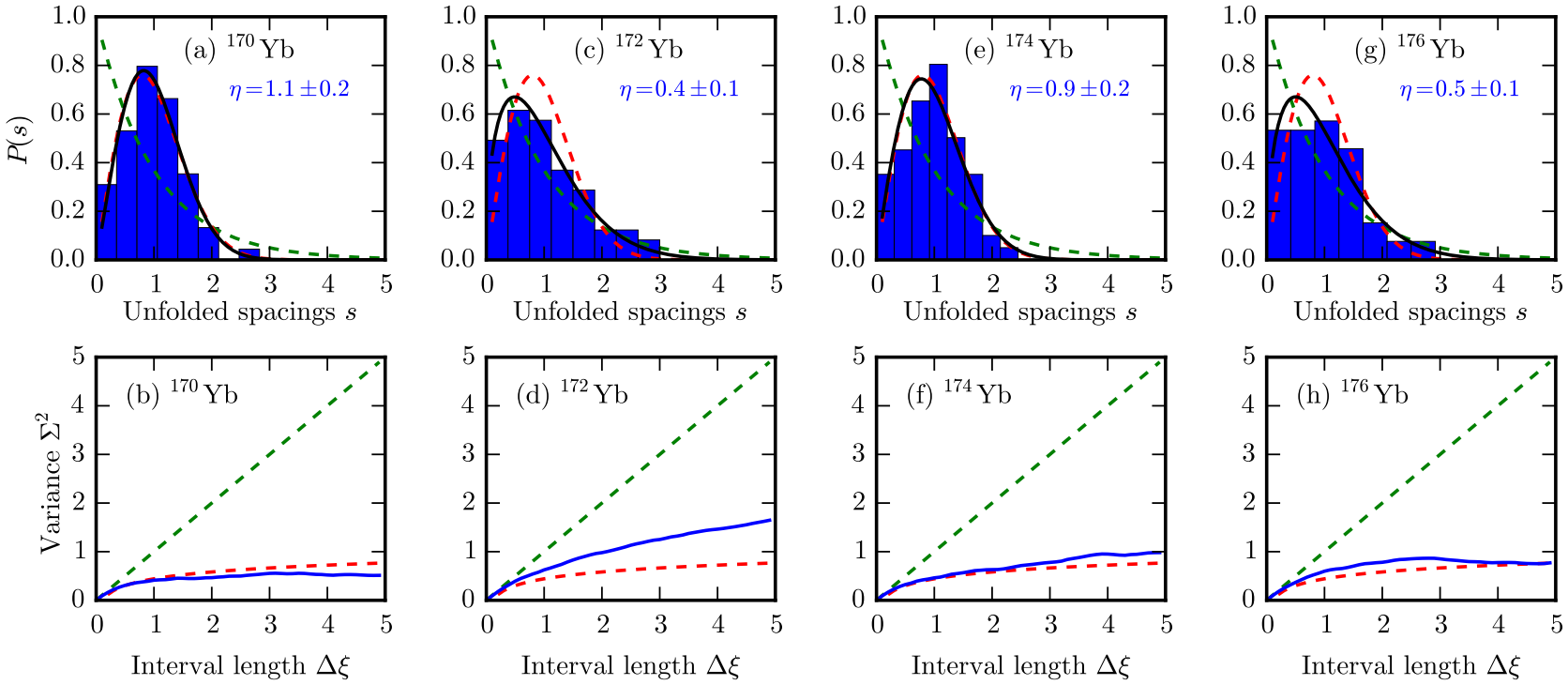

Figure 4.13: Statistical analysis of Feshbach resonance positions with respect to magnetic field for different isotopes of Yb. Upper panels show NNS distributions $P(s)$: coupled-channel calculations (blue histograms); fitted Brody distributions (black lines, with the corresponding Brody parameters stated); Poisson and Wigner-Dyson distributions (green and red dashed lines respectively). Lower panels show the corresponding number variances $\Sigma^2(\Delta\xi)$: coupled-channel calculations (blue solid lines); Poisson and GOE results (green and red dashed lines, respectively).

the isotopic mass, so the results in fig. 4.13 are representative of typical behaviour, rather than specific predictions for individual isotopes. Signatures of chaos emerge at somewhat different fields for different cases, but are always strongly present for fields over 600 G. These signatures will be observable if current experiments on Feshbach resonances in Yb(^{1}S$_0$)+Yb(^{3}P$_2$) [328, 329] can be extended to suitable magnetic fields.

The results in figs. 4.12 and 4.13 show that a large number of electronic states is not required for signatures of chaos to emerge in ultracold collisions, as may have been expected from the Er and Dy examples. We conclude that chaos in Yb+Yb* emerges as a result of the combination of strongly anisotropic interactions and magnetic field, consistent with the findings for Dy+Dy [128]. As a counterexample, we have analysed the Feshbach resonance positions in Cs(^{2}S)+Cs(^{2}S) collisions in magnetic field [163], where there are two electronic states but only very weak anisotropy. We find no deviations from Poisson statistics for Cs.

4.4 Conclusions and Future Work

In this chapter we have analysed positions of zero-energy Feshbach resonances in terms of RMT and quantum chaos. We began with an overview of RMT and statistical analysis, which we hope will be useful for others approaching the field of chaos from ultracold physics or chemistry. In particular, we hope that we have made it accessible to those without the strong abstract mathematical background that sometimes seems required for introductions to RMT and quantum chaos.

We have carried out calculations on threshold and near-threshold bound states of atom + rigid-rotor models of Li+CaH and Li+CaF, and performed statistical analysis of the resulting level sequences. For Li+CaH with zero total angular momentum we have found the strongest signs of chaos yet observed for a realistic ultracold collision system in either theory or experiment. However, for non-zero total angular momentum we found a nearly good quantum number which we identified as the body-fixed projection K of the total angular momentum J. The presence of this nearly conserved quantity significantly alters the overall statistics, but the statistics

for individual values of K still show chaotic behaviour. The superposition of two nearly independent level sequences in the $J = 1$ case produces an NNS distribution that is distinct from the Poisson, Wigner-Dyson and Brody distributions.

The ratio of the anisotropy to the diatom rotational constant is significantly larger for Li+CaF than for Li+CaH. Nevertheless, contrary to expectation, Li+CaF shows less strongly chaotic behaviour even for $J = 0$. The similarity of the statistics with the case of Li+CaH ($J = 1$) suggests the presence of another nearly good quantum number in Li+CaF. The existence of this quantum number may be related to an adiabatic separation between a slow bending vibration and a faster intermolecular stretch.

Finally, we have investigated how the statistics change between and beyond our two systems by varying the rotational constant with a fixed potential. We observe astonishing fluctuations in the levels of chaos in the system. It thus cannot even be assumed that a system that is partway between two closely related chaotic systems will itself be chaotic. The origin of this surprising effect is unclear. One possibility is that stronger chaos emerges when the bending and stretching frequencies are close to rational multiples of one another.

From our results for Yb+Yb*, we have shown that a large number of electronic states is not required for signatures of chaos to exist in ultracold atomic collisions, as may have been expected from the Er and Dy examples. We conclude that chaos in Yb+Yb* emerges as a result of the combination of strongly anisotropic interactions and magnetic field, consistent with the findings for Dy+Dy [128]. As a counterexample, we have also analysed the Feshbach resonance positions in Cs(^{2}S)+Cs(^{2}S) collisions in magnetic field [163], where there are two electronic states and hyperfine structure, but only very weak anisotropy. We find no deviations from Poisson statistics for Cs.

It is clear that there is much to be learned from studying chaos in ultracold collisions and high-lying bound states of atoms and molecules. Statistical analysis can provide valuable insight when the spectra are too complex for direct analysis. However, this study has highlighted that deviations from chaotic behaviour can be difficult to predict, even in apparently simple systems.

One topic for future work is to look at a wider selection of statistics. In particular it will be interesting to include analysis of the widths of the resonances, not just the positions, as these may be important for the enhanced 3-body recombination rates proposed by Bohn and coworkers [207, 208]. It is also important to understand exactly which statistical measures are important to determine if a system should be considered "chaotic" for our purposes. The NNS distribution is conceptually simple and easy to calculate, but inherently captures effects of coupling only between levels that are close to each other. A crucial aspect of chaos is the degree of coupling and correlation between levels that are far removed from each other. Significantly more work is needed to understand if this aspect of chaos is important for our understanding of ultracold collisions and bound states, and which statistics are most useful for quantifying these effects.

It is also important to understand the origins of chaotic or non-chaotic statistics in increasingly complex systems. One question of particular importance is whether, in real systems, all degrees of freedom are involved in the chaotic behaviour, or whether there is a hierarchy of couplings that leaves some degrees of freedom uninvolved. Our results for Li+CaH ($J = 1$) represent a particularly simple example of a case with a clear hierarchy, and our results for Li+CaF ($J = 0$) show that such a hierarchy may arise is places and ways that are unexpected.

Chapter 5

Time Delay in Cold and Ultracold Collisions

The idea, put forward by John Bohn and co-workers [207, 208], that low-energy collisions of highly complex particles are very long-lived, is rapidly becoming popular in the field of cold and ultracold atoms and molecules. These 'sticky collisions' are thought to enhance the possibility of three-body collisions dramatically, resulting in rapid loss even for species that had previously been thought to be stable to collisional decay (such as molecules in their absolute ground state). This proposed process can be written as

$$\begin{aligned} \mathrm{A} + \mathrm{A} &\rightleftharpoons \mathrm{A}_2^\star \\ \mathrm{A}_2^\star + \mathrm{A} &\rightarrow \mathrm{A}_2 + \mathrm{A} + E_\mathrm{k} \\ &\Rightarrow 3 \text{ A lost from sample.} \end{aligned}$$

In this picture, the loss rate is proportional to the lifetime, τ, of the $\mathrm{A}_2^\star$ intermediate. This process is not in itself novel (it is closely related to Lindemann theory [330]) but the new feature of this idea is the suggestion that it is the dominant process for complex molecules at ultralow energies. Apparent rapid three-body losses which may be due to this have been reported experimentally for Rb+KRb [145], RbCs [50] and others [52, 53], although the experiments are very far from conclusive on the subject. The overall process $3\mathrm{A} \rightarrow \mathrm{A}_2 + \mathrm{A} + E_\mathrm{k}$ is termed three-body recombination, and

includes contributions from the direct process without the intermediate step. This direct three-body recombination is usually greatly suppressed if densities are low, as is the case in most experiments with ultracold atoms and molecules. However, the rate is known to scale as a^4 [331] at low energy and can become considerable for large scattering lengths, particularly near resonances [167].

High complexity in a system would usually manifest itself as a large number of channels in calculations on the system. As we are usually interested in the lowest threshold or lowest few thresholds, almost all of these many channels will be closed and the main effect of added complexity is expected to be in the form of a large number of Feshbach resonances. Bohn's theory attempts to arrive at a statistical description of the Feshbach resonances using RMT, under the assumption that the system displays quantum chaos [207]. There is some experimental evidence of *spacings* between resonances following a chaotic statistical distribution [127, 128], but this provides no direct information on collision times, or even the resonance widths which are crucial for Bohn's arguments. As reported in chapter 4 and elsewhere [127–130], theoretical investigations have shown signatures of chaos too, but they have also shown that in some cases the assumption of complete mixing of all degrees of freedom may break down in ways both expected and unexpected. It is not clear how those new theoretical results may affect the effects proposed by Bohn.

In Bohn's theory [207], collision lifetimes τ are inferred simplistically from resonance widths (in energy) Γ_E through the relation

$$\tau = \frac{\hbar}{\Gamma_E}. \tag{5.0.1}$$

Note that this is actually the time for an existing quasi-bound state to decay, and we should expect that the total lifetime of a collision to be twice this - this is because the state must first form in a collision, which takes the same amount of time as decay because it is same process but time-reversed. Three-body losses are then assumed to be a two-stage process with the long-lived collision complex as an intermediate, leading to a loss rate that is proportional to the lifetime to a first approximation. Bohn further assumes that the level widths are proportional to the level spacings,

leading to a description of three-body decay that depends only upon the two-body density of states. There are several problems with this approach, including how to treat many overlapping resonances and what effect threshold effects may have, both of which seem likely to be relevant. A much more rigorous and complete approach to collision times is Smith's lifetime matrix $\mathbf{Q}$ [332] which is defined for any scattering situation. This theory is well established and robust at higher temperatures, but in the threshold region the results require careful interpretation.

It is not even clear if it is valid to think about three-body recombination at ultracold energies in terms of the lifetime of a metastable intermediate. That model for three-body recombination is intuitive and persuasive, but classically motivated and we should be cautious about believing or applying it in a context where we already know that many classical ideas are no longer valid. Unfortunately, rigorous quantum theory of three-body collisions is highly challenging and, although the formalisms exist, existing calculations at ultralow energies have focussed on particular aspects of three-body collisions – namely Efimov physics and the various associated effects [331, 333–340] – and have not sought to address the questions relevant to Bohn's idea of three-body recombination at low energy via a metastable intermediate. In practice, we cannot currently calculate three-body recombination rates for any highly complex system, but much may still be learned about three-body collisions without explicit calculations.

In this chapter we will first consider the collision lifetime as defined by Smith [332] and discuss some of the problems that arise when applying it to ultracold collisions. We explore some alternative related quantities, but do not reach a definitive conclusion on which is the relevant quantity to consider. In an attempt to resolve what quantity is most relevant to enhancement of 3-body collisions, we explicitly consider the 3-body scattering equations. We do not perform any explicit calculations on 3-body systems, but we discuss what aspects of quantum 3-body scattering are likely to correspond to the classical physical picture put forward by Bohn. We then find ways to relate important elements of the 3-body scattering to a closely related 2-body problem. We hope this will pave the way for future work to identify precisely what aspects of a particular 2-body collisional system will enhance the

processes of interest in the associated 3-body system.

5.1 Smith Time Delay and Related Quantities

5.1.1 Original Formulation of Smith's Time Delay

This section introduces the key ideas and equations from Smith's original formulation of collision lifetimes [332]. Similar results had previously been obtained by Eisenbud and Wigner [341, 342] in a formulation based on wave-packet scattering, but Smith's formulation is based on time-independent stationary-state scattering theory, as described in section 1.2 and used throughout this thesis, so we prefer to use this formulation. Note that some of Smith's notation and other minor details are not in line with modern usage in this field and what is used in this thesis; in particular, Smith's definition of the phase shift is twice the value of the usual definition of the phase shift.

It seems at first surprising that it is possible to understand time delays in collisions from a time-independent formalism. Smith resolves this difficulty by applying the fact that, if a system is in a steady state, the average time spent by a particle in a certain region can be obtained as the quantity in that region divided by the flux in or out of that region. For the our case, the quantity is readily given as the integral of the squared magnitude of the wavefunction, and the flux can be obtained if the wavefunction is written in terms of a sum of travelling waves, as in the usual S-matrix boundary condition of eq. (1.2.13). This gives us a ready definition of the time spent in any particular region, but this will diverge as the region expands. For some uses it may suffice to define a specific region of interest – for example for separations less than a certain value, $R \leq R_{\max}$ – but a more general method is to consider the *excess* quantity in the region by subtracting the quantity that would be present without the interaction. Thus it is possible to get a definition of the collision lifetime that does not diverge even if the region is taken to extend out to infinite separation.

We now specialise to a one-dimensional single-channel system and formalise the arguments of the preceding paragraph, although the results readily generalise to

more complex cases. As usual, the wavefunction of the system is the solution to the Schrödinger equation, eq. (1.2.7), that vanishes at $R = 0$ and behaves as

$$\psi(R) \overset{R\to\infty}{\sim} \frac{k^{-1/2}}{i}(-e^{-i(kR+\delta)} + e^{i(kR+\delta)}) = 2k^{-1/2}\sin(kR+\delta) \tag{5.1.2}$$

$$= {}_\infty\psi(R). \tag{5.1.3}$$

The travelling waves that make up this boundary condition are already normalised to give a constant flux of $\hbar/\mu$ independent of energy. Therefore we can define the collision lifetime Q as

$$Q = \frac{\mu}{\hbar}\int_0^{R_{\max}} (\psi(R)^*\psi(R) - A)\, dR, \tag{5.1.4}$$

where A is a reference density that would have been present even without the interaction. Smith takes this to be simply the average density in the absence of a potential

$$A = \lim_{L\to\infty}\frac{1}{L}\int_0^L {}_\infty\psi(R)^*{}_\infty\psi(R)\, dR \tag{5.1.5}$$

$$= \frac{2}{k}, \tag{5.1.6}$$

independent of R. However, this has the drawback of introducing terms in Q that oscillate with R out to infinite R; to proceed with this choice requires that these terms are removed by a further stage of averaging. Smith mentions in passing the possibility of an alternative definition of the lifetime which uses the functional form of the asymptotic wavefunction to give an R-dependent reference density that allows the integral to converge. This gives an alternative definition of the lifetime as

$$Q' = \frac{\mu}{\hbar}\int_0^{R_{\max}} (\psi(R)^*\psi(R) - {}_\infty\psi(R)^*{}_\infty\psi(R))\, dR, \tag{5.1.7}$$

which is related to the previous definition by

$$Q' = Q - \frac{\hbar}{2E}\sin 2\delta. \tag{5.1.8}$$

At moderate energies this difference is small enough to be ignored, but here we are specifically interested in cold and ultracold scattering so we will probably need to consider the effects of this additional term.

The integrals in eqs. (5.1.4) and (5.1.7) may not be easy to perform explicitly in practice for a variety of reasons. It is also desirable to be able to simply relate the lifetime Q to other commonly used and well understood quantities in ultracold scattering, such as the S-matrix or phase shift. In order to do this, Smith shows that starting from the Schrödinger equation and its energy derivative, it is possible to write

$$\psi^*\psi = -\frac{\hbar^2}{2\mu}\frac{\partial}{\partial R}\left[\psi^*\frac{\partial^2\psi}{\partial R\partial E} - \left(\frac{\partial\psi}{\partial E}\right)\left(\frac{\partial\psi^*}{\partial R}\right)\right]. \tag{5.1.9}$$

This expression is now easy to integrate, and if we assume that $\psi(R)$ has converged to ${}_\infty\psi(R)$ by $R = R_{\max}$ we obtain

$$\int_0^{R_{\max}} \psi(R)^*\psi(R)\,dR = 2\hbar\frac{\partial\delta}{\partial E} + \frac{2}{k}R_{\max} - \frac{\hbar}{2E}\sin(2kR + 2\delta). \tag{5.1.10}$$

The second term in this is exactly the contribution that is removed by the reference density A, and the last term is the oscillating term introduced by this choice of reference density. Removing these two terms[1] leaves

$$Q = 2\hbar\frac{\partial\delta}{\partial E}, \tag{5.1.11}$$

which relates the collision lifetime to the phase shift, which is in agreement with the earlier work of Eisenbud and Wigner [341, 342].

A similar analysis is possible if there are multiple open channels, leading Smith to define a lifetime *matrix*

$$\mathbf{Q} = i\hbar\frac{d\mathbf{S}}{dE}\mathbf{S}^\dagger, \tag{5.1.12}$$

where $\mathbf{S}$ is the usual multichannel S-matrix. The diagonal elements Q_{ii} are interpreted as the average time delay for a collision that is incoming in channel i, including flux that is outgoing in a different channel. The off-diagonal elements of

[1] This process can be formalised but in this case the result is obvious.

Q do not have a simple interpretation, but are used when rotating **Q** to a different basis set. If there are multiple channels, but only one of them is an open channel, then the definitions given for the single-channel case apply. We will remain focussed on this single-open-channel case through the remainder of this section as the effects we are interested in are already present in that case and there is no need to introduce the additional complexities involved with considering the multichannel case.

The simple relationship between the lifetime and phase shift means that any features in the phase shift will have a corresponding feature in the lifetime. In particular, consider an isolated narrow resonance at energy E_0 that is not near a threshold, with energy-independent width $\Gamma_E \ll E_0$. The phase shift follows the standard Breit-Wigner form

$$\delta = \delta_{\text{bg}} + \arctan\left(\frac{\Gamma_E/2}{(E_0 - E)}\right), \tag{5.1.13}$$

and the time delay shows a Lorentzian peak

$$Q = Q_{\text{bg}} + \frac{\hbar\Gamma_E}{(E_0 - E)^2 + (\Gamma_E/2)^2} \tag{5.1.14}$$

which peaks at four times the quasi-bound state decay lifetime of eq. (5.0.1), or twice the standard collision lifetime inferred from the width. Smith shows that a suitably weighted average over the resonance results in an average lifetime which is equivalent to that inferred from the width. Further, for a magnetically tuneable resonance (or any resonance similarly tuneable by an external parameter), with a width independent of field and energy, the time delay will also show a Lorentzian peak in field at fixed energy with a width determined by the resonance width in field, Γ_B, but a height determined by its width in energy, $\Gamma_E = \Gamma_B \delta\mu_B$ where $\delta\mu_B$ is a difference in magnetic moment between the continuum state and the quasi-bound state causing the resonance.

5.1.2 Threshold behaviour

Threshold laws and behaviours dominate scattering in the low-energy regimes that we are interested in [158]. In the simplest case where scattering is wholly determined by an energy-independent scattering length a, the phase shift is

$$\delta = \arctan(-ka) \tag{5.1.15}$$

$$\approx -ka \quad \text{if} \quad |ka| \ll 1, \tag{5.1.16}$$

which gives a time delay

$$Q = \frac{-2a\mu}{\hbar k} = -2\frac{a}{v}, \tag{5.1.17}$$

where $v = k\hbar/\mu$ is the relative velocity. This is the classical time-delay associated with a hard sphere of radius a, agreeing with the usual interpretation of the scattering length as an effective hard-sphere radius. This means that around a zero-energy Feshbach resonance (and close enough to threshold for the scattering lengths to be constant), where the scattering length shows a pole, we expect the time delay to show large positive and negative peaks. Unlike the scattering length it must remain finite at finite energy (the condition in eq. (5.1.16) prevents Q diverging when a diverges). This is qualitatively very different from the simple Lorentzian behaviour seen away from threshold. This is understood by considering the known threshold behaviour of resonances; in particular the Breit-Wigner width Γ_E of a resonance is known to be linear in k near threshold [34, 204], whereas the width Δ associated with the scattering length does not vary with energy, to a first approximation. The high-energy form of Q in eq. (5.1.14) assumed a constant Γ_E, and rapid energy variation of Γ_E due to threshold effects is responsible for the difference between the two cases.

Figure 5.1 shows Q calculated for a sample resonance. The system is ^{87}RbCs, with the interaction potentials of Takekoshi et al. [42] but with only $L = 0$ basis functions included. The resonance is at $B_0 = 792$ G and fairly broad, $\Delta_B \approx 4$ G.[343] In the low-energy region, up to tens or hundreds of nK, eq. (5.1.17) holds well and the positive and negative peaks in the time delay are well defined, nearly equal and

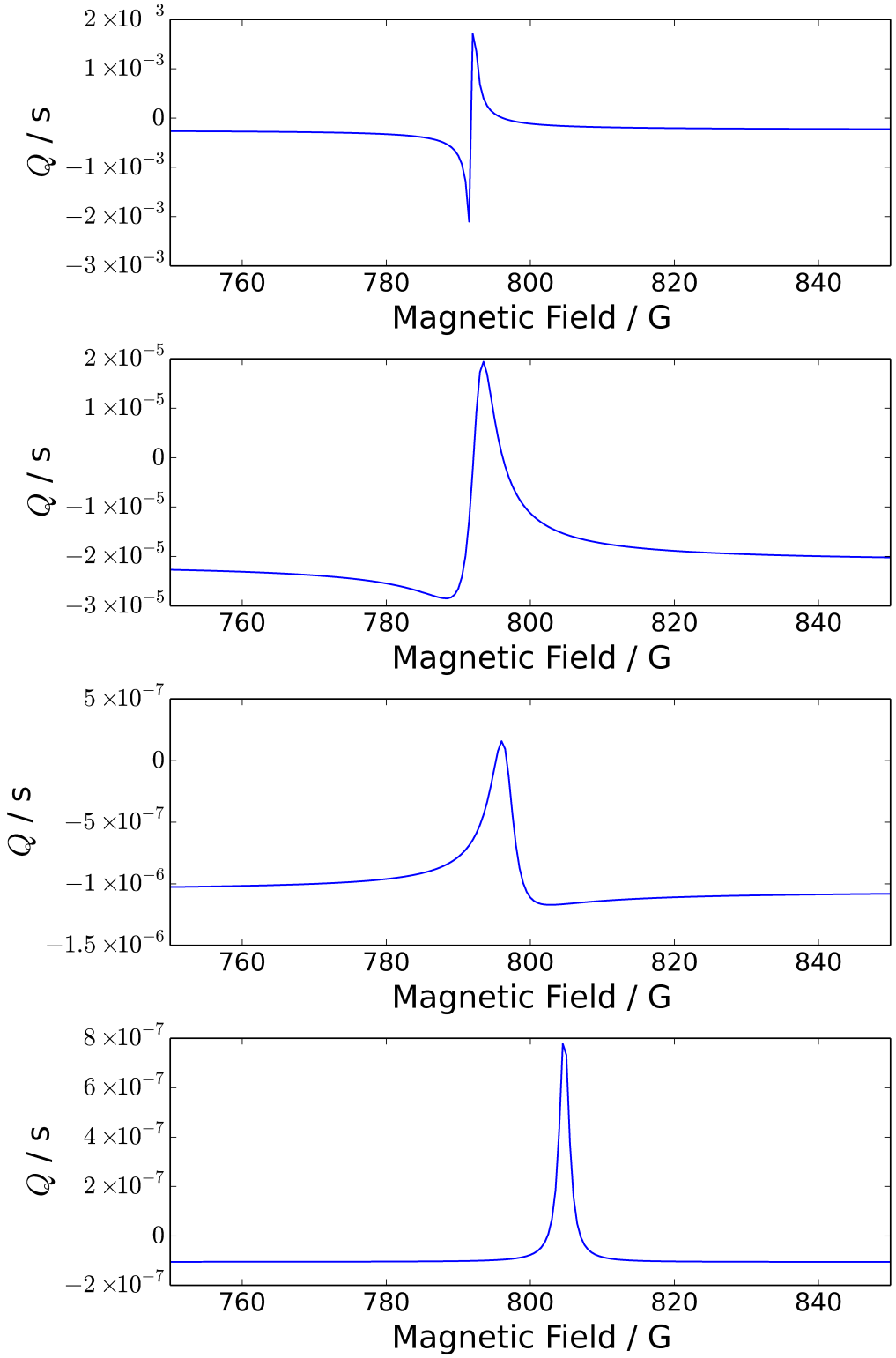

Figure 5.1: Smith's collision lifetime, Q, around the 792 G resonance ^{87}RbCs for 10 nK (top), 1 μK, 40 μK and 1 mK (bottom). Note the changing scale.

fairly sharp. Around 1 μK we enter an intermediate region as both peaks broaden and become unequal, with the negative side fading away. This is associated with the energy rising above the threshold regime, so that the width no longer increases linearly with k; an alternative view is that the approximation $\delta = -ka$ with a constant a no longer holds. 1 mK is well away from threshold behaviour and the expected Lorentzian shape is clear. Below the high-energy region, most clearly at 40 μK, there is a peculiar dip on the high-field side of the peak, similar to the dip observed on the low-field side around 1 μK. This is attributed to a *narrowing* of the resonance in that energy range causing the opposite effect of the widening seen at lower energies, albeit much weaker. This narrowing of the resonance can be understood through a multi-channel QDT description of resonances [204], but this effect is not important for our main discussion.

This near-threshold behaviour of Q raises some puzzling issues. The lifetime at a particular energy appears to cancel somewhat between opposite sides of the resonance, if the particular case samples both. This is unlikely to be relevant in the RbCs case discussed immediately above, but if there are a large number of very narrow resonances (as is likely in the cases Bohn and co-workers consider [207, 208]) then the variation of the magnetic field through the sample in a real experiment could be enough to cover many widths. In that case the average lifetime will be much smaller in magnitude than the lifetime at most particular fields. Conversely, at a fixed field if there are many resonances within the range of the thermal energy $k_{\mathrm{B}}T$ then the phase shift across this range of energy will still increase by π for each one, provided their widths are small enough. As $\int Q dE = 2\hbar\delta$, such an increase in the phase shift will transfer directly to the average lifetime. Further, if the width of a particular resonance is small compared to both its position E_0 and $k_{\mathrm{B}}T$, then the contribution to the average lifetime depends only on the thermal distribution at its particular energy and not on its width. Therefore, in this understanding and approximation, the average collision lifetime depends not on the details of the resonances, but simply on the density of resonances.

The difference in the apparent behaviours between averaging over energy at a fixed field and averaging over field at a fixed energy (or just a sufficiently low tem-

perature) do not necessarily indicate a fundamental problem, but at the very least makes interpretation difficult without detailed knowledge of the experimental situation under consideration. In any case, the interpretation of Bohn and co-workers [207] that an average resonance width implies a certain lifetime seems simplistic. However, in their analysis, they take the average resonance width to be approximately equal to the average resonance spacing – although not examined in detail here, this is itself a questionable assumption – and therefore find that the average lifetime is proportional to the average density of resonances, the same as we have concluded for the case of a thermal average at a fixed field.

5.1.3 Alternative possible definitions of the collision lifetime

We now turn to considering alternative definitions of the collision lifetime. For Q' defined by eqs. (5.1.7) and (5.1.8) and δ given by eq. (5.1.16), we find that if a is independent of energy then the term $-\hbar\sin(2\delta)/2E$ in eq. (5.1.8) exactly cancels the value of Q and we find that $Q' = 0$. Note that, unlike eq. (5.1.17), this result does not depend on $|ka| \ll 1$. Hence, non-zero values of Q' arise only due to the variation of a with energy. Resonances are one prominent feature which will cause a to vary [160], but such variation is typically concentrated in a region of field that is much narrower than the width of the resonance.

Figure 5.2 shows Q' for the RbCs resonance shown previously. The results show very different behaviour to Q. At the lowest energy, 10 nK, Q' shows a narrow negative peak corresponding to the position of the pole in a, but this dies off very quickly away from the pole position. At 1 μK this sharp peak has broadened and become asymmetric. Again, once the energy is 1 mK, the expected Lorentzian high-energy line-shape is recovered. Also, note that the scales on the results for 10 nK and 1 μK are much smaller than in fig. 5.1, meaning that the overall magnitude of Q' is significantly smaller than Q when near threshold.

If we consider the case of averaging over many resonances in field at a fixed energy or low temperature, then at first it seems as if Q' behaves rather differently to Q. However, insofar as it is formally possible to do so, integrating the difference term between the two, $-\hbar\sin 2\delta/2E$, over a single resonance would appear to give

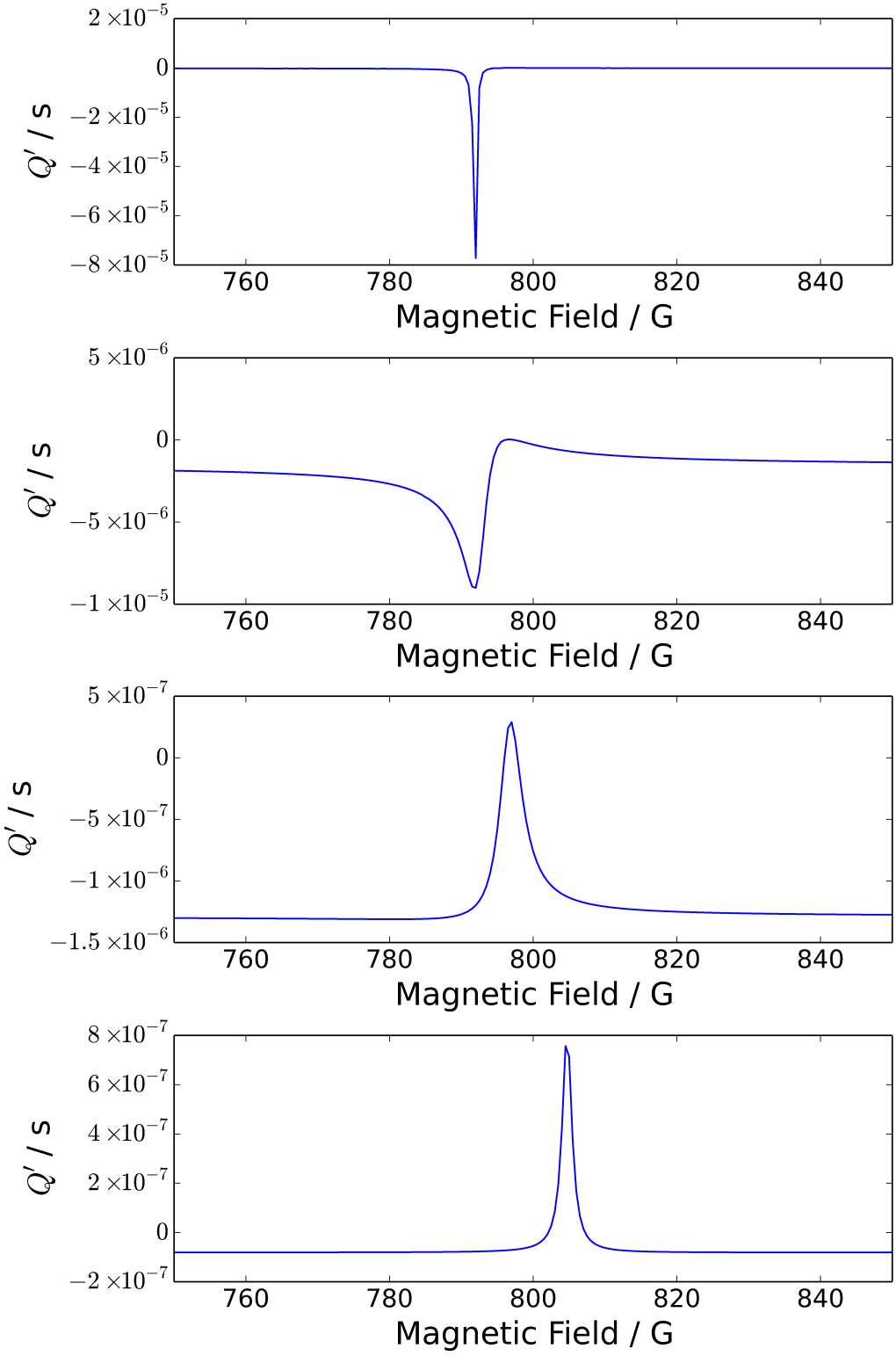

Figure 5.2: Alternative collision lifetime, Q', around the 792 G resonance ^{87}RbCs for 10 nK (top), 1 μK, 10 μK and 1 mK (bottom). Note the different scales compared to fig. 5.1.

an average contribution of zero if the background phase δ_{bg} is approximated to zero. Hence, it appears that in that case the two definitions might give the same averaged behaviour, although very different detailed behaviour.

A further possible definition of the lifetime comes from simply considering the density in closed channels. We define

$$Q'' = \frac{\mu}{\hbar} \sum_{i \in \text{closed channels}} \int_0^\infty |\langle i|\Psi(R,\tau)|i\rangle|^2 dR, \tag{5.1.18}$$

$$= \frac{\mu}{\hbar} \sum_{i \in \text{closed channels}} \int_0^\infty |\psi_i(R)|^2 dR, \tag{5.1.19}$$

where ψ_i is the component of the multichannel wavefunction Ψ in channel i. This quantity lacks a clear interpretation as a time delay because there is no obvious flux in and out of the closed channels, but instead implicitly uses the asymptotic incoming and outgoing flux. Also, it is not easily expressible in terms of asymptotic quantities, so we cannot derive analytic expressions for it and evaluating it numerically is slow and computationally expensive. However, it requires no reference density to be subtracted, because the wavefunction in closed channels dies off and so the integral converges; note that this means it can never be negative, unlike Q and Q'. It also very clearly corresponds to Bohn's original concept of the collision complex transferring energy to degrees of freedom other than R [290], and it may be an instructive quantity to consider.

5.1.4 Contributions to integrals for collision lifetimes.

We now examine the actual contributions to the various integrals, eqs. (5.1.4), (5.1.7) and (5.1.19), that define the collision lifetimes Q, Q', and Q''. For this, we use a model 2-channel system: the potential of each channel is a Lennard-Jones potential, eq. (3.1.17), with parameters chosen to approximately represent Rb+KRb [207]. The channels are coupled by a small coupling term (also L.-J. in form with maximum value ≈ 1 cm^{-1}) to replicate the narrow resonances predicted by Mayle et al. [207]. We use a fixed collision energy of 300 nK and to create a resonance, we directly varying the asymptotic energy of the closed channel to tune a state across threshold.

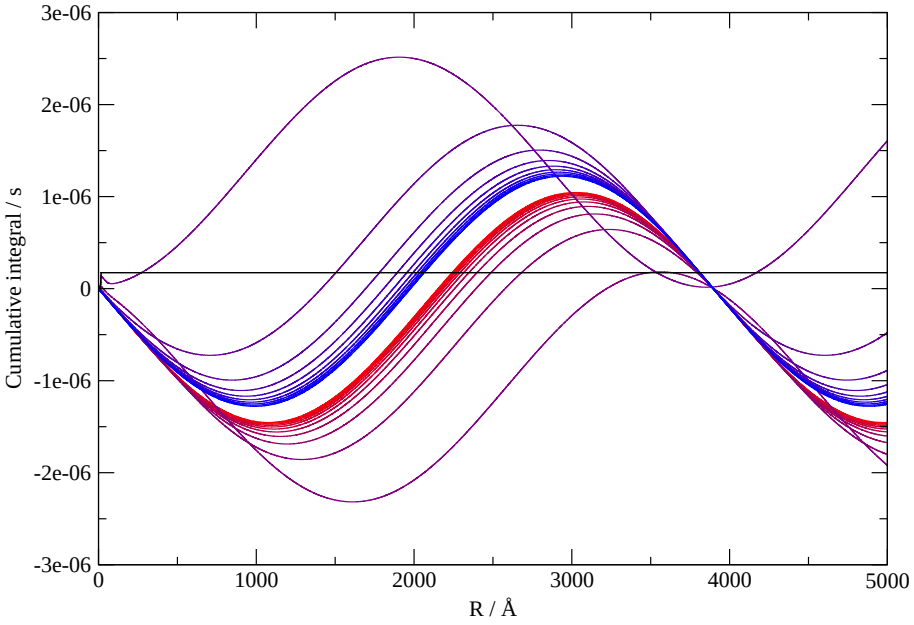

Figure 5.3: Cumulative integrals for Q from a series of point across a resonance in a model 2-channel system, showing very large long-range oscillations. The colouring runs from red on one side of resonance to blue on the other and the two bands approaching the background situation can clearly be seen. Also shown in black for comparison is the cumulative integral for Q'' right on resonance, i.e. the maximum closed-channel contribution.

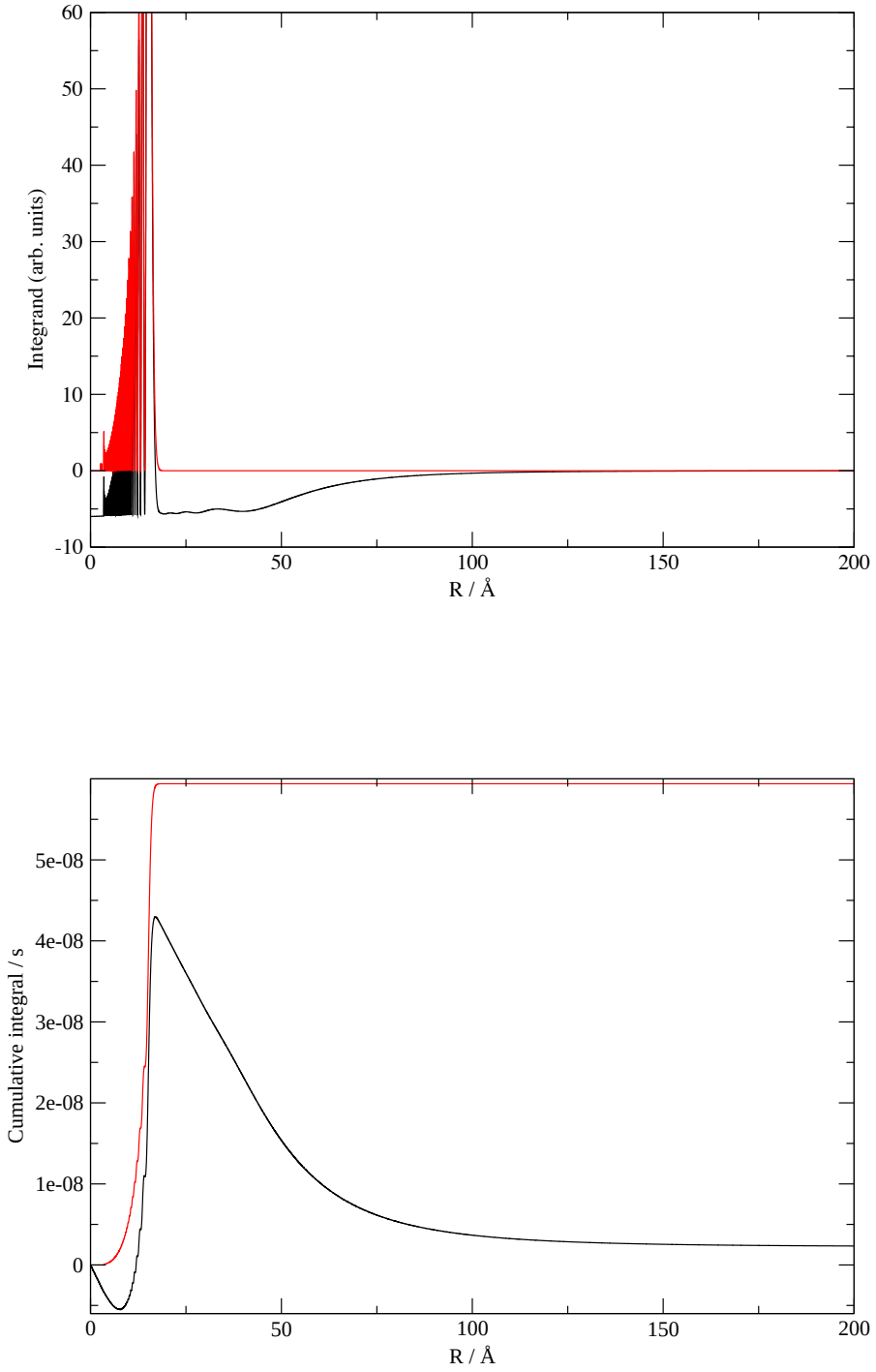

Figure 5.4: Integrand (top) and cumulative integral (bottom) for Q' (black) and Q'' (red) at one point right on resonance in a model 2-channel system.

Figure 5.3 shows the cumulative value of the integral, eq. (5.1.4), for a set of calculations across the resonance out to a large $R_{\max}$. The long-range oscillations are the dominant feature in this figure, and the value of Q for each calculation could be obtained by averaging over these oscillations. All the waves are still relatively close together at a value of R which is outside the short-range region, but small on the scale of these long-range oscillations, but they then diverge rapidly depending upon the phase in the oscillation at which they start. Therefore, the range of values of Q has little to do with any short-range effects, which are almost entirely lost on this scale, and are almost entirely determined by the phase shift.

Figure 5.4 compares Q' and Q'' in a shorter-range region for a single calculation right on resonance. The contributions to Q'' are concentrated at short range, as expected, and rise to an effective lifetime of about 60 ns The contributions to Q' contain all the same terms, plus a contribution from the open channel that appears to be much smaller than that from the closed channel, at least at short range. However, it also contains negative terms due to the reference density, which appears constant on this scale and is not cancelled out by the open-channel contribution until nearly $R = 100$ Å. It can be seen in the cumulative integral of Q' that this reference contribution almost exactly cancels out the closed channel contribution and Q' converges to a value close to zero.

It is obvious that, in the region of this example resonance, Q has overwhelming contributions from the very-long-range region and at these energies Q cannot be said to reflect any short-range behaviour. Even in the case of multiple resonances in the energy range of interest, the magnitude of the contributions from the very-long-range will be similarly large, and Q will still not represent any short-range effects. Q' is more representative of the short-range interactions, but still shows significant contributions at moderate range, which often cancel most or all of the apparent short-range contributions. However, the case explored numerically was at an energy where the scattering was still well described by an energy-independent scattering length, and we expect different behaviour of Q' when this is not the case. Q'' appears promising from these results, but has several problems: it is currently highly inconvenient to calculate, it neglects density at short range in the

open channel(s), and it is not clear that it can be interpreted as a lifetime in any meaningful way.

Thus all three possible definitions of the collision lifetime have been considered and we have not been able to make a convincing argument for any one of them to be considered the 'correct' lifetime for determining rates of three-body recombination. However, we can state a clear preference for Q' over Q at low energy, due to the above-mentioned very large contributions to Q from the very-long-range region.

5.2 Relationship to 3-body Scattering

As we have been unable to make a convincing argument for any of the definitions of collision lifetime considered in section 5.1 to determine three-body recombination, we now turn to explicit consideration of three-body collision theory. This is a complicated topic that could provide material for an entire thesis by itself, so we will endeavour to discuss only the most relevant elements of the theory. We will also attempt to keep the discussion based on clear physical concepts rather than abstract mathematics, although this will not always be possible.

In this section we will make essentially two principal arguments. First, we will consider how a long-lived metastable intermediate would be expected to appear in results of three-body scattering calculations; a simple corollary is that the effect of such metastable states is separate from the Efimov-like scattering which is the subject of most if not all ultracold three-body scattering studies to date. Second, we consider the mechanisms by which a metastable state will influence the 3-body scattering and how to relate important quantities back to an effective two-body problem in which we might identify something which appears to be a collision lifetime. These considerations will each immediately suggest potentially useful ways to proceed.

5.2.1 The appearance of long-lived metastable states in three-body scattering

We must first introduce certain important elements of three-body scattering theory. We follow the notation of Parker et al. [344], but the theory presented mostly

originates in the much older work of Smith [345] and Delves [346].

Jacobi coordinates, and basic classical dynamics

We consider three particles, A, B, and C, which we assume, for now, to be structureless particles with masses m_{A}, m_{B}, and m_{C}. After removing the centre-of-mass motion, we can describe the system using a usual set of Jacobi coordinates. $\mathbf{R}_{\mathrm{A}}$ the vector from the centre-of-mass of BC to A, and $\mathbf{r}_{\mathrm{A}}$ is that from B to C. These coordinates obviously correspond to the system being formally considered as A+BC, and equivalent sets of coordinates are defined for the other two formal arrangements (called $\mathbf{R}_{\mathrm{B}}$ etc.). It is convenient to rescale the coordinates to

$$\mathbf{S}_X = d_X \mathbf{R}_X \tag{5.2.20}$$

$$\mathbf{s}_X = \frac{1}{d_X} \mathbf{r}_X \tag{5.2.21}$$

where d_X is a known dimensionless mass scaling factor which depends only on the masses of the three particles and which arrangement is being considered [344, 345]. The main benefits of this rescaling are that it allows motion associated with each of the vectors to be described by the same effective mass, and is makes interconversion between different sets of scaled Jacobi coordinates a simple rotation in 6-D space. In these coordinates, all three particles are close when both $\mathbf{S}_X$ and $\mathbf{s}_X$ are small; this corresponds to a local region near the origin in the 6-D space. However, two particles are close when any one of the $\mathbf{s}_X$ is small (although it will be a different pair of particles in the different cases); this corresponds to extended regions that can be thought of as being near certain axes. This is schematically represented for 1 spatial dimension in fig. 5.5, which is a reproduction of Fig. 1 of Smith [345].

We now consider some *classical* dynamics of a 3-body collision. If there is no interaction between the particles, the collision trajectory is just a straight line in the 6-D space of $\mathbf{S}_X$ and $\mathbf{s}_X$. An important feature of such a trajectory is the distance of closest approach to the origin, $R_{\mathrm{min}} = \sqrt{|\mathbf{S}_X|^2 + |\mathbf{s}_X|^2}$, which characterises how close the trajectory comes to all three particles being close to each other; this is analogous to the impact parameter b in classical 2-particle scattering. This closest

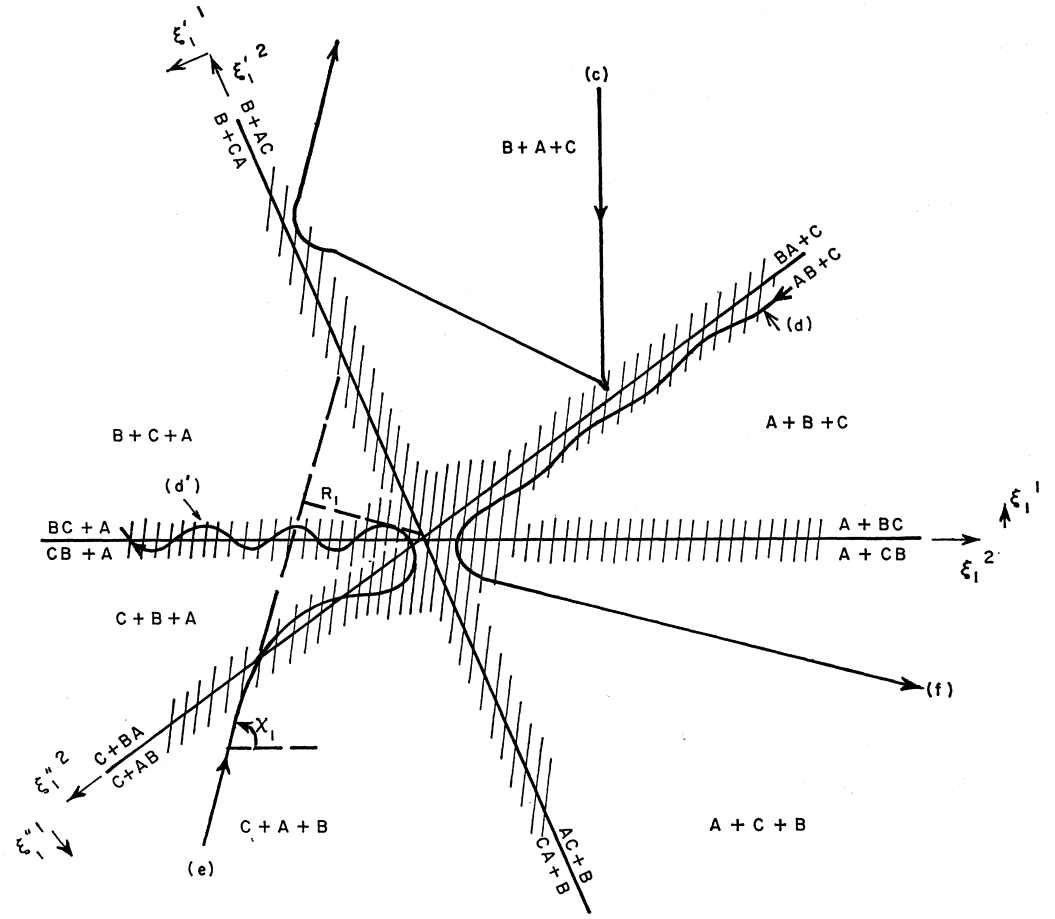

Figure 5.5: Some possible 3-body trajectories. Figure reproduced from Ref. [345]. Trajectories are for collisions on a line, but apply schematically to collisions in space. Smith's coordinates are $\xi_1^2 = \mathbf{S}_{\mathrm{A},x}$, $\xi_1^1 = \mathbf{s}_{\mathrm{A},x}$, $\xi_1'^2 = \mathbf{S}_{\mathrm{B},x}$, $\xi_1'^1 = \mathbf{s}_{\mathrm{B},x}$, $\xi_1''^2 = \mathbf{S}_{\mathrm{C},x}$, and $\xi_1''^1 = \mathbf{s}_{\mathrm{C},x}$. The different coordinates and extra axes shown are simply different ways of describing the same 2D space rather than an indication of a higher dimensionality. Hatched regions show schematically the regions where the interaction is significant. Note in particular trajectory (e).

approach is shown as R_1 for trajectory (e) in fig. 5.5. As with the 2-body impact parameter, $R_{\min}$ has a relationship to an angular momentum

$$\Lambda^2 = 2\mu E_{\mathrm{k}} R_{\min}^2 \tag{5.2.22}$$

which introduces Λ^2 as Smith's classical 'total grand angular momentum' [345]. This quantity is defined and discussed at length by Smith, but we consider only a few of its characteristics that are relevant to our purpose. It is a single real positive-definite quantity that is a constant of a trajectory in the absence of any interaction. However, any interaction will generally change it, even if the interaction affects only two of the three particles and even if the interactions are spherically symmetric. For a collision to be a pure three-body collision then the initial value of Λ^2 before the collision must be small. However, if Λ^2 reaches a small value sometime during the collision, the trajectory may reach the region near the origin with all three particles interacting – and so could result in three-body recombination – even if the initial value of Λ^2 is not small. This can happen through a two-body interaction which can change the value of Λ^2 significantly through the course of the collision if the two particles form a metastable collision complex. This corresponds to trajectory (e) in fig. 5.5.

It is clear that the process described qualitatively by Bohn and co-workers [207, 208] can be described in these terms. A long-lived two-body collision complex leading to three-body recombination, directly corresponds to a classical three-body collision trajectory that is schematically like trajectory (e) in fig. 5.5. The trajectory starts with a large value of Λ^2 but a two-body interaction corresponding to a long-lived metastable state allows Λ^2 to change to a much smaller value and so allows the trajectory to reach the region of three-body interactions which can cause three-body recombination. This is now the correct classical description of 3-body recombination for us to transfer to a quantum description in a way which can be precise and corresponds directly to rigorous quantum theory.

Hyperspherical coordinates, and basic quantum dynamics

To discuss the quantum 3-body collision theory we must change from Jacobi to hyperspherical coordinates. First, we separate $\mathbf{S}_X$ and $\mathbf{s}_X$ into their magnitudes, S_X and s_X, and their directions, $\hat{\mathbf{S}}_X$ and $\hat{\mathbf{s}}_X$. The 4 degrees of freedom of the two directions cover both the three external rotations and an internal coordinate

$$\Theta_X = \arccos\left[\hat{\mathbf{S}}_X.\hat{\mathbf{s}}_X\right], \tag{5.2.23}$$

which is just the usual diatom rotation coordinate in atom-diatom Jacobi coordinates. The magnitudes S_X and s_X are transformed to the hyperradius

$$\rho = \sqrt{S_X^2 + s_X^2} \tag{5.2.24}$$

and the Delves hyperangle

$$\theta_X = \arctan\frac{s_X}{S_X}, \tag{5.2.25}$$

which is defined on the range $\theta_X \in [0, \pi/2]$. The inverse transformation is

$$s_X = \rho \sin\theta_X \tag{5.2.26}$$

$$S_X = \rho \cos\theta_X. \tag{5.2.27}$$

For convenience we sometimes group all the angular coordinates as $\Omega = \{\theta_X, \hat{\mathbf{S}}_X, \hat{\mathbf{s}}_X\}$. The hyperradius can be understood as describing the overall size of the system. It is large whenever any one of the particles is far from any other of the particles, and so it can be large even when two of the particles are close if the third is far away. In this way $\rho \to \infty$ can describe fragmentation to either 3 free particles or 1 free particle and the other two bound together as a diatom. The hyperangle θ_X describes the shape of the system but not its size. For example, small θ_A corresponds to B and C close together (small s_A) and A as far away as the value of ρ allows, whereas θ_A close to $\pi/2$ corresponds to A being close to the centre-of-mass of BC, but with B and C separated as much as ρ allows. These coordinates have mapped the two infinite ranges of S_X and s_X onto the finite range of θ_X and the single infinite range

of ρ. This has reduced the problematic double continuum – which would otherwise have appeared in 3-body quantum scattering calculations – to a single continuum that can be handled by relatively standard means. Essentially all explicit quantum 3-body scattering calculations make use of a transformation of this type in one form or another.

We can now write the Hamiltonian for 3-body scattering as

$$\hat{H} = T_\rho + \frac{\hat{\Lambda}^2}{2\mu_3\rho^2} + V(\rho, \theta_X, \Theta_X), \tag{5.2.28}$$

where

$$\hat{T}_\rho = -\frac{\hbar^2}{2\mu_3\rho^5}\frac{\partial}{\partial\rho}\rho^5\frac{\partial}{\partial\rho} \tag{5.2.29}$$

$$= -\frac{\hbar}{2\mu}\rho^{-5/2}\frac{\partial^2}{\partial\rho^2}\rho^{5/2} + \frac{\hbar^2}{2\mu}\frac{15}{4}\rho^{-2} \tag{5.2.30}$$

is the kinetic energy for motion in ρ, $V(\rho, \theta_X, \Theta_X)$ is the interaction potential, $\mu_3 = [m_\mathrm{A} m_\mathrm{B} m_\mathrm{C}/(m_\mathrm{A} + m_\mathrm{B} + m_\mathrm{C})]^{1/2}$ is the three-body reduced mass, and $\hat{\Lambda}^2$ is now the quantum grand angular momentum operator whose eigenfunctions are hyperspherical harmonics in Ω and eigenvalues are $\hbar^2\lambda(\lambda + 4)$ where the quantum number λ is a non-negative integer. This grand angular momentum introduces a ρ^{-2} effective potential which is analogous to the centrifugal potential in 2-body scattering. Asymptotically, when all three particles separate and V approaches zero, λ becomes a good quantum number and determines the asymptotic behaviour of the channel's effective potential. It is obvious that in order for all three particles to approach close to each other simultaneously, λ cannot be too large or the effective potential will prevent penetration to small ρ; this accords with the interpretation of Λ^2 in the classical case.

If we now include the interaction potential V, we need to consider the hyperspherical adiabats. These are defined as the eigenvalues ε of the adiabatic Hamiltonian

$$\hat{H}_\mathrm{ad}(\Omega; \rho) = \frac{\hat{\Lambda}^2}{2\mu\rho^2} + V(\rho, \theta_X, \Theta_X) \tag{5.2.31}$$

which parametrically varies with ρ. In general, the adiabats for a real system can be

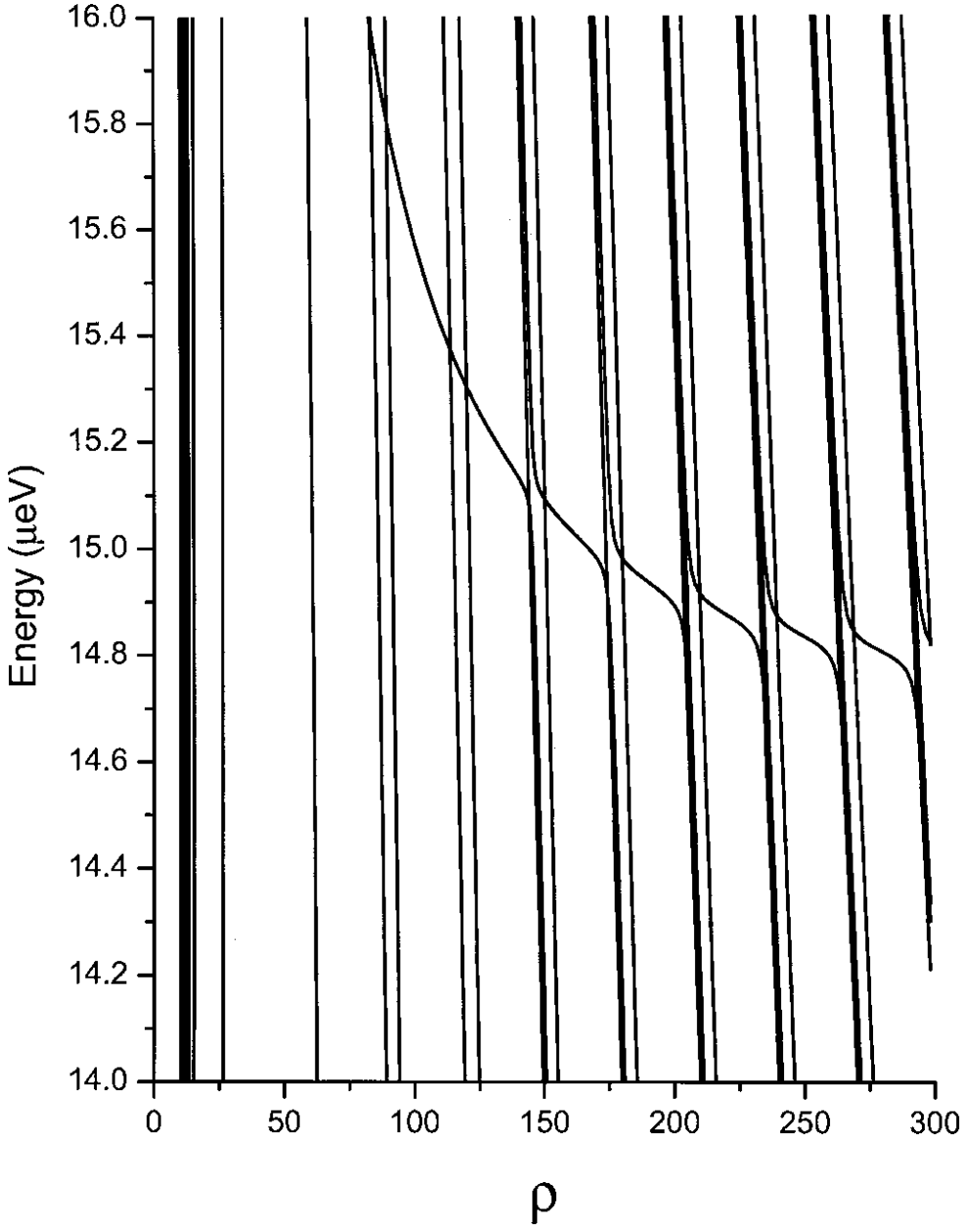

Figure 5.6: Example 3-body hyperspherical adiabats for H+Ne_2, reproduced from Parker et al. [344]. This shows a quasi-bound state approaching its asymptotic value of about 14.8 μeV. The steep lines crossing this state are adiabats corresponding to all three particles separating, which are dying off as ρ^{-2} asymptotically. The adiabats within each group of lines have the same value of λ but are split due to different values for other quantum numbers.

very complicated – see, for example, Fig. 2 of Quéméner et al. [347] – but the features we are interested in may appear in much more simple ways. If the interaction is such that the 2-body B+C system supports a quasibound state, then this state will appear in the 3-body adiabats as a level that approaches a constant positive value as $\rho \to \infty$. This level will be crossed by levels corresponding to states which have all three particles separating; these levels vary as ρ^{-2} with different pre-factors depending on their value of λ. Therefore the level which corresponds to the quasibound state may have a large number of avoided crossings with the states corresponding to the 3-body continuum. An example of this from Ref. [344] is reproduced in fig. 5.6. This provides a mechanism for flux to transfer from one continuum channel to the quasibound state and then out to another continuum state with a different value of λ. This is now seen to be the characteristic quantum mechanism which corresponds to the classical picture of a metastable state changing the classical Λ^2, which can enhance penetration of flux to small enough ρ to allow 3-body recombination. This interpretation seems obvious, and although it may not have found practical application to date, it would be surprising to us if it has not been given previously in the literature. However, if it has been given explicitly we have failed to find it, and it does not appear to have be mentioned in the literature concerning ultracold scattering, so it is worthwhile repeating here anyway.

Viewing the three-body collision dynamics in this way allows us to identify exactly which features we should look for in 3-body scattering which can be interpreted as the influence of long-lived 2-body collision intermediates. In this picture, three-body recombination would be dominated by contributions from incoming channels with large values of λ, even at low energy where scattering in these channels is usually suppressed. It will be worth bearing in mind that individual contributions from each of these channels is still expected to be quite small, but the number of such channels may be large. Additionally, if a system will show large 3-body recombination because of this effect, it will also show large cross sections for collisions which change the value of λ without inducing 3-body recombination or other processes. Such collisions may be easier to characterise in theoretical calculations than 3-body recombination, and it should certainly be easier to perform calculations that show

λ-changing collisions than three-body recombination.

A simple corollary of the interpretation presented here is that the effect of metastable 2-body collision intermediates is distinct from the a^4 scaling of three-body recombination at ultracold energies predicted by Efimov physics [331].[2] This can be understood simply from the fact that Efimov physics requires that the 2-body scattering length of at least 2 of the three pairs of particles must be large [338]. However, the effect of a metastable state relies on the interaction between only one pair of particles, and the interactions between the other two pairs can be zero or otherwise negligible.

5.2.2 Explicit link between three-body and two-body scattering

The ideas discussed in the preceding section suggest what features to look for in three-body scattering, and how they might be interpreted. However, they do not directly tell us about 3-body recombination in complex systems, or shed light on the potential connection between a 2-body collision lifetime and features in a description of 3-body scattering. Here we will make the first steps towards such a connection, although this line of research has not yet proceeded very far; the contents of this section should be regarded as proposals for future work rather than conclusions that have been reached from work performed.

The basic strategy we employ is a change of variables to reintroduce the BC diatom bond length $r_{\mathrm{A}} = |\mathbf{r}_{\mathrm{A}}|$ as a coordinate in place of θ_{A}. This allows the adiabatic equation $\hat{H}_{\mathrm{ad}}\Phi = \varepsilon\Phi$ to be expressed and solved in the manner of a 2-body collision with r_{A} as the distance coordinate, and ρ entering only as a parameter. Of course, the resulting problem is not actually a collision problem, but analogous to a 2-body *bound-state* problem. However, the link between collision and bound-state problems is strong and generally well understood, so should allow any results in this picture to be correctly interpreted. For this discussion we will assume that the

[2] We use 'Efimov physics' [338] quite generally to cover many associated effects, not just the appearance of an infinite series of bound states originally considered by Efimov [348].

only interaction potential present in the system is between B and C, $V(\rho, \theta_X, \Theta_X) = V_{\rm BC}(r_{\rm A})$, which will not allow 3-body recombination but will, as discussed, allow λ-changing collisions which we believe will be correlated with 3-body recombination.

To get the adiabatic equations into a suitable form for the change of variables, we must first expand the grand angular momentum operator as

$$\hat{\Lambda}^2 = -\frac{\hbar^2}{\sin^2 2\theta_{\rm A}} \frac{\partial}{\partial \theta_{\rm A}} \sin^2 2\theta_{\rm A} \frac{\partial}{\partial \theta_{\rm A}} + \frac{\hat{\mathcal{L}}_{\rm A}^2}{\cos^2 \theta_{\rm A}} + \frac{\hat{\mathcal{J}}_{\rm A}^2}{\sin^2 \theta_{\rm A}} \tag{5.2.32}$$

$$= \frac{2}{\sin 2\theta_{\rm A}} \frac{\partial^2}{\partial \theta_{\rm A}^2} \frac{\sin 2\theta_{\rm A}}{2} + 4 + \frac{\hat{\mathcal{L}}_{\rm A}^2}{\cos^2 \theta_{\rm A}} + \frac{\hat{\mathcal{J}}_{\rm A}^2}{\sin^2 \theta_{\rm A}}. \tag{5.2.33}$$

Here, $\hat{\mathcal{L}}_{\rm A}$ and $\hat{\mathcal{J}}_{\rm A}$ are the angular momentum operators corresponding to the angular motion of A with BC, and B with C, respectively; this is in accordance with their usual definitions for the atom+diatom system A+BC. This allows us to rewrite the adiabatic equation in the form

$$\frac{\partial^2}{\partial \theta_{\rm A}^2} \phi(\theta_{\rm A}; \rho) = W(\theta_{\rm A}; \rho) \phi(\theta_{\rm A}; \rho), \tag{5.2.34}$$

with the replacement $\phi = \frac{2}{\sin 2\theta_{\rm A}} \Phi$. W contains contributions from many different terms, and so we will not write W explicitly in its entirety, but merely consider pertinent contributions.

The method for a change of variable for an equation like eq. (5.2.34) is given explicitly in Ref. [349], although the general method is, of course, well known. We map from $\theta_{\rm A}$ to $r_{\rm A} = d_{\rm A} \rho \sin \theta_{\rm A}$, and write

$$\frac{\partial^2}{\partial r_{\rm A}^2} \chi(r_{\rm A}) = \mathcal{W}(r_{\rm A}) \chi(r_{\rm A}), \tag{5.2.35}$$

where $\chi(r_{\rm A}) = (dr_{\rm A}/d\theta_{\rm A})^{1/2} \phi(\theta_{\rm A})$ and an explicit expression for $\mathcal{W}(r_{\rm A})$ is given in Ref. [349] in terms of W and the Jacobian for the transformation. In this form, it would probably be possible to implement this problem directly in some bound-state programs, such as BOUND.

We now pick out some of the important terms in $\mathcal{W}$. First, we consider

$$\left(\frac{1}{1-\frac{r_{\mathrm{A}}^2}{\rho^2 d_{\mathrm{A}}^2}}\right)\frac{2\mu_3}{\hbar^2 d_{\mathrm{A}}^2}\left[V_{\mathrm{BC}}(r_{\mathrm{A}})-\varepsilon+\frac{\hat{\mathcal{J}}^2}{2\mu_{BC}r_{\mathrm{A}}^2}\right], \tag{5.2.36}$$

where μ_{BC} is the usual 2-body reduced mass of B and C.[3] The term in square brackets here exactly corresponds to the description of the interaction of the two particles B and C (where $\hat{\mathcal{J}}$ describes the end-over-end angular momentum, which would usually have been given the symbol $\hat{\mathcal{L}}$ in a purely 2-body description). This is scaled by the term in round brackets which starts at 1 at $r_{\mathrm{A}}=0$ and increases on a length scale set by ρd_{A} before diverging at $r_{\mathrm{A,max}}=\rho d_{\mathrm{A}}$. Note that this divergence goes as only $(r_{\mathrm{A,max}}-r_{\mathrm{A}})^{-1}$ and so the singularity in eq. (5.2.35) is integrable even when it diverges to $-\infty$, although care will need to be taken over both boundary conditions and numerical propagation of solutions. Another important physical term in $\mathcal{W}$ is

$$\left(\frac{1}{1-\frac{r_{\mathrm{A}}^2}{\rho^2 d_{\mathrm{A}}^2}}\right)^2\frac{2\mu_3}{\hbar^2\rho^2}\frac{\hat{\mathcal{L}}^2}{2\mu_{\mathrm{A-BC}}}, \tag{5.2.37}$$

where $\mu_{\mathrm{A-BC}}=d_{\mathrm{A}}^2\mu_3$ is the reduced mass of A and BC. This term describes the centrifugal motion of A about the centre of mass of BC, and it is less obvious in structure than eq. (5.2.36) because the coordinates we have chosen are far from a natural set for this term. It diverges as $r_{\mathrm{A}}\to r_{\mathrm{A,max}}$, which is when $\theta_{\mathrm{A}}\to\pi/2$ and A approaches the CM of BC, as expected; also note that it diverges faster than the term in eq. (5.2.36), so if the angular momentum $\hat{\mathcal{L}}$ is non-zero then the overall divergence of $\mathcal{W}$ as $r_{\mathrm{A}}\to r_{\mathrm{A,max}}$ will be repulsive and formally non-integrable and therefore numerically easier to handle in practice. There are other terms in $\mathcal{W}$, but they do not have such easily understandable physical interpretations. It is not clear whether those extra terms are physically important, or may become physically important at low energy, so further work in this direction is needed.

Finding bound-state solutions to eq. (5.2.35) will hopefully allow us to understand important quantities in the three-body problem. It should be feasible to char-

[3]The 2- and 3- body reduced masses and the mass scaling factor d_X are related by $d_{\mathrm{A}}^2\mu_{\mathrm{BC}}=\mu_3$.

acterise the avoided crossing of metastable and continuum levels, and also calculate the associated non-adiabatic couplings. A productive first step would probably be to identify and characterise these quantities in a high-energy region, where we do expect the classical picture to hold, and to find that the 2-body collision lifetime does indeed determine some or all of the important quantities. Once this has been achieved, and this description of the three-body physics is better understood, then the low-energy behaviours can be usefully investigated.

At large ρ, the scaling in eq. (5.2.36) will remain near unity for most or all of the range of r_{A} for which the two-body interaction is important. Therefore, in this region the system can be considered to behave exactly as it would in the pure two-body case. The deviations from the two-body case will occur as r_{A} becomes larger and approaches ρd_{A} and the system in this region will behave independently of the details at short range. This suggests that an approach based on QDT might be a productive direction to investigate. The general form of the problem is not too dissimilar to QDT in a harmonic trap [350–352]; the effective potentials are obviously very different, but the same basic QDT ideas may be useful.

5.3 Conclusions and future directions

We have considered the ideas of John Bohn and co-workers [207, 208] that at ultracold temperatures three-body recombination is dramatically enhanced by long-lived 2-body collisions. We have attempted to put the theory on a more rigorous footing by considering the lifetime matrix of Smith [332], which we investigated numerically at ultracold energies. However, the definition used by Smith neglects a term proportional to E^{-1}, which we found to dominate in the case of ultracold resonant collisions. More detailed consideration of the contributions to the lifetime showed that this contribution arises from long-range oscillations and not any short-range behaviour. Therefore, while Smith's definition is perfectly useful for many situations, it is a fatally flawed quantity for considering the mechanism envisaged by Bohn.

We considered two other candidate definitions of a collision lifetime, which were more promising. We numerically explored their behaviour in the ultracold regime.

However, we did not find either has a persuasive case to represent the lifetime of a collision complex at short-range, or to determine 3-body recombination. Therefore, we approached the three-body scattering problem directly.

From consideration of the three-body problem we concluded that the process proposed by Bohn corresponds to scattering originating in channels with large values of the grand angular momentum quantum number λ, and that a simple characteristic indicator of this process would be large cross sections for elastic 3-body collisions which cause a large change in the value of λ. Three-body scattering calculations for this process may be significantly easier than those for 3-body recombination. We also observed that the effect proposed by Bohn is distinct from the Efimov physics considered by the majority of explicit ultracold three-body scattering calculations to date.

In the final section, we put forward the idea of reformulating the hyperspherical adiabatic equation in a form that makes clear the analogy to a two-body scattering (or bound-state) problem. These ideas are not fully developed and significant further work is needed to know if they will prove to be useful. Explicit calculations of adiabats using BOUND is likely achievable in the near future. We suggest a preference for the use of BOUND, or a similar program, because of its suitability for considering problems that are closely related to scattering problems. Hopefully this explicit connection to 2-body interactions will allow us to apply our accumulated knowledge to help shed light on the problem.

Beyond this, we can immediately suggest some explicit calculations that may be possible with suitable three-body scattering codes. There are three features we think may be important for such calculations:

1. Perform calculations that deliberately do not show Efimov physics. The model we considered featured an interaction between only two of the three particles with the third completely non-interacting, which is an extreme limit of this.

2. Consider higher grand angular momentum λ.

3. Consider a resonance that is both at low energy (say, $E_{\rm res} \ll E_6$) and narrow in energy ($\Gamma_E \ll E_0$), to consider directly the effects of the very narrow

resonances proposed by Bohn.

Without direct expertise in use of three-body scattering programs, it is difficult to say if any or all of these desired features will pose problems in practice. The first should not be difficult to guarantee, provided the program is not restricted to work only with identical particles. The second should be trivial to implement if the programs are already written to deal with arbitrary λ; some three-body scattering programs clearly are, but it is not immediately clear if those used for ultracold scattering calculations are. However, even if the program is capable of dealing with this in principle, it will increase significantly the number of channels and the computational expense of the calculations. The third should be straightforward to implement for code that is able to include closed 2-body channels that can support Feshbach resonances explicitly [340].

Chapter 6

Conclusions and Future Work

In this thesis we have explored a wide variety of features of complex cold and ultracold collisions. In chapter 2 we investigated QDT, and in particular AQDT, for a series of increasingly complex systems. We found that it went from an excellent quantitatively predictive model for the simplest systems to predicting typical general behaviours for more complex systems. Even this level of predictive power for complex systems is impressive for such a simple model. We then went on to demonstrate a QDT model of loss that produced a quantitative model for the *range* of possible behaviour when the interaction potential was uncertain.

In chapter 3 we considered and discussed several effects of thermalisation that were not wholly new, but were in need of greater consideration and understanding. Firstly, consideration of the correct cross section for thermalisation $\sigma_\eta^{(1)}$ was shown to be important for determination of scattering lengths from thermalisation measurements to account for the variation in deflection angles for scattering outside the s-wave regime. Understanding deflection angles also played an important role in high quality simulations of sympathetic cooling in a microwave trap. These simulations showed cooling of CaF with Rb to be likely to succeed, even if the scattering length of the system happens to be moderately unfavourable. The importance of correctly differentiating between centre-of-mass and laboratory frames was also highlighted, playing an important role in the decision that Li was likely not the most suitable coolant for CaF in a microwave trap. This subsequently allowed reanalysis of previous results for sympathetic cooling in a magnetic trap, leading to a suggestion that

sympathetic cooling might be possible starting at considerably higher temperatures than previously thought. The small mass of Li might make it an excellent coolant for magnetically trapped CaF because of both the large centrifugal barriers in outgoing channels and a large ratio between laboratory frame and CM energies; in this case, the cooling may be able to start from molecular temperatures in excess of 100 mK.

In chapter 4 we analysed various systems in terms of quantum chaos and RMT. We found very clear signs of chaos for Li+CaH for $J = 0$. However, for other cases including Li+CaH in $J = 1$ and Li+CaF, we found clear signs that the motion is *not* fully chaotic, and there are approximately conserved constants of the motion, even where we expected none. We have demonstrated the complicated nature of the relationship between coupling strength and chaos. Starting from a chaotic system and increasing the strength of a coupling does not necessarily lead to an increase in chaos. This should not be surprising in principle: if a single term in a hamiltonian becomes dominant, that term defines nearly good quantum numbers for the system. We also studied Yb+Yb* and showed that chaotic spectra in atomic collisions do not require large numbers of electronic states and can arise in quite simple systems if the anisotropy is strong enough.

Finally, in chapter 5, we considered whether long-lived 2-body collisions cause large enhancements of 3-body recombination at low energy. The idea is persuasive, but has proved difficult to consider rigorously. We tried to analyse it in terms of Smith's collision lifetime [332], but found this was not a suitable quantity to represent short-range effects at low energy. We considered various elements of explicit three-body collision theory, and made some general arguments about how we would expect long-lived 2-body metastable states to appear in three-body scattering theory. We then proposed some practical directions forward, both for full three-body calculations, and for attempting to understand the link between two-body and three-body collisions.

Chapter 7

Bibliography

[1] M. H. Anderson, J. R. Ensher, M. R. Matthews, C. E. Wieman, and E. A. Cornell, *Observation of Bose-Einstein condensation in a dilute atomic vapor*, Science 269, 198 (1995).

[2] K. B. Davis, M.-O. Mewes, M. R. Andrews, N. J. van Druten, D. S. Durfee, D. M. Kurn, and W. Ketterle, *Bose-Einstein condensation in a gas of sodium atoms*, Phys. Rev. Lett. 75, 3969 (1995).

[3] W. Ketterle, *Nobel lecture: When atoms behave as waves: Bose-Einstein condensation and the atom laser*, Rev. Mod. Phys. 74, 1131 (2002).

[4] E. A. Cornell and C. E. Wieman, *Nobel lecture: Bose-Einstein condensation in a dilute gas, the first 70 years and some recent experiments*, Rev. Mod. Phys. 74, 875 (2002).

[5] Sir William Ramsay, *Nobel lecture: The rare gases of the atmosphere* (1904), in *Nobel Lectures, Chemistry 1901-1921* (Elsevier Publishing Company, Amsterdam, 1966).

[6] H. K. Onnes, *Nobel lecture: Investigations into the properties of substances at low temperatures, which have led, amongst other things, to the preparation of liquid helium* (1913), in *Nobel Lectures, Physics 1901-1921* (Elsevier Publishing Company, Amsterdam, 1967).

[7] B. DeMarco and D. S. Jin, *Onset of fermi degeneracy in a trapped atomic gas*, Science 285, 1703 (1999).

[8] T. Hänsch and A. Schawlow, *Cooling of gases by laser radiation*, Optics Communications 13, 68 (1975).

[9] A. Ashkin, *Trapping of atoms by resonance radiation pressure*, Phys. Rev. Lett. 40, 729 (1978).

[10] S. V. Andreev, V. I. Balykin, V. S. Letokhov, and V. G. Minogin, *Radiative slowing and reduction of the energy spread of a beam of sodium atoms to 1.5 K in an oppositely directed laser-beam*, JETP Lett. 34, 442 (1981).

[11] W. D. Phillips, *Nobel lecture: Laser cooling and trapping of neutral atoms*, Rev. Mod. Phys. 70, 721 (1998).

[12] W. D. Phillips and H. Metcalf, *Laser deceleration of an atomic-beam*, Phys. Rev. Lett. 48, 596 (1982).

[13] E. L. Raab, M. Prentiss, A. Cable, S. Chu, and D. E. Pritchard, *Trapping of neutral sodium atoms with radiation pressure*, Phys. Rev. Lett. 59, 2631 (1987).

[14] S. Chu, L. Hollberg, J. E. Bjorkholm, A. Cable, and A. Ashkin, *3-dimensional viscous confinement and cooling of atoms by resonance radiation pressure*, Phys. Rev. Lett. 55, 48 (1985).

[15] P. D. Lett, R. N. Watts, C. I. Westbrook, W. D. Phillips, P. L. Gould, and H. J. Metcalf, *Observation of atoms laser cooled below the doppler limit*, Phys. Rev. Lett. 61, 169 (1988).

[16] J. Dalibard and C. Cohen-Tannoudji, *Laser cooling below the doppler limit by polarization gradients - simple theoretical-models*, J. Opt. Soc. Am. B – Opt. Phys. 6, 2023 (1989).

[17] N. Masuhara, J. M. Doyle, J. C. Sandberg, D. Kleppner, T. J. Greytak, H. F. Hess, and G. P. Kochanski, *Evaporative cooling of spin-polarized atomic-hydrogen*, Phys. Rev. Lett. 61, 935 (1988).

[18] W. Petrich, M. H. Anderson, J. R. Ensher, and E. A. Cornell, *Stable, tight confining magnetic trap for evapoative cooling of neutral atoms*, Phys. Rev. Lett. 74, 3352 (1995).

[19] C. J. Myatt, E. A. Burt, R. W. Ghrist, E. A. Cornell, and C. E. Wieman, *Production of two overlapping Bose-Einstein condensates by sympathetic cooling*, Phys. Rev. Lett. 78, 586 (1997).

[20] I. Bloch, M. Greiner, O. Mandel, T. W. Hänsch, and T. Esslinger, *Sympathetic cooling of* ^{85}Rb *and* ^{87}Rb, Phys. Rev. A 64, 021402 (2001).

[21] F. Schreck, G. Ferrari, K. L. Corwin, J. Cubizolles, L. Khaykovich, M. O. Mewes, and C. Salomon, *Sympathetic cooling of bosonic and fermionic lithium gases towards quantum degeneracy*, Phys. Rev. A 64, 011402 (2001).

[22] A. G. Truscott, K. E. Strecker, W. I. McAlexander, G. B. Partridge, and R. G. Hulet, *Observation of fermi pressure in a gas of trapped atoms*, Science 291, 2570 (2001).

[23] Z. Hadzibabic, C. A. Stan, K. Dieckmann, S. Gupta, M. W. Zwierlein, A. Görlitz, and W. Ketterle, *Two-species mixture of quantum degenerate bose and fermi gases*, Phys. Rev. Lett. 88, 160401 (2002).

[24] G. Modugno, G. Ferrari, G. Roati, R. J. Brecha, A. Simoni, and M. Inguscio, *Bose-Einstein condensation of potassium atoms by sympathetic cooling*, Science 294, 1320 (2001).

[25] K. M. Jones, E. Tiesinga, P. D. Lett, and P. S. Julienne, *Ultracold photoassociation spectroscopy: long-range molecules and atomic scattering*, Rev. Mod. Phys. 78, 483 (2006).

[26] C. P. Koch and M. Shapiro, *Coherent control of ultracold photoassociation*, Chemical Reviews 112, 4928 (2012).

[27] H. R. Thorsheim, J. Weiner, and P. S. Julienne, *Laser-induced photoassociation of ultracold sodium atoms*, Phys. Rev. Lett. 58, 2420 (1987).

[28] Y. B. Band and P. S. Julienne, *Ultracold-molecule production by laser-cooled atom photoassociation*, Phys. Rev. A 51, R4317 (1995).

[29] J. L. Bohn and P. S. Julienne, *Semianalytic treatment of two-color photoassociation spectroscopy and control of cold atoms*, Phys. Rev. A 54, R4637 (1996).

[30] A. Fioretti, D. Comparat, A. Crubellier, O. Dulieu, F. Masnou-Seeuws, and P. Pillet, *Formation of cold Cs_2 molecules through photoassociation*, Phys. Rev. Lett. 80, 4402 (1998).

[31] P. S. Julienne, K. Burnett, Y. B. Band, and W. C. Stwalley, *Stimulated raman molecule production in Bose-Einstein condensates*, Phys. Rev. A 58, R797 (1998).

[32] R. Wynar, R. S. Freeland, D. J. Han, C. Ryu, and D. J. Heinzen, *Molecules in a Bose-Einstein condensate*, Science 287, 1016 (2000).

[33] T. Köhler, K. Góral, and P. S. Julienne, *Production of cold molecules via magnetically tunable Feshbach resonances*, Rev. Mod. Phys. 78, 1311 (2006).

[34] F. H. Mies, E. Tiesinga, and P. S. Julienne, *Manipulation of Feshbach resonances in ultracold atomic collisions using time-dependent magnetic fields*, Phys. Rev. A 61, 022721 (2000).

[35] J. Cubizolles, T. Bourdel, S. J. J. M. F. Kokkelmans, G. V. Shlyapnikov, and C. Salomon, *Production of long-lived ultracold Li_2 molecules from a fermi gas*, Phys. Rev. Lett. 91, 240401 (2003).

[36] S. Jochim, M. Bartenstein, A. Altmeyer, G. Hendl, S. Riedl, C. Chin, J. Hecker Denschlag, and R. Grimm, *Bose-Einstein condensation of molecules*, Science 302, 2101 (2003).

[37] C. A. Regal, C. Ticknor, J. L. Bohn, and D. S. Jin, *Creation of ultracold molecules from a fermi gas of atoms*, Nature 424, 47 (2003).

[38] J. Herbig, T. Kraemer, M. Mark, T. Weber, C. Chin, H. C. Nägerl, and R. Grimm, *Preparation of a pure molecular quantum gas*, Science 301, 1510 (2003).

[39] K. Xu, T. Mukaiyama, J. R. Abo-Shaeer, J. K. Chin, D. E. Miller, and W. Ketterle, *Formation of quantum-degenerate sodium molecules*, Phys. Rev. Lett. 91, 210402 (2003).

[40] S. Dürr, T. Volz, A. Marte, and G. Rempe, *Observation of molecules produced from a Bose-Einstein condensate*, Phys. Rev. Lett. 92, 020406 (2004).

[41] C. Ospelkaus, S. Ospelkaus, L. Humbert, P. Ernst, K. Sengstock, and K. Bongs, *Ultracold heteronuclear molecules in a 3D optical lattice*, Phys. Rev. Lett. 97, 120402 (2006).

[42] T. Takekoshi, M. Debatin, R. Rameshan, F. Ferlaino, R. Grimm, H.-C. Nägerl, C. R. Le Sueur, J. M. Hutson, P. S. Julienne, S. Kotochigova, and E. Tiemann, *Towards the production of ultracold ground-state RbCs molecules: Feshbach resonances, weakly bound states, and coupled-channel models*, Phys. Rev. A 85, 032506 (2012).

[43] A. Frisch, M. Mark, K. Aikawa, S. Baier, R. Grimm, A. Petrov, S. Kotochigova, G. Quéméner, M. Lepers, O. Dulieu, and F. Ferlaino, *Ultracold dipolar molecules composed of strongly magnetic atoms*, Phys. Rev. Lett. 115, 203201 (2015).

[44] P. S. Żuchowski, J. Aldegunde, and J. M. Hutson, *Ultracold RbSr molecules can be formed by magnetoassociation*, Phys. Rev. Lett. 105, 153201 (2010).

[45] D. A. Brue and J. M. Hutson, *Magnetically tunable Feshbach resonances in ultracold Li-Yb mixtures*, Phys. Rev. Lett. 108, 043201 (2012).

[46] D. A. Brue and J. M. Hutson, *Prospects of forming molecules in $^2\Sigma$ states by magnetoassociation of alkali-metal atoms with Yb*, Phys. Rev. A 87, 052709 (2013).

[47] K. Bergmann, H. Theuer, and B. W. Shore, *Coherent population transfer among quantum states of atoms and molecules*, Rev. Mod. Phys. 70, 1003 (1998).

[48] K. Winkler, F. Lang, G. Thalhammer, P. van der Straten, R. Grimm, J. Hecker Denschlag, A. J. Daley, A. Kantian, H. P. Büchler, and P. Zoller, *Coherent optical transfer of Feshbach molecules to a lower vibrational state*, Phys. Rev. Lett. 98, 043201 (2007).

[49] K.-K. Ni, S. Ospelkaus, M. H. G. de Miranda, A. Pe'er, B. Neyenhuis, J. J. Zirbel, S. Kotochigova, P. S. Julienne, D. S. Jin, and J. Ye, *A high phase-space-density gas of polar molecules in the rovibrational ground state*, Science 322, 231 (2008).

[50] T. Takekoshi, L. Reichsöllner, A. Schindewolf, J. M. Hutson, C. R. Le Sueur, O. Dulieu, F. Ferlaino, R. Grimm, and H.-C. Nägerl, *Ultracold dense samples of dipolar RbCs molecules in the rovibrational and hyperfine ground state*, Phys. Rev. Lett. 113, 205301 (2014).

[51] P. K. Molony, P. D. Gregory, Z. Ji, B. Lu, M. P. Köppinger, C. R. Le Sueur, C. L. Blackley, J. M. Hutson, and S. L. Cornish, *Creation of ultracold* $^{87}Rb^{133}Cs$ *molecules in the rovibrational ground state*, Phys. Rev. Lett. 113, 255301 (2014).

[52] J. W. Park, S. A. Will, and M. W. Zwierlein, *Ultracold dipolar gas of fermionic* $^{23}Na^{40}K$ *molecules in their absolute ground state*, Phys. Rev. Lett. 114, 205302 (2015).

[53] M. Guo, B. Zhu, B. Lu, X. Ye, F. Wang, R. Vexiau, N. Bouloufa-Maafa, G. Quéméner, O. Dulieu, and D. Wang, *Creation of an ultracold gas of ground-state dipolar* $^{23}Na^{87}Rb$ *molecules*, Phys. Rev. Lett. 116, 205303 (2016).

[54] J. M. Doyle, B. Fredrich, J. Kim, and D. Patterson, *Buffer-gas loading of atoms and molecules into a magnetic trap*, Phys. Rev. A 52, R2515 (1995).

[55] J. Kim, B. Friedrich, D. P. Katz, D. Patterson, J. D. Weinstein, R. DeCarvalho, and J. M. Doyle, *Buffer-gas loading and magnetic trapping of atomic europium*, Phys. Rev. Lett. 78, 3665 (1997).

[56] R. deCarvalho, J. M. Doyle, B. Friedrich, T. Guillet, J. Kim, D. Patterson, and J. D. Weinstein, *Buffer-gas loaded magnetic traps for atoms and molecules: A primer*, Eur. Phys. J. D 7, 289 (1999).

[57] D. Egorov, W. C. Campbell, B. Friedrich, S. E. Maxwell, E. Tsikata, L. D. van Buuren, and J. M. Doyle, *Buffer-gas cooling of NH via the beam loaded buffer-gas method*, Eur. Phys. J. D 31, 307 (2004).

[58] D. Egorov, T. Lahaye, W. Schöllkopf, B. Friedrich, and J. M. Doyle, *Buffer-gas cooling of atomic and molecular beams*, Phys. Rev. A 66, 043401 (2002).

[59] J. D. Weinstein, R. deCarvalho, T. Guillet, B. Friedrich, and J. M. Doyle, *Magnetic trapping of calcium monohydride molecules at millikelvin temperatures*, Nature 395, 148 (1998).

[60] J. D. Weinstein, R. deCarvalho, K. Amar, A. Boca, B. C. Odom, B. Friedrich, and J. M. Doyle, *Spectroscopy of buffer-gas cooled vanadium monoxide in a magnetic trapping field*, The Journal of Chemical Physics 109, 2656 (1998).

[61] D. Egorov, J. D. Weinstein, D. Patterson, B. Friedrich, and J. M. Doyle, *Spectroscopy of laser-ablated buffer-gas-cooled PbO at 4 K and the prospects for measuring the electric dipole moment of the electron*, Phys. Rev. A 63, 030501 (2001).

[62] K. Maussang, D. Egorov, J. S. Helton, S. V. Nguyen, and J. M. Doyle, *Zeeman relaxation of CaF in low-temperature collisions with helium*, Phys. Rev. Lett. 94, 123002 (2005).

[63] W. C. Campbell, E. Tsikata, H.-I. Lu, L. D. van Buuren, and J. M. Doyle, *Magnetic trapping and zeeman relaxation of NH ($X^3\Sigma^-$)*, Phys. Rev. Lett. 98, 213001 (2007).

[64] M. Stoll, J. M. Bakker, T. C. Steimle, G. Meijer, and A. Peters, *Cryogenic buffer-gas loading and magnetic trapping of CrH and MnH molecules*, Phys. Rev. A 78, 032707 (2008).

[65] M. T. Hummon, W. C. Campbell, H.-I. Lu, E. Tsikata, Y. Wang, and J. M. Doyle, *Magnetic trapping of atomic nitrogen (^{14}N) and cotrapping of NH ($X^3\Sigma^-$)*, Phys. Rev. A 78, 050702 (2008).

[66] E. Tsikata, W. C. Campbell, M. T. Hummon, H.-I. Lu, and J. M. Doyle, *Magnetic trapping of NH molecules with 20 s lifetimes*, New J. Phys. 12, 065028 (2010).

[67] S. E. Maxwell, N. Brahms, R. deCarvalho, D. R. Glenn, J. S. Helton, S. V. Nguyen, D. Patterson, J. Petricka, D. DeMille, and J. M. Doyle, *High-flux beam source for cold, slow atoms or molecules*, Phys. Rev. Lett. 95, 173201 (2005).

[68] D. Patterson, J. Rasmussen, and J. M. Doyle, *Intense atomic and molecular beams via neon buffer-gas cooling*, New J. Phys. 11, 055018 (2009).

[69] D. Patterson and J. M. Doyle, *Bright, guided molecular beam with hydrodynamic enhancement*, J. Chem. Phys. 126, 154307 (2007).

[70] J. M. Doyle and W. C. Campbell, *Cooling, trap loading, and beam production using a cryogenic helium buffer gas*, in W. C. . Stwalley, R. V. . Krems, , and B. Friedrich (Editors), *Cold Molecules: Theory, Experiment, Applications* (CRC Press, 2009), ISBN 978-1-4200-5903-8.

[71] N. R. Hutzler, H.-I. Lu, and J. M. Doyle, *The buffer gas beam: An intense, cold, and slow source for atoms and molecules*, Chemical Reviews 112, 4803, pMID: 22571401 (2012).

[72] N. E. Bulleid, S. M. Skoff, R. J. Hendricks, B. E. Sauer, E. A. Hinds, and M. R. Tarbutt, *Characterization of a cryogenic beam source for atoms and molecules*, Phys. Chem. Chem. Phys. 15, 12299 (2013).

[73] H. L. Bethlem, G. Berden, and G. Meijer, *Decelerating neutral dipolar molecules*, Phys. Rev. Lett. 83, 1558 (1999).

[74] E. Narevicius, C. G. Parthey, A. Libson, J. Narevicius, I. Chavez, U. Even, and M. G. Raizen, *An atomic coilgun: using pulsed magnetic fields to slow a supersonic beam*, New J. Phys. 9, 358 (2007).

[75] S. D. Hogan, M. Motsch, and F. Merkt, *Deceleration of supersonic beams using inhomogeneous electric and magnetic fields*, Phys. Chem. Chem. Phys. 13, 18705 (2011).

[76] H. L. Bethlem, G. Berden, F. M. H. Crompvoets, R. T. Jongma, A. J. A. van Roij, and G. Meijer, *Electrostatic trapping of ammonia molecules*, Nature 406, 491 (2000).

[77] S. A. Meek, H. L. Bethlem, H. Conrad, and G. Meijer, *Trapping molecules on a chip in traveling potential wells*, Phys. Rev. Lett. 100, 153003 (2008).

[78] A. Osterwalder, S. A. Meek, G. Hammer, H. Haak, and G. Meijer, *Deceleration of neutral molecules in macroscopic traveling traps*, Phys. Rev. A 81, 051401 (2010).

[79] E. Lavert-Ofir, L. David, A. B. Henson, S. Gersten, J. Narevicius, and E. Narevicius, *Stopping paramagnetic supersonic beams: the advantage of a co-moving magnetic trap decelerator*, Phys. Chem. Chem. Phys. 13, 18948 (2011).

[80] Trimeche, A., Bera, M.N., Cromières, J.-P., Robert, J., and Vanhaecke, N., *Trapping of a supersonic beam in a traveling magnetic wave*, Eur. Phys. J. D 65, 263 (2011).

[81] A. Mizouri, *A Moving-Trap Zeeman Decelerator*, Ph.D. thesis, Durham University (2016).

[82] M. S. Elioff, J. J. Valentini, and D. W. Chandler, *Subkelvin cooling NO molecules via "billiard-like" collisions with argon*, Science 302, 1940 (2003).

[83] K. Takase, L. A. Rahn, D. W. Chandler, and K. E. Strecker, *The kinematic cooling of molecules with laser-cooled atoms*, New J. Phys. 11, 055033 (2009).

[84] J. J. Kay, S. Y. T. van de Meerakker, K. E. Strecker, and D. W. Chandler, *Production of cold ND_3 by kinematic cooling*, Faraday Discuss. 142, 143 (2009).

[85] J. J. Kay, J. Kłos, M. H. Alexander, K. E. Strecker, and D. W. Chandler, *Cold atoms by kinematic cooling*, Phys. Rev. A 82, 032709 (2010).

[86] A. Trottier, D. Carty, and E. Wrede, *Photostop: production of zero-velocity molecules by photodissociation in a molecular beam*, Molecular Physics 109, 725 (2011).

[87] W. G. Doherty, M. T. Bell, T. P. Softley, A. Rowland, E. Wrede, and D. Carty, *Production of cold bromine atoms at zero mean velocity by photodissociation*, Phys. Chem. Chem. Phys. 13, 8441 (2011).

[88] N. R. Warner, *Advances in photostop*, Ph.D. thesis, Durham University (2016).

[89] M. Kajita, *Collision between magnetically trapped NH molecules in the ($N = 0$, $J = 1$) state*, Phys. Rev. A 74, 032710 (2006).

[90] L. M. C. Janssen, P. S. Żuchowski, A. van der Avoird, J. M. Hutson, and G. C. Groenenboom, *Cold and ultracold NH–NH collisions: the field-free case*, J. Chem. Phys. 134, 124309 (2011).

[91] L. M. C. Janssen, P. S. Żuchowski, A. van der Avoird, G. C. Groenenboom, and J. M. Hutson, *Cold and ultracold NH–NH collisions in magnetic fields*, Phys. Rev. A 83, 022713 (2011).

[92] L. M. C. Janssen, A. van der Avoird, and G. C. Groenenboom, *Quantum reactive scattering of ultracold* $\mathrm{NH}(X\,^3\Sigma^-)$ *radicals in a magnetic trap*, Phys. Rev. Lett. 110, 063201 (2013).

[93] B. K. Stuhl, M. T. Hummon, M. Yeo, G. Quéméner, J. L. Bohn, and J. Ye, *Evaporative cooling of the dipolar hydroxyl radical*, Nature 492, 396 (2012).

[94] P. Soldán and J. M. Hutson, *Interaction of NH($X^3\Sigma^-$) molecules with rubidium atoms: Implications for sympathetic cooling and the formation of extremely polar molecules*, Phys. Rev. Lett. 92, 163202 (2004).

[95] M. T. Cvitaš, P. Soldán, J. M. Hutson, P. Honvault, and J. M. Launay, *Ultracold collisions involving heteronuclear alkali metal dimers*, Phys. Rev. Lett. 94, 200402 (2005).

[96] M. Lara, J. L. Bohn, D. Potter, P. Soldán, and J. M. Hutson, *Ultracold Rb-OH collisions and prospects for sympathetic cooling*, Phys. Rev. Lett. 97, 183201 (2006).

[97] P. S. Żuchowski and J. M. Hutson, *The prospects for producing ultracold NH_3 molecules by sympathetic cooling: a survey of interaction potentials*, Phys. Rev. A 78, 022701 (2008).

[98] P. S. Żuchowski and J. M. Hutson, *Low-energy collisions of NH_3 and ND_3 with ultracold Rb atoms*, Phys. Rev. A 79, 062708 (2009).

[99] P. Soldán, P. S. Żuchowski, and J. M. Hutson, *Prospects for sympathetic cooling of polar molecules: NH with alkali-metal and alkaline-earth atoms – a new hope*, Faraday Discuss. 142, 191 (2009).

[100] A. O. G. Wallis and J. M. Hutson, *Production of ultracold NH molecules by sympathetic cooling with Mg*, Phys. Rev. Lett. 103, 183201 (2009).

[101] T. V. Tscherbul, J. Kłos, A. Dalgarno, B. Zygelman, Z. Pavlovic, M. T. Hummon, H.-I. Lu, E. Tsikata, and J. M. Doyle, *Collisional properties of cold spin-polarized nitrogen gas: Theory, experiment, and prospects as a sympathetic coolant for trapped atoms and molecules*, Phys. Rev. A 82, 042718 (2010).

[102] T. V. Tscherbul, H.-G. Yu, and A. Dalgarno, *Sympathetic cooling of polyatomic molecules with S-state atoms in a magnetic trap*, Phys. Rev. Lett. 106, 073201 (2011).

[103] M. L. González-Martínez and J. M. Hutson, *Effect of hyperfine interactions on ultracold molecular collisions: NH($^3\Sigma^-$) with Mg(^1S) in magnetic fields*, Phys. Rev. A 84, 052706 (2011).

[104] L. P. Parazzoli, N. J. Fitch, P. S. Żuchowski, J. M. Hutson, and H. J. Lewandowski, *Large effects of electric fields on atom-molecule collisions at millikelvin temperatures*, Phys. Rev. Lett. 106, 193201 (2011).

[105] M. T. Hummon, T. V. Tscherbul, J. Kłos, H.-I. Lu, E. Tsikata, W. C. Campbell, A. Dalgarno, and J. M. Doyle, *Cold N + NH collisions in a magnetic trap*, Phys. Rev. Lett. 106, 053201 (2011).

[106] A. O. G. Wallis, E. J. J. Longdon, P. S. Żuchowski, and J. M. Hutson, *The prospects of sympathetic cooling of NH molecules with Li atoms*, Eur. Phys. J. D 65, 151 (2011).

[107] T. V. Tscherbul, J. Kłos, and A. A. Buchachenko, *Ultracold spin-polarized mixtures of $^2\Sigma$ molecules with S-state atoms: Collisional stability and implications for sympathetic cooling*, Phys. Rev. A 84, 040701 (2011).

[108] A. Volpi and J. L. Bohn, *Magnetic-field effects in ultracold molecular collisions*, Phys. Rev. A 65, 052712 (2002).

[109] M. L. González-Martínez and J. M. Hutson, *Sympathetic cooling of fluorine atoms with ultracold atomic hydrogen*, Phys. Rev. A 88, 053420 (2013).

[110] M. L. González-Martínez and J. M. Hutson, *Ultracold hydrogen atoms: a versatile coolant to produce ultracold molecules*, Phys. Rev. Lett. 111, 203004 (2013).

[111] D. DeMille, D. R. Glenn, and J. Petricka, *Microwave traps for cold polar molecules*, Eur. Phys. J. D 31, 375 (2004).

[112] S. Tokunaga, W. Skomorowski, R. Moszynski, P. S. Żuchowski, J. M. Hutson, E. A. Hinds, and M. R. Tarbutt, *Prospects for sympathetic cooling of molecules in electrostatic, ac and microwave traps*, Eur. Phys. J. D 65, 141 (2011).

[113] J. Lim, M. D. Frye, J. M. Hutson, and M. R. Tarbutt, *Modeling sympathetic cooling of molecules by ultracold atoms*, Phys. Rev. A 92, 053419 (2015).

[114] E. S. Shuman, J. F. Barry, and D. DeMille, *Laser cooling of a diatomic molecule*, Nature 467, 820 (2010).

[115] V. Zhelyazkova, A. Cournol, T. E. Wall, A. Matsushima, J. J. Hudson, E. A. Hinds, M. R. Tarbutt, and B. E. Sauer, *Laser cooling and slowing of CaF molecules*, Phys. Rev. A 89 (2014).

[116] B. Hemmerling, E. Chae, A. Ravi, L. Anderegg, G. K. Drayna, N. R. Hutzler, A. L. Collopy, J. Ye, W. Ketterle, and J. M. Doyle, *Laser slowing of CaF molecules to near the capture velocity of a molecular MOT*, Journal of Physics B: Atomic, Molecular and Optical Physics 49, 174001 (2016).

[117] M. Yeo, M. T. Hummon, A. L. Collopy, B. Yan, B. Hemmerling, E. Chae, J. M. Doyle, and J. Ye, *Rotational state microwave mixing for laser cooling of complex diatomic molecules*, Phys. Rev. Lett. 114 (2015).

[118] M. T. Hummon, M. Yeo, B. K. Stuhl, A. L. Collopy, Y. Xia, and J. Ye, *Magneto-optical trapping of diatomic molecules*, Phys. Rev. Lett. 110, 143001 (2013).

[119] J. F. Barry, D. J. McCarron, E. B. Norrgard, M. H. Steinecker, and D. DeMille, *Magneto-optical trapping of a diatomic molecule*, Nature 512, 286 (2014).

[120] D. J. McCarron, E. B. Norrgard, M. H. Steinecker, and D. DeMille, *Improved magneto-optical trapping of a diatomic molecule*, New. J. Phys. 17 (2015).

[121] E. B. Norrgard, D. J. McCarron, M. H. Steinecker, M. R. Tarbutt, and D. DeMille, *Submillikelvin dipolar molecules in a radio-frequency magneto-optical trap*, Phys. Rev. Lett. 116, 063004 (2016).

[122] M. H. Steinecker, D. J. McCarron, Y. Zhu, and D. DeMille, *Improved radio-frequency magneto-optical trap of SrF molecules*, ChemPhysChem 17, 3664 (2016).

[123] L. D. Carr, D. DeMille, R. V. Krems, and J. Ye, *Cold and ultracold molecules: science, technology and applications*, New J. Phys. 11, 055049 (2009).

[124] J. P. Covey, S. A. Moses, J. Ye, and D. S. Jin, *Controlling a quantum gas of polar molecules in an optical lattice*, arXiv:1609.07671 (2016).

[125] A. O. G. Wallis and J. M. Hutson, *Optically induced conical intersections in traps for ultracold atoms and molecules*, Phys. Rev. A 84, 051402(R) (2011).

[126] A. O. G. Wallis, S. A. Gardiner, and J. M. Hutson, *Conical intersections in laboratory coordinates with ultracold molecules*, Phys. Rev. Lett. 103, 083201 (2009).

[127] A. Frisch, M. Mark, K. Aikawa, F. Ferlaino, J. L. Bohn, C. Makrides, A. Petrov, and S. Kotochigova, *Quantum chaos in ultracold collisions of gas-phase erbium atoms*, Nature 507, 475 (2014).

[128] T. Maier, H. Kadau, M. Schmitt, M. Wenzel, I. Ferrier-Barbut, T. Pfau, A. Frisch, S. Baier, K. Aikawa, L. Chomaz, M. J. Mark, F. Ferlaino, C. Makrides, E. Tiesinga, A. Petrov, and S. Kotochigova, *Emergence of chaotic scattering in ultracold Er and Dy*, Phys. Rev. X 5, 041029 (2015).

[129] D. G. Green, C. L. Vaillant, M. D. Frye, M. Morita, and J. M. Hutson, *Quantum chaos in ultracold collisions between $Yb(^1S_0)$ and $Yb(^3P_2)$*, Phys. Rev. A 93, 022703 (2016).

[130] M. D. Frye, M. Morita, C. L. Vaillant, D. G. Green, and J. M. Hutson, *Approach to chaos in ultracold atomic and molecular physics: Statistics of near-threshold bound states for Li+CaH and Li+CaF*, Phys. Rev. A 93, 052713 (2016).

[131] T. E. Wall, *Preparation of cold molecules for high-precision measurements*, Journal of Physics B: Atomic, Molecular and Optical Physics 49, 243001 (2016).

[132] J. J. Hudson, D. M. Kara, J. Smallman, B. E. Sauer, M. R. Tarbutt, and E. A. Hinds, *Improved measurement of the shape of the electron*, Nature London 473, 493 (2011).

[133] M. R. Tarbutt, B. E. Sauer, J. J. Hudson, and E. A. Hinds, *Design for a fountain of YbF molecules to measure the electron's electric dipole moment*, New Journal of Physics 15, 053034 (2013).

[134] C. Chin, V. V. Flambaum, and M. G. Kozlov, *Ultracold molecules: new probes on the variation of fundamental constants*, New J. Phys. 11, 055048 (2009).

[135] C. Chin and V. V. Flambaum, *Enhanced sensitivity to fundamental constants in ultracold atomic and molecular systems near Feshbach resonances*, Phys. Rev. Lett. 96, 230801 (2006).

[136] R. A. Hart, X. Xu, R. Legere, and K. Gibble, *A quantum scattering interferometer*, Nature 446, 892 (2007).

[137] D. DeMille, S. Sainis, J. Sage, T. Bergeman, S. Kotochigova, and E. Tiesinga, *Enhanced sensitivity to variation of m_e/m_p in molecular spectra*, Phys. Rev. Lett. 100, 043202 (2008).

[138] D. DeMille, *Quantum computation with trapped polar molecules*, Phys. Rev. Lett. 88, 067901 (2002).

[139] S. F. Yelin, K. Kirby, and R. Côté, *Schemes for robust quantum computation with polar molecules*, Phys. Rev. A 74, 050301 (2006).

[140] E. Kuznetsova, T. Bragdon, R. Côté, and S. F. Yelin, *Cluster-state generation using van der Waals and dipole-dipole interactions in optical lattices*, Phys. Rev. A 85, 012328 (2012).

[141] M. L. Wall, E. Bekaroglu, and L. D. Carr, *Molecular Hubbard Hamiltonian: Field regimes and molecular species*, Phys. Rev. A 88, 023605 (2013).

[142] M. L. Wall and L. D. Carr, *Hyperfine molecular Hubbard Hamiltonian*, Phys. Rev. A 82, 013611 (2010).

[143] B. Yan, S. A. Moses, B. Gadway, J. P. Covey, K. R. A. Hazzard, A. M. Rey, D. S. Jin, and J. Ye, *Observation of dipolar spin-exchange interactions with lattice-confined polar molecules*, Nature 501, 521 (2013).

[144] R. V. Krems, *Cold controlled chemistry*, Phys. Chem. Chem. Phys. 10, 4079 (2008).

[145] S. Ospelkaus, K.-K. Ni, D. Wang, M. H. G. de Miranda, B. Neyenhuis, G. Quéméner, P. S. Julienne, J. L. Bohn, D. S. Jin, and J. Ye, *Quantum-state controlled chemical reactions of ultracold KRb molecules*, Science 327, 853 (2010).

[146] V. Singh, K. S. Hardman, N. Tariq, M.-J. Lu, A. Ellis, M. J. Morrison, and J. D. Weinstein, *Chemical reactions of atomic lithium and molecular calcium monohydride at 1 K*, Phys. Rev. Lett. 108, 203201 (2012).

[147] T. V. Tscherbul and R. V. Krems, *Controlling electronic spin relaxation of cold molecules with electric fields*, Phys. Rev. Lett. 97, 083201 (2006).

[148] M. S. Child, *Molecular Collision Theory* (Academic Press, London, 1974).

[149] J. M. Hutson, *Theory of cold atomic and molecular collisions*, in R. V. Krems, W. C. Stwalley, and B. Friedrich (Editors), *Cold Molecules: Theory, Experiment, Applications*, pages 3–37 (Taylor & Francis, London, 2009).

[150] R. V. Krems and A. Dalgarno, *Collisions of atoms and molecules in external magnetic fields*, in E. J. Brändas and E. S. Kryachko (Editors), *Fundamental World of Quantum Chemistry*, volume 3, pages 273–294 (Kluwer Academic, 2004).

[151] G. C. Maitland, M. Rigby, E. B. Smith, and W. A. Wakeham, *Intermolecular Forces* (Clarendon Press, Oxford, 1981).

[152] R. G. Gordon, *A new method for constructing wavefunctions for bound states and scattering*, J. Chem. Phys. 51, 14 (1969).

[153] B. R. Johnson, *Renormalized Numerov method applied to calculating bound states of coupled-channel Schrödinger equation*, J. Chem. Phys. 69, 4678 (1978).

[154] B. R. Johnson, *New numerical methods applied to solving one-dimensional eigenvalue problem*, J. Chem. Phys. 67, 4086 (1977).

[155] J. M. Hutson, *Coupled-channel methods for solving the bound-state Schrödinger equation*, Comput. Phys. Commun. 84, 1 (1994).

[156] D. E. Manolopoulos, *An improved log-derivative method for inelastic scattering*, J. Chem. Phys. 85, 6425 (1986).

[157] B. R. Johnson, *Multichannel log-derivative method for scattering calculations*, J. Comput. Phys. 13, 445 (1973).

[158] E. P. Wigner, *On the behavior of cross sections near thresholds*, Phys. Rev. 73, 1002 (1948).

[159] O. Hinckelmann and L. Spruch, *Low-energy scattering by long-range potentials*, Phys. Rev. A 3, 642 (1971).

[160] C. L. Blackley, P. S. Julienne, and J. M. Hutson, *Effective-range approximations for resonant scattering of cold atoms*, Phys. Rev. A 89, 042701 (2014).

[161] H. A. Bethe, *Theory of disintegration of nuclei by neutrons*, Phys. Rev. 47, 747 (1935).

[162] J. M. Hutson, E. Tiesinga, and P. S. Julienne, *Avoided crossings between bound states of ultracold cesium dimers*, Phys. Rev. A 78, 052703 (2008).

[163] M. Berninger, A. Zenesini, B. Huang, W. Harm, H.-C. Nägerl, F. Ferlaino, R. Grimm, P. S. Julienne, and J. M. Hutson, *Feshbach resonances, weakly bound molecular states and coupled-channel potentials for cesium at high magnetic field*, Phys. Rev. A 87, 032517 (2013).

[164] J. M. Hutson, *Feshbach resonances in the presence of inelastic scattering: threshold behavior and suppression of poles in scattering lengths*, New J. Phys. 9, 152 (2007).

[165] J. R. Taylor, *Scattering Theory: The Quantum Theory of Nonrelativistic Collisions*, pages 411–412 (Wiley, New York, 1972).

[166] P. Courteille, R. S. Freeland, D. J. Heinzen, F. A. van Abeelen, and B. J. Verhaar, *Observation of a Feshbach resonance in cold atom scattering*, Phys. Rev. Lett. 81, 69 (1998).

[167] S. Inouye, M. R. Andrews, J. Stenger, H. J. Miesner, D. M. Stamper-Kurn, and W. Ketterle, *Observation of Feshbach resonances in a Bose-Einstein condensate*, Nature 392, 151 (1998).

[168] A. J. Moerdijk, B. J. Verhaar, and A. Axelsson, *Resonances in ultracold collisions of* ^{6}*Li,* ^{7}*Li, and* ^{23}*Na*, Phys. Rev. A 51, 4852 (1995).

[169] C. Chin, R. Grimm, E. Tiesinga, and P. S. Julienne, *Feshbach resonances in ultracold gases*, Rev. Mod. Phys. 82, 1225 (2010).

[170] J. M. Calvert and W. D. Davison, *Oscillation theory and computational procedures for matrix Sturm-Liouville eigenvalue problems, with an application to the hydrogen molecular ion*, Journal of Physics A: General Physics 2, 278 (1969).

[171] J. M. Hutson and S. Green, MOLSCAT *computer program* (2011).

[172] J. M. Hutson, BOUND *computer code* (2011).

[173] M. H. Alexander, D. E. Manolopoulos, H.-J. Werner, and B. Follmeg, HIBRIDON *computer program*, http://www2.chem.umd.edu/groups/alexander/hibridon/hib43/ (1987-).

[174] J. M. Hutson, FIELD *computer program, version 1* (2011).

[175] M. D. Frye and J. M. Hutson, *Collision cross sections for the thermalization of cold gases*, Phys. Rev. A 89, 052705 (2014).

[176] M. D. Frye, P. S. Julienne, and J. M. Hutson, *Cold atomic and molecular collisions: approaching the universal loss regime*, New J. Phys. 17, 045019 (2015).

[177] M. J. Seaton, *Quantum defect theory I. General formulation*, Proc. Phys. Soc. 88, 801 (1966).

[178] M. J. Seaton, *Quantum defect theory*, Rep. Prog. Phys. 46, 167 (1983).

[179] M. J. Seaton, *The quantum defect method*, Monthly Notices of the Royal Astronomical Society 118, 504 (1958).

[180] M. Gaĭlitis, *Behavior of cross sections near threshold of a new reaction in the case of a Coulomb attraction field*, Sov. Phys. JETP 17, 1328 (1962).

[181] F. H. Mies, *A multichannel quantum defect analysis of diatomic predissociation and inelastic atomic scattering*, J. Chem. Phys. 80, 2514 (1984).

[182] C. H. Greene, U. Fano, and G. Strinati, *General form of the quantum-defect theory*, Phys. Rev. A 19, 1485 (1979).

[183] B. Yoo and C. H. Greene, *Implementation of the quantum-defect theory for arbitrary long-range potentials*, Phys. Rev. A 34, 1635 (1986).

[184] B. Gao, *General form of the quantum-defect theory for* $-1/r^{\alpha}$ *type of potentials with* $\alpha > 2$, Phys. Rev. A 78, 012702 (2008).

[185] P. S. Julienne and F. H. Mies, *Collisions of ultracold trapped atoms*, J. Opt. Soc. Am. B 6, 2257 (1989).

[186] J. P. Burke, C. H. Greene, and J. L. Bohn, *Multichannel cold collisions: Simple dependences on energy and magnetic field*, Phys. Rev. Lett. 81, 3355 (1998).

[187] B. Gao, *Quantum-defect theory of atomic collisions and molecular vibration spectra*, Phys. Rev. A 58, 4222 (1998).

[188] F. H. Mies and M. Raoult, *Analysis of threshold effects in ultracold atomic collisions*, Phys. Rev. A 62, 012708 (2000).

[189] B. Gao, E. Tiesinga, C. J. Williams, and P. S. Julienne, *Multichannel quantum-defect theory for slow atomic collisions*, Phys. Rev. A 72, 042719 (2005).

[190] Z. Idziaszek and P. S. Julienne, *Universal rate constants for reactive collisions of ultracold molecules*, Phys. Rev. Lett. 104, 113202 (2010).

[191] J. F. E. Croft, A. O. G. Wallis, J. M. Hutson, and P. S. Julienne, *Multichannel quantum defect theory for cold molecular collisions*, Phys. Rev. A 84, 042703 (2011).

[192] J. F. E. Croft, J. M. Hutson, and P. S. Julienne, *Optimized multichannel quantum defect theory for cold molecular collisions*, Phys. Rev. A 86, 022711 (2012).

[193] J. F. E. Croft and J. M. Hutson, *Multichannel quantum defect theory for cold molecular collisions with a strongly anisotropic potential energy surface*, Phys. Rev. A 87, 032710 (2012).

[194] K. Jachymski, M. Krych, P. S. Julienne, and Z. Idziaszek, *Quantum theory of reactive collisions for* $1/r^n$ *potentials*, Phys. Rev. Lett. 110, 213202 (2013).

[195] K. Jachymski, M. Krych, P. S. Julienne, and Z. Idziaszek, *Quantum-defect model of a reactive collision at finite temperature*, Phys. Rev. A 90, 042705 (2014).

[196] Z. Idziaszek, G. Quéméner, J. L. Bohn, and P. S. Julienne, *Simple quantum model of ultracold polar molecule collisions*, Phys. Rev. A 82, 020703 (2010).

[197] P. S. Julienne, T. M. Hanna, and Z. Idziaszek, *Universal ultracold collision rates for polar molecules of two alkali-metal atoms*, Phys. Chem. Chem. Phys. 13, 19114 (2011).

[198] Z. Idziaszek, T. Calarco, P. S. Julienne, and A. Simoni, *Quantum theory of ultracold atom-ion collisions*, Phys. Rev. A 79, 010702 (2009).

[199] B. Gao, *Universal properties in ultracold ion-atom interactions*, Phys. Rev. Lett. 104, 213201 (2010).

[200] M. Li and B. Gao, *Quantum-defect theory of resonant charge exchange*, Phys. Rev. A 86, 012707 (2012).

[201] B. Gao, *Quantum-defect theory for $-1/r^4$-type interactions*, Phys. Rev. A 88, 022701 (2013).

[202] M. Li, L. You, and B. Gao, *Multichannel quantum-defect theory for ion-atom interactions*, Phys. Rev. A 89, 052704 (2014).

[203] M. Raoult and F. H. Mies, *Feshbach resonance in atomic binary collisions in the Wigner threshold law regime*, Phys. Rev. A 70, 012710 (2004).

[204] P. S. Julienne and B. Gao, *Simple theoretical models for resonant cold atom interactions*, AIP Conference Proceedings 869, 261 (2006).

[205] B. Gao, *Analytic description of atomic interaction at ultracold temperatures. II. Scattering around a magnetic Feshbach resonance*, Phys. Rev. A 84, 022706 (2011).

[206] B. Gao, *Analytic description of atomic interaction at ultracold temperatures: The case of a single channel*, Phys. Rev. A 80, 012702 (2009).

[207] M. Mayle, B. P. Ruzic, and J. L. Bohn, *Statistical aspects of ultracold resonant scattering*, Phys. Rev. A 85, 062712 (2012).

[208] M. Mayle, G. Quéméner, B. P. Ruzic, and J. L. Bohn, *Scattering of ultracold molecules in the highly resonant regime*, Phys. Rev. A 87, 012709 (2013).

[209] F. H. Mies and P. S. Julienne, *A multichannel quantum defect analysis of two-state couplings in diatomic molecules*, J. Chem. Phys. 80, 2526 (1984).

[210] F. H. Mies, *A multichannel quantum defect analysis of diatomic predissociation and inelastic atomic scattering*, J. Chem. Phys. 80, 2514 (1984).

[211] B. Gao, *Solutions of the schrödinger equation for an attractive $1/r^6$ potential*, Phys. Rev. A 58, 1728 (1998).

[212] B. Gao, *Zero-energy bound or quasibound states and their implications for diatomic systems with an asymptotic van der Waals interaction*, Phys. Rev. A 62, 050702 (2000).

[213] B. Gao, *Angular-momentum-insensitive quantum-defect theory for diatomic systems*, Phys. Rev. A 64, 010701 (2001).

[214] B. Gao, *Binding energy and scattering length for diatomic systems*, J. Phys. B 37, 4273 (2004).

[215] B. Gao, *Routines to calculate the AQDT parameters for an attractive* $1/r^6$ *potential, Version 2*, university of Toledo, Ohio (2003).

[216] G. F. Gribakin and V. V. Flambaum, *Calculation of the scattering length in atomic collisions using the semiclassical approximation*, Phys. Rev. A 48, 546 (1993).

[217] P. Zhang, H. R. Sadeghpour, and A. Dalgarno, *Structure and spectroscopy of ground and excited states of LiYb*, J. Chem. Phys. 133, 044306 (2010).

[218] A. O. G. Wallis, *Ultracold Molecules: The Effect of Electromagnetic Fields*, Ph.D. thesis, University of Durham (2010).

[219] S. Kotochigova, *Dispersion interactions and reactive collisions of ultracold polar molecules*, New J. Phys. 12, 073041 (2010).

[220] N. F. Mott and H. S. W. Massey, *The Theory of Atomic Collisions* (Clarendon Press, Oxford, 1965), 3rd edition.

[221] T. M. Hanna, E. Tiesinga, and P. S. Julienne, *Prediction of Feshbach resonances from three input parameters*, Phys. Rev. A 79, 040701 (2009).

[222] C. Ticknor, C. A. Regal, D. S. Jin, and J. L. Bohn, *Multiplet structure of Feshbach resonances in nonzero partial waves*, Phys. Rev. A 69, 042712 (2004).

[223] J. M. Hutson, *An introduction to the dynamics of Van der Waals molecules*, in *Advances in Molecular Vibrations and Collision Dynamics*, volume 1A, pages 1–45 (JAI Press, Greenwich, Connecticut, 1991).

[224] B. Gao, *Universal model for exoergic bimolecular reactions and inelastic processes*, Phys. Rev. Lett. 105, 263203 (2010).

[225] B. Gao, *Quantum langevin model for exoergic ion-molecule reactions and inelastic processes*, Phys. Rev. A 83, 062712 (2011).

[226] A. B. Henson, S. Gersten, Y. Shagam, J. Narevicius, and E. Narevicius, *Observation of resonances in penning ionization reactions at sub-kelvin temperatures in merged beams*, Science 338, 234 (2012).

[227] W. Skomorowski, F. Pawłowski, T. Korona, R. Moszynski, P. S. Żuchowski, and J. M. Hutson, *Interaction between a lithium hydride molecule and a lithium atom from state-of-the-art electronic structure calculations*, J. Chem. Phys. 134, 114109 (2011).

[228] J. M. Hutson and P. Soldán, *Molecular collisions in ultracold atomic gases*, Int. Rev. Phys. Chem. 26, 1 (2007).

[229] J. M. Hutson, M. Beyene, and M. L. González-Martínez, *Dramatic reductions in inelastic cross sections for ultracold collisions near Feshbach resonances*, Phys. Rev. Lett. 103, 163201 (2009).

[230] T. M. Hanna, E. Tiesinga, and P. S. Julienne, *Creation and manipulation of Feshbach resonances with radiofrequency radiation*, New J. Phys. 12, 083031 (2010).

[231] G.-R. Wang, T. Xie, W. Zhang, Y. Huang, and S.-L. Cong, *Prediction of Feshbach resonances using an analytical quantum-defect matrix*, Phys. Rev. A 85, 032706 (2012).

[232] G. Ferrari, M. Inguscio, W. Jastrzebski, G. Modugno, G. Roati, and A. Simoni, *Collisional properties of ultracold K-Rb mixtures*, Phys. Rev. Lett. 89, 053202 (2002).

[233] M. Anderlini, E. Courtade, M. Cristiani, D. Cossart, D. Ciampini, C. Sias, O. Morsch, and E. Arimondo, *Sympathetic cooling and collisional properties of a Rb–Cs mixture*, Phys. Rev. A 71, 061401 (2005).

[234] H.-W. Cho, D. J. McCarron, M. P. Köppinger, D. L. Jenkin, K. L. Butler, P. S. Julienne, C. L. Blackley, C. R. Le Sueur, J. M. Hutson, and S. L. Cornish, *Feshbach spectroscopy of an ultracold mixture of* ^{85}Rb *and* ^{133}Cs, Phys. Rev. A 87, 010703(R) (2013).

[235] G. Delannoy, S. G. Murdoch, V. Boyer, V. Josse, P. Bouyer, and A. Aspect, *Understanding the production of dual Bose-Einstein condensation with sympathetic cooling*, Phys. Rev. A 63, 051602 (2001).

[236] G. C. Maitland, M. Rigby, E. B. Smith, and W. A. Wakeham, *Intermolecular Forces* (Oxford University Press, Oxford, 1981), ISBN 0-19-855641-1.

[237] W.-K. Liu, F. R. McCourt, D. E. Fitz, and D. J. Kouri, *Production and relaxation cross sections for the shear viscosity Senftleben–Beenakker effect. I. Formal expressions and their coupled-states and infinite-order–sudden approximations for atom–diatom systems*, J. Chem. Phys. 71, 415 (1979).

[238] M. Anderlini and D. Guéry-Odelin, *Thermalization in mixtures of ultracold gases*, Phys. Rev. A 73, 032706 (2006).

[239] L. Vichi, *Collisional damping of the collective oscillations of a trapped Fermi gas*, Journal of Low Temperature Physics 121, 177 (2000).

[240] G. M. Kavoulakis, C. J. Pethick, and H. Smith, *Collisional relaxation in diffuse clouds of trapped bosons*, Phys. Rev. A 61, 053603 (2000).

[241] M. Lewenstein, J. I. Cirac, and P. Zoller, *Master equation for sympathetic cooling of trapped particles*, Phys. Rev. A 51, 4617 (1995).

[242] F. Baumer, *Isotope dependent interactions in a mixture of ultracold atoms*, Ph.D. thesis, Heinrich-Heine-Universität, Düsseldorf (2010).

[243] F. Baumer, F. Münchow, A. Görlitz, S. E. Maxwell, P. S. Julienne, and E. Tiesinga, *Spatial separation in a thermal mixture of ultracold* ^{174}Yb *and* ^{87}Rb *atoms*, Phys. Rev. A 83, 040702 (2011).

[244] F. Münchow, C. Bruni, M. Madalinski, and A. Görlitz, *Two-photon photoassociation spectroscopy of heteronuclear YbRb*, Phys. Chem. Chem. Phys. 13, 18734 (2011).

[245] F. Münchow, *2-photon photoassociation spectroscopy in a mixture of Ytterbium and Rubidium*, Ph.D. thesis, Heinrich-Heine-Universität, Düsseldorf (2012).

[246] M. Borkowski, P. S. Żuchowski, R. Ciuryło, P. S. Julienne, D. Kedziera, L. Mentel, P. Tecmer, F. Münchow, C. Bruni, and A. Görlitz, *Scattering lengths in isotopologues of the RbYb system*, Phys. Rev. A 88, 052708 (2013).

[247] V. V. Ivanov, A. Y. Khramov, A. H. Hansen, W. H. Dowd, F. Münchow, A. O. Jamison, and S. Gupta, *Sympathetic cooling in an optically trapped mixture of alkali and spin-singlet atoms*, Phys. Rev. Lett. 106, 153201 (2011).

[248] H. Hara, Y. Takasu, Y. Yamaoka, J. M. Doyle, and Y. Takahashi, *Quantum degenerate mixtures of alkali and alkaline-earth-like atoms*, Phys. Rev. Lett. 106, 205304 (2011).

[249] V. D. Vaidya, J. Tiamsuphat, S. L. Rolston, and J. V. Porto, *Degenerate Bose-Fermi mixtures of rubidium and ytterbium*, Phys. Rev. A 92, 043604 (2015).

[250] S. L. Kemp, K. L. Butler, R. Freytag, S. A. Hopkins, E. A. Hinds, M. R. Tarbutt, and S. L. Cornish, *Production and characterization of a dual species magneto-optical trap of cesium and ytterbium*, Review of Scientific Instruments 87, 023105 (2016).

[251] S. A. Hopkins, K. Butler, A. Guttridge, S. Kemp, R. Freytag, E. A. Hinds, M. R. Tarbutt, and S. L. Cornish, *A versatile dual-species zeeman slower for caesium and ytterbium*, Review of Scientific Instruments 87, 043109 (2016).

[252] A. Guttridge, S. A. Hopkins, S. L. Kemp, M. D. Frye, J. M. Hutson, and S. L. Cornish, *Interspecies thermalization in an ultracold mixture of Cs and Yb in an optical trap*, arXiv:1704.03270 (2017).

[253] D. P. Dunseith, S. Truppe, R. J. Hendricks, B. E. Sauer, E. A. Hinds, and M. R. Tarbutt, *A high quality, efficiently coupled microwave cavity for trapping cold molecules*, J. Phys. B 48, 045001 (2015).

[254] T. E. Wall, J. F. Kanem, J. M. Dyne, J. J. Hudson, B. E. Sauer, E. A. Hinds, and M. R. Tarbutt, *Stark deceleration of CaF molecules in strong- and weak-field seeking states*, Phys. Chem. Chem. Phys. 13, 18991 (2011).

[255] J. E. van den Berg, S. C. Mathaven, C. Meinema, J. Nauta, T. H. Nijbroek, K. Jungmann, H. L. Bethlem, and S. Hoekstra, *Traveling-wave deceleration of SrF molecules*, J. Mol. Spectrosc. 300, 22 (2014).

[256] S. Y. Buhmann, M. R. Tarbutt, S. Scheel, and E. A. Hinds, *Surface-induced heating of cold polar molecules*, Phys. Rev. A 78, 052901 (2008).

[257] M. T. Cvitaš, P. Soldán, J. M. Hutson, P. Honvault, and J. M. Launay, *Interactions and dynamics in Li + Li_2 ultracold collisions*, J. Chem. Phys. 127, 074302 (2007).

[258] W. J. Childs, L. S. Goodman, U. Nielsen, and V. Pfeufer, *Electricdipole moment of CaF ($X^2\Sigma^+$) by molecular beam, laserrf, doubleresonance study of Stark splittings*, J. Chem. Phys. 80, 2283 (1984).

[259] A. Derevianko, S. G. Porsev, and J. F. Babb, *Electric dipole polarizabilities at imaginary frequencies for the alkali-metal, alkaline-earth, and inert gas atoms*, Atomic Data and Nuclear Data Tables 96, 323 (2010).

[260] K. T. Tang, *Dynamic polarizabilities and van der Waals coefficients*, Phys. Rev. 177, 108 (1969).

[261] J. J. Lutz and J. M. Hutson, *Reactions between cold methyl halide molecules and alkali-metal atoms*, J. Chem. Phys. 140, 014303 (2014).

[262] M. Kajita and A. V. Avdeenkov, *Collisions between linear polar molecules trapped in a microwave field*, Eur. Phys. J. D 41, 499 (2007).

[263] A. V. Avdeenkov, *Collisions of bosonic ultracold polar molecules in microwave traps*, New J. of Phys. 11, 055016 (2009).

[264] W. Ketterle and N. J. Van Druten, *Evaporative cooling of trapped atoms*, Adv. At. Mol. Opt. Phys. 37, 181 (1996).

[265] M. Lu, N. Q. Burdick, S. H. Youn, and B. L. Lev, *Strongly dipolar Bose-Einstein condensate of dysprosium*, Phys. Rev. Lett. 107, 190401 (2011).

[266] B. Pasquiou, E. Maréchal, L. Vernac, O. Gorceix, and B. Laburthe-Tolra, *Thermodynamics of a Bose-Einstein condensate with free magnetization*, Phys. Rev. Lett. 108, 045307 (2012).

[267] K. Aikawa, A. Frisch, M. Mark, S. Baier, A. Rietzler, R. Grimm, and F. Ferlaino, *Bose-Einstein condensation of erbium*, Phys. Rev. Lett. 108, 210401 (2012).

[268] K. Baumann, N. Q. Burdick, M. Lu, and B. L. Lev, *Observation of low-field Fano-Feshbach resonances in ultracold gases of dysprosium*, Phys. Rev. A 89, 020701 (2014).

[269] T. Maier, I. Ferrier-Barbut, H. Kadau, M. Schmitt, M. Wenzel, C. Wink, T. Pfau, K. Jachymski, and P. S. Julienne, *Broad universal Feshbach resonances in the chaotic spectrum of dysprosium atoms*, Phys. Rev. A 92, 060702 (2015).

[270] M. Morita and J. M. Hutson, *Ultracold collision of Li(^{2}S)+CaH/CaF($^2\Sigma$) in a magnetic field*, in preparation (2016).

[271] M. L. Mehta, *Random Matrices* (Academic Press, 1991), 2nd edition.

[272] T. Guhr, A. Müller-Groeling, and H. A. Weidemüller, *Random matrix theories in quantum physics: common concepts*, Phys. Rep. 299, 189 (1998).

[273] E. P. Wigner, *On the statistical distribution of the widths and spacings of nuclear resonance levels*, Math. Proc. Cambridge 47, 790 (1951).

[274] E. P. Wigner, *On a class of analytic functions from the quantum theory of collisions*, Ann. Math. 53, 36 (1951).

[275] E. P. Wigner, *Characteristic vectors of bordered matrices with infinite dimensions*, Ann. Math. 62, pp. 548 (1955).

[276] E. P. Wigner, *Characteristics vectors of bordered matrices with infinite dimensions II*, Ann. Math. 65, 203 (1957).

[277] E. P. Wigner, *On the distribution of the roots of certain symmetric matrices*, Ann. Math. 67, 325 (1958).

[278] N. Rosenzweig and C. E. Porter, *'Repulsion of energy levels' in complex atomic spectra*, Phys. Rev. 120, 1698 (1960).

[279] M. Mehta, *On the statistical properties of the level-spacings in nuclear spectra*, Nuclear Physics 18, 395 (1960).

[280] M. Mehta and M. Gaudin, *On the density of eigenvalues of a random matrix*, Nuclear Physics 18, 420 (1960).

[281] M. Gaudin, *Sur la loi limite de l'espacement des valeurs propres d'une matrice aleatoire*, Nuclear Physics 25, 447 (1961).

[282] F. J. Dyson, *Statistical theory of the energy levels of complex systems. I*, J. Math. Phys. 3, 140 (1962).

[283] F. J. Dyson, *Statistical theory of the energy levels of complex systems. II*, J. Math. Phys. 3, 157 (1962).

[284] F. J. Dyson, *Statistical theory of the energy levels of complex systems. III*, J. Math. Phys. 3, 166 (1962).

[285] F. J. Dyson and M. L. Mehta, *Statistical theory of the energy levels of complex systems. IV*, J. Math. Phys. 4, 701 (1963).

[286] H. Friedrich and D. Wintgen, *The hydrogen atom in a uniform magnetic field — an example of chaos*, Phys. Rep. 183, 37 (2002).

[287] O. Bohigas, M. J. Giannoni, and C. Schmit, *Characterization of chaotic quantum spectra and universality of level fluctuation laws*, Phys. Rev. Lett. 52, 1 (1984).

[288] S. Müller, S. Heusler, P. Braun, F. Haake, and A. Altland, *Semiclassical foundation of universality in quantum chaos*, Phys. Rev. Lett. 93, 014103 (2004).

[289] S. Heusler, S. Müller, A. Altland, P. Braun, and F. Haake, *Periodic-orbit theory of level correlations*, Phys. Rev. Lett. 98, 044103 (2007).

[290] J. L. Bohn, A. V. Avdeenkov, and M. P. Deskevich, *Rotational Feshbach resonances in ultracold molecular collisions*, Phys. Rev. Lett. 89, 203202 (2002).

[291] P. S. Żuchowski and J. M. Hutson, *Reactions of ultracold alkali metal dimers*, Phys. Rev. A 81, 060703(R) (2010).

[292] M. L. González-Martínez and P. S. Żuchowski, *Magnetically tunable Feshbach resonances in Li+Er*, Phys. Rev. A 92, 022708 (2015).

[293] J. Mur-Petit and R. A. Molina, *Spectral statistics of molecular resonances in erbium isotopes: How chaotic are they?*, Phys. Rev. E 92, 042906 (2015).

[294] K. Jachymski and P. S. Julienne, *Chaotic scattering in the presence of a dense set of overlapping Feshbach resonances*, Phys. Rev. A 92, 020702 (2015).

[295] F. Haake, *Quantum signatures of chaos* (Springer, 2001), 2nd edition.

[296] L. E. Reichl, *The Transition to Chaos: Conservative Classical Systems and Quantum Manifestations* (Springer, 2004), 2nd edition.

[297] M. Aszmann, J. Thewes, D. Frohlich, and M. Bayer, *Quantum chaos and breaking of all anti-unitary symmetries in rydberg excitons*, Nature Materials advance online publication, (2016).

[298] A. Petrov, E. Tiesinga, and S. Kotochigova, *Anisotropy-induced Feshbach resonances in a quantum dipolar gas of highly magnetic atoms*, Phys. Rev. Lett. 109, 103002 (2012).

[299] T. A. Brody, J. Flores, J. B. French, P. A. Mellow, A. Pandey, and S. S. M. Wong, *Random-matrix physics: spectrum and strength fluctuations*, Rev. Mod. Phys. 53, 385 (1981).

[300] M. V. Berry and M. Tabor, *Level clustering in the regular spectrum*, Proc. R. Soc. A 356, 375 (1977).

[301] T. Brody, *A statistical measure for the repulsion of energy levels*, Lett. Nuovo Cimento 7, 482 (1973).

[302] M. V. Berry and M. Robnik, *Semiclassical level spacings when regular and chaotic orbits coexist*, J. Phys. A 17, 2413 (1984).

[303] F. Izrailev, *Quantum localization and statistics of quasienergy spectrum in a classically chaotic system*, Phys. Lett. A 134, 13 (1988).

[304] R. J. Barlow, *Statistics: A Guide to the Use of Statistical Methods in the Physical Sciences* (Wiley, 1989).

[305] R. B. Bernstein (Editor), *Atom-Molecule Collision Theory: a Guide for the Experimentalist* (Plenum Press, New York, 1979).

[306] H.-I. Lu, I. Kozyryev, B. Hemmerling, J. Piskorski, and J. M. Doyle, *Magnetic trapping of molecules via optical loading and magnetic slowing*, Phys. Rev. Lett. 112, 113006 (2014).

[307] T. E. Wall, S. K. Tokunaga, E. A. Hinds, and M. R. Tarbutt, *Nonadiabatic transitions in a Stark decelerator*, Phys. Rev. A 81, 033414 (2010).

[308] R. V. Krems, A. Dalgarno, N. Balakrishnan, and G. C. Groenenboom, *Spin-flipping transitions in $^2\Sigma$ molecules induced by collisions with structureless atoms*, Phys. Rev. A 67, 060703 (2003).

[309] M. Mizushima, *Theory of Rotating Diatomic Molecules* (Wiley, New York, 1975).

[310] S. L. Holmgren, M. Waldman, and W. Klemperer, *Internal dynamics of van der Waals complexes. I. Born–Oppenheimer separation of radial and angular motion*, J. Chem. Phys. 67, 4414 (1977).

[311] J. M. Hutson and B. J. Howard, *Spectroscopic properties and potential surfaces for atom-diatom van der Waals molecules*, Mol. Phys. 41, 1123 (1980).

[312] J. M. Hutson and B. J. Howard, *Anisotropic intermolecular forces. I. Rare gas-hydrogen chloride systems*, Mol. Phys. 45, 769 (1982).

[313] C. R. Le Sueur, J. R. Henderson, and J. Tennyson, *Gateway states and bath states in the vibrational spectrum of* H_3^+, Chem. Phys. Lett. 206, 429 (1993).

[314] G. G. de Polavieja, F. Borondo, and R. M. Benito, *Scars in groups of eigenstates in a classically chaotic system*, Phys. Rev. Lett. 73, 1613 (1994).

[315] N. J. Wright and J. M. Hutson, *Regular and irregular vibrational states: Localized anharmonic modes in* Ar_3, J. Chem. Phys. 110, 902 (1999).

[316] N. J. Wright and J. M. Hutson, *Regular and irregular vibrational states: Localized anharmonic modes and transition-state spectroscopy of* Na_3, J. Chem. Phys. 112, 3214 (2000).

[317] Y. X. Wang and M. Dolg, *Pseudopotential study of the ground and excited states of* Yb_2, Theor. Chem. Acc. 100, 124 (1998).

[318] M. L. González-Martínez and J. M. Hutson, *Magnetically tunable Feshbach resonances in Li +* $Yb(^3P_J)$, Phys. Rev. A 88, 020701(R) (2013).

[319] J. Callaway and E. Bauer, *Inelastic collisions of slow atoms*, Phys. Rev. 140, A1072 (1965).

[320] R. H. G. Reid and A. Dalgarno, *Fine-structure transitions and shape resonances*, Phys. Rev. Lett. 22, 1029 (1969).

[321] V. Aquilanti and G. Grossi, *Angular momentum coupling schemes in the quantum mechanical treatment of P state atom collisions*, J. Chem. Phys. 73, 1165 (1980).

[322] R. V. Krems, G. C. Groenenboom, and A. Dalgarno, *Electronic interaction anisotropy between atoms in arbitrary angular momentum states*, J. Phys. Chem. A 108, 8941 (2004).

[323] A. J. Stone, *The Theory of Intermolecular Forces* (Oxford University Press, Oxford, 1996).

[324] S. G. Porsev, M. S. Safronova, A. Derevianko, and C. W. Clark, *Long-range interaction coefficients for ytterbium dimers*, Phys. Rev. A 89, 012711 (2014).

[325] W. F. Meggers and J. L. Tech, *The first spectrum of ytterbium (Yb I)*, J. Res. Natl. Bur. Stand. (U.S.) 83, 13 (1978).

[326] S. Uetake, R. Murakami, J. M. Doyle, and Y. Takahashi, *Spin-dependent collision of ultracold metastable atoms*, Phys. Rev. A 86, 032712 (2012).

[327] D. G. Green, C. L. Vaillant, and J. M. Hutson, *Feshbach resonances and inelastic decay in ultracold* $Yb(^1S_0)+Yb(^3P_2)$ *collisions*, in preparation (2016).

[328] S. Kato, S. Sugawa, K. Shibata, R. Yamamoto, and Y. Takahashi, *Control of resonant interaction between electronic ground and excited states*, Phys. Rev. Lett. 110, 173201 (2013).

[329] S. Taie, S. Watanabe, T. Ichinose, and Y. Takahashi, *Feshbach-resonance-enhanced coherent atom-molecule conversion with ultranarrow photoassociation resonance*, Phys. Rev. Lett. 116, 043202 (2016).

[330] F. A. Lindemann, S. Arrhenius, I. Langmuir, N. R. Dhar, J. Perrin, and W. C. McC. Lewis, *Discussion on "the radiation theory of chemical action"*, Trans. Faraday Soc. 17, 598 (1922).

[331] B. D. Esry, C. H. Greene, and J. P. Burke, *Recombination of three atoms in the ultracold limit*, Phys. Rev. Lett. 83, 1751 (1999).

[332] F. T. Smith, *Lifetime matrix in collision theory*, Phys. Rev. 118, 349 (1960).

[333] P. O. Fedichev, M. W. Reynolds, and G. V. Shlyapnikov, *Three-body recombination of ultracold atoms to a weakly bound s level*, Phys. Rev. Lett. 77 (1996).

[334] B. D. Esry, C. H. Greene, and H. Suno, *Threshold laws for three-body recombination*, Phys. Rev. A 65, 010705 (2001).

[335] E. Braaten and H. W. Hammer, *Three-body recombination into deep bound states in a bose gas with large scattering length*, Phys. Rev. Lett. 8716, 160407 (2001).

[336] E. Nielsen, H. Suno, and B. D. Esry, *Efimov resonances in atom-diatom scattering*, Phys. Rev. A 66, 012705 (2002).

[337] T. Weber, J. Herbig, M. Mark, H. C. Nägerl, and R. Grimm, *Three-body recombination at large scattering lengths in an ultracold atomic gas*, Phys. Rev. Lett. 91, 123201 (2003).

[338] J. P. D'Incao and B. D. Esry, *Scattering length scaling laws for ultracold three-body collisions*, Phys. Rev. Lett. 94, 213201 (2005).

[339] J. Wang, J. P. D'Incao, B. D. Esry, and C. H. Greene, *Origin of the three-body parameter universality in efimov physics*, Phys. Rev. Lett. 108, 263001 (2012).

[340] Y. Wang and P. S. Julienne, *Universal van der Waals physics for three cold atoms near Feshbach resonances*, Nat Phys 10, 768 (2014).

[341] L. Eisenbud, dissertation (1948).

[342] E. P. Wigner, *Lower limit for the energy derivative of the scattering phase shift*, Phys. Rev. 98, 145 (1955).

[343] M. P. Köppinger, , D. J. McCarron, D. L. Jenkin, P. K. Molony, H.-W. Cho, S. L. Cornish, C. R. Le Sueur, C. L. Blackley, and J. M. Hutson, *Production of optically trapped $^{87}Rb^{133}Cs$ feshbach molecules*, Phys. Rev. A 89, 033604 (2014).

[344] G. A. Parker, R. B. Walker, B. K. Kendrick, and R. T Pack, *Accurate quantum calculations on three-body collisions in recombination and collision-induced dissociation. I. converged probabilities for the H+Ne_2 system*, J. Chem. Phys. 117, 6083 (2002).

[345] F. T. Smith, *Generalized angular momentum in many-body collisions*, Phys. Rev. 120, 1058 (1960).

[346] L. Delves, *Tertiary and general-order collisions*, Nuclear Physics 9, 391 (1958–1959).

[347] G. Quéméner, P. Honvault, J. M. Launay, P. Soldán, D. E. Potter, and J. M. Hutson, *Ultracold quantum dynamics: Spin-polarized $K+K_2$ collisions with three identical bosons or fermions*, Phys. Rev. A 71, 032722 (2005).

[348] V. Efimov, *Energy levels arising from resonant two-body forces in a three-body system*, Physics Letters B 33, 563 (1970).

[349] J. Blandon, G. A. Parker, and C. Madrid, *Mapped grid methods applied to the slow variable discretization–enhanced renormalized numerov approach*, The Journal of Physical Chemistry A 120, 785, pMID: 26797269 (2016).

[350] Y. Chen and B. Gao, *Multiscale quantum-defect theory for two interacting atoms in a symmetric harmonic trap*, Phys. Rev. A 75, 053601 (2007).

[351] K. Jachymski, Z. Idziaszek, and T. Calarco, *Feshbach resonances in a nonseparable trap*, Phys. Rev. A 87, 042701 (2013).

[352] K. Jachymski, *Impact of overlapping resonances on magnetoassociation of cold molecules in tight traps*, Journal of Physics B: Atomic, Molecular and Optical Physics 49, 195204 (2016).